

Ministry of Education and Science of the Russian Federation
Saint Petersburg National Research University of Information
Technologies, Mechanics, and Optics

NANOSYSTEMS:
PHYSICS, CHEMISTRY, MATHEMATICS

2018, volume 9(1)

Наносистемы: физика, химия, математика

2018, том 9, № 1



NANOSYSTEMS:

PHYSICS, CHEMISTRY, MATHEMATICS

ADVISORY BOARD MEMBERS

Chairman: V.N. Vasiliev (*St. Petersburg, Russia*),
V.M. Buznik (*Moscow, Russia*); V.M. Ievlev (*Voronezh, Russia*), P.S. Kop'ev (*St. Petersburg, Russia*), N.F. Morozov (*St. Petersburg, Russia*), V.N. Parmon (*Novosibirsk, Russia*),
A.I. Rusanov (*St. Petersburg, Russia*),

EDITORIAL BOARD

Editor-in-Chief: I.Yu. Popov (*St. Petersburg, Russia*)

Section Co-Editors:

Physics – V.M. Uzdin (*St. Petersburg, Russia*),

Chemistry, material science – V.V. Gusarov (*St. Petersburg, Russia*),

Mathematics – I.Yu. Popov (*St. Petersburg, Russia*).

Editorial Board Members:

V.M. Adamyan (*Odessa, Ukraine*); O.V. Al'myasheva (*St. Petersburg, Russia*);
A.P. Alodjants (*Vladimir, Russia*); S. Bechta (*Stockholm, Sweden*); J. Behrndt (*Graz, Austria*);
M.B. Belonenko (*Volgograd, Russia*); V.G. Bepalov (*St. Petersburg, Russia*); J. Brasche
(*Clausthal, Germany*); A. Chatterjee (*Hyderabad, India*); S.A. Chivilikhin (*St. Petersburg, Russia*);
A.V. Chizhov (*Dubna, Russia*); A.N. Enyashin (*Ekaterinburg, Russia*), P.P. Fedorov
(*Moscow, Russia*); E.A. Gudilin (*Moscow, Russia*); V.K. Ivanov (*Moscow, Russia*),
H. Jónsson (*Reykjavik, Iceland*); A.A. Kiselev (*Durham, USA*); Yu.S. Kivshar (*Canberra, Australia*);
S.A. Kozlov (*St. Petersburg, Russia*); P.A. Kurasov (*Stockholm, Sweden*);
A.V. Lukashin (*Moscow, Russia*); V.A. Margulis (*Saransk, Russia*); I.V. Melikhov (*Moscow, Russia*);
G.P. Miroshnichenko (*St. Petersburg, Russia*); I.Ya. Mittova (*Voronezh, Russia*);
H. Neidhardt (*Berlin, Germany*); V.V. Pankov (*Minsk, Belarus*); K. Pankrashkin (*Orsay, France*);
A.V. Ragulya (*Kiev, Ukraine*); V. Rajendran (*Tamil Nadu, India*); A.A. Rempel
(*Ekaterinburg, Russia*); V.Ya. Rudyak (*Novosibirsk, Russia*); D. Shoikhet (*Karmiel, Israel*);
P. Stovicek (*Prague, Czech Republic*); V.M. Talanov (*Novocherkassk, Russia*); A.Ya. Vul'
(*St. Petersburg, Russia*); A.V. Yakimansky (*St. Petersburg, Russia*), V.A. Zagrebnoy
(*Marseille, France*).

Editors:

I.V. Blinova; A.I. Popov; A.I. Trifanov; E.S. Trifanova (*St. Petersburg, Russia*),
R. Simoneaux (*Philadelphia, Pennsylvania, USA*).

Address: University ITMO, Kronverkskiy pr., 49, St. Petersburg 197101, Russia.

Phone: +7(812)312-61-31, **Journal site:** <http://nanojournal.ifmo.ru/>,

E-mail: popov1955@gmail.com

AIM AND SCOPE

The scope of the journal includes all areas of nano-sciences. Papers devoted to basic problems of physics, chemistry, material science and mathematics inspired by nanosystems investigations are welcomed. Both theoretical and experimental works concerning the properties and behavior of nanosystems, problems of its creation and application, mathematical methods of nanosystem studies are considered.

The journal publishes scientific reviews (up to 30 journal pages), research papers (up to 15 pages) and letters (up to 5 pages). All manuscripts are peer-reviewed. Authors are informed about the referee opinion and the Editorial decision.

CONTENT

From Guest Editorial	5
I.V. Mikheev, L.O. Usoltseva, D.A. Ivshukov, D.S. Volkov, M.V. Korobov, M.A. Proskurnin Thermal-lens spectrometer for studying termophysical properties of fullerenes	14
L.O. Usoltseva, D.S. Volkov, N.V. Avramenko, M.V. Korobov, M.A. Proskurnin Nanodiamond aqueous dispersions as potential nanofluids: the determination of properties by thermal lensing and other techniques	17
S.V. Kidalov, V.V. Shnitov, M.V. Baidakova, M. Brzhezinskaya, A.T. Dideikin, M.S. Shestakov, D.A. Smirnov, I.T. Serenkov, V.I. Sakharov, V.V. Sokolov, N.I. Tatarnikov, A.Ya. Vul' Chemical composition of surface and structure of defects in diamond single crystals produced from detonation nanodiamonds	21
V.N. Khabashesku, V.P. Filonenko, A.S. Anokhin, E.V. Kukueva Phase stability of fluorinated nanodiamonds under HPHT treatment	25
K.P. Meletov, J. Arvanitidis, D. Christofilos, G. Kourouklis, V.A. Davydov Stability at high temperature and decomposition kinetics of the fullerene dimers and photopolymers	29
A.V. Kuzmin, D.V. Konarev, S.S. Khasanov, K.P. Meletov Crystal structure and Raman spectra of molecular complex $[\{Cd(Et_2dtc)\}_2 \cdot DABCO] \cdot C_{60} \cdot (DABCO)_2$ at high pressure	33
A.V. Bazhenov, D.N. Borisenko, E.B. Borisenko, A.S. Senchenkov, A.V. Egorov, N.N. Kolesnikov, A.A. Levchenko Terrestrial development of the experiments on the fullerite C_{60} crystal growth in microgravity	38
I.V. Mikheev, M.O. Pirogova, T.A. Bolotnik, D.S. Volkov, M.V. Korobov, M.A. Proskurnin Optimization of the solvent-exchange process for high-yield synthesis of aqueous fullerene dispersions	41
N.M. Safyannikov, N.A. Charykov, P.V. Garamova, K.N. Semenov, V.A. Keskinov, A.V. Kurilenko, I.A. Cherepcova, D.P. Tyurin, V.V. Klepikov, M.Yu. Matuzenko, N.A. Kulenova, A.A. Zolotarev Cryometry data in the binary systems bis-adduct of C_{60} and indispensable aminoacids – lysine, threonine, oxyproline	46
A.M. Vervald, S.A. Burikov, I.I. Vlasov, O.A. Shenderova, T.A. Dolenko Interactions of nanodiamonds and surfactants in aqueous suspensions	49
E.A. Ekimov, V.S. Krivobok, S.G. Lyapin, P.S. Sheri, V.A. Gavva, M.V. Kondrin Isotopic effects in impurity-vacancy complexes in diamond	52
S.G. Lyapin, I.D. Ilichev, A.P. Novikov, V.A. Davydov, V.N. Agafonov Study of optical properties of the NV and SiV centres in diamond at high pressures	55
V.E. Korsukov, P.N. Butenko, A.G. Kadomtsev, M.M. Korsukova, V.S. Levitskii, I.A. Nyapshaev, B.A. Obidov Effect of heat treatment and tension on the surface morphology of thin Pt foils	58
O.Yu. Ananina, O.V. Ponomarev, A.I. Ryazanova, N.A. Lvova Hemisorption of hydrogen on the diamond surface containing a “boron + vacancy” defect	61
E.N. Vervald, K.A. Laptinskiy, I.I. Vlasov, O.A. Shenderova, T.A. Dolenko DNA–nanodiamond interactions influence on fluorescence of nanodiamonds	64
S.G. Lyapin, A.A. Razgulov, A.P. Novikov, E.A. Ekimov, M.V. Kondrin High pressure photoluminescence studies of diamond with GeV centres	67

O.B. Tomilin, E.V. Rodionova, E.A. Rodin, E.E. Muryumin Influence of admixture atoms chemisorption on properties of p-electron conjugated system of open carbon nanotubes	70
S.A. Sozykin, V.P. Beskachko Optical properties of defective carbon nanotube (7,7)	73
M.V. Il'ina, O.I. Il'in, N.N. Rudyk, A.A. Konshin, O.A. Ageev The memristive behavior of non-uniform strained carbon nanotubes	76
N.P. Boroznina, I.V. Zaporotskova, S.V. Boroznin Sensitivity of carboxyl-modified carbon nanotubes to alkaline metals	79
G.S. Bocharov, M.S. Egin, A.V. Eletskii, V.L. Kuznetsov Filling carbon nanotubes with argon	85
Yu.A. Polikarpov, A.V. Romashkin, V.A. Petukhov, V.K. Nevolin Formation of the nanoscale contacts structure based on cross-junction of carbon nanotubes for the study of organic materials	89
O.I. Il'in, M.V. Il'ina, N.N. Rudyk, A.A. Fedotov, O.A. Ageev The growth temperature effect on vertically aligned carbon nanotubes parameters	92
S.P. Lebedev, V.Yu. Davydov, D.Yu. Usachov, A.N. Smirnov, V.S. Levitskii, I.A. Eliseyev, E.V. Guschina, M.S. Dunaevskiy, O.Yu. Vilkov, A.G. Rybkin,, A.A. Lebedev, S.N. Novikov, Yu.N. Makarov Graphene on silicon carbide as a basis for gas- and biosensor applications	95
G.S. Bocharov, A.V. Eletskii, V.P. Mel'nikov Electrical properties of thermally reduced graphene oxide	98
A.N. Blokhin, T.P. Dyachkova, A.K. Sukhorukov, D.E. Kobzev, E.V. Galunin, A.V. Maksimkin, A.S. Mostovoy, A.P. Kharitonov Composite materials using fluorinated graphene nanoplatelets	102
O.A. Shinkarenko, M.V. Pozharov, A.S. Kolesnikova, A.S. Chumakov, A.J.K. Al-Alwani, O.Yu. Tsevtkova, E.G. Glukhovskoy Catalytic pyrene and pyrene butyric acid condensation as a means of producing graphene	106
A.V. Arkhipov, A.M. Zhurkin, O.E. Kvashenkina, V.S. Osipov, P.G. Gabdullin Electron overheating during field emission from carbon island films due to phonon bottleneck effect	110
A.E. Kucherova, I.V. Burakova, A.E. Burakov, E.V. Galunin, A.V. Babkin, E.A. Neskromnaya An equilibrium study of the liquid-phase sorption of Lead (II) ions on nanoporous carbon materials	114
A.V. Babkin, I.V. Burakova, A.E. Burakov, E.A. Neskromnaya, A.E. Kucherova, D.A. Kurnosov Kinetics of the Cu(II) sorption from aqueous solutions by carbon nanomaterials	117
A.S. Garanina, I.I. Kireev, I.B. Alieva, A.G. Majouga, V.A. Davydov, S. Murugesan, V.N. Khabashesku, V.N. Agafonov, R.E. Uzbekov New superparamagnetic fluorescent Fe@C-C₅ON₂H₁₀-Alexa Fluor 647 nanoparticles for biological applications	120
E.A. Kiseleva, M.A. Zhurilova, E.I. Shkolnikov Electrodes of supercapacitors from nanoporous carbon with nanocarbon additives	123
A.P. Voznyakovskii, A.Yu. Neverovskaya, Ja.A. Otvalko, E.V. Gorelova, A.N. Zabelina Facile synthesis of 2D carbon structures as a filler for polymer composites	125
S.N. Kapustin, M.K. Eseev Ion sputtering of nanoclusters, fullerenes and carbon nanotubes	129
A.V. Igo Influence of geometry of nanocrystals on the Raman spectra	132
Information for authors	136

From Guest Editorial

This special volume of **“NANOSYSTEMS: PHYSICS, CHEMISTRY, MATHEMATICS”** presents the Proceedings of the 13-th Biennial International Conference “Advanced Carbon Nanostructures” (ACNS’2017) held on July 3-7, 2017 in St. Petersburg, Russia.

The tradition of the Conference takes its beginning in 1993 in St. Petersburg from the first International Workshop “Fullerenes and Atomic Clusters” (IWFAC). Since that time, it has been held every two years, attracting members of the nanocarbon scientific community from all over in the world. In 2011, the Conference was joined with International Symposium “Detonation Nanodiamonds: Technology, Properties and Applications” under the title “Advanced Carbon Nanostructures”.

The 13th Conference ACNS’2017 has brought together 199 participants from the leading scientific centers and universities of Russia, Belarus, Australia, China, Czech Republic, Finland, France, Germany, India, Italy, Israel, Japan, Kazakhstan, USA, Iran, Spain, Sweden, and the UK. We believe that ACNS’2017 has become one of the most representative meetings in the field of the nanocarbon science. All aspects of nanocarbon research were covered by the Conference and the appropriate articles were included in the Proceedings. The topics of the papers include not only various questions of physics, chemistry of fullerenes, nanodiamond particles, nanotubes, graphene and other nanocarbon materials, but also covered the wide range of their applications.

The ACNS’2017, was organized by Ioffe Institute, St. Petersburg Nuclear Physics Institute, National Research Center “Kurchatov Institute”, Moscow, and St. Petersburg State Technological Institute (Technical University), St. Petersburg. We would like to express our gratitude to the official partners of the ACNS’2017 – Russian Foundation for Basic Research, Fund for Infrastructure and Educational Programs, DIACEL Corporation, SOL Instruments Ltd, Technoinfo Ltd, as well as the Journal “Nanosystems: Physics, Chemistry, Mathematics”. We greatly appreciate the active help of the International Advisory Committee and Program Committee members for their important advices in determining subject area of ACNS’2017, the list of invited speakers and oral speakers and invaluable help in reviewing the manuscripts for Proceedings.

Taking into account the wishes of all the participants of our conferences, it was decided to organize the next conference “Advanced Carbon Nanostructures” on July 2019, and we will be pleased to welcome the members of world nanocarbon community to St.Petersburg.

Artur T. Dideikin, Alexander P. Meilakhs and Larisa V. Sharonova.
Guest editors of ACNS’2017

Special Issue: Proceedings of the 13th Biennial International Conference “Advanced Carbon Nanostructures” (ACNS’2017)

Organizers

- Ioffe Institute, St. Petersburg, Russia
- National Research Centre "Kurchatov Institute", Moscow, Russia
- Petersburg Nuclear Physics Institute named after B.P. Konstantinov of National Research Centre "Kurchatov Institute", St. Petersburg, Russia
- St. Petersburg State Technological Institute “Technical University”, St. Petersburg, Russia

Official Partners

- Russian Foundation for Basic Research
- Fund for Infrastructure and Educational Programs
- DAICEL Corporation
- SOL instruments Ltd.
- Technoinfo Ltd.

International Advisory Committee

Banhart F.	Strasbourg University, France
Davidson J.	Vanderbilt University, USA
Echegoyen L.	University of Texas At El Paso, USA
Enoki T.	Tokyo Institute of Technology, Japan
Gruen D.	Argonne National Laboratory, USA
Guldi D.	University of Erlangen-Nurnberg, Germany
Kalish R.	Israel Institute of Technology, Technion, Israel
Kraetschmer W.	Max-Planck Institute, Germany
Osawa E.	Nanocarbon Research Institute Ltd., Japan
Shinohara H.	Nagoya University, Japan
Wudl F.	University of California, USA

International Programme Committee

Dideikin A.T.	Chair , Ioffe Institute, St. Petersburg, Russia
Meilakhs A.P.	Secretary , Ioffe Institute, St. Petersburg, Russia
Shnitov V.V.	Secretary , Ioffe Institute, St. Petersburg, Russia
Aksenov V.L.	Joint Institute for Nuclear Research, Dubna, Russia
Aleksensky A.E.	Ioffe Institute, St. Petersburg, Russia
Artjomov A.S.	Prokhorov General Physics Institute, Moscow, Russia
Baidakova M.V.	Ioffe Institute, St. Petersburg, Russia
Dolmatov V.Yu.	Federal State Unitary Enterprise "Special Design and Technological Office "Technolog", St. Petersburg, Russia
Eletskii A.V.	National Research Center "Kurchatov Institute", Russia
Korobov M.V.	Moscow State University, Russia
Kozyrev S.V.	Peter the Great St. Petersburg Polytechnical University, St. Petersburg, Russia
Krestinin A.V.	Institute of Problems of Chemical Physics, Russia
Kulakova I.I.	Moscow State University, Russia
Kuznetsov V.L.	Boreskov Institute of Catalysis, Novosibirsk, Russia
Piotrovskiy L.B.	Institute of Experimental Medicine, St. Petersburg, Russia
Shenderova O.A.	International Technology Center, USA

Shikin A.M.	St. Petersburg State University, Russia
Sokolov V.I.	Institute of Organoelement Compounds, Moscow, Russia
Titov V.M.	Institute of Hydrodynamics, Novosibirsk, Russia
Vozniakovskii A.P.	Federal State Unitary Enterprise Scientific Research Institute for Synthetic Rubber, St. Petersburg, Russia
Vul' A.Ya.	Ioffe Institute, St. Petersburg, Russia

Organizing Committee

Vul' A.Ya.	Conference Chair , Ioffe Institute, Russia
Vorobyova I.V.	Secretary , Ioffe Institute, St. Petersburg, Russia
Chaivanov B.B.	National Research Center "Kurchatov Institute", Russia
Eremenko I.L.	Kurnakov Institute of General and Inorganic Chemistry, Russia
Ezhov V.F.	Petersburg Nuclear Physics Institute named by B.P. Konstantinov of National Research Centre "Kurchatov Institute", St. Petersburg, Russia
Kop'ev P.S.	Ioffe Institute, St. Petersburg, Russia
Kveder V.V.	Institute of Solid State Physics, Chernogolovka, Russia
Romanovsky M.Yu.	Department of General Physics, Russian Academy of Science
Shevchik A.P.	St. Petersburg State Technological Institute (technical university), Russia
Tsyganov S.A.	Russian Foundation for Basic Research, Russia
Zabrodsky A.G.	Ioffe Institute, Russia

List of Participants

Alekseev Nikolai LETI University <i>NIAllekseyev@yandex.ru</i>	Russia	Anisimov Andrey Ioffe Institute <i>aan0100@gmail.com</i>	Russia
Ageeva Ekaterina Technological Institute for Superhard and Novel Carbon Materials <i>ageeva@phystech.edu</i>	Russia	Arkipov Alexander St. Petersburg Polytechnic University <i>arkhipov@rphf.spbstu.ru</i>	Russia
Ahmadi Kashani Mina University of Kashan <i>ahmadimina133@gmail.com</i>	Iran	Babkin Alexander Tambov State Technical University <i>flex_trol@mail.ru</i>	Russia
Akhmetov Arslan Institute of Petrochemistry and Catalysis of RAS <i>ahmetov_arslan@mail.ru</i>	Russia	Banhart Florian University of Strasbourg <i>florian.banhart@ipcms.unistra.fr</i>	France
Amsharov Konstantin Friedrich-Alexander-University-Erlangen-Nurnberg <i>konstantin.amsharov@fau.de</i>	Germany	Baranov Alexander ITMO University <i>a_v_baranov@yahoo.com</i>	Russia
Amusia Miron Ioffe Institute <i>miron.amusia@mail.ioffe.ru</i>	Russia	Begletsova Nadejda Saratov State University <i>nadya-beg98@yandex.ru</i>	Russia
Andreev Sergey NRC Institute of Immunology FMBA <i>sm.andreev@nrcii.ru</i>	Russia	Bessho Takeshi Nagoya University <i>bessho@gvm.nagoya-u.ac.jp</i>	Japan
		Blokhin Alexander Tambov State Technical University <i>cha-cha@rambler.ru</i>	Russia

Bocharov Grigoriy National Research University "Moscow Power Engineering Institute" <i>BocharovGS@mail.ru</i>	Russia	Dolmatov Valerii FSUE SCTB "Technolog" <i>diamondcentre@mail.ru</i>	Russia
Bogdanov Sergey Institute of Applied Physics RAS <i>bogser@appl.sci-nnov.ru</i>	Russia	Dubois Marc Institut de Chimie de Clermont-Ferrand <i>marc.dubois@uca.fr</i>	France
Borisenko Dmitrii Institute of Solid State Physics <i>bdn@issp.ac.ru</i>	Russia	Dvuzhilov Ilya Volgograd State University <i>dvuzhilov.ilya@gmail.com</i>	Russia
Boroznin Sergei Volgograd State University <i>sboroznin@mail.ru</i>	Russia	Eidelman Evgeny Ioffe Institute; St.Petersburg Chemical-Pharmaceutical Academy <i>9929617@mail.ru</i>	Russia
Boroznina Natalia Volgograd State University <i>n.z.1103@mail.ru</i>	Russia	Elbakyan Lusine Volgograd State University <i>lusniak-e@yandex.ru</i>	Russia
Chernozatonskiy Leonid Emanuel Institute of Biochemical Physics RAS <i>chernol-43@mail.ru</i>	Russia	Eletskii Alexander Moscow Power Engineering Institute (Technical University) <i>Eletskii@mail.ru</i>	Russia
Chernysheva Maria Lomonosov Moscow State University <i>masha.chernysheva@gmail.com</i>	Russia	Elistratova Marina Ioffe Institute <i>elistratovamari@yandex.ru</i>	Russia
Chesnokov Vladimir Boreskov Institute of Catalysis <i>chesn@catalysis.ru</i>	Russia	Emelianov Aleksei National Research University of Electronic Technology <i>emmsowton@gmail.com</i>	Russia
Churilov Grigory Kirensky Institute of Physics Federal Research Center KSC SBR <i>churilov@iph.krasn.ru</i>	Russia	Enoki Toshiaki Tokyo Institute of Technology <i>tenoki@chem.titech.ac.jp</i>	Japan
Cigler Petr Institute of Organic Chemistry and Biochemistry AS CR <i>cigler@uochb.cas.cz</i>	Czech Republic	Ershov Igor Don State Technical University <i>thijd@mail.ru</i>	Russia
Davydov Valery L.F. Vereshchagin Institute for High Pressure Physics <i>vdavydov@hppi.troitsk.ru</i>	Russia	Estyunin Dmitry Saint-Petersburg State University <i>estyunin@gmail.com</i>	Russia
Dehghani Ghorbi Hossein Department of Inorganic Chemistry, Faculty of Chemistry, University of Kashan, Kashan, Iran <i>dehghani@kashanu.ac.ir</i>	Iran	Evlashin Stanislav Moscow State University <i>stevlashin@gmail.com</i>	Russia
Deshpande Parag Arvind Indian Institute of Technology Kharagpur <i>parag@che.iitkgp.ernet.in</i>	India	Faradzheva Mislmat SPbPU <i>mislmat92@gmail.com</i>	Russia
		Fomina Irina IGIC RAS <i>fomina@igic.ras.ru</i>	Russia

Galunin Evgeny Tambov State Technical University <i>evgeny.galunin@gmail.com</i>	Russia	Ilin Oleg Southern Federal University <i>oleg.ilin.sfedu@gmail.com</i>	Russia
Gazizov Ruslan Moscow State University <i>rushim@bk.ru</i>	Russia	Ilina Marina Southern Federal University <i>mailina@sfedu.ru</i>	Russia
Girard Hugues CEA, LIST, Diamond Sensors Laboratory <i>hugues.girard@cea.fr</i>	France	Ismailov Daniyar Kazakh National University Al-Farabi <i>Ismailov_Daniyar_V@bk.ru</i>	Kazakhstan
Goloudina Svetlana Saint-Petersburg Electrotechnical University "LETY" <i>goloudina@mail.ru</i>	Russia	Ivanov Michail Ural Federal University <i>m.g.ivanov@urfu.ru</i>	Russia
Golov Andrey Samara Center for Theoretical Materials Science, Samara University <i>angolov1990@mail.ru</i>	Russia	Kaalbac Martin J. Heyrovsky Institute of Physical Chemistry <i>kalbac@jh-inst.cas.cz</i>	Czech Republic
Goryunkov Alexey Lomonosov Moscow State University <i>aag@thermo.chem.msu.ru</i>	Russia	Kalbáčová Vejpravová Jana Charles University <i>jana@mag.mff.cuni.cz</i>	Czech Republic
Goryunov Andrey Institute of Biology, Karelian Research Centre RAS <i>goryunov@krc.karelia.ru</i>	Russia	Kalyuzhnyy Sergey LLC MC Rusnano <i>Sergey.Kalyuzhnyi@rusnano.com</i>	Russia
Grudinkin Sergey Ioffe Institute <i>grudink@gvg.ioffe.ru</i>	Russia	Kapystin Sergey Northern (Arctic) Federal University named after M.V. Lomonosov <i>hare22@yandex.ru</i>	Russia
Gudkov Maksim Semenov Institute of Chemical Physics RAS <i>GOOD_ok-eee@mail.ru</i>	Russia	Kauppinen Esko Aalto University School of Science <i>esko.kauppinen@aalto.fi</i>	Finland
Gurova Olga Nikolaev Institute of Inorganic Chemistry SB RAS <i>olga.gurov@gmail.com</i>	Russia	Khabashesku Valery Baker Hughes Inc. <i>khvalery@gmail.com</i>	United States
Heggie Malcolm University of Loughborough <i>malcolm.heggie@gmail.com</i>	United Kingdom (Great Britain),	Kidalov Sergey Ioffe Institute <i>Kidalov@mail.ioffe.ru</i>	Russia
Herraiz Michael Institut de Chimie de Clermont-Ferrand <i>michael.herraiz@uca.fr</i>	France	Kiseleva Elena Joint Institute for High Temperatures RAS <i>kanna787@mail.ru</i>	Russia
Ichino Ryoichi Nagoya University <i>arara.iori.ryo@gmail.com</i>	Japan	Komarov Ivan National Research University of Electronic Technology <i>master_kom@mail.ru</i>	Russia
Igo Alexander Ulyanovsk State University <i>igoalexander@mail.ru</i>	Russia	Konarev Dmitry Institute of Problems of Chemical Physics RAS <i>konarev3@yandex.ru</i>	Russia

Kondrin Mikhail Institute for High Pressure Physics <i>mkondrin@hppi.troitsk.ru</i>	Russia	Kyzyma Olena Joint Institute for Nuclear Research <i>kizima@nf.jinr.ru</i>	Russia
Koniakhin Sergei St. Petersburg Academic University <i>roch@ya.ru</i>	Russia	Lebedev Sergey Ioffe Institute <i>lebedev.sergey@mail.ioffe.ru</i>	Russia
Konobeeva Natalia Volgograd State University <i>yana_nn@inbox.ru</i>	Russia	Lebedev Vasily Petersburg Nuclear Physics Institute, NRC Kurchatov Institute <i>lebedev_vt@pnpi.nrcki.ru</i>	Russia
Korobov Mikhail Moscow State University <i>mkorobov49@gmail.com</i>	Russia	Lebedev Vyacheslav ITMO University <i>lebedev@oi.ifmo.ru</i>	Russia
Korsukov Vjacheslav Ioffe Institute <i>vjacheslav.korsukov@mail.ioffe.ru</i>	Russia	Leshchev Dmitrii CAS of Peter the Great St.Petersburg Polytechnic University <i>dimvovich@narod.ru</i>	Russia
Kosaya Mariya MSU <i>maria.cosaya@yandex.ru</i>	Russia	Liu Ming Daicel Corporation <i>liu_ming@jp.daicel.com</i>	Japan
Kostogrud Ilya Institute of Thermophysics SB RAS <i>ikostogrud@gmail.com</i>	Russia	Loktionov Alexey ITKOR <i>cstalexey@gmail.com</i>	Russia
Kotin Igor Rzhanov Institute of Semiconductor Physics SB RAS <i>kotin@isp.nsc.ru</i>	Russia	Machida Tomoki Institute of Industrial Science, University of Tokyo <i>tmachida@iis.u-tokyo.ac.jp</i>	Japan
Kozyrev Sergey SPbPU, Center for Advanced Studies <i>kozyrev@spbcas.ru</i>	Russia	Maltsev Alexander Emanuel Institute of Biochemical Physics <i>aam.0205@yandex.ru</i>	Russia
Krasheninnikov Arkady Helmholtz-Zentrum Dresden-Rossendorf <i>a.krasheninnikov@hzdr.de</i>	Germany	Meilakhs Aleksandr Ioffe Institute <i>estfi@mail.ru</i>	Russia
Krupka Miloslav OZM Research <i>krupka@ozm.cz</i>	Czech Republic	Meletov Konstantin Institut of Solid State Physics RAS <i>mele@issp.ac.ru</i>	Russia
Kudryavtsev Oleg Prokhorov General Physics Institute RAS <i>leolegk@mail.ru</i>	Russia	Meshkov Georgy Lomonosov Moscow State University <i>meshkov@polly.phys.msu.ru</i>	Russia
Kulakova Inna Lomonosov Mocsow State University <i>inna-kulakova@yandex.ru</i>	Russia	Mikhailova Svetlana al-Farabi Kazakh National University <i>skysvetik91@mail.ru</i>	Kazachstan
Kuzmin Alexey Institute of Solid State Physics RAS <i>kuzminav@issp.ac.ru</i>	Russia	Mikheev Ivan Lomonosov Moscow Sate University <i>mikheev.ivan@gmail.com</i>	Russia
Kuznetsov Nikita NRC "Kurchatov Institute" <i>kyz993@yandex.ru</i>	Russia		

Mordkovich Vladimir Technological Institute for Superhard and Novel Carbon Materials <i>mordkovich@tisnum.ru</i>	Russia	Petrov Mikhail Saint-Petersburg State University <i>m.p.petrov@spbu.ru</i>	Russia
Moshnikov Igor Institute of Geology Karelian Research Centre of RAS <i>igorm@krc.karelia.ru</i>	Russia	Plastun Inna Saratov State Technical University named after Y.A. Gagarin <i>inna_pls@mail.ru</i>	Russia
Myasnikov Ivan Lomonosov MSU <i>myasnikov751@gmail.com</i>	Russia	Polikarpov Yuri National Research University of Electronic Technology <i>jurij.polikarpov@yandex.ru</i>	Russia
Nehlig Emilie LMT / SCBM / Joliot / CEA Saclay <i>Emilie.Nehlig@cea.fr</i>	France	Popov Alexey Leibniz Institute for Solid State and Materials Research (IFW Dresden) <i>a.popov@ifw-dresden.de</i>	Germany
Nagorna Tetiana Joint Institute for Nuclear Research <i>tanya@nf.jinr.ru</i>	Russia	Popov Vladimir National University of Science and Technology "MISIS" <i>popov58@inbox.ru</i>	Russia
Naydenov Boris Institut of Quantum Optics, University of Ulm <i>boris.naydenov@uni-ulm.de</i>	Germany	Popov Konstantin Nikolaev Institute of Inorganic Chemistry SB RAS <i>popovkm90@mail.ru</i>	Russia
Nebogatikova Nadezhda Rzhanov Institute of Semiconductors Physics SB RAS <i>nadonebo@gmail.com</i>	Russia	Porodenko Elena Lomonosov Moscow State University Chemical Department <i>porodenko@gmail.com</i>	Russia
Nelson Dmitrii Ioffe Institute <i>d.nelson@mail.ioffe.ru</i>	Russia	Pozdnyakov Aleksei Ioffe Institute <i>ao.pozd@mail.ioffe.ru</i>	Russia
Nesterenko Pavel University of Tasmania <i>pavel.nesterenko@utas.edu.au</i>	Australia	Preobrajenski Alexei MAX IV Laboratory <i>alexei.preobrajenski@maxiv.lu.se</i>	Sweden
Nezvorova Yulia Volgograd State University <i>nevzorkina@yandex.ru</i>	Russia	Proserpio Davide Università degli Studi di Milano <i>davide.proserpio@unimi.it</i>	Italy
Nguyen Binh Belarusian State University <i>diamondcentre@mail.ru</i>	Belarus	Proskurnin Mikhail Lomonosov Moscow State University <i>proskurnin@gmail.com</i>	Russia
Okotrub Alexander Nikolaev Institute of Inorganic Chemistry SB RAS <i>spectrum@niic.nsc.ru</i>	Russia	Pudikov Dmitrii Saint-Petersburg State University <i>gelbry@mail.ru</i>	Russia
Orlova Tatiana Ioffe Institute <i>orlova.t@mail.ioffe.ru</i>	Russia	Pykhova Anastasiia Lomonosov Moscow State University <i>a.d.pykhova@gmail.com</i>	Russia
Panich Alexander Ben-Gurion University of the Negev <i>pan@bgu.ac.il</i>	Israel	Rabchinskii Maxim Ioffe Institute <i>maxrabchinskii@gmail.com</i>	Russia

Rasoolzadeh Reza	Iran	Schuepfer Dominique	Germany
Young Researchers and Elites Club Science and Research Branch, Islamic Azad University <i>reza.rasoolzadeh@yahoo.com</i>		Institute of Experimental Physics I, Justus Liebig University <i>dominique.b.schuepfer@exp1.physik.uni-giessen.de</i>	
Razgulov Aleksandr	Russia	Semak Bogdan	Russia
MIPT <i>aleksandr.razgulov@phystech.edu</i>		Peter the Great St.Petersburg Polytechnic University <i>spacejh1@gmail.com</i>	
Rebrikova Anastasiia	Russia	Semivrazhskaya Olesya	Russia
Lomonosov Moscow State University <i>rebrikovaat@phys.chem.msu.ru</i>		Lomonosov Moscow State University <i>semivrazhskaya@gmail.com</i>	
Rodin Evgeniy	Russia	Shashkov Sergej	Belarus
N. P. Ogarev's Mordovia State University <i>evg.rodin54@gmail.com</i>		SOL Instruments Ltd. <i>sales@solinstruments.com</i>	
Romanov Nikolai	Russia	Shavelkina Marina	Russia
Peter the Great St.Petersburg Polytechnic University <i>nikromanov.90@gmail.com</i>		Joint Institute for High Temperatures RAS <i>shavelkinamb@ihed.ras.ru</i>	
Rozhkov Sergey	Russia	Shepel Denis	Russia
Institute of Geology Karelian Research centre RAS <i>rozhkovserg@mail.ru</i>		Technoinfo <i>sales@technoinfo.ru</i>	
Rubtsov Ivan	Russia	Shestakov Mikhail	Russia
Lavrentyev Institute of Hydrodynamics SB RAS <i>rubtsov@hydro.nsc.ru</i>		Ioffe Institute <i>mikhail.shestakov@gmail.com</i>	
Ryazanova Anna	Russia	Shevchenko Nikolay	Russia
Technological Institute for Superhard and Novel Carbon Materials <i>ryazanova@phystech.edu</i>		AO "Petrovskisientific Centre" FUGAS@ <i>pncfugas@bk.mail</i>	
Rybalchenko Alexey	Russia	Shevelev Victor	Russia
Lomonosov Moscow State University <i>alexry@gmail.com</i>		Saint Petersburg State University <i>victorshevelev@yandex.ru</i>	
Rybkina Anna	Russia	Shinkarenko Oksana	Russia
Saint-Petersburg State University <i>rybkina-anna@bk.ru</i>		Saratov State University <i>oksana.sh63@mail.ru</i>	
Sabirov Denis	Russia	Shnitov Vladimir	Russia
Institute of Petrochemistry and Catalysis, RAS <i>diozno@mail.ru</i>		Ioffe Institute <i>v.shnitov@mail.ioffe.ru</i>	
Safyannikov Nikolay	Russia	Shvidchenko Aleksandr	Russia
Saint Petersburg Electrotechnical University "ETUI" <i>matuzenko@bk.ru</i>		Ioffe Institute <i>alexshvidchenko@mail.ru</i>	
Sarmanova Olga	Russia	Sigalaev Sergey	Russia
Lomonosov Moscow State University <i>oe.sarmanova@physics.msu.ru</i>		Keldish Institute <i>nanocentre@kerc.msk.ru</i>	
		Simunin Mikhail	Russia
		Krasnoyarsk Scientific Centre SB RAS <i>michanel@mail.ru</i>	

Sinitza Alexander Kurchatov Institute <i>alexsinitza91@gmail.com</i>	Russia	Terranova Maria Letizia University Tor Vergata <i>terranova@roma2.infn.it</i>	Italy
Skokan Evgenii Lomonosov Moscow State University <i>skokan@phys.chem.msu.ru</i>	Russia	Tikhomirova Galina Ural Federal University <i>galina.tihomirov@mail.ru</i>	Russia
Skryleva Elena NUST MISIS <i>17sea@rambler.ru</i>	Russia	Troyanov Sergey Lomonosov Moscow State University, Chemistry Department <i>stroyano@thermo.chem.msu.ru</i>	Russia
Soboleva Oxana Lomonosov Moscow State University Chemistry Department <i>Oxana_Soboleva@mail.ru</i>	Russia	Tuktarov Airat Institute of Petrochemistry and Catalysis of RAS <i>tuktarovar@gmail.com</i>	Russia
Sokolovsky Dmitry Ural Federal University <i>sokolovskyd1@gmail.com</i>	Russia	Usachev Dmitrii Saint Petersburg State University <i>dmitry.usachov@spbu.ru</i>	Russia
Solodovnichenko Vera Institute of Computational Modeling SB RAS <i>vsolodovnichenko@gmail.com</i>	Russia	Ushakova Iraida Institute of Metallurgy and Material Science RAS <i>ushakovairaida@yandex.ru</i>	Russia
Sozykin Sergey South Ural State University <i>sozykinsa@susu.ru</i>	Russia	Usoltseva Liliia Lomonosov Moscow State University, Chemistry Department <i>usoltsevalilya@gmail.com</i>	Russia
Stoliarova Svetlana Nikolaev Institute of Inorganic Chemistry SBRAS <i>stolyarova@niic.nsc.ru</i>	Russia	Uzbekov Rustem Tours University <i>rustem.uzbekov@univ-tours.fr</i>	France
Stolyarova Dina Enikolopov Institute of Synthetic Polymeric Materials <i>stolyarova.d@gmail.com</i>	Russia	Vins Viktor VELMAN Ltd. <i>vgvins@gmail.com</i>	Russia
Struchkov Nikolay National Research University of Electronic Technology <i>struchkov.nikolaj@gmail.com</i>	Russia	Vedyagin Aleksey Boreskov Institute of Catalysis SB RAS <i>vedyagin@catalysis.ru</i>	Russia
TREUSSART François Ecole Normale Supérieure de Paris-Saclay <i>francois.treussart@ens-cachan.fr</i>	France	Veliev Eldar ITMO University <i>eldarveliyev@gmail.com</i>	Russia
Takagi Mikiharu TOYOHASHI PLATING CO.,LTD. <i>m.takagi@toyohashiplateing.co.jp</i>	Japan	Vereshchagin Alexander Byisk Institute of Technology of Altay State Technical University <i>info@bti.secna.ru</i>	Russia
Tamburri Emanuela University of Rome "Tor Vergata" <i>emanuela.tamburri@uniroma2.it</i>	Italy	Vervalde Alexey Lomonosov Moscow State University <i>amver@mail.ru</i>	Russia
Tei Takahiro DAICEL Corporation <i>teitakahiro@gmail.com</i>	Japan		

Verval'd Ekaterina	Russia	Yang G.W.	China
Lomonosov Moscow State University		Sun Yat-sen University	
<i>en.khusainova@physics.msu.ru</i>		<i>stsygw@mail.sysu.edu.cn</i>	
Voznyakovskii Aleksei	Russia	Yudina Elena	Russia
Ioffe Institute		Ioffe Institute	
<i>alexey_inform@mail.ru</i>		<i>electa@yandex.ru</i>	
Voznyakovskii Alexander	Russia	Zhukova Ekaterina	Russia
S.V. Lebedev Resarch Istitute for		Technological Institute for	
Sythetic Rubber		Superhard and Novel Carbon Materials	
<i>voznap@mail.ru</i>		<i>katyazhu@tisnum.ru</i>	
Vysochanskaya Olga	Russia	Zhuravlev Maxim	Russia
Lomonosov Moscow State University		National Research University	
<i>lavrolja@mail.ru</i>		of Electronic Technology	
Yakimchuk Evgenyi	Russia	<i>maxim@org.miet.ru</i>	
Rzhanov Institute of Semiconductor Physics		Ziatdinov Albert	Russia
Siberian Branch of Russian Academy of Sciences		Institute of Chemistry SB RAS	
<i>eayakimchuk@isp.nsc.ru</i>		<i>ziatdinov@ich.dvo.ru</i>	
Yakovlev Ruslan	Russia		
Vernadsky Institute of Geochemistry			
and Analytical Chemistry of Russian			
Academy of Sciences			
<i>yarules@yandex.ru</i>			

Thermal-lens spectrometer for studying thermophysical properties of fullerenes

I. V. Mikheev^{1,2}, L. O. Usoltseva^{1,2}, D. A. Ivshukov¹, D. S. Volkov^{1,2}, M. V. Korobov¹, M. A. Proskurnin^{1,2}

¹Chemistry Department, Lomonosov Moscow State University, Moscow, Russia

²Analytical Centre of Lomonosov Moscow State University / Agilent Technologies Authorized Partner Laboratory, Moscow, Russia

mikheev.ivan@gmail.com, usoltsevalilya@gmail.com, dima._iv@mail.ru, dmsvolkov@gmail.com, mkorobov49@gmail.com, proskurnin@gmail.com

DOI 10.17586/2220-8054-2018-9-1-14-16

A thermal-lens spectrometer implementing back-synchronized detection technique with a mode-mismatched optical scheme was constructed. Steady-state and transient signals of thermal-lens spectrometry are used to characterize concentration parameters of aqueous fullerene dispersions (AFDs) at the level of 10^{-7} – 10^{-5} M and to assess thermophysical properties of AFDs. The detection limits of fullerenes in AFDs are 100 nM for C₆₀, 80 nM for C₇₀ and C₇₈ – C₈₈, and 60 nM for Y@C₈₂, which are 20-fold lower than for spectrophotometry. Suitable precision of measurements of thermal diffusivity and thermal effusivity for AFDs is shown.

Keywords: thermal-lens spectrometry, pristine fullerenes, aqueous fullerene dispersions, thermal diffusivity.

Received: 21 June 2017

Revised: 10 September 2017

1. Introduction

Thermal-lens spectrometry (TLS) is used for the complex characterization of various materials [1,2]. This method is used for assessing the material optical parameters in UV/Vis/NIR governing or associated with the distribution of heat of different materials giving both thermal and optical properties in a single experiment [1,3]. In this paper, we constructed a thermal-lens setup to obtain the concentration parameters with high sensitivity and to estimate thermal diffusivity of aqueous fullerene dispersion (AFD) samples.

2. Materials and methods

The thermal-lens spectrometer (Fig. 1) uses a cw diode excitation laser working at 445 nm (power range in the sample 40 – 400 mW), beam waist diameter $300 \pm 10 \mu\text{m}$. Absorption of the excitation radiation by the sample induces refractive heterogeneity (the thermal-lens effect) causing defocusing of a TEM00 He–Ne laser probe beam (HRP020, ThorLabs, USA; 632.8 nm; waist size – $25.0 \pm 0.2 \mu\text{m}$; power – 4 mW). The excitation beam goes through an electromechanical chopper, is focused with the lens L1 (focal length 330 mm), goes through a dichroic mirror DM of ZR-100 type (Russia) and, next, to the sample. A part of excitation beam energy is reflected with the flat plate to the synchronizing photodiode (L-3DP3C, Panasonic, Japan), connected to the Control Unit. The probe beam is directed to the adjustment mirror using a system of a dichroic mirror and a focusing lens L2 (focal length 185 mm). After the sample the excitation and probe beams are preliminarily separated with a dichroic mirror of ZR-100 type. The excitation beam is directed to Photometry PD to account for the photometric (transmission) signal of the excitation beam. Also, this mirror avoids the blooming of a thermal lens in the following bandpass filter. The excitation beam is absorbed by the composed filter (KS-11 color glass, 2 mm depth, Russia). The probe beam passes through the pinhole (diameter mm) centered at the optical axis and hits the Primary PD photodiode (L-3DP3C, Panasonic, Japan). The signal is converted and amplified by the Control Unit and enters the ADC–DAC unit. Lenses L1 and L2 and the sample compartment can be moved along directions of beams (step, 0.2 mm). The spectrometer implements a Secondary PD channel (Fig. 1) for gathering scattering or luminescence signals, if present. An ADC–DAC homemade unit based on C8051F061 board (two 16-bit ADC and two 12-bit DAC channels, ADC time, 2 μs ; readout frequency, 1 – 5 kHz; Silicon Labs, USA) was used in the external-trigger mode from the PC. The homemade software communicates with the unit through a RS-232 interface.

Absorbance measurements in the UV/vis range were carried out using an Agilent Cary 4000 (Australia). A DCS-30 TA Mettler-Toledo instrument (Switzerland) was used to measure specific heats from 288 to 323 K (scanning rate 10 K/min; sample mass 20 – 30 mg). A GRAD 28-35 ultrasound bath (Grad-Technology, Russia) was used. Densities were determined with a VIP-2MP (Russia) vibrating-tube densimeter. Water from a Milli Q water-purification system (Millipore, France) was used: specific resistance 18.2 M Ω ×cm; dissolved SiO₂ 3 ppb; total ion amount < 0.2 ppb; TOC < 10 ppb; the own thermal-lens signal 0.004 ± 0.001 . Commercially available

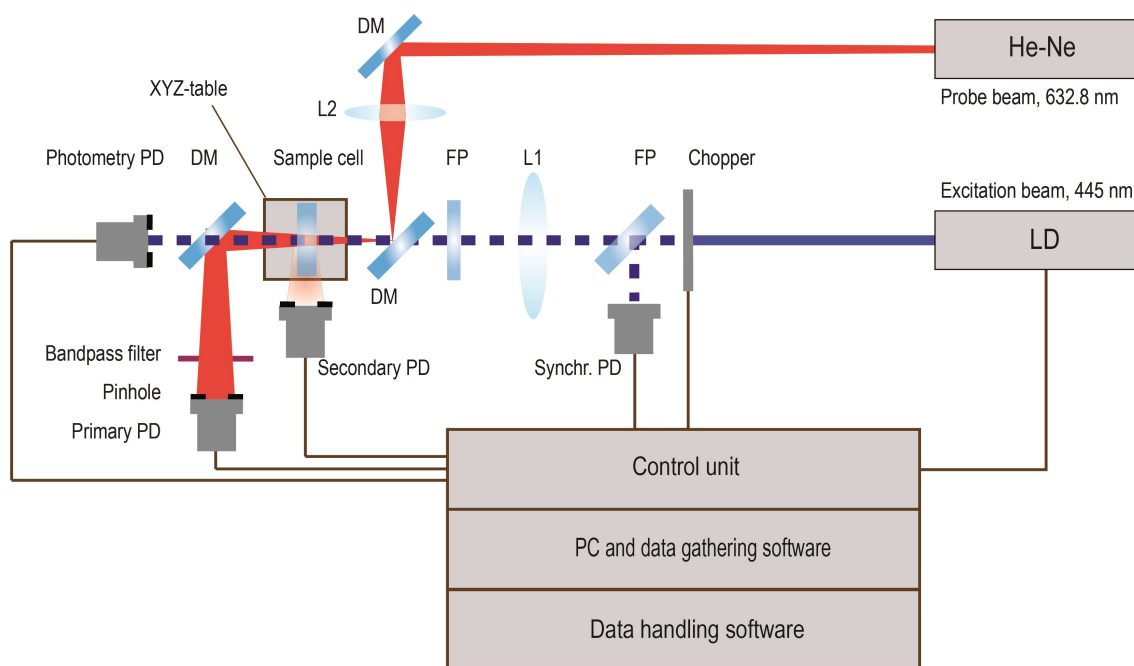


FIG. 1. The scheme of the thermal-lens setup

fullerenes C_{60} and C_{70} , 99.5 % (LLC Neo Tech Product, Russia) were used. The synthesis of $Y@C_{82}$ from fullerene-enriched soot after an arc-discharge synthesis is described previously [4, 5]. Unseparated $C_{78} - C_{88}$ fractions were obtained by HPLC purification of the soot. AFDs were produced by a standard ultrasound-assisted solvent-exchange procedure. 1.10-phenanthroline iron (II) complex (ferroin sulfate, $0.025 \text{ mol}\cdot\text{L}^{-1}$, Merck) was used as is.

3. Results and discussion

The implemented back-synchronized mode of the spectrometer features different measurement conditions for the blooming and dissipating of the transient thermal lens [2]. The advantage is the possibility of transient and steady-state measurements within a single set of experiments. Also, thermal-lens spectrometers usually have a tightly focused excitation beam (beam waist size is *ca.* $50 - 60 \mu\text{m}$ [2, 6]), which gives a sufficient heating, and, therefore, high sensitivity of optical detection. However, such schematic is not well-suited for studying the thermophysical parameters of disperse systems because for the samples with different thermal conductivities, the heat flows from a small laser-heated zone differ. Hence, the size of the thermal lens would also be different, thus affecting the sensitivity and precision. Thus, for each sample, it would be necessary to change the geometry of the optical scheme to match the sizes of the thermal lens and probe beam. To overcome this, we designed a spectrometer with a wide excitation beam (waist size $300 \mu\text{m}$) rendering longer times for attaining a thermal equilibrium.

Despite the aim of thermophysical estimation, we achieved rather low detection limits (by 1 – 2 orders of magnitude lower than for photometry). The LOD for ferroin as a model system is 300 nM (at 400 mW excitation), which is an order of magnitude higher than for classical TLS setups [2], the linear range is slightly wider than two orders of magnitude (the corresponding range of absorptivities for 10 mm optical paths is $1 \cdot 10^{-5}$ to $2 \cdot 10^{-3} \text{ cm}^{-1}$). The local increase in temperature due to the thermal-lens effect is $0.01 - 20 \text{ }^\circ\text{C}$. LODs for fullerenes are 100 nM for C_{60} , 80 nM for C_{70} and $C_{78} - C_{88}$, and 60 nM for $Y@C_{82}$, which correlate with absorptivities of ferroin and fullerenes at the working wavelength. The spectrometer has a response time of $0.05 - 200 \text{ s}$.

Thermal diffusivity was measured from transient thermal-lens curves by the previously reported approach [3]. The transient curves at the time of attainment of the thermal equilibrium for $10^{-6} - 10^{-5} \text{ M}$ of all the studied fullerenes are fit with the theoretical equations well, and we used the final part of transient curves for estimating the bulk thermophysical properties of AFDs at the thermal equilibrium. The thermal diffusivity values $(1.43 \pm 0.03)10^{-7} \text{ m}^2\text{s}^{-1}$; thermal effusivities $(1.55 \pm 0.04)10^2 \text{ Jm}^{-2}\text{K}^{-1}\text{s}^{-1/2}$, and thermal conductivities for AFDs for all the studied fullerenes from thermal-lens data (with heat capacity and density obtained from other methods) show a negligible change compared to water, which is in rather good concordance with the previous

papers on fullerenes solubilized in water [7,8]. This approach can be expanded using a more detailed characterization by the deconstruction of transient thermal-lens curves [3], which could provide estimation for thermophysical properties of the dispersed phase, which would be useful for characterizing carbon nanoparticles.

4. Conclusions

Thus, we designed the thermal-lens spectrometer with a wide excitation beam, which is suitable for simultaneous determination of substances by optical absorption and the estimation of thermophysical parameters of solutions. Suitable precision of measurements of thermophysical parameters of aqueous fullerene dispersions including metallofullerenes – thermal diffusivity, thermal effusivity, and thermal conductivity – was obtained.

Acknowledgements

The work is supported by The Russian Science Foundation, grant no. 14-23-00012-P. We are grateful to Dr. I. E. Kareev (Institute of Problems of Chemical Physics of the Russian Academy of Sciences, Chernogolovka, Russia) for the support of endofullerenes and higher fullerene fractions.

References

- [1] Vargas H., Miranda L. Photothermal techniques applied to thermophysical properties measurements (plenary). *Rev. Sci. Instrum.*, 2003, **74** (1), P. 794–799.
- [2] Proskurnin M.A., Volkov D.S., et al. Advances in thermal lens spectrometry. *J. Anal. Chem.*, 2015, **70** (3), P. 249–276 (in Russian).
- [3] Mikheev I.V., Usoltseva L.O., et al. Approach to the Assessment of Size-Dependent Thermal Properties of Disperse Solutions: Time-Resolved Photothermal Lensing of Aqueous Pristine Fullerenes C₆₀ and C₇₀. *J. Phys. Chem. C*, 2016, **120**, P. 28270–28287.
- [4] Bubnov V.P., Laukhina E.E., et al. Endohedral Metallofullerenes: A Convenient Gram-Scale Preparation. *Chem. Mater.*, 2002, **14** (3), P. 1004–1008.
- [5] Kareev I.E., Laukhina E., et al. Harnessing Electron Transfer from the Perchlorotriphenylmethide Anion to Y@C₈₂(C_{2v}) to Engineer an Endometallofullerene-Based Salt. *Chemphyschem*, 2013, **14** (8), P. 1670–1675.
- [6] Zharov V.P. Ultrasharp nonlinear photothermal and photoacoustic resonances and holes beyond the spectral limit. *Nat. Photonics*, 2011, **5** (2), P. 110–116.
- [7] Hwang Y., Lee J., et al. Stability and thermal conductivity characteristics of nanofluids. *Thermochimica Acta*, 2007, **455** (1), P. 70–74.
- [8] Hwang Y., Park H., Lee J., Jung W. Thermal conductivity and lubrication characteristics of nanofluids. *Curr. Appl. Phys.*, 2006, **6**, P. 67–71.

Nanodiamond aqueous dispersions as potential nanofluids: the determination of properties by thermal lensing and other techniques

L. O. Usoltseva, D. S. Volkov, N. V. Avramenko, M. V. Korobov, M. A. Proskurnin

Lomonosov Moscow State University, 119991 Moscow, Russia

usoltsevalilya@gmail.com, proskurnin@gmail.com

DOI 10.17586/2220-8054-2018-9-1-17-20

Thermal-lens spectrometry was used to characterize thermal diffusivity and thermal conductivity of aqueous nanodiamond dispersions at the level of mg/mL, accompanied by heat capacity, density, and viscosity measurements and modelling. The data from thermal lensing corresponding to thermal equilibrium show 3 – 7 % increase in thermal conductivity of the studied dispersions, show good precision and agree with the existing data.

Keywords: nanodiamond nanofluid, thermal lensing.

Received: 19 June 2017

Revised: 17 September 2017

1. Introduction

More effective cooling fluids are required for nuclear energy industry, operation of solar panels, state-of-the-art computers etc. Recently, nanofluids have been actively studied: they are two-component systems consisting of a base fluid (water or a mineral oil) and dispersed nanoparticles enhancing thermal conductivity. As the latter, metal or oxide nanoparticles are often used. However, carbon nanofluids are more stable, chemically inert, and more environmentally benign. The thermal conductivity of such systems, to date, has not been fully studied and novel experimental techniques are required. Photothermal techniques and thermal-lens spectrometry (TLS) are among the methods widely used for the evaluation of properties of different materials giving both thermal and optical data [1,2]. The objective of this study is thermophysical characterization of aqueous nanodiamond (ND) dispersions. We applied TLS to obtain thermal diffusivity, which was used in calculating thermal conductivity. The specific heat capacities and densities of ND dispersions necessary for such calculations were also measured. The characterization of ND dispersions was implemented with the viscosity determination.

2. Materials and methods

2.1. Photothermal spectrometer and other instruments

Back-synchronized dual-beam mode-mismatched thermal-lens measurements are described elsewhere [2]. The principle is based on recording an excitation-laser induced (Innova 90-6, Coherent, USA; 488.0 and 514.5 nm; waist diameter, $59.8 \pm 0.5 \mu\text{m}$; power, 1 – 250 mW) refractive heterogeneity (the thermal lens effect) causing defocusing of a collinear He–Ne laser probe beam (SP-106-1, Spectra Physics, USA; 632.8 nm; diameter, $25.0 \pm 0.2 \mu\text{m}$; power, 4 mW) and hence a reduction in the probe beam intensity at its center was detected by a far-field photodiode (sample-to-detector distance $120 \pm 0.1 \text{ cm}$) supplied with a KS-11 stained-glass bandpass filter and a 2-mm-diameter pinhole and connected to the custom-made software.

DCS-30 TA Mettler instrument (Switzerland) was used to measure specific heats from 288 to 323 K (scanning rate, 10 K/min; sample mass, 20 – 30 mg). A Kern 770 analytical balance (Germany) was used for dry powder sample weighing. An Ecos 6500 shaker (Russia) and a GRAD 28-35 ultrasound bath from Grad-Technology (Russia) were used for preparing ND dispersions in water. A SNOL 20/300 heating oven (Snol-Term Ltd., Russia) was used for the evaporation of ND aqueous dispersions. A microVISC microfluidic slit rheometer with a microfluidic device, microVISC Type A chipset (13HA05100058, Rheosense Inc., USA) was used to measure steady shear viscosities of ND solutions. Water was used before each measurement as a reference liquid to ensure the accuracy of the rheometer. Densities were determined with a VIP-2MP (Russia) vibrating-tube densimeter. Calibration was performed at 298.15 K by known densities and oscillation periods of ambient air, ultrapure water and REP-12 standard material ($1090.32 \text{ kg}\cdot\text{m}^{-3}$, produced and certified by Mendeleev Institute for Metrology, Russia). The temperature was maintained by the built-in thermostat; the temperature uncertainty was 0.02 °C. The standard deviation for measurements of solution density is $0.1 \text{ kg}\cdot\text{m}^{-3}$.

2.2. Materials

All the reagents and solvents used were of cp grade or higher. The glassware was washed with acetone followed by conc. nitric acid. Water from a Milli Q water purification system (Millipore, France) was used: pH 6.8, specific resistance 18.2 M Ω cm. Commercially available NDs (RUDDM and RDDM, powdered “Real-Dzerzhinsk” Ltd., Dzerzhinsk, Russia and SDND, an aqueous dispersion, PlasmaChem GmbH, Germany) were used throughout. Aqueous dispersions were produced as reported elsewhere [3]. The concentrations of the stock solutions were established by gravimetry. If a stock solution was stored for more than a day, it was manually stirred vigorously. Then, series of working solutions with the concentrations 1 – 190 mg/mL for RUDDM, 0.7 – 30 mg/mL for RDDM, and 1 – 50 mg/ml for SDND were prepared.

3. Results and discussion

Three types of ND capable of forming concentrated solutions were selected for the study. The viscosities of aqueous dispersions are shown in Fig. 1 (left). Concentration dependences are different for the three systems studied, but, as for RUDDM and RDDM, they are similar to the corresponding results of Vul’ and collaborators [4]. When the concentration exceeds 50 mg/ml for RUDDM and 90 mg/ml for RDDM, the viscosity vs. concentration dependence begins to deviate from linearity.

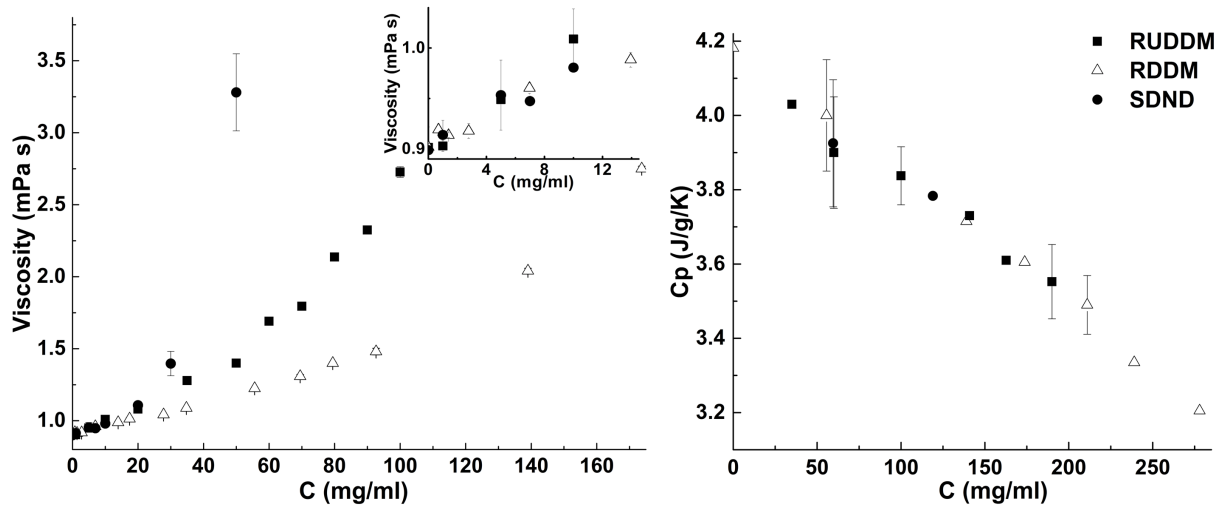


FIG. 1. Viscosity (left) and specific heat (right) of aqueous RUDDM, RDDM and SDND (squares, triangles and circles, respectively) at 25 °C as functions of concentration. Inset: a larger scale for viscosity at low concentrations

According to Sundar and colleagues [5], available theoretical formulas for viscosity estimation include particle volume concentration to the different power. Since viscosity plays a key role in systems involved in a fluid flow, these dependences should be useful in selecting ND suspensions with the best thermal performance.

The results of density measurements of ND-dispersions are given in Table 1. We observed a linear density vs. concentration of ND (mg/ml) dependences for all the three systems studied. The corresponding slopes and R^2 -factors are given in Table 1. For μ m-sized particles, the equation is known for the concentration dependence of density in the two-phase mixtures [6]. Pak and Cho [7] implemented the same equation for nano-sized particles, which is expressed as $\rho_{nfl} = \phi\rho_p + (1 - \phi)\rho_{fl}$, where ρ_{nfl} , ρ_p , ρ_{fl} are densities of the two-phase mixture, particles, and pure fluid, respectively, and ϕ is the particle volume fraction. Density measurements of nanofluids of inorganic particles (Al_2O_3 , Sb_2O_5 , SnO_2 , and ZnO) in 60:40 ethylene glycol/water showed good agreement with this theoretical equation, but the deviation was higher for ZnO and increased with the particle volume concentration [8]. This equation is used for nanofluid densities for aqueous [9, 10], mixed [11], and organic [12] ND dispersions. To use the equation, densities of the base fluid and particles are needed. The latter is determined by a hydrostatic weighing in distilled water [13] or by pycnometry (helium) [14, 15]. As for ND powders, manufacturers do not often provide this parameter. We estimated ND density (according to NIST, diamond density is 3.515 g/ml) assuming a linear dependence of nanofluid density on the volume fraction, which can be obtained if concentration (in mg/ml) is divided into ρ_{nd} (constant); hence, $\text{slope} = 1 - \rho_{\text{H}_2\text{O}}/\rho_{nd}$. ND type does not dramatically change fluid density even for 50 mg/ml (Table 1).

TABLE 1. Density study of aqueous dispersions of ND

ND	Slope $\times 10^4$	R^2	ρ_{nfl} , g/ml (enhancement, %) for 50 mg/ml	ρ_{nd} , g/ml
RUDDM	6.51 ± 0.02	0.99999	1.029 ± 0.003 (3.3)	2.86 ± 0.01
RDDM	7.10 ± 0.01	0.99999	1.032 ± 0.002 (3.6)	3.44 ± 0.01
SDND	7.21 ± 0.03	0.99997	1.033 ± 0.003 (3.6)	3.57 ± 0.01

TABLE 2. Thermal diffusivity and thermal conductivity of aqueous dispersions of ND

Trademark	Concentration, mg/mL	Thermal diffusivity $\times 10^7$, m^2s^{-1}	Thermal conductivity, $W m^{-1}K^{-1}$ (enhancement, %)
Water	—	1.43 ± 0.01	0.595 ± 0.008
RUDDM	0.2	1.48 ± 0.01	0.61 ± 0.01 (3)
	1	1.49 ± 0.01	0.62 ± 0.01 (5)
	4	1.53 ± 0.01	0.63 ± 0.02 (7)
RDDM	1	1.50 ± 0.01	0.61 ± 0.02 (4)
	4	1.53 ± 0.01	0.63 ± 0.02 (7)
SDND	0.2	1.48 ± 0.01	0.61 ± 0.01 (3)
	1	1.50 ± 0.01	0.62 ± 0.01 (5)
	4	1.52 ± 0.01	0.63 ± 0.02 (7)

The specific heats vs. concentration dependences for the three ND fluids studied are presented in Fig. 1 (right). As seen from the Fig. 1, ND type does not influence the specific heat of the nanofluid significantly. The dependence on concentration c ($T = 298$ K) is expressed by one and the same linear equation $C_{p,nfl} = (4.16 \pm 0.03) - (3.3 \pm 0.2) \cdot 10^{-3}c$ ($R^2 = 0.98$).

For specific heat of nanofluids, Pak and Cho [7] and Xuan and Roetzel [16] provided two expressions, $C_{p,nf} = \phi C_{p,nd} + (1 - \phi) C_{p,fl}$ and $(\rho C_p)_{nfl} = \phi (\rho C_p)_{nd} + (1 - \phi) (\rho C_p)_{fl}$. Model I and II, respectively, based on nanofluid volume fraction, ϕ . DCS is the most commonly used technique for measuring specific heats [17]. Ghazvini et al. [18] presented a correlation of specific heat of nanofluids with a 1 % w/w fraction of ND in engine oil as a function of temperature. Model I was used for the estimation of nanofluid specific heat for aqueous ND dispersions [9]. The results of our study do not correlate well with the theoretical equations of Models I or II. For Model I, poor correlation was observed in the whole concentration range, while Model II did work especially for highly concentrated dispersions. To make these calculations, the specific heat of NDs was measured (0.75 ± 0.04 and 0.5 ± 0.02 J/g/K for RUDDM and RDDM) and estimated values of ND density were used.

The experimental data on thermal diffusivity (D_T) of the three ND fluids at different concentrations are given in Table 2. Plots for the thermal-lens signal on concentrations for all the three NDs are linear up to 0.2 mg/mL [3], at which point, they deviate due to changes in thermal conductivity. Thermal diffusivity was measured using the approach previously proposed for aqueous fullerene dispersions [2]. For concentrations below 0.1 mg/mL for all the NDs, it is negligibly different from water. For higher concentrations (Table 2), a 10 % increase in thermal diffusivity is observed with good precision. Thermal conductivity was calculated as $k = \rho_{nfl} C_{p,nfl} D_T$ using the data and models for specific heat and density discussed above. The results show a 3 to 7 % increase in thermal conductivity, which is in rather good agreement with the previous data [19–21]. Satisfactory precision of measurements should be specially mentioned.

4. Conclusions

In this study, the appropriate precision of thermal lensing of aqueous nanodiamond dispersions was achieved, making possible accurate measurements of thermal diffusivity and thermal conductivity. A 3 – 7 % increase in thermal conductivity relative to pure water was confirmed. The TLS approach can be used for a more detailed characterization by the deconstruction of transient curves [2], which could provide the estimation of thermophysical properties of the dispersed phase, which would be useful for nanofluid characterization.

Acknowledgements

The work is supported by The Russian Science Foundation, grants no. 14-23-00012-P and 15-03-02168.

References

- [1] Vargas H., Miranda L. Photothermal techniques applied to thermophysical properties measurements (plenary). *Rev. Sci. Instrum.*, 2003, **74** (1), P. 794–799.
- [2] Mikheev I.V., Usoltseva L.O., et al. Approach to the Assessment of Size-Dependent Thermal Properties of Disperse Solutions: Time-Resolved Photothermal Lensing of Aqueous Pristine Fullerenes C60 and C70. *J. Phys. Chem. C*, 2016, **120** (49), P. 28270–28287.
- [3] Volkov D.S., Semenyuk P.I., Korobov M.V., Proskurnin M.A. Quantification of nanodiamonds in aqueous solutions by spectrophotometry and thermal lens spectrometry. *J. Anal. Chem. (Russ.)*, 2012, **67** (10), P. 842–850.
- [4] Vul A.Y., Eydelman E., Inakuma M., Ōsawa E. Correlation between viscosity and absorption of electromagnetic waves in an aqueous UNCD suspension. *Diam. Relat. Mater.*, 2007, **16** (12), P. 2023–2028.
- [5] Sundar L.S., Sharma K., Naik M., Singh M.K. Empirical and theoretical correlations on viscosity of nanofluids: a review. *Renew. Sustain. Energy Rev.*, 2013, **25**, P. 670–686.
- [6] Chermisinoff N.P. *Encyclopedia of Fluid Mechanics: Slurry Flow Technology*. Gulf Publishing Company, Book Division, 1986.
- [7] Pak B.C., Cho Y.I. Hydrodynamic and heat transfer study of dispersed fluids with submicron metallic oxide particles. *Intern. J. Exp. Heat Transfer*, 1998, **11** (2), P. 151–170.
- [8] Vajjha R., Das D., Mahagaonkar B. Density measurement of different nanofluids and their comparison with theory. *Pet. Sci. Technol.*, 2009, **27** (6), P. 612–624.
- [9] Sundar L.S., Hortiguera M.J., Singh M.K., Sousa A.C. Thermal conductivity and viscosity of water based nanodiamond (ND) nanofluids: An experimental study. *Intern. Commun. Heat and Mass Transfer*, 2016, **76**, P. 245–255.
- [10] Yu Q., Kim Y.J., Ma H. Nanofluids with plasma treated diamond nanoparticles. *Appl. Phys. Lett.*, 2008, **92** (10), 103111.
- [11] Sundar L.S., Singh M.K., Sousa A.C. Enhanced thermal properties of nanodiamond nanofluids. *Chem. Phys. Lett.*, 2016, **644**, P. 99–110.
- [12] Taha-Tijerina J.J., Narayanan T.N., et al. Nanodiamond-Based Thermal Fluids. *ACS Appl. Mater. & Interfaces*, 2014, **6** (7), P. 4778–4785.
- [13] Kidalov S., Shakhov F., Vul A.Y. Thermal conductivity of nanocomposites based on diamonds and nanodiamonds. *Diam. Relat. Mater.*, 2007, **16** (12), P. 2063–2066.
- [14] Larionova I., Frolov A., Poleva L., Bychin N. Study of the composition and physicochemical properties of diamond hydrogels. *Colloid J.*, 2004, **66** (3), P. 372–374.
- [15] Larionova I., Kuznetsov V., et al. Properties of individual fractions of detonation nanodiamond. *Diam. Relat. Mater.*, 2006, **15** (11), P. 1804–1808.
- [16] Xuan Y., Roetzel W. Conceptions for heat transfer correlation of nanofluids. *Intern. J. Heat and Mass Transfer*, 2000, **43** (19), P. 3701–3707.
- [17] Shahrlul I., Mahbulul I., Khaleduzzaman S., Saidur R., Sabri M. A comparative review on the specific heat of nanofluids for energy perspective. *Renew. Sustain. Energy Rev.*, 2014, **38**, P. 88–98.
- [18] Ghazvini M., Akhavan-Behabadi M., Rasouli E., Raisee M. Heat transfer properties of nanodiamondengine oil nanofluid in laminar flow. *Heat Transfer Engin.*, 2012, **33** (6), P. 525–532.
- [19] Yeganeh M., Shahtahmasebi N., et al. Volume fraction and temperature variations of the effective thermal conductivity of nanodiamond fluids in deionized water. *Intern. J. Heat and Mass Transfer*, 2010, **53** (15), P. 3186–3192.
- [20] Torii S. Experimental study on thermal transport phenomenon of nanofluids as working fluid in heat exchanger. *Intern. J. of Air-Conditioning and Refrigeration*, 2014, **22** (01), 1450005.
- [21] Jang S.P., Choi S.U. Cooling performance of a microchannel heat sink with nanofluids. *Appl. Therm. Eng.*, 2006, **26** (17), P. 2457–2463.

Chemical composition of surface and structure of defects in diamond single crystals produced from detonation nanodiamonds

S. V. Kidalov¹, V. V. Shnitov¹, M. V. Baidakova¹, M. Brzhezinskaya², A. T. Dideikin¹, M. S. Shestakov¹,
D. A. Smirnov², I. T. Serenkov¹, V. I. Sakharov¹, V. V. Sokolov¹, N. I. Tatarnikov¹, A. Ya. Vul¹

¹Ioffe Institute, Polytechnicheskaya 26, St. Petersburg, 194021, Russia

²Helmholtz Zentrum Berlin Mat & Energie, D-12489 Berlin, Germany

Kidalov@mail.ioffe.ru

PACS 78.55.-m, 78.70.-g

DOI 10.17586/2220-8054-2018-9-1-21-24

We present the results from our investigation of the structure and composition of microcrystalline diamonds obtained by sintering at high pressures and at high temperatures of detonation nanodiamond particles. Using XPS, XAS and photoluminescence spectroscopy, we found that the surface's chemical composition and a defects structure of microcrystalline diamonds significantly differ from the initial detonation nanodiamonds. This indicates the essential transformation of structure and composition of initial detonation nanodiamonds particles during the formation of single crystals at high pressure and temperature.

Keywords: detonation nanodiamond, HPHT sintering, single crystal, XPS and XAS spectroscopy, photoluminescence, defects.

Received: 20 June 2017

Revised: 27 September 2017

1. Introduction

The possibility of growing bulk single crystals from detonation nanodiamond (DND) particles by oriented attachment in the presence of alcohols or/and hydrocarbons was predicted and experimentally demonstrated by our group in previous works [1–3]. It is assumed that diamond single crystals of size between 500 nm and 15 μm are formed directly from 4 – 5 nm sized diamond nanoparticles under conditions of high pressure and high temperature (HPHT) ($P \approx 7$ GPa, $T \approx 1300 - 1700$ °C). One of the most promising applications of synthesized diamond microcrystals is related to the formation of luminescent impurity centers inside diamond lattice from their own system of defects originating during crystal growth. The distinction of composition and structure of lattices defects in sintered microcrystals and initial DND particles was found for the first time by ESR [4, 5]. The goal of present work is studying transformation of composition and structure of defects of DND resulting from forming microcrystals by HPHT sintering, as well as estimating the possibility of obtaining of the luminescence centers (nitrogen-vacancy) in microcrystals obtained by sintering of DND particles.

2. Experimental details

Samples of highly purified deagglomerated DND were obtained in accordance with the procedure described in [6, 7]. Samples of diamond single crystals of size between 500 nm and 2 μm were prepared by HPHT sintering of DND at the pressure of ~ 7 GPa and the temperature of ~ 1550 °C for 8 – 15 s in the presence of hydrocarbons (hexane). Initial DND particles for spectral measurements were deposited to the surface of silicon substrates by aerosolization. The thickness of layer was about 100 nm. Microcrystals obtained by sintering of DND, were dented into the surface of copper substrates. The thicknesses of obtained layers were approximately 50 μm.

For transformation of the structure of defects in the initial DND and in the synthesized diamond microcrystals, we applied ion irradiation and annealing. We used ions of nitrogen (N^+) with energy $E = 227$ keV and doze $D = 2.5 \cdot 10^{15}$ cm⁻². The annealing was carried out at temperature $T = 750$ °C in a vacuum chamber ($P = 10^{-8}$ Torr) for 1 h.

X-ray photoelectron (XPS) and CK edge X-ray absorption (XAS) spectra were measured at the Russian–German beamline of electron storage ring BESSY-II (Helmholtz-Zentrum Berlin) using the beam line ultra-high vacuum (UHV) experimental station [8]. The XPS spectra were acquired at fixed photon energies using hemispherical analyzer SPECS Phoibos 150 operated in constant-pass-energy mode. The CK edge XAS spectra were measured in the mode of total electron yield (TEY) by recording a value of the sample drain current as a function of the energy of the incident photons.

Photoluminescence (PL) studies were performed at room temperature using spectrometer Ocean Optics Maya2000 Pro with spectral range 200 – 1100 nm and resolution 0.45 nm. The excitation wavelength was 532 nm.

3. Results and discussion

Typical SEM image of microdiamond particles produced by HPHT sintering of DNDs is presented in Fig. 1a. Respective survey XPS spectra of initial DND and synthesized diamond microcrystals are presented in Fig. 1b.

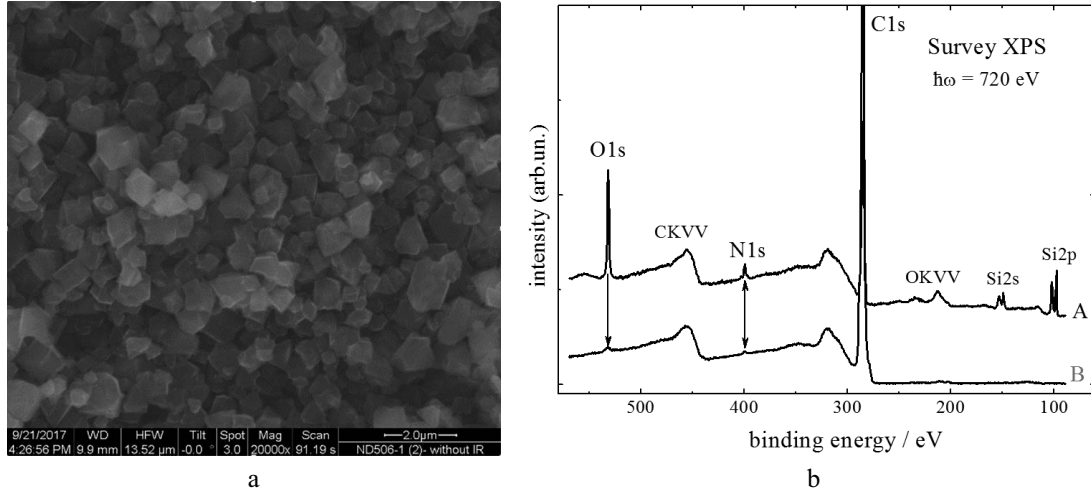


FIG. 1. a) SEM images of synthesized diamond microcrystals obtained by sintering of DND under HPHT conditions. Scale ruler – 2 μm . The average crystal size is 1 μm . b) Survey XPS spectra of DND (curve A) and of synthesized diamond microcrystals (curve B) recorded at the energy of monochromatic synchrotron radiation equals to 720 eV

Figure 1a, confirms the above-mentioned size range for synthesized diamond microcrystals and gives proof for their single crystal nature. Fig. 1b expectedly shows that initial DND and synthesized diamond microcrystals have almost the same chemical composition, which includes three elements: carbon, oxygen and nitrogen. However, the obtained XPS spectra clearly show that unlike initial DNDs, the chemical composition of synthesized diamond microcrystals does not contain any discernible traces of nitrogen (N1s core level peak (BE \sim 401 eV) is completely absent in the XPS spectra of synthesized diamond microcrystals). Thus, we may assume that process of HPHT sintering of DND is accompanied by stringent removal of nitrogen from the near surface layers of the produced diamond single crystals.

Figure 2 presents CK edge XAS spectra of the same diamond particles measured, respectively, on the untreated samples (spectra 1), on the samples first irradiated by nitrogen ions with the energy of 227 keV and the dose of $2.6 \cdot 10^{15}$ ions/cm² (spectra 2) and then on the same samples annealed during 1 h at the temperature of 750 °C under high vacuum (spectra 3).

Analysis of XAS spectra clearly shows that besides removal of nitrogen, DND sintering is also accompanied by essential transformation of their bulk electronic structure and of their surface chemistry. Proof for this is shown by a number of new spectral features which were absent in the XAS of initial DNDs (spectrum 1A), but they appear in respective spectra (spectrum 1B) of synthesized diamond microcrystals. These are the following post-edge ($h\nu > 289$ eV) features: a very narrow (\sim 0.3 eV) peak of C1s core exciton at \sim 289.3 eV, broad bulk σ^* -resonances at \sim 290.8, \sim 295.3 and distinctive shoulder at \sim 303.3 eV. All of these features are commonly considered signs of high structural perfection of diamond [9, 10] and point that HPHT sintering converts DNDs into single crystal diamonds whose bulk electronic structure and degree of structural perfection are very similar to quality synthetic diamonds.

The prominent distinction in the shape of pre-edge regions ($h\nu < 289$ eV) points out the difference in the surface chemistry of initial DNDs and synthesized diamond microcrystals. It could be related to the strong functionalization of synthesized diamond microcrystals surface by C–H groups revealing itself in high intensity of $\sigma^*(\text{C–H})$ -resonance at \sim 287.3 eV [9, 10].

The other XAS spectra also presented in Fig. 2 (spectra 2 and 3) show that irradiation of nano- and micro-sized diamonds by nitrogen ions with energy of 227 keV and dose of $2.6 \cdot 10^{15}$ ions/cm² can produce just only moderate and reversible transformation of their bulk electronic structure. The noticeable decrease of C1s core exciton (\sim 289.3 eV) gives evidence for the respective decrease of microdiamonds structural perfection. Some increase in the intensity of $\pi^*(\text{C=C})$ resonances (\sim 285.1 eV) and corresponding decrease in the intensity of σ^* -resonances we regard as the formation of the surface layer of sp²-coordinated carbons.

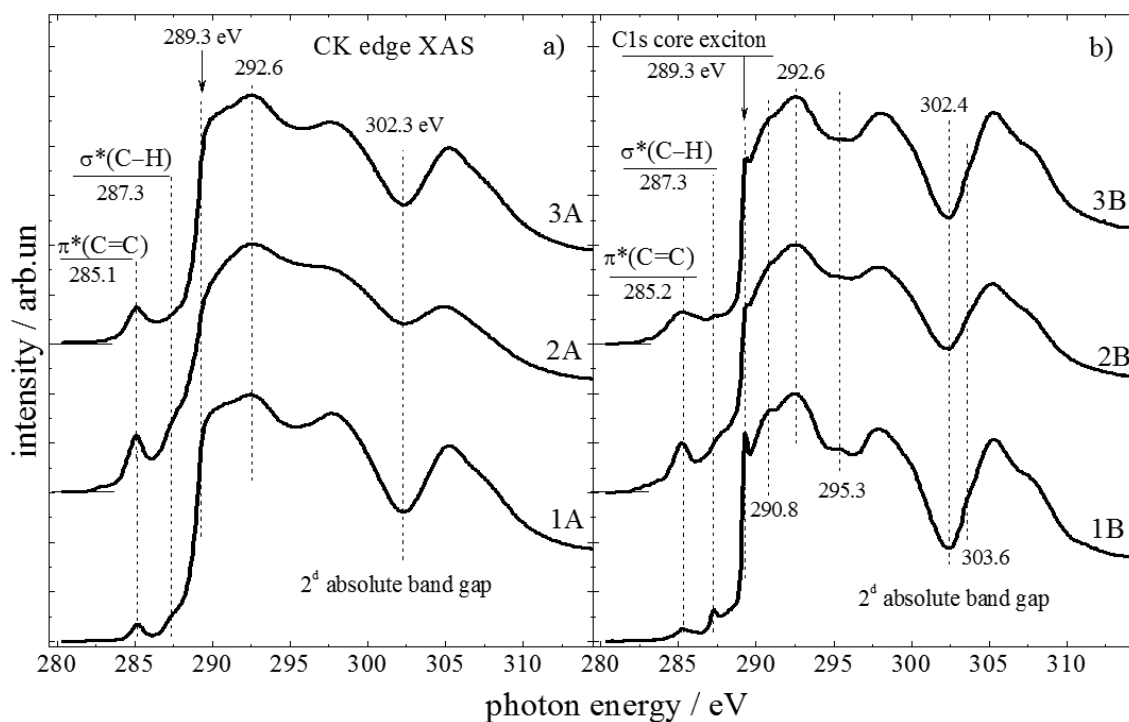


FIG. 2. CK edge XAS spectra of the samples prepared from deagglomerated DND (panel a) and synthesized diamond microcrystals (panel b). Spectra 1A, 1B correspond to the untreated diamond samples. Spectra 2A, 2B – to the same samples irradiated by nitrogen ions with energy of 227 keV and dose of $2.6 \cdot 10^{15}$ ions/cm². Spectra 3A, 3B – the irradiated samples after their 1-hour annealing in high vacuum conditions at 750 °C

Comparison of spectra 2 and 3 shows that 1-hour annealing at 750 °C provides only partial restoration of the bulk structural perfection but inevitably results in an irreversible increase in the surface graphitization degree both for nano- and microdiamond particles.

Figure 3a presents typical PL spectra of the initial powder of DND (spectrum 1A) and of a high-quality type Ib single crystal diamond plate that was fabricated commercially by Element6 using HPHT growth and initially contained 200 ppm of *N*. The sample was irradiated with 3 – 5 MeV neutrons at the temperatures close to room temperature to a total dose of 10^{18} cm⁻², then annealed at the temperature $T = 800$ °C for 2 h in the presence of a forming gas (H_2) in order to achieve a high density of NV^- centers (Fig. 3a, spectrum 2A). The spectrum 1A featured by wide band of photoluminescence with maximum at wavelength 570 nm and the spectrum 2A featured by wide band of photoluminescence with maximum at wavelength 680 nm.

Figure 3b (curve 1B) demonstrates PL spectrum of single crystal diamonds obtained by sintering of DND. It is featured by wide band of photoluminescence between 540 and 900 nm. Bright band at the wavelength of 575 nm can be attributed to the emission of $N-V^0$ defects, points to significant concentration of them in diamond microcrystals sintered from DND.

Meanwhile, synthesized diamond microcrystals subjected to ion irradiation and subsequent annealing demonstrate the prominent transformation of the PL spectrum (Fig. 3b, curve 2B) approaching to the same of perfect single crystalline diamond (Fig. 3a, curve 2A). Maximum of PL spectrum of synthesized diamond microcrystals subjected to ion irradiation on subsequent annealing is as 680 nm compare to wide band of PL as 540 nm to 900 nm of non-irradiated synthesized diamond microcrystals.

The expressed line at 638 nm points to effective formation of luminescent $N-V^-$ centers during processes of ionic irradiation and subsequent annealing.

4. Conclusions

Thus, HPHT sintering of 4 – 5 nm DND particles provides effective formation of 0.5 – 2 μ m sized single crystal diamonds with bulk electronic structure and structural perfection intrinsic to macroscopic high quality single crystal diamonds. Unlike initial DND, the single crystal diamonds obtained by sintering of DND contains

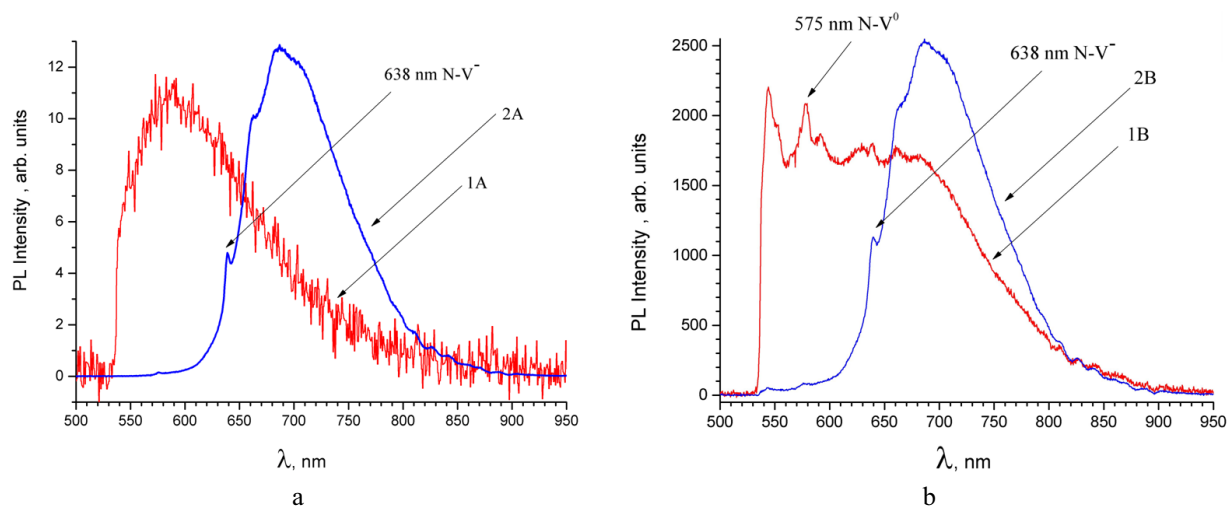


FIG. 3. a) Curve 1A – Typical PL spectra of the initial powders of DND, curve 2A – PL spectra of high-quality synthetic diamond from Element6. b) curve 1B – typical PL spectrum of diamond microcrystals obtained by sintering of DND, curve 2B – PL spectrum of the same microdiamond after ion irradiation and annealing

no nitrogen in the near surface layers. Irradiation of synthesized microcrystalline diamond by 227 keV nitrogen ions ($Q = 2.51015$ ions/cm²) and sequential 1-hour high vacuum annealing of these particles at the temperature of 750 °C results in the transformation of their PL spectra to the shape inherent to the perfect crystalline diamond with noticeable content of luminescent N-V⁻ centers. These results open the way to effective technologies of production the luminescent microdiamonds for various applications.

Acknowledgements

The S.V.K., A.Ya.V. acknowledge financial support of the Russian Science Foundation (project 14-13-00795). V.V.S., M.V.B., A.T.D., M.S.S. thank Russian German Laboratory at synchrotron BESSY II (Berlin) for the support of the XAS and XPS measurements and Helmholtz-Zentrum Berlin (HZB) for the allocation of synchrotron radiation beam time. S.V.K. thanks V. Soltamov for providing the irradiated and annealed high-quality diamond (Element6) for testing.

References

- [1] Kidalov S.V., Shakhov F.M., et al. Growth of diamond microcrystals by the oriented attachment. *Tech. Phys. Lett.*, 2017, **43** (1), P. 53–56.
- [2] Dideikin A.T., Eidelman E.D., et al. Oriented-attachment growth of diamond single crystal from detonation nanodiamonds. *Diam. Relat. Mater.*, 2017, **75**, P. 85–90.
- [3] Kidalov S.V., Shakhov, F.M., Vul' A.Ya., Ozerin A.N. Grain-boundary heat conductance in nanodiamond composites. *Diam. Relat. Mater.*, 2010, **19** (7–9), P. 976–980.
- [4] Osipov V.Yu., Shakhov F.M., et al. Identification of paramagnetic nitrogen centers (P1) in diamond crystallites synthesized via the sintering of detonation nanodiamonds at high pressure and temperature. *Phys. Solid State*, 2017, **59** (6), P. 1146–1153.
- [5] Soltamova A.A., Ilyin I.V., et al. Detection and identification of nitrogen defects in nanodiamond as studied by EPR. *Physica B: Condens. Matter*, 2009, **404** (23–24), P. 4518–4521.
- [6] Aleksenskiy A.E., Eydelman E.D., Vul' A.Ya. Deagglomeration of detonation nanodiamonds. Rehybridization of carbon on facets of detonation diamond nanocrystals and forming hydrosols of individual particles. *Nanosci. Nanotech. Lett.*, 2011, **3** (1), P. 68–74.
- [7] Dideikin A.T., Aleksenskii A.E., et al. Phase transition on facets of detonation diamond nanocrystals and forming hydrosols of individual particles. *Carbon*, 2017, **122**, P. 737–745.
- [8] Molodtsov S.L., Fedoseenko S.I., et al. High-resolution RussianGerman beamline at BESSY. *Appl. Phys. A*, 2009, **94**, P. 501–505.
- [9] Shpilman Z., Gouzman I., et al. A near edge X-ray absorption fine structure study of oxidized single crystal and polycrystalline diamond surfaces. *Diam. Relat. Mater.*, 2014, **45**, P. 20–27.
- [10] Zagrebina E.M., Generalov A.V., et al. Comparative NEXAFS, NMR, and FTIR Study of Various-Sized Nanodiamonds: As-Prepared and Fluorinated. *J. Phys. Chem. C*, 2015, **119**, P. 835–844.

Phase stability of fluorinated nanodiamonds under HPHT treatment

V. N. Khabashesku¹, V. P. Filonenko², A. S. Anokhin³, E. V. Kukueva⁴

¹Center for Technology Innovation, Baker Hughes a GE Company, Houston, TX, USA

²Vereshchagin Institute for High Pressure Physics RAS, Moscow, Troitsk, Russia

³A. A. Baikov Institute of Metallurgy and Materials Science RAS, Moscow, Russia

⁴Lomonosov Moscow State University, Moscow, Russia

valery.khabashesku@bakerhughes.com, filv@hppi.troitsk.ru, alexanderanokhin@yahoo.com,
elena.kukueva@gmail.com

PACS 62.50.-p, 81.07.-b, 81.05.ug

DOI 10.17586/2220-8054-2018-9-1-25-28

The aspects of phase and size stability of surface fluorinated nanoscale diamond powders during their treatment under conditions of high pressures and high temperatures (HPHT) are considered. In the studied powder, fluorine is covalently bonded to diamond particles, replacing the other functional groups on their surface. In this case, under pressure of 8.0 GPa the transition of 10-nm-size diamond nanoparticles into a graphene layered carbon forms does not occur up to temperatures of 1700 °C, and their size does not change. The addition of submicro-sized aluminum powder to fluorinated nanodiamond results in the fast growth of particles to a micrometer size range. The observed unprecedented enlargement of nanodiamonds to micro-sized crystals is explained by occurrences of Wurtz-type reactions in the C–Al–F system which activate the formation of new interfacial carbon–carbon bonds between nanoparticles and their coalescence under HPHT conditions.

Keywords: fluorinated nanodiamonds, high pressure-high temperature treatment, aluminum fluoride.

Received: 13 June 2017

Revised: 7 December 2017

1. Introduction

Nanocarbons tend to undergo different phase transformations depending on particle size. Studies of the relationships between ensembles of nanoparticles under P–T conditions of stability of diamond phase on carbon diagram are of particular interest. The phase transformation pathway depends on thermodynamic conditions, size and morphology of the nanoparticles and composition of surface contaminants. As an example, globular turbostratic carbon was shown to transform into diamond nanocrystals through a reordering of multi-layered carbon structures under HPHT treatment at pressure of 8.0 GPa in the temperature range of 1300 – 1500 °C [1]. On contrary, under the same P–T parameters, nanodiamonds transform into graphite after reaching an average particle size of 20 nm [2].

Important role in the kinetics of crystallization and growth of diamonds under high and low pressures is being played by hydrogen. It is known that the HPHT treatment of hydrocarbons at 8 GPa and 1300 °C leads to the formation of micro-sized diamond crystals [3], while the addition of naphthalene (C₁₀H₈) to detonation nanodiamonds activates particle growth under similar thermobaric conditions [4]. In the C–H–F system, both micro- and nanodiamonds are formed under HPHT treatment. On the example of thermobaric action on C₁₀H₈–C₁₀F₈ mixture, the mechanism of such transformations has been interpreted by simultaneous generation of two types of carbon precursors – non-graphitic nano-sized and graphitic micro-sized particles [5–7]. The micro-sized diamond fractions are formed directly from graphitic precursors, while the nano-sized fraction of diamond is formed from 5 – 15 nm onion-like carbon nanoparticles. An important role in the transformation processes is played by the gas-phase or fluid-phase transport of carbon and surface chemical reactions. In comparison, the formation of diamonds from fluorographite (CF_{1.1}) at 8.0 GPa was not observed at all within the whole range of the temperatures studied, up to 1500 °C. The present work shows the effect of HPHT treatment on phase stability of fluorinated nanodiamonds (FND).

2. Experimental section

The diamond nanopowder, comprised of 10 nm average size particles of spherical shape, has been produced by detonation method followed by high energy grinding to crush the tightly bonded agglomerates. Fluorinated nanodiamonds (FND10), containing 7 wt% of fluorine covalently bonded to carbon atoms on the surface, were obtained by F₂–He treatment of the nanopowder at 340 °C. Aluminum powder, comprised of spherical particles of

0.8 μm average size, was used as an additive to diamond powder. Powders were mixed in the ethanol media with the aid of ultrasound.

HPHT treatment of samples was carried out under pressure of 8.0 GPa and different temperatures up to 1700 $^{\circ}\text{C}$ in the Toroid-type cell. The pressure was generated with the tungsten carbide anvils by a uniaxial hydraulic system. Samples (5 mm diameter, 3 mm height) were quenched under pressure, recovered at ambient conditions, and then characterized by X-ray diffraction, Raman spectroscopy, scanning (SEM) and transmission (TEM) electron microscopies.

3. Results and discussion

It was found that fluorinated diamond nanoparticles do not transform into graphite structures after treatment at the pressure of 8.0 GPa, a temperature of 1500 $^{\circ}\text{C}$ and an isothermal exposure time of 60 s (Fig. 1). The TEM images on Fig. 1 show that after thermobaric treatment, the size of FND crystals did not change while the electron diffraction pattern after the HPHT treatment looks more diffused in comparison with the initial material. The Raman spectra (not shown) of the high pressure compacts differentiated from the starting fluorinated powder by only a slight broadening and shifting of the peaks' maxima. Reflections due to the graphite phase were also not observed in the XRD of compacts. Elemental analysis of the fracture surface of the compact has indicated that fluorine content is several times reduced, to 1.5 – 2.0 wt%, after the thermobaric treatment of FND10.

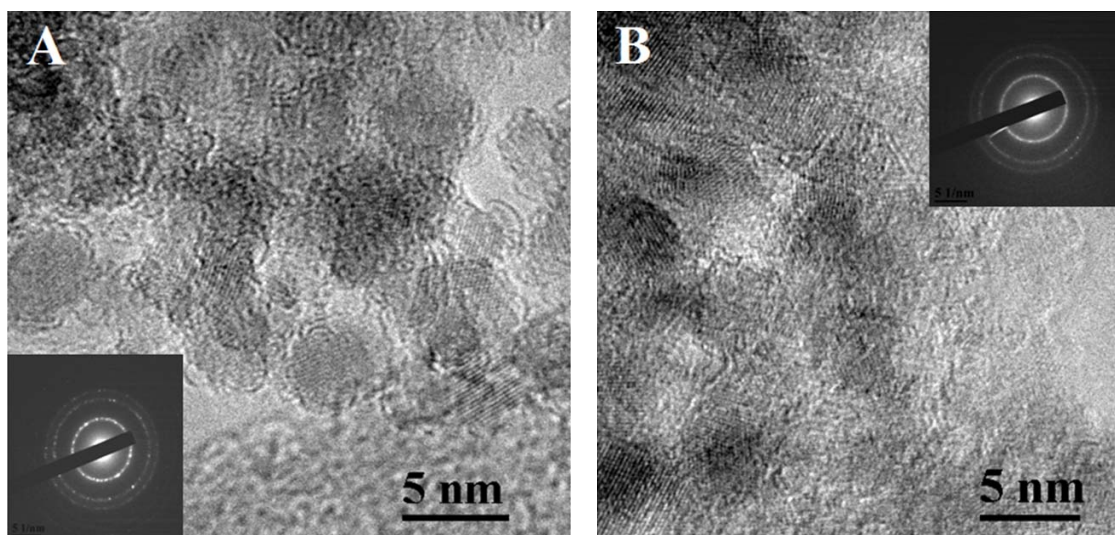


FIG. 1. TEM images of fluorinated diamond nanopowder taken before (A) and after HPHT treatment (B)

During heating at temperatures above 700 $^{\circ}\text{C}$ fluorine detaches from diamond surface and then exists within the volume of compact in the form of inert fluid which does not provide a mass transfer of carbon which is needed for growth of nanodiamond particles. It should be noted that the thermobaric treatment of a non-fluorinated nanodiamond powder under the same pressure and temperature conditions has led to its substantial graphitization. Thus, the presence of fluorine on the surface of diamond nanoparticles helps to stabilize the cubic structure and slow down the process of graphitization.

Aluminum submicropowder (up to 15 wt%) was admixed to FND10 nanopowder with the idea of scavenging and chemically trapping and binding the fluorine in the volume of HPHT treated fluorinated nanodiamond compact sample. In this case, the void-free grain boundaries were observed to form between nanodiamond particles along with the formation of aluminum fluoride. As a result, an unprecedented growth and enlargement of diamond crystals from nano to micro sizes was discovered to occur in this system on HPHT treatment at 1700 $^{\circ}\text{C}$. In addition to that, a complete absence of formation of even trace amounts of graphite phase has been noted.

From the diffraction patterns in Fig. 2, it is seen that at temperatures around 1600 $^{\circ}\text{C}$ a sharp peak, characteristic of micrometer-sized diamond particles, appears on the top of the initially broad peak of nanodiamond. If the temperature of the thermobaric treatment is increased to 1700 $^{\circ}\text{C}$, all nanodiamonds become fused into crystals of micrometer size. They do not show any external signs of conservation of the nanostructured state. The morphology of diamond particles obtained after the thermobaric treatment at 1700 $^{\circ}\text{C}$ is shown in Fig. 3.

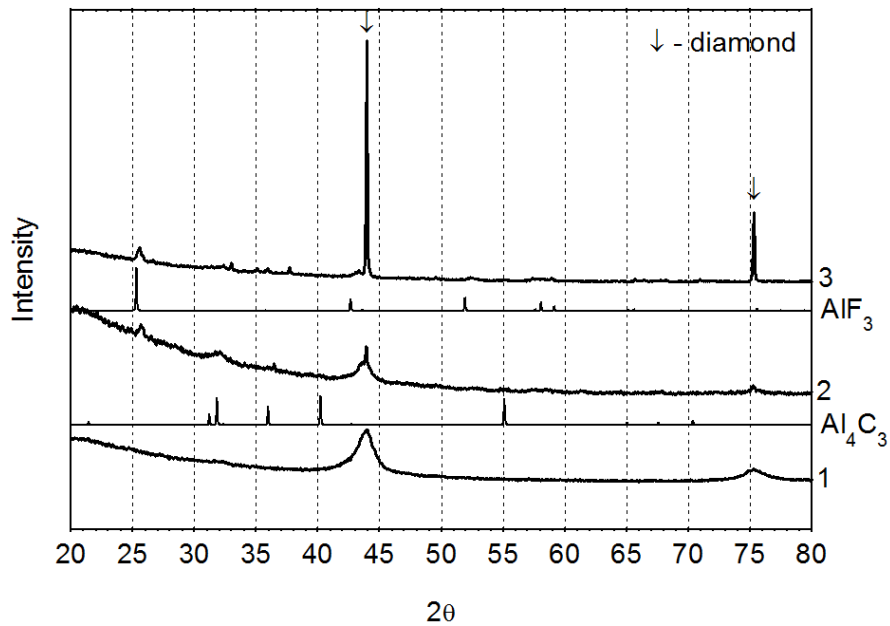


FIG. 2. X-ray analysis of mixtures FND10–15Al: 1 – nanopowder FND10 before thermobaric treatment; 2 – mixture FND10–15Al after treatment at 7.5 – 8.0 GPa, 1550 – 1600 °C, 30 s; 3 – mixture FND10–15Al after treatment at 7.5 – 8.0 GPa, 1650 – 1700 °C, 30 s

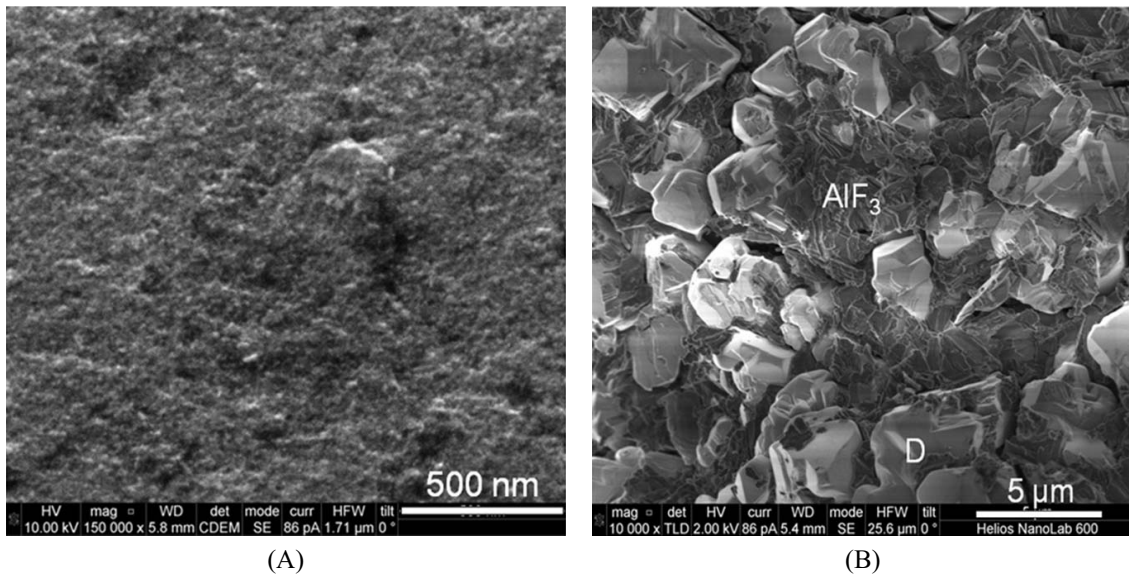


FIG. 3. SEM images of initial (A) and treated at 7.5 – 8.0 GPa, 1650 – 1700 °C, 30 s (B) mixtures FND10–15Al

The micro-sized diamond crystals, formed from the nanoparticles, exhibit well-faceted shapes and are separated by aluminum fluoride. It should be noted that the process of unusual growth and enlargement of nanodiamonds to the micro-sized species observed in the C–Al–F system occurs in a quite narrow temperature range. This is partly determined by the thermodynamics, namely the tendency of the system to reduce energy by reducing the total surface of the interfacial grain boundaries. Temperatures of 1600 – 1700 °C and pressures not lower than 7.5 GPa are required for the realization of the growth process in the whole volume of the sample. An increase in temperature or decrease in pressure leads to a partial transition of nano- and microdiamonds to a graphite phase. It is seen from the diffraction pattern that aluminum fluoride is required for the enlargement growth of nanodiamonds. Aluminum fluoride melts at a temperature of about 1300 °C. Under the applied thermobaric treatment conditions, it is in a liquid state, and in such state, it can activate the transport of carbon from the surface of diamond nanoparticles.

Therefore, the anomalous growth of nanodiamonds up to the micro-sized diamond crystals observed in the present work, can be associated with both the realization of Wurtz-type reaction under the HPHT conditions and with the formation of the fluid Al–C–F phases in the samples volume, accelerating the mass transport and re-crystallization of nanodiamonds.

References

- [1] Filonenko V., Zibrov I., et al. Structural and morphological transformations of nanosized globular carbon during thermobaric treatment. *Inorg. Mater.*, 2017, **53** (5), P. 1–8.
- [2] Davydov V., Rakhmanina A., Agafonov V., Khabashesku V. Size-dependent nanodiamond-graphite phase transition at 8 GPa. *JETP Lett.*, 2007, **86** (7), P. 462–464.
- [3] Davydov V.A., Rakhmanina A.V., et al. Conversion of polycyclic aromatic hydrocarbons to graphite and diamond at high pressures. *Carbon*, 2004, **42**, P. 261–269.
- [4] Varfolomeeva T.D., Lyapin A.G., et al. Behavior of detonation nanodiamond at high pressures and temperatures in the presence of a hydrogen-containing fluid. *Inorg. Mater.*, 2016, **52** (4), P. 351–356.
- [5] Davydov V.A., Rakhmanina A.V., Agafonov V.N., Khabashesku V.N. Synergistic effect of fluorine and hydrogen on processes of graphite and diamond formation from fluorographite-naphthalene mixtures at high pressures. *J. Phys. Chem. C*, 2011, **115**, P. 21000–21008.
- [6] Davydov V.A., Rakhmanina A.V., Agafonov V.N., Khabashesku V.N. On the nature of simultaneous formation of nano- and micro-size diamond fractions under pressure-temperature-induced transformations of binary mixtures of hydrocarbon and fluorocarbon compounds. *Carbon*, 2015, **90**, P. 231–233.
- [7] Davydov V.N., Agafonov V.N., Khabashesku V.N. Comparative study of condensation routes for formation of nano- and micro-sized carbon forms in hydrocarbon, fluorocarbon, and fluoro-hydrocarbon systems at high pressures and temperatures. *J. Phys. Chem. C*, 2016, **120** (51), P. 29498–29509.

Stability at high temperature and decomposition kinetics of the fullerene dimers and photopolymers

K. P. Meletov^{1*}, J. Arvanitidis², D. Christofilos², G. Kourouklis², V. A. Davydov³

¹Institute of Solid State Physics, Russian Academy of Sciences, 142432 Chernogolovka, Moscow region, Russia

²Aristotle University of Thessaloniki, GR-54124 Thessaloniki, Greece

³Institute of High Pressure Physics, Russian Academy of Sciences, 42092 Troitsk, Moscow region, Russia

*mele@issp.ac.ru

PACS 78.30.Na

DOI 10.17586/2220-8054-2018-9-1-29-32

The decomposition kinetics of the fullerene dimers and photo-oligomers was studied at elevated temperature by Raman scattering. The polymeric content decreases exponentially with the thermal treatment time while the decay time constant decreases at higher temperatures. The activation-type behavior is well described by the Arrhenius law that gives the activation energy $E_A = (1.71 \pm 0.06)$ eV/molecule for the dimers and $E_A = (0.87 \pm 0.06)$ eV/molecule for the C_{60} photopolymer.

Keywords: fullerene polymers, Raman spectroscopy, decomposition kinetics.

Received: 14 June 2017

Revised: 22 September 2017

1. Introduction

The photopolymerization of C_{60} occurs in thin films or surfaces of bulk samples resulting in rather disordered oligomers $(C_{60})_n$ that appear via the $[2 + 2]$ cyclo-addition mechanism [1–3]. The treatment of C_{60} under various conditions of high pressure and high temperature (HPHT) results in the formation of bulk polymers [4, 5]. The lowering of the C_{60} molecular symmetry leads to the splitting and softening of phonon bands and the Raman examination of polymers is based on the behavior of the $A_g(2)$ pentagon pinch (PP) mode frequency which decreases from 1468 cm^{-1} for the C_{60} monomer to 1463, 1458, 1446 and 1408 cm^{-1} for the dimers, linear orthorhombic, planar tetragonal and rhombohedral polymers, respectively [5, 6]. Fullerene polymers are stable at ambient conditions but revert to the monomeric state at elevated temperature [7, 8]. The differential scanning calorimetry (DSC) of the HPHT polymers shows transitions in the range $170 - 280 \text{ }^\circ\text{C}$ which depend on the polymeric phase and somewhat on the scanning rate, indicating that the process is controlled by kinetics. The decomposition kinetics of polymers was studied by X-ray thermal expansion and Raman measurements [7, 9]. In the case of photopolymers, the small amount of the photo-transformed material on the surfaces of samples makes the DSC and X-ray measurements inappropriate, so the Raman spectroscopy becomes a unique tool in the study of the photopolymer decomposition. Here, we report the Raman study of the decomposition kinetics of the C_{60} dimers and photopolymers. The intensity of the polymer-related PP-mode decreases exponentially with the thermal treatment time. Decomposition becomes faster at elevated temperatures and the activation energy E_A , obtained from the Arrhenius dependence of the exponential decay time constant on temperature, is (1.71 ± 0.06) and (0.87 ± 0.12) eV for dimers and photopolymers, respectively.

2. Experimental details

The dimeric samples, prepared by HPHT treatment of pristine C_{60} , were a mixture 4:1 of C_{60} dimer and monomer [10]. The C_{60} photopolymer was formed under laser irradiation at the wavelength $\lambda_{exc} = 785 \text{ nm}$ and $180 \text{ } \mu\text{W}$ power. The photopolymer decomposition was studied by Raman probing at $\lambda_{exc} = 785 \text{ nm}$ with $18 \text{ } \mu\text{W}$ power under continuous thermal treatment up to 400 min at an elevated temperature. The Raman measurements were performed in the back-scattering geometry using a LabRam HR spectrometer and a high temperature cell with a quartz window equipped by a temperature controller unit [11].

3. Results and discussion

The dimeric samples are sensitive to visible light and may be subjected to further photopolymerization during long acquisition Raman experiments. On the other hand, the spectra recorded at $\lambda_{exc} = 785$ nm and laser power of $80 \mu\text{W}$ do not show any changes for irradiation time up to 200 min. The kinetics of dimer decomposition was studied at these conditions under thermal treatment at temperatures ranging from $130 - 177$ °C. The Raman spectra were measured in the frequency region of the PP-mode with fixed acquisition time, consecutively, during continuous thermal treatment, using a new fresh sample for each temperature.

The inset of Fig. 1 depicts the evolution of the Raman spectra of the C_{60} dimers upon thermal treatment at 155 °C. In the bottom spectrum, recorded at ambient conditions, the PP-mode component of dimers is dominant, while subsequent spectra recorded at 155 °C exhibit an intensity increase of the monomer component at the expense of the dimer one. The top spectrum recorded after 97 min of thermal treatment is dominated by the PP-mode component of the monomer while the dimer component becomes negligible. Open circles in Fig. 1 represent the fractional intensity of the dimer PP-mode as a function of the thermal treatment time, whereas the dotted line is the fit of the data by the exponential decay function:

$$D(t) = D_0 \exp(-t/\tau), \quad (1)$$

where $D(t)$ and D_0 are the current and the initial contents of dimers and τ is the decay time constant.

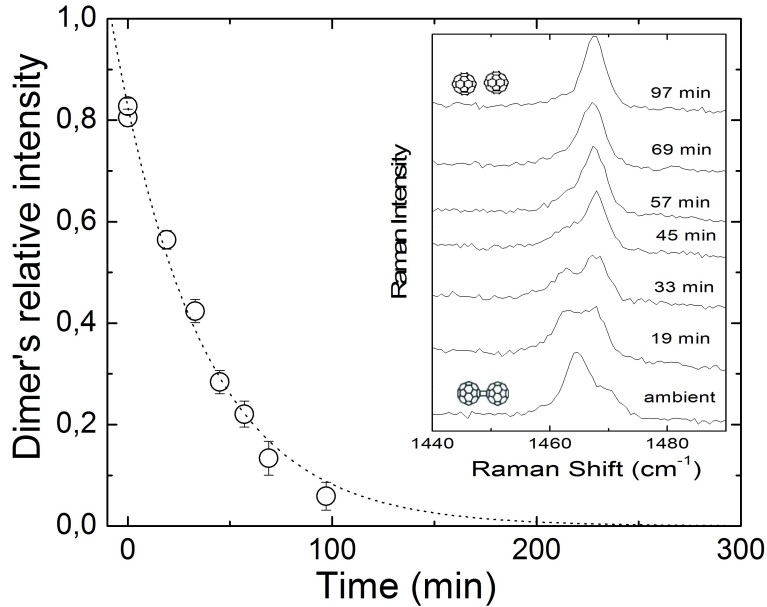
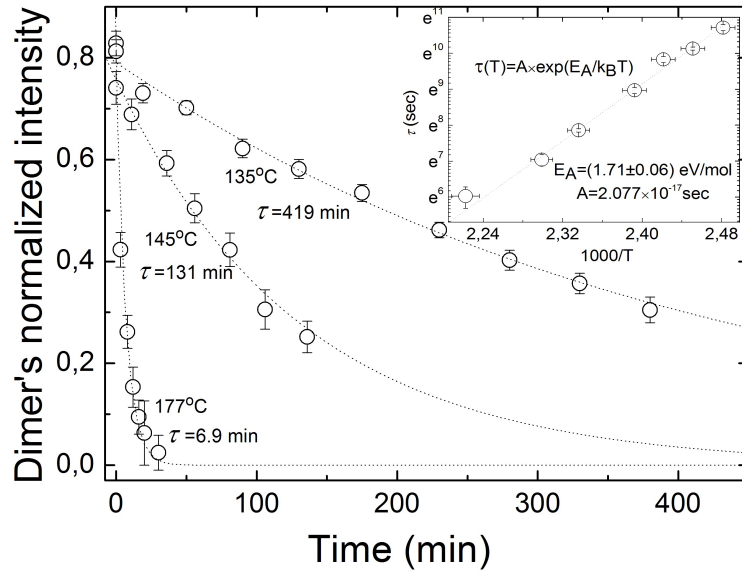
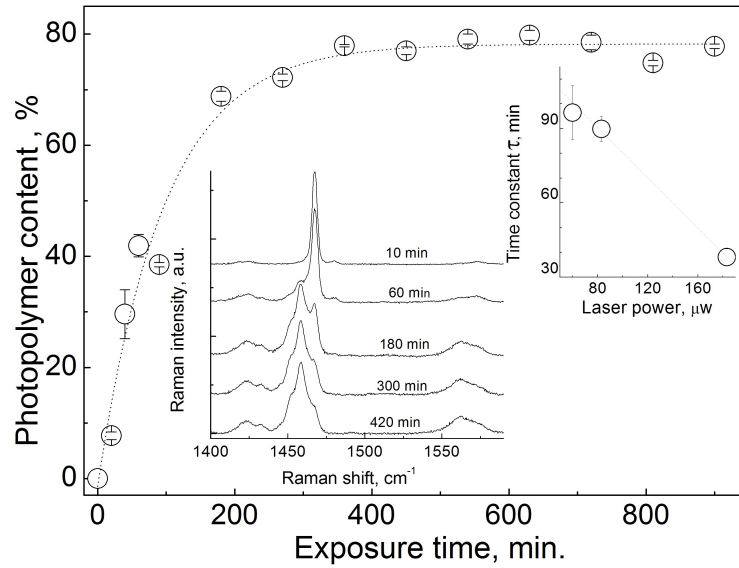


FIG. 1. Evolution of the Raman spectra of the C_{60} dimers under thermal treatment at 155 °C

Figure 2 illustrates the decomposition kinetics of dimers, which is relatively slow at 135 °C with $\tau = 419$ min, while it becomes very fast at the highest temperature of 177 °C with $\tau = 6.9$ min. The activation energy of the dimer decomposition reaction can be described by the Arrhenius equation:

$$\tau(T) = A \exp(E_A/k_B T), \quad (2)$$

where E_A is the energy barrier between the dimeric and the monomeric states, k_B is the Boltzmann constant, T is the treatment temperature and τ the decay time constant. The constant A , related to the characteristic phonon frequency, is measured in time units [9]. The corresponding Arrhenius plot is included in the Fig. 2 inset. The experimental data exhibit a good linear dependence in logarithmic scale, yielding an activation energy of $E_A = (1.71 \pm 0.06)$ eV/molecule. This value is close to the $E_A = (1.75 \pm 0.05)$ eV/molecule obtained from the X-ray thermal expansion studies of powdered dimeric samples, synthesized by a solid-state mechanochemical reaction of C_{60} with potassium cyanide, as well as to the activation energy $E_A = (1.9 \pm 0.1)$ eV/molecule of the 1D and 2D polymers decomposition [9]. It is interesting to compare these data with the decomposition kinetics of fullerene photooligomers $(\text{C}_{60})_n$. The Raman spectra of the photopolymerized fullerene prepared at $\lambda_{exc} = 532$ nm and $60 \mu\text{W}$ laser power are shown in the left inset of Fig. 3. The initial spectrum recorded in the region of the $A_g(2)$ PP-mode is typical for the C_{60} monomer while the following spectra recorded with 60 min exposure under

FIG. 2. Decomposition kinetics of the C_{60} dimersFIG. 3. Raman spectra and photopolymerization kinetics of the C_{60} fullerite

continuous illumination show gradual decrease of the PP-mode intensity of the monomer and increase of the new PP-modes intensity. The intensity distribution between the new modes shows that photo-oligomers are mainly linear chains and conjugated linear chains. Open circles depict the dependence of the photopolymer content on the irradiation time whereas the dotted line is the fit by the exponential growth function:

$$P(t) = P_{sat} \{1 - \exp(-t/\tau)\}, \quad (3)$$

where $P(t)$ and P_{sat} are the current and the saturated contents of the photopolymer, τ is the time constant that linearly decreases with laser power (right inset).

The stability of the photo-oligomers, prepared on the surface of the C_{60} crystals at $\lambda_{exc} = 785$ nm and laser power 180 μW , was studied by Raman spectroscopy with $\lambda_{exc} = 785$ nm, 18 μW and short acquisition time to prevent further polymerization and ensure accurate measurements.

Figure 4 illustrates the kinetics of the photo-oligomer decomposition. The relatively slow decomposition at 130 $^{\circ}\text{C}$ with $\tau = 109$ min becomes very fast at 170 $^{\circ}\text{C}$ with $\tau = 9.6$ min. The activation energy of the decomposition can be estimated from the Arrhenius plot included in the Fig. 4 inset. The experimental data exhibit a good

linear dependence in logarithmic scale, yielding an activation energy of $E_A = 0.87 \pm 0.06$ eV/molecule. Note that a value of 1.25 eV/molecule was obtained earlier in the Raman study of the C_{60} photopolymer decomposition [7]. The Arrhenius data allows the estimation of the photopolymer complete decomposition temperature (decrease of its content to 1 % within 15 min as in DSC experiments [8]). Despite of the twice as large activation energy of the C_{60} dimers, their complete decomposition temperature is ~ 180 °C, lying close to that of ~ 190 °C for the photopolymers due to the giant difference in the A constant of the Arrhenius dependence. Finally, the recent study of the photopolymerization in the fullerene layers of the $\{Pt(dbdtc)_2\} \cdot C_{60}$ complex shows that the activation energy of the layered photopolymer decomposition is $E_A = 1.12 \pm 0.11$ eV/molecule while the temperature of its complete decomposition is ~ 130 °C [12]. Note, that the 2D polymers appear to be the most stable among the polymeric forms of C_{60} , characterized by a complete decomposition temperature of ~ 260 °C [8].

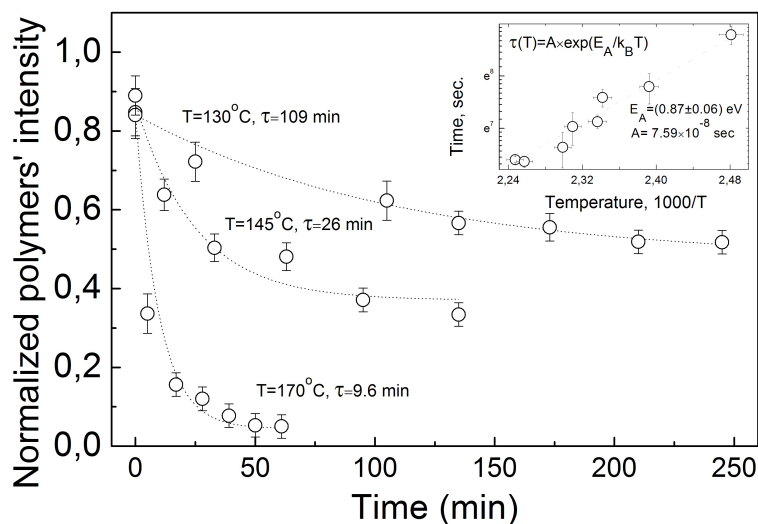


FIG. 4. Time dependencies of the C_{60} photopolymer content under treatment at various temperatures and their fit by exponential decay functions (dotted lines). Inset: Arrhenius dependence of the decay time constant on temperature

Acknowledgements

The authors are thankful to the Center of Interdisciplinary Research and Innovation of the Aristotle University of Thessaloniki (KEΔEK) for the access to the Raman instrumentation. K.P.M. acknowledges the main financial support by the Federal Agency for Scientific Organizations, the partial support by the Russian Foundation for Fundamental Research, grant 15-02-01495, the RAS Presidium Program “Physics of compressed matter”, as well as the hospitality of the Aristotle University of Thessaloniki.

References

- [1] Rao A.M., Zhou P., et al. Photoinduced polymerization of solid C_{60} films. *Science*, 1993, **259**, P. 955–957.
- [2] Zhou P., Dong Z.H., Rao A.M., Ecklund P.C. Reaction-mechanism for photopolymerization of solid fullerene C_{60} . *Chem. Phys. Lett.*, 1993, **211**, P. 337–340.
- [3] Pusztai T., Oszlanyi G., et al. Bulk structure of phototransformed C_{60} . *Solid State Commun.*, 1999, **111**, P. 595–599.
- [4] Nunez-Regueiro M., Marques L., et al. Polymerized fullerite structures. *Phys. Rev. Lett.*, 1995, **74**, P. 278–281.
- [5] Iwasa Y., Arima T., et al. New phases of C_{60} synthesized at high pressure. *Science*, 1994, **264**, P. 1570–1572.
- [6] Senyavin V.M., Davydov V.A., et al. Spectroscopic properties of individual pressure-polymerized phases of C_{60} . *Chem. Phys. Lett.*, 1999, **313**, P. 421–425.
- [7] Wang Ying, Holden J.M., Bi Xiang-xin, Ecklund P.C. Thermal decomposition of polymeric C_{60} . *Chem Phys. Lett.*, 1994, **217**, P. 413–417.
- [8] Iwasa Y., Tanoue K., Mitani T., Yagi T. Energetics of polymerized fullerites. *Phys. Rev. B*, 1998, **58**, P. 16374–16377.
- [9] Nagel P., Pasler V., et al. C_{60} one- and two-dimensional polymers, dimers, and hard fullerite: Thermal expansion, anharmonicity, and kinetics of depolymerization. *Phys. Rev. B*, 1999, **60**, P. 16920–16927.
- [10] Moret R., Launois P., et al. Single-crystal study of the pressure-temperature-induced dimerization of C_{60} . *Eur. Phys. J. B*, 2004, **37**, P. 25–37.
- [11] Meletov K.P., Krestinin A.V., et al. Temperature effects in the Raman spectra of bundled single-wall carbon nanotubes. *Chem. Phys. Lett.*, 2009, **477**, P. 336–339.
- [12] Meletov K.P., Velkos G., et al. Raman study of the photopolymer formation in the $\{Pt(dbdtc)_2\} \cdot C_{60}$ fullerene complex and the decomposition kinetics of the photo-oligomers. *Chem. Phys. Lett.*, 2017, **681** (1), P. 124–129.

Crystal structure and Raman spectra of molecular complex $[\{\text{Cd}(\text{Et}_2\text{dtc})\}_2 \cdot \text{DABCO}] \cdot \text{C}_{60} \cdot (\text{DABCO})_2$ at high pressure

A. V. Kuzmin¹, D. V. Konarev², S. S. Khasanov¹, K. P. Meletov¹

¹Institute of Solid State Physics, Russian Academy of Sciences, 142432 Chernogolovka, Moscow region, Russia

²Institute of Problems of Chemical Physics, Russian Academy of Sciences,
 142432 Chernogolovka, Moscow region, Russia

kuzmin@issp.ac.ru

PACS 78.30.Na

DOI 10.17586/2220-8054-2018-9-1-33-37

The crystal structure of the molecular donor-acceptor complex $[\{\text{Cd}(\text{Et}_2\text{dtc})\}_2 \cdot \text{DABCO}] \cdot \text{C}_{60} \cdot (\text{DABCO})_2$ (where dtc is dithiocarbamate, DABCO is diazabicyclooctane) was studied by X-ray diffraction (XRD) at high pressure using the diamond anvil cell (DAC) technique. The pressure dependence of lattice parameters is smooth and monotonous, the bulk modulus and its derivative $B_0 = 7.94$ GPa and $B' = 9.65$ are close to those of pristine C_{60} . Raman spectra of the complex measured at $\lambda_{exc} = 532$ nm showed a peculiarity in the pressure dependence of $A_g(1)$, $A_g(2)$, $H_g(1)$ and $H_g(7)$ modes of the C_{60} molecule near 2 GPa. This peculiarity relates to pressure-assisted photopolymerization in the fullerene layers which is suppressed in Raman measurements at $\lambda_{exc} = 785$ nm showing smooth pressure behavior of phonon modes.

Keywords: high pressure, fullerene complexes, crystal structure, photopolymerization.

Received: 14 June 2017

Revised: 14 September 2017

1. Introduction

The behavior of fullerene complexes at high pressure is of interest due to their layered structure in which the close-packed molecules in the fullerene layers alternate with the layers of the molecular donor. The squeezing of these layers makes intermolecular distances shorter and, hence, increases the overlap between the highest occupied molecular orbitals (HOMOs) of the molecular donor and the lowest unoccupied molecular orbital (LUMO) of the fullerene acceptor that stimulates charge transfer. On the other hand, numerous Raman measurements show that fullerenes can undergo polymerization in molecular complexes at high pressure [1–4]. The Raman spectra of the $\{\text{Cd}(\text{dedtc})_2\}_2 \cdot \text{C}_{60}$ complex show time-dependent changes near 2 GPa that look like photopolymerization of pristine C_{60} [4, 5]. The photopolymerization of C_{60} can occur in thin surface layers of bulk samples via a [2+2] cyclo-addition mechanism. It requires a suitable mutual orientation of the molecules [6] which can be realized at their rotation or in the process of crystal growth. Unlike disordered photopolymer, bulk polymers synthesized under high-pressure/high-temperature (HPHT) treatment are highly ordered and their crystal structures were identified by XRD to be orthorhombic, tetragonal and rhombohedral lattices [7–9]. C_{60} molecular symmetry lowering leads to the splitting and softening of some phonon bands. As a rule, Raman examination of fullerene polymers is based on the behavior of the $A_g(2)$ PP-mode frequency which decreases from 1468 cm^{-1} for the monomer to 1463, 1458, 1446 and 1408 cm^{-1} for the dimers, linear orthorhombic, planar tetragonal and rhombohedral polymers, respectively [10–12]. Here, we report the XRD and Raman study of the $[\{\text{Cd}(\text{Et}_2\text{dtc})\}_2 \cdot \text{DABCO}] \cdot \text{C}_{60} \cdot (\text{DABCO})_2$ fullerene complex at high pressure. The pressure dependence of lattice parameters is smooth and monotonous, the bulk modulus and its derivative, $B_0 = 7.94$ GPa and $B' = 9.65$, are close to those for pristine C_{60} . The Raman spectra measured at $\lambda_{exc} = 532$ nm show a peculiarity near 2 GPa, which disappears at near infra-red laser excitation 785 nm when photopolymerization in the fullerene layers is suppressed.

2. Experimental details

The crystals of the donor-acceptor complex $[\text{big}\{\{\text{Cd}(\text{Et}_2\text{dtc})\}_2 \cdot \text{DABCO}\}] \cdot \text{C}_{60} \cdot (\text{DABCO})_2$ were synthesized as described in [13]. The structural data were obtained for the single crystals at pressures up to 3 GPa using DAC and a four-circle Oxford Diffraction Gemini-R diffractometer equipped with two-dimensional CCD. The Raman spectra were recorded in back-scattering geometry using an Acton SpectraPro-2500i spectrograph and a LabRam HR micro-Raman setup equipped with a Peltier cooled CCD. The 532 nm and 785 nm laser lines were used for the Raman scattering measurements with laser power up to $\sim 180 \mu\text{W}$ before the DAC while the 4:1 methanol/ethanol mixture and the ruby fluorescence technique were used as pressure transmitting medium and a pressure calibration tool, respectively [14].

3. Results and discussion

The XRD data show that the $[\{\text{Cd}(\text{Et}_2\text{dte})\}_2 \cdot \text{DABCO}] \cdot \text{C}_{60} \cdot (\text{DABCO})_2$ complex acquires a tetragonal structure, space group $Pbam$ with unit cell parameters $a = 10.583 \text{ \AA}$, $b = 17.178 \text{ \AA}$, $c = 21.273 \text{ \AA}$, $V = 3867 \text{ \AA}^3$. In the fullerene layers, each C_{60} molecule is surrounded by six neighbors with the shortest distances between the centers of molecules $d = 10.088$ (four neighbors) and $d' = 10.583 \text{ \AA}$ (two neighbors). No C–C bonds were found between the fullerene molecules under ambient conditions. Fig. 1 depicts the pressure dependence of lattice parameters of the complex at pressures up to 3 GPa while the inserts shows the arrangement of molecules in view along a and c axes at a pressure of $P = 0.66 \text{ GPa}$. Circles denote the pressure dependence of cell volume V/V_0 , squares – lattice parameter c/c_0 perpendicular to molecular layers, hexagons – the shortest distance between the fullerene molecules d/d_0 , and dotted lines are fits by Murnaghan equation of state:

$$(V/V_0)^{-B'} = \{1 + P(B'/B_0)\}, \quad (1)$$

where $B_0 = 7.94 \text{ GPa}$ is the bulk modulus and $B' = 9.65$ is its derivative. The values of bulk modulus and its derivative are close to those of the C_{60} fullerite in simple cubic phase [15]. The pressure dependence of lattice parameters is smooth and monotonous. Compressibility within molecular layers is smaller than that in the perpendicular direction that can be ascribed to the layered structure. According to XRD data, there is no phase transition in the pressure range under investigation.

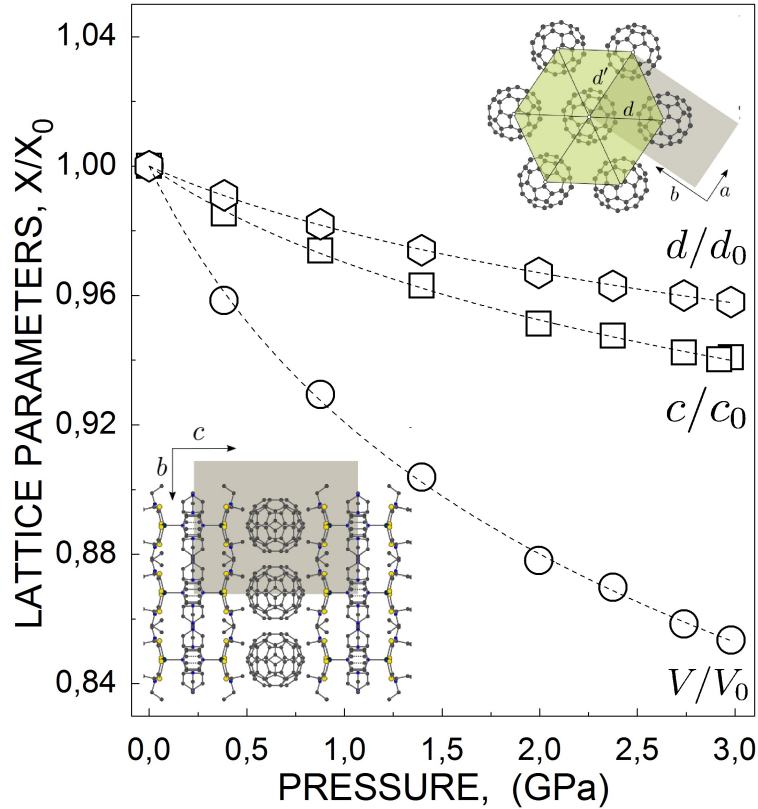


FIG. 1. Pressure dependences of lattice parameters of the $[\{\text{Cd}(\text{Et}_2\text{dte})\}_2 \cdot \text{DABCO}] \cdot \text{C}_{60} \cdot (\text{DABCO})_2$ complex and arrangement of molecules in the lattice at $P = 0.66 \text{ GPa}$

Possible polymerization within fullerene layers may be expected at a pressure of $\sim 17 \text{ GPa}$ when the shortest interfullerene distances approach 9.15 \AA which is a typical inter-cage distance in fullerene polymers [8, 9].

Figure 2 shows the Raman spectra of the $[\{\text{Cd}(\text{Et}_2\text{dte})\}_2 \cdot \text{DABCO}] \cdot \text{C}_{60} \cdot (\text{DABCO})_2$ complex collected at pressure up to $\sim 6 \text{ GPa}$ at $\lambda_{exc} = 532 \text{ nm}$ (left panel) and $\lambda_{exc} = 785 \text{ nm}$ (right panel). The spectra in the left panel were obtained with laser power $\sim 180 \mu\text{W}$ and 300 minutes exposure, whereas spectra series in the right panel was collected with $\sim 34 \mu\text{W}$ laser and 16 min exposure time. The Raman spectra measured at a fixed site of the sample show the phonon modes of the C_{60} molecule due to its dominant contribution to the Raman

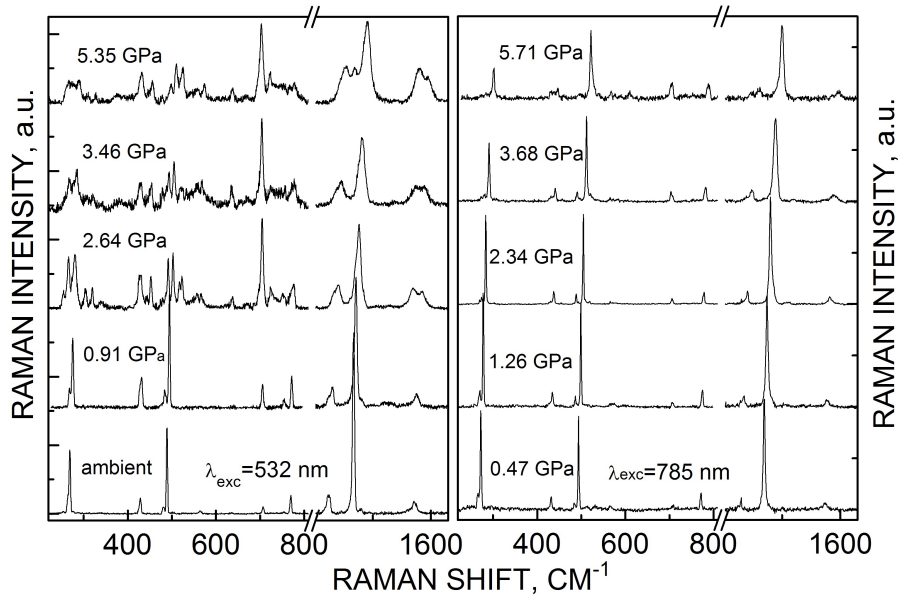


FIG. 2. Raman spectra of the $[\text{Cd}(\text{Et}_2\text{dtc})_2\cdot\text{DABCO}]\cdot\text{C}_{60}\cdot(\text{DABCO})_2$ complex at different pressures recorded at 532 nm (left panel) and 785 nm (right panel) laser excitations

cross-section of complexes [5]. The spectra at ambient conditions are identical in both panels and demonstrate positive pressure shift whereas their intensity distribution does not depend on exposure time.

The difference in pressure behavior appears near ~ 2 GPa when the phonon bands in the left panel split and broaden, whereas in the right panel, they remain unchanged. Similar time-dependent changes observed earlier in the fullerene complex $\{\text{Cd}(\text{dedtc})_2\}_2\cdot\text{C}_{60}$ were attributed to the pressure-assisted photopolymerization [4].

We examined the possibility of pressure-induced photopolymerization in the fullerene layers of the $[\{\text{Cd}(\text{Et}_2\text{dtc})\}_2\cdot\text{DABCO}]\cdot\text{C}_{60}\cdot(\text{DABCO})_2$ complex by using laser excitations at two different wavelengths. The Raman spectra recorded every 15 min ($\lambda_{exc} = 532$ nm, 180 μW laser power) show fast transformation that occurs in the first Raman scan and further scans do not affect the spectra. Fig. 3 shows evolution of the spectra near the $A_g(2)$ PP-mode recorded consequently every 30 minutes at $\lambda_{exc} = 785$ nm, laser power 134 μW , and 10 minute exposure at 2.34 GPa (left panel) and 4.3 GPa (right panel) pressure. The spectra at 2.34 GPa are stable whereas at 4.3 GPa, they evolve new components observed near $A_g(2)$ PP-mode and are related to the photo-oligomers of C_{60} . In addition, the five-fold degenerate H_g modes split. The initial spectrum at 4.3 GPa is not yet transformed and resembles the spectra of monomer recorded at 2.34 GPa. This means that spectra in the right panel of Fig. 2 recorded at ~ 34 μW and 16 min exposure can also be related to the monomer.

The pressure dependence of phonon modes is shown in Fig. 4. The open circles and squares mark the frequencies of the $A_g(1)$, $H_g(1)$, $A_g(2)$ and $H_g(7)$ modes recorded at $\lambda_{exc} = 532$ nm, laser power 180 μW and 300 min exposure, whereas the filled circles refer to the data recorded at $\lambda_{exc} = 785$ nm, laser power 34 μW and 16 minutes exposure. Solid and dotted lines are linear fits of the experimental data for the $A_g(2)$ and $H_g(7)$ modes and sub linear fits for the $A_g(1)$ and $H_g(1)$ modes. The pressure dependence of the $A_g(2)$ PP-mode frequency measured at $\lambda_{exc} = 532$ nm exhibits an irregularity near ~ 2 GPa: the pressure coefficient between 2 and 3 GPa is almost zero, whereas outside this region, it is ~ 5 $\text{cm}^{-1}/\text{GPa}$.

A similar peculiarity was observed for the $A_g(1)$, $H_g(1)$ and $H_g(7)$ modes, as well as $H_g(1)$ splits. Extrapolation of the linear fit for the $A_g(2)$ mode to normal pressure gives a value of ~ 1464 cm^{-1} that is the frequency of dimers C_{120} . On the other hand, the data obtained at $\lambda_{exc} = 785$ nm show smooth and monotonous pressure behavior. Thus, the peculiarity in the pressure behavior of phonon modes relates to pressure-assisted photo-induced polymerization under visible laser excitation which is suppressed under near infra-red laser excitation.

4. Conclusions

The XRD analysis of single crystals of $[\{\text{Cd}(\text{Et}_2\text{dtc})\}_2\cdot\text{DABCO}]\cdot\text{C}_{60}\cdot(\text{DABCO})_2$ complex at high pressure shows a smooth and monotonous pressure dependence of lattice parameters with bulk modulus $B_0 = 7.94$ GPa and its derivative $B' = 9.65$. The pressure dependence of phonon modes in the Raman spectra recorded at $\lambda_{exc} = 532$ nm shows a peculiarity near ~ 2 GPa which is not observed in the spectra recorded at $\lambda_{exc} = 785$ nm.

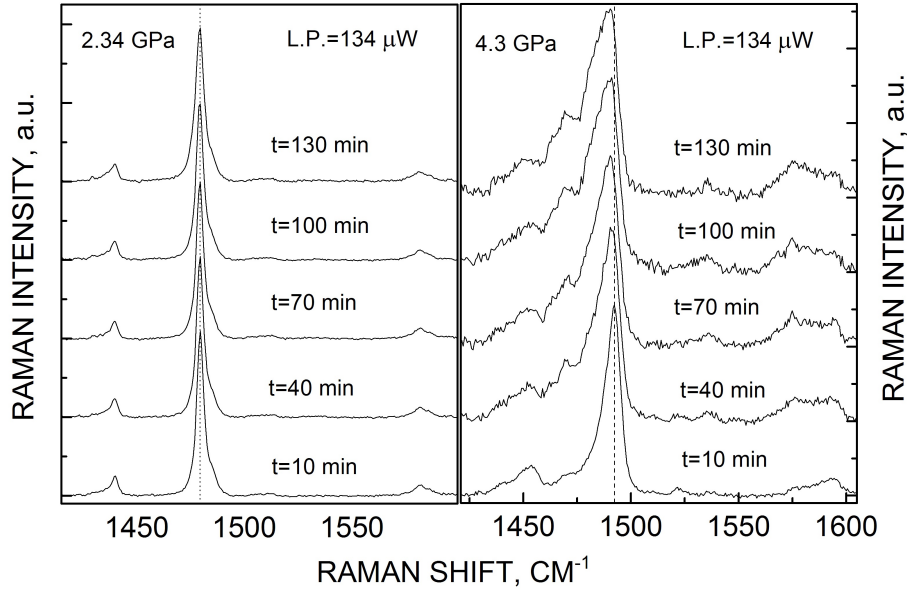


FIG. 3. Time evolution of Raman spectra recorded near the $A_g(2)$ PP-mode at $\lambda_{exc} = 785$ nm and 10 min exposure at 2.34 GPa (left panel) and 4.3 GPa (right panel) pressure. L. P. – laser power

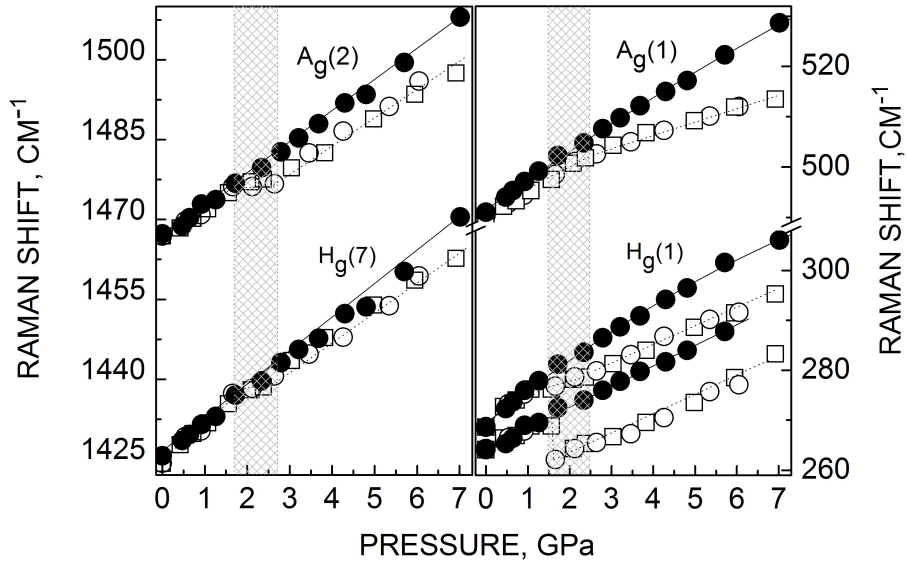


FIG. 4. Pressure dependence of $A_g(1)$, $H_g(1)$, $A_g(2)$ and $H_g(7)$ modes of the $[\text{Cd}(\text{Et}_2\text{dtc})_2 \cdot \text{DABCO}] \cdot \text{C}_{60} \cdot (\text{DABCO})_2$ complex. Open symbols – laser excitation 515 nm, filled symbols – laser excitation 785 nm, solid and dotted lines – fits

This peculiarity relates to the pressure-assisted photo-induced polymerization in the fullerene layers, which is suppressed under near infra-red laser excitation. The absence of photopolymerization at ambient conditions means that close proximity of fullerene molecules is suppressed by the interaction with donor molecules. The most intriguing is high-pressure photopolymerization, which means the emergence of rotation at elevated pressure. Finally, we suppose that the pressure-induced transformations previously observed in numerous Raman studies of fullerene complexes can also be related to the pressure-assisted photo-induced transformations instead of pressure-induced transformations.

Acknowledgements

The main financial support by the Federal Agency for Scientific Organizations is greatly acknowledged. The partial support by the Russian Foundation for Basic Research, grant No. 15-02-01495, and the RAS Presidium Program "Physics of compressed matter" are greatly acknowledged. K. P. M. thanks the Aristotle University of Thessaloniki for hospitality.

References

- [1] Cui Wen, Yao Mingguang, et al. Reversible polymerization in doped fullerides under pressure: the case of $C_{60} \cdot \{Fe(C_5H_5)_2\}_2$. *J. Phys. Chem. B*, 2012, **116**, P. 2643–2650.
- [2] Meletov K.P., Konarev D.V. Raman study of the pressure-induced phase transitions in the molecular donor-acceptor complex $\{Pt(dbdtc)_2\} \cdot C_{60}$. *Chem. Phys. Lett.*, 2012, **553**, P. 21–25.
- [3] Meletov K.P. Phase transitions at high pressure in the fullerene C_{60} molecular donor-acceptor complex $\{Hg(dedtc)_2\}_2 \cdot C_{60}$. *Phys. Solid State*, 2014, **56**, P. 1689–1695.
- [4] Meletov K.P., Konarev D.V., Tolstikova A.O. Phase transitions and photoinduced transformations at high pressure in the molecular donor-acceptor fullerene complex $\{Cd(dedtc)_2\}_2 \cdot C_{60}$. *JETP*, 2015, **120**, P. 989–997.
- [5] Rao A.M., Zhou P., et al. Photoinduced polymerization of solid C_{60} films. *Science*, 1993, **259**, P. 955–957.
- [6] Zhou P., Dong Z.H., Rao A.M., Ecklund P.C. Reaction mechanism for photopolymerization of solid fullerene C_{60} . *Chem. Phys. Lett.*, 1993, **211**, P. 337–340.
- [7] Pusztai T., Oszlanyi G., et al. Bulk structure of phototransformed C_{60} . *Solid State Commun.*, 1999, **111**, P. 595–599.
- [8] Iwasa Y., Arima T., et al. New phases of C_{60} synthesized at high pressure. *Science*, 1994, **264**, P. 1570–1572.
- [9] Nunez-Regueiro M., Marques L., et al. Polymerized fullerite structures. *Phys. Rev. Lett.*, 1995, **74**, P. 278–281.
- [10] Rao A.M., Ecklund P.C., et al. Infrared and Raman studies of pressure-polymerized C_{60} . *Phys. Rev. B*, 1997, **55**, P. 4766–4773.
- [11] Wägberg T., Jacobsson P., Sundqvist B. Comparative Raman study of the photopolymerized and pressure-polymerized C_{60} films. *Phys. Rev. B*, 1999, **60**, P. 4535–4538.
- [12] Davydov V.A., Kashevarova L.S., et al. Spectroscopic study of pressure polymerized phases of C_{60} . *Phys. Rev. B*, 2000, **61**, P.11936–11945.
- [13] Konarev D.V., Khasanov S.S., et al. Fullerene complexes with divalent metal dithiocarbamates: structures, magnetic properties, and photoconductivity. *Russ. Chem. Bull., Int. Ed.*, 2007, **56**, P. 2145–2161.
- [14] Jayaraman A. Ultrahigh pressures. *Rev. Sci. Instrum.*, 1986, **57**, P. 1013–1031.
- [15] Lundin A., Sundqvist B. Compressibility of C_{60} in the temperature range 150–335 K up to a pressure of 1 GPa. *Phys. Rev. B*, 1996, **53**, P. 8329–8336.

Terrestrial development of the experiments on the fullerite C₆₀ crystal growth in microgravity

A. V. Bazhenov¹, D. N. Borisenko¹, E. B. Borisenko¹, A. S. Senchenkov², A. V. Egorov²,
N. N. Kolesnikov¹, A. A. Levchenko¹

¹Institute of Solid State Physics, Russian Academy of Sciences, Chernogolovka, Russia

²Research and Development Institute for Launch Complexes, Moscow, Russia

bazhenov@issp.ac.ru, bdn@issp.ac.ru, borisenk@issp.ac.ru, 022@niisk.ru, nkolesn@issp.ac.ru, levch@issp.ac.ru

PACS 81.10.h; 81.10.Bk

DOI 10.17586/2220-8054-2018-9-1-38-40

Microgravity creates favorable conditions to reduce dislocations and grain boundaries density in growing crystals due to absence of close contact with the ampoule walls and absence of plastic deformation of the crystal under its own weight. For improvement of the fullerite C₆₀ crystal growth technology before the scheduled space experiments on the ISS the growing of the high purity grade fullerite C₆₀ crystals with the sufficiently high structural perfection were carried out on the Earth from the C₆₀ vapor in sealed quartz ampoules (pre-evacuated to the pressure of 10⁻³ Pa) at temperatures in the evaporation zone ranging from 560 – 610 °C with a temperature gradient between the evaporation and deposition zones of 3 – 10 K/cm within 72 h. The grown single crystals had a size of ~ 5 × 5 × 5 mm and habitus corresponding to the fcc lattice. IR spectroscopy shows the high purity fullerite C₆₀.

Keywords: fullerite, C₆₀, crystal growth, sublimation, microgravity, IR spectroscopy.

Received: 16 June 2017

Revised: 17 October 2017

1. Introduction

To investigate the electron–electron correlation and polaron effects caused by the small conduction band (width of 0.05 eV) the perfect fullerite C₆₀ crystals with sufficiently large overall dimensions (about several millimeters) are required. The continuous growth of fullerite C₆₀ crystals by physical vapor transport has been described by the various authors [1–3]. The fullerite C₆₀ crystals grown in the first experiments in microgravity aboard the FOTON-M3 spacecraft [4] had more perfect crystal structure in comparison with the crystals grown on the Earth: microgravity creates favorable conditions to reduce the dislocations density and grain boundaries in the growing crystals due to absence of close contact with the ampoule walls and absence of plastic deformation of the crystal under its own weight.

2. Experimental

For further improvement of the technology before the scheduled space experiments on the ISS, the growing of the high purity grade fullerite C₆₀ crystals with the sufficiently high structural perfection were performed on the Earth from the C₆₀ vapor in sealed quartz ampoules (pre-evacuated to the pressure of 10⁻³ Pa) at temperatures in the evaporation zone ranging from 560 – 610 °C with the temperature gradient between the evaporation and deposition zones of 3 – 10 K/cm within 72 h. The preparation of initial samples for analogous growth experiments was studied in detail in the previous work [5] and in our case, includes a low-temperature treatment of the fullerene C₆₀ powder under dynamic vacuum of 10⁻³ Pa at the temperature of 350 – 400 °C within 3 h, then this powder was sublimated under dynamic vacuum of 10⁻³ Pa at 600 – 650 °C within 8 h. From this sublimated powder the primary fullerite C₆₀ crystals were grown under a static vacuum of 10⁻³ Pa in sealed quartz ampoules at the temperature 610 °C with the temperature gradient between the evaporation and deposition zones 5 K/cm within 72 h. Then the regrowth of the primary deposit was run at the same conditions, yielding the high purity material. After these purification procedures, the resulting material was charged into quartz ampoules evacuated to a pressure of 10⁻³ Pa, hermetically sealed and placed into the multi-zone growth furnace for crystal growth. Three types of the gradients used in the experiments are shown in Fig. 1. The polycrystalline deposits of C₆₀ were obtained in the runs #1 and #2. The fullerite C₆₀ single crystal was grown in the run #3.

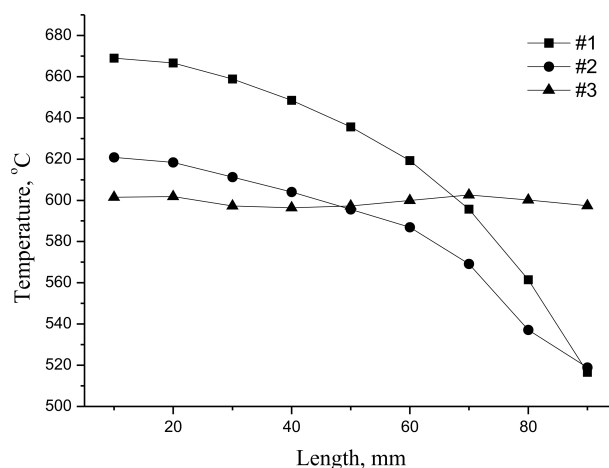


FIG. 1. Three types of the gradients of the multi-zone growth furnace (runs #1, #2, #3)

3. Results and discussion

The single crystals grown in the run #3 have the size of about $5 \times 5 \times 5$ mm and habitus corresponding to the fcc phase of C_{60} (see Fig. 2). The presence of twins was revealed using the optical microscopy and the single-crystal diffractometer Oxford Diffraction Gemini-R. The twins interface corresponds to the $\{111\}$ fcc conjunction plane.

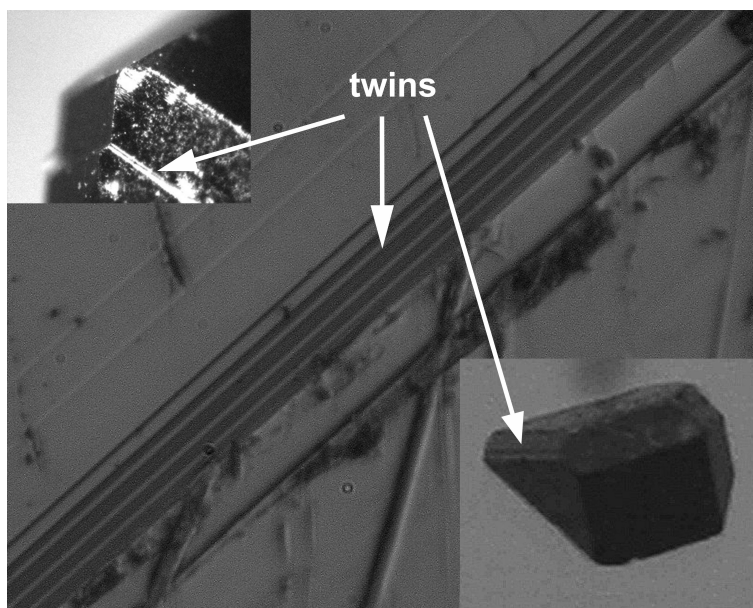


FIG. 2. Optical image of the twins (arrows point “rungs” – the twins interface)

IR transmission spectrum of the C_{60} powder produced from the fullerite of run #3 is represented in Fig. 3. Strong scattering on shorter waves is explained by the KBr surface roughness. These data show the high purity of fullerite C_{60} after the overall technology chain.

4. Conclusions

The heating rate and the temperature distribution in the furnace must be carefully controlled because they have strong influence on the nucleation and growth rate and hence on the perfection of the grown crystals. Optimizing these parameters, the large C_{60} single crystals of good quality with size more than 5 mm can be grown reproducibly.

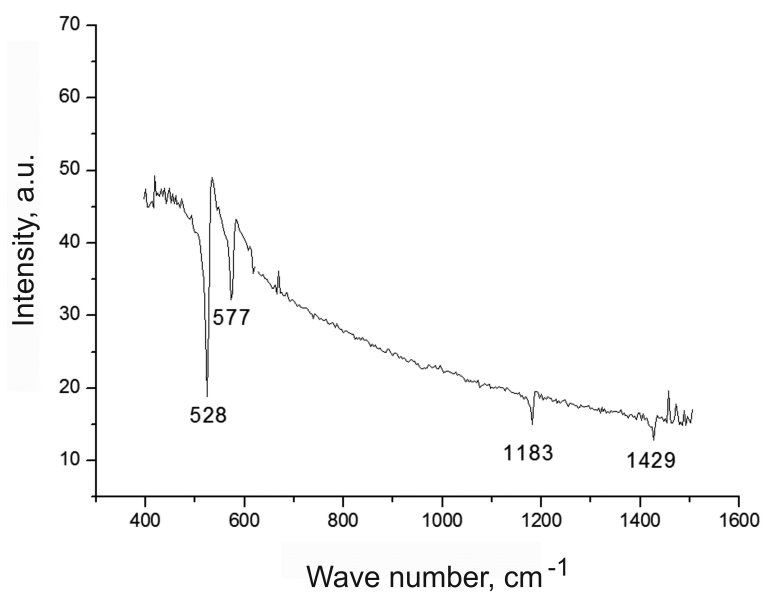


FIG. 3. IR spectrum measured for fullerite C₆₀ single crystal from the run #3

References

- [1] De Bruijn J., Dworki A., et al. Thermodynamic properties of a single crystal of fullerene 60: a DSC Study. *Europhys. Lett.*, 1993, **24** (7), P. 551–557.
- [2] Xiao Rong-Fu. Growth of large fullerene C₆₀ crystals and highly oriented thin films by physical vapor transport. *J. Cryst. Growth*, 1997, **174**, P. 821–827.
- [3] Verheijen M.A., van Enkevort W.J.P., Meijer G. Growth phenomena on C₆₀ crystals. *Chem. Phys. Lett.*, 1993, **216** (1–2), P. 72–80.
- [4] Bazhenov A. Fullerit C₆₀ single crystal growth aboard the FOTON-M3 spacecraft. *Proceedings of 60th Intern. Astronautical Congress*, Daejeon, Republic of Korea 12–16 October 2009, P. 630–633.
- [5] Sidorov N.S., Palnichenko A.V., et al. The method of the high purity grade fullerene C₆₀ crystals production. Patent 2442847 Russia: MPK C30B 23/00, 2010119780/05, 20.02.2012, Bull. 5.

Optimization of the solvent-exchange process for high-yield synthesis of aqueous fullerene dispersions

I. V. Mikheev^{1,2}, M. O. Pirogova¹, T. A. Bolotnik^{1,2}, D. S. Volkov^{1,2}, M. V. Korobov¹, M. A. Proskurnin^{1,2}

¹Chemistry Department, Lomonosov Moscow State University, Moscow, Russia

²Analytical Centre of Lomonosov Moscow State University / Agilent Technologies Authorized Partner Laboratory, Moscow, Russia

mikheev.ivan@gmail.com, mariy7991@yandex.ru, timab@tut.by, dmsvolkov@gmail.com, mkorobov49@gmail.com, proskurnin@gmail.com

PACS 68.55.ap, 81.05.ub

DOI 10.17586/2220-8054-2018-9-1-41-45

The ultrasound-assisted solvent-exchange technique for aqueous fullerene dispersions (AFD) of C₆₀ (10⁻⁴ – 10⁻⁶ M) have been improved for high-yield synthesis, thereby achieving AFDs with total recovery over 90 %. Using ICP-AES, HPLC-UV, HGC-MS, the elemental and residual organic compounds have been estimated as not exceeding 3 ppm. The possible structure of fullerene clusters in AFD was assumed as {n[C₆₀]mC₆H₅COO⁻(m-x)Na⁺}xNa⁺.

Keywords: solvent-exchange process, fullerene C₆₀, stability, atomic spectroscopy.

Received: 16 June 2017

Revised: 1 September 2017

1. Introduction

Fullerene-based materials have already been used in new composite materials with superconducting properties, photoresist masks, lubricants, etc. [1–8]. Fullerenes find the application in medicine and cosmetology, as well as in such areas as theranostics, nanomedicine, drug delivery, etc. Among the most promising are aqueous fullerene dispersions (AFDs), with a wide range of applications in medicine and other fields that require fullerenes in aqueous media [9–13]. AFDs of unmodified fullerenes are preferable due to biocompatibility and safety: owing to their open surface without moieties, they are not involved in metabolic processes. This is especially the case of endohedral metallofullerene (EMF) AFDs, which are promising contrast agents.

Expanding the range of AFD applications requires improvement in their preparation. Derivatization and solubilization have been disregarded in this field. The most relevant techniques of AFD preparation are solvent exchange [11, 14, 15], dialysis [16], and mixing [17–19]. However, the total yield of fullerene transfer into water of 100 % has not yet been achieved, which leads to significant losses and increases for the cost of the final product, especially for EMFs. The ultrasound-assisted solvent-exchange procedure produces AFDs from a range of neat solvents, both polar and nonpolar, and that are stable for long periods. There was no previously described exact mechanism for the solubilization, although some research has dealt with the prediction of dispersion stability.

Apart from the yield, the main drawback for the solvent-exchange process is significant amounts of hazardous organic substances in AFDs [11, 14, 15]. However, not much attention is paid to the purity of the produced dispersions, which is unacceptable for biomedicine. Therefore, it is necessary to develop techniques for purification and determination of the residual amounts of organic substances. Here, the ultrasound-assisted solvent-exchange procedure has been optimized for preparing AFD with a yield close to 100 %. We selected widely available fullerene C₆₀ and toluene due to its lower volatility compared to benzene and good solubility of C₆₀.

2. Materials and methods

To produce AFD and improve reagent dissolution during the preparation, a GRAD 180-35 (LLC Grad-Technology, Russia) ultrasonic bath was used. Weighing was performed on an Ohaus DV-114C analytical balance (Switzerland). Absorbance measurements in the UV/vis range were carried out using an Agilent Cary 4000 (Australia). Pure toluene Reakhim (Russia), ultra-pure water “type 1” from a Milli-Q Millipore Corporation water purification system, 18.2 mΩ×cm, pure potassium hydrogen phthalate “Merck” (Germany), fullerene C₆₀ 99.5 % LLC NeoTechProdukt (Russia) were used. Elemental analysis was performed by an Agilent ICP-AES 720 (Malaysia) with ICP Expert software 2.0.5 according to ISO 11885:2007(en). All emission lines (Table 1) were measured simultaneously (a MultiCal mode). To estimate volatile organic compounds, Headspace Gas Chromatography – Mass Spectrometry (HGC-MS) Shimadzu, Germany was used. A CP Sil 5 CB column (25 m×0.25 mm×0.4 μM,

starting temperature 40 °C, isotherm for 5 min, temperature increase up to 130 °C, temperature pitch 9 °C/min, isotherm for 3 min). For benzoate detection in AFDs, Agilent 1200 HPLC-UV was used with an Eclipse XDB-C18 column (Agilent, USA) 150 × 4.6 mm, sorbent particle diameter, 5 μm; precolumn Security Guard C18 (4 × 3 mm; Phenomenex, USA); column temperature: 35 °C; sample volume: 100 μL; mobile phase: Eluent A, 0.2 % phosphoric acid (83 % v/v), Eluent B, acetonitrile (17 % v/v); mobile phase rate: 1 mL/min; detection conditions: wavelength 235 nm, spectral bandwidth 4 nm. LOD and LOQ were calculated according to IUPAC 1998 recommendations.

TABLE 1. ICP–AES measurements conditions

Instrumental conditions settings	
RF power (kW)	1.40
Plasma flow (L/min)	15
Axial flow (L/min)	1.50
Nebulizer flow (L/min)	0.70
Replicate read time (s)	5
Plasma stabilization delay (s)	15
Replicates	3
Sample introduction settings	
Sample uptake delay (s)	15
Pump rate (rpm)	15

3. Results and discussion

Aqueous fullerene C₆₀ dispersions were obtained by the ultrasound-assisted solvent exchange process that is generally known in colloidal chemistry. This approach was previously applied for AFDs [11, 12, 20]. Nevertheless, here, we have applied and developed methods and approaches to improve the yield and physicochemical properties, as well as the sample purity. We have previously published [1–4] the data concerning fullerene state in pristine fullerene samples before ultrasound treatment and as well fullerene ultrasound-assisted solvent-exchange process. We have not observed any peaks with masses higher than the molecular ion peak [M]⁺ (e.g. epoxy-, hydroxyl-, derivatives, and polymeric structures: dimeric, trimeric, etc.) for both pristine fullerene and their aqueous dispersions).

3.1. Quantitative determination of fullerenes

For the quantification of fullerenes both in the aqueous and in the organic phases, UV/vis spectroscopy was used. For toluene, the absorption spectra and the apparent molar absorptivity ($\epsilon_{407} = 3.5 \pm 0.2 \text{ M}^{-1} \text{ cm}^{-1}$) coincide with the existing data [17, 21, 22]. For the quantification, a wavelength of 407 nm was used. LOD and LOQ for C₆₀ fullerene in toluene are 100 and 400 nM. These values are acceptable for the optimization of solvent-exchange procedures for a wide range of concentrations up to micromolar. Quantification of fullerenes in the aqueous phase requires a strict control of carbon species. A drawback of solvent-exchange procedures is residual organic solvents, which result in overestimation of fullerenes by a TOC analyzer. By purging for 16 h, we reduced up to 44 % the total quantity of the volatile organic matter (Fig. 1 and Fig. 2). The initial content of toluene in AFD is 0.044 ± 0.005 ppm (Fig. 1) and about 25 hours are necessary to reduce its content to ppb level or less. To the best of our knowledge, it is the first description of purging for purification of AFDs C₆₀ from nonpolar organic admixtures. This approach is cheaper and no less effective compared to solid-phase extraction (using C18-sorbents).

After checking the aqueous dispersions, a combination of TOC and UV/vis. measurements allowed us to calculate an apparent molar absorptivity (Table 2) [9, 11]. These data have a good correlation with existing data that we used for fullerene quantification. LOD and LOQ were 100 and 300 nM, respectively (at 349 nm). Thus, due to the selected conditions with coincided performance parameters for fullerene C₆₀ in toluene and in their AFD, we can proceed to the adjusting of optimal conditions for obtaining AFD in high-yield synthesis.

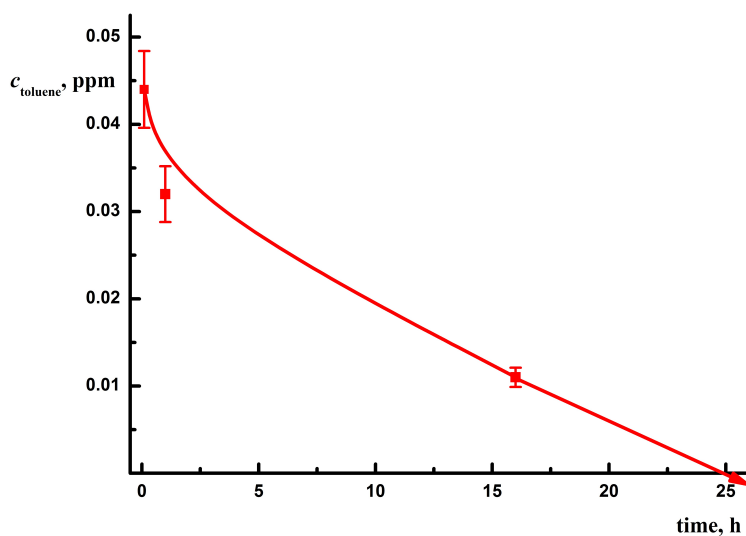


FIG. 1. Dependence of toluene concentration in AFD on the argon purging time (rate, 100 mL/min) by HGC-MS

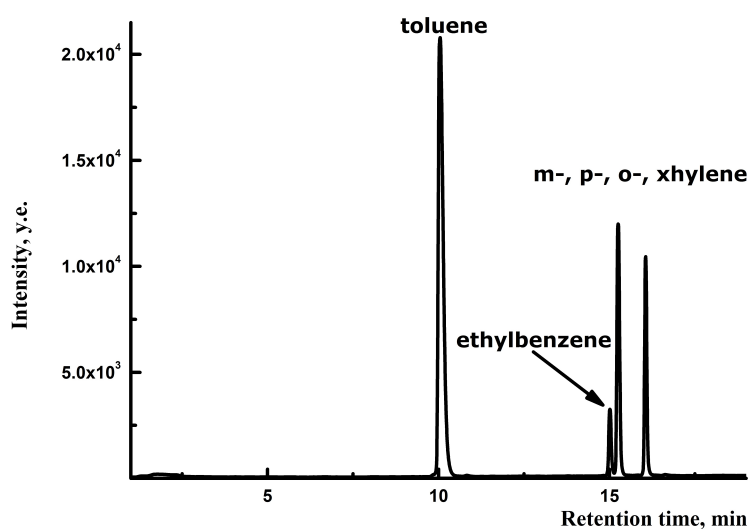


FIG. 2. Representative HS GC-MS chromatograms are registered on 91 Da m/z for non-purging AFD C_{60}

TABLE 2. Apparent molar absorptivities for C_{60} in water and its deviation from existing data

λ , nm	$\varepsilon \times 10^3 \text{ M}^{-1}\text{cm}^{-1}$	$\varepsilon \times 10^3 \text{ M}^{-1}\text{cm}^{-1}$ [9, 11]	$\delta\varepsilon, \%$
349	49 ± 1	49 ± 2	0.7
268	71 ± 8	67 ± 6	5.6
220	69 ± 8	60 ± 6	13.0

3.2. Optimization of the solvent-exchange process for fullerene C_{60} AFD from toluene

Having calculated the LOD and LOQ for fullerene C_{60} in toluene and in AFD, we improved the conditions for obtaining AFD using ultrasound baths with higher electric power (up to 1 kW) and Erlenmeyer flasks with the lowest glass thickness (down to 3 mm). The main optimization point consisted of using different ratios of fullerene in toluene and water. It was found that the appropriate recovery values (more 50 %) was achieved for the fullerene

concentration in toluene in the range of $n \times 10^{-5}$ M. The concentration range from $n \times 10^{-6}$ M to $n \times 10^{-4}$ M was tested.

At different ratios of C_{60} in toluene to water, the total volume of the toluene-water system did not differ by more than 15 % by volume. Thus, we could use the same Erlenmeyer flasks for 250 mL to obtain more reproducible results. The average time of ultrasonic treatment was about 12 h at an electric power of 0.9 kW.

Hydrophobic fullerene nanoparticles in AFDs show a negative zeta-potential in water. In all cases, we found values < -20 mV. Polydispersity indexes for all solutions were 0.10 – 0.15. These values are close to those for a material with a unimodal distribution of nanoparticles. The optimum conditions provide the transfer of fullerene up to 100 % into aqueous media for C_{60} . ICP-AES was used for determining elemental composition for major components of the glass vessel (sodium, silicon, calcium etc.) in the final solution; the total concentration of elements is 3 ppm (Table 3).

TABLE 3. The recovery of fullerenes in two parallel experiments, the average recovery value, ($n = 2$, $P = 0.95$) and the results of elemental analysis using the ICP-AES ($n = 3$, $P = 0.95$)

C_{60} toluene/water ratio	Recovery (I) C_{60} into aqueous phase, %	Recovery (II) C_{60} into aqueous phase, %	Average recovery (I) C_{60} into aqueous phase, %	Sodium, ppb ¹	Silicon, ppb ¹
2 : 1	29 ± 5	22 ± 3	26 ± 8	160 ± 24	102 ± 15
1 : 2	34 ± 5	26 ± 6	30 ± 11	580 ± 87	2081 ± 312
1 : 1	55 ± 2	49 ± 4	52 ± 6	199 ± 30	280 ± 42
1 : 5	91 ± 5	93 ± 5	92 ± 10	211 ± 32	550 ± 83
1 : 10	6 ± 2	3 ± 1	4 ± 3	266 ± 40	319 ± 48
1 : 25	1.5 ± 0.2	1.7 ± 0.3	1.6 ± 0.5	35 ± 5	36 ± 5

¹Another elements concentration: Ag, Al, As, Ba, Be, Cd, Co, Cr, Fe, K, Li, Mn, Mo, Ni, Pb, Sb, Sn, Sr, Ti, Tl, V, W, Zr < 1 ppb, Cu < 3 ppb, K, Mg, Ca < 80 ppb, B < 100 ppb

HPLC-UV showed that the total value of benzoate (a product of ultrasound oxidation of toluene) was no more 30 ppb. We assumed the possible clustered structure of the micelle which including $\{n[C_{60}]mC_6H_5COO^-(m-x)Na^+\}xNa^+$, which can provide, apparently, the most probable source of stabilization of fullerenes. It has no impact on increasing ionic strength and AFD stability. In certain conditions, there is a complete shift of the equilibrium in a one-component system towards AFD formation.

4. Conclusions

The conditions for high-yield preparation of all types of AFDs have been found. Our results highlighted optimization techniques for obtaining stable aqueous dispersions. Obviously, in the future, this technique should be employed for higher-order fullerenes and metallofullerenes. A special role in this, of course, will be played by metal-containing fullerenes. First, since the cost of the initial samples is now very high. Secondly, in view of the unique structure and their paramagnetic properties (*e.g.* Gd^{3+}) of aqueous dispersions, there are promising applications for studying and using them as contrast agents in MRI. Additionally, such work will provide a means to approach solutions for difficult problems, such as establish the nature of the fullerenes' stability in their AFDs.

Acknowledgements

The work is supported by The Russian Science Foundation, grant no. 14-23-00012-P. We are grateful to Agilent Technologies – Russia and its CEO, Dr. Konstantin Evdokimov, for the equipment used in this study.

References

- [1] Dresselhaus S., Dresselhaus G., Eklund P.C. *Science of Fullerenes and Carbon Nanotubes: Their Properties and Applications*. Elsevier Science, 1996.
- [2] Thakur V.K., Thakur M.K. *Chemical Functionalization of Carbon Nanomaterials: Chemistry and Applications*. CRC Press, 2015.
- [3] Yang S., Wang C.R. *Endohedral Fullerenes: From Fundamentals to Applications*. World Scientific Publishing Company, 2014.
- [4] Karas M., Bahr U., et al. Principles and applications of matrix-assisted UV-laser desorption/ionization mass spectrometry. *Analytica Chimica Acta*, 1990, **241** (2), P. 175–185.

- [5] Jensen A.W., Wilson S.R., Schuster D.I. Biological applications of fullerenes. *Bioorganic & Medicinal Chemistry*, 1996, **4**(6), P. 767–779.
- [6] Georgakilas V., Perman J.A., Tucek J., Zboril R. Broad Family of Carbon Nanoallotropes: Classification, Chemistry, and Applications of Fullerenes, Carbon Dots, Nanotubes, Graphene, Nanodiamonds, and Combined Superstructures. *Chem. Rev.*, 2015, **115** (11), P. 4744–4822.
- [7] Anilkumar P., Lu F., et al. Fullerenes for applications in biology and medicine. *Curr. Med. Chem.*, 2011, **18** (14), P. 2045–2059.
- [8] Bakry R., Vallant R.M., et al. Medicinal applications of fullerenes. *Intern. J. Nanomedicine*, 2007, **2** (4), P. 639–649.
- [9] Andrievsky G.V., Klochkov V.K., Bordyuh A.B., Dovbeshko G.I. Comparative analysis of two aqueous-colloidal solutions of C₆₀ fullerene with help of FTIR reflectance and UVVis spectroscopy. *Chem. Phys. Lett.*, 2002, **364** (1–2), P. 8–17.
- [10] Mchedlov-Petrossyan N.O., Klochkov V.K., Andrievsky G.V. Colloidal dispersions of fullerene C₆₀ in water: some properties and regularities of coagulation by electrolytes. *J. Chem. Soc., Faraday Trans.*, 1997, **93** (24), P. 4343–4346.
- [11] Mikheev I.V., Khimich E.S., et al. Quasi-equilibrium distribution of pristine fullerenes C₆₀ and C₇₀ in a watertoluene system. *Carbon*, 2017, **111**, P. 191–197.
- [12] Mikheev I.V., Volkov D.S., Proskurnin M.A., Korobov M.V. Monitoring of Aqueous Fullerene Dispersions by Thermal-Lens Spectrometry. *Intern. J. Thermophysics*, 2015, **36** (5–6), P. 956–966.
- [13] Kyzyma E.A., Tomchuk A.A., et al. Structure and toxicity of aqueous fullerene C₆₀ solutions. *J. Surf. Investigation. X-ray, Synchrotron and Neutron Techniques*, 2015, **9** (1), P. 1–5.
- [14] Hilburn M.E., Murdianti B.S., et al. Synthesizing aqueous fullerene colloidal suspensions by new solvent-exchange methods. *Colloids and Surfaces A: Physicochem. Engin. Aspects*, 2012, **401**, P. 48–53.
- [15] Maples R.D., Hilburn M.E., et al. Optimized solvent-exchange synthesis method for C₆₀ colloidal dispersions. *J. Colloid Interface Sci.*, 2012, **370** (1), P. 27–31.
- [16] Andreev S.M., Purgina D.D., et al. Facile preparation of aqueous fullerene C₆₀ nanodispersions. *Nanotechnologies in Russia*, 2014, **9** (7), P. 369–379.
- [17] Chang X., Vikesland P.J. UVvis Spectroscopic Properties of nC₆₀ Produced via Extended Mixing. *Environmental Sci. & Technol.*, 2011, **45** (23), P. 9967–9974.
- [18] Brant J.A., Labille J., Bottero J.-Y., Wiesner M.R. Characterizing the Impact of Preparation Method on Fullerene Cluster Structure and Chemistry. *Langmuir*, 2006, **22** (8), P. 3878–3885.
- [19] Zhang W., Rattanadompol U.s., Li H., Bouchard D. Effects of humic and fulvic acids on aggregation of aqu/nC₆₀ nanoparticles. *Water Research*, 2013, **47** (5), P. 1793–1802.
- [20] Mikheev I.V., Usoltseva L.O., et al. Approach to the Assessment of Size-Dependent Thermal Properties of Disperse Solutions: Time-Resolved Photothermal Lensing of Aqueous Pristine Fullerenes C₆₀ and C₇₀. *J. Phys. Chem. C*, 2016, **120** (49), P. 28270–28287.
- [21] Hare J.P., Kroto H.W., Taylor R. Preparation and UV / visible spectra of fullerenes C₆₀ and C₇₀. *Chem. Phys. Lett.*, 1991, **177** (4–5), P. 394–398.
- [22] Bensasson R.V., Bienvenue E., et al. C₆₀ in Model Biological Systems. A Visible-UV Absorption Study of Solvent-Dependent Parameters and Solute Aggregation. *J. Phys. Chem.*, 1994, **98** (13), P. 3492–3500.

Cryometry data in the binary systems bis-adduct of C₆₀ and indispensable aminoacids – lysine, threonine, oxyproline

N. M. Safyannikov¹, N. A. Charykov¹, P. V. Garamova², K. N. Semenov², V. A. Keskinov², A. V. Kurilenko², I. A. Cherepcova², D. P. Tyurin², V. V. Klepikov², M. Yu. Matuzenko², N. A. Kulenova³, A. A. Zolotarev²

¹St. Petersburg Electrotechnical University “LETI”, St. Petersburg, Russia

²St. Petersburg State Technological Institute (Technical University), Department of Physical Chemistry, St. Petersburg, Russia

³D. Serikbayev East Kazakhstan State Technical University, Ust-Kamenogorsk, Kazakhstan
keskinov@mail.ru

DOI 10.17586/2220-8054-2018-9-1-46-48

The article continues the development of the investigations, presented in particular in the cycle of articles, devoted to the synthesis, identification and investigation of physical-chemical properties of water soluble derivatives of light fullerene C₆₀, such as: complex esters of dicarboxylic acids (malonates, oxalates); poly-hydroxylated forms (fullerenols); amino-acid derivatives (arginine, alanine). The investigation of the excess thermodynamic functions, to the best of our knowledge, has, until now, not been provided, except for two original works [Matuzenko M.Yu., Tyurin D.P., et al. (2015); Matuzenko M.Yu., Shestopalova A.A., et al. (2015)].

Keywords: fullerenes, aminoacids, cryometry.

Received: 20 June 2017

Revised: 30 September 2017

1. Introduction

Previous articles [1–9] were devoted to the investigation of the physical-chemical properties of light fullerenes adducts with amino-acids and their solutions. Cryometry investigation in the binary systems C₆₀(C₆H₁₃N₂O₂)₂-H₂O, C₆₀(C₄H₈NO₃)₂-H₂O, C₆₀(C₅H₉NO₃)₂-H₂O at 273.15 – 272.50 K was used for determination of the concentration dependencies of the temperatures corresponding to beginning of ice crystallization from the solution (liquidus temperatures). Solution concentrations (in molar fraction) vary in the wide range $X_{bis-adduct} = 6 \times 10^{-6} - 2 \times 10^{-4}$ rel.un. Liquidus temperatures were determined with the help of Beckman thermometer with the linear resolution of the device scale $\Delta T/\Delta h \approx 0.01$ K/mm (h – height of Hg capillary raising). Cryometry data $\Delta T(X_{bis-adduct})$ in Fig. 1 (typical example for the system with oxyproline bis-adduct C₆₀(C₅H₉NO₃)₂-H₂O). The dependencies $\Delta T(X_{bis-adduct})$ are sharply nonlinear, which prove high solution non-ideality for all solutions, even very dilute ones. In Fig. 1, for comparison by the arrow, the values ΔT^{id} for the ideal non-electrolyte solution are presented. As we can see, the experimental ΔT exceeds ΔT^{id} one-two orders of magnitude (for comparable concentrated and dilute solutions). Thus, one should expect probably gigantic positive deviations of the solution from ideality in the thermodynamic sense.

For the calculation of water activity, we have used well-known equation, obtained from the equality of the chemical H₂O potentials in pure solid ice and non-ideal liquid solution [10, 11]:

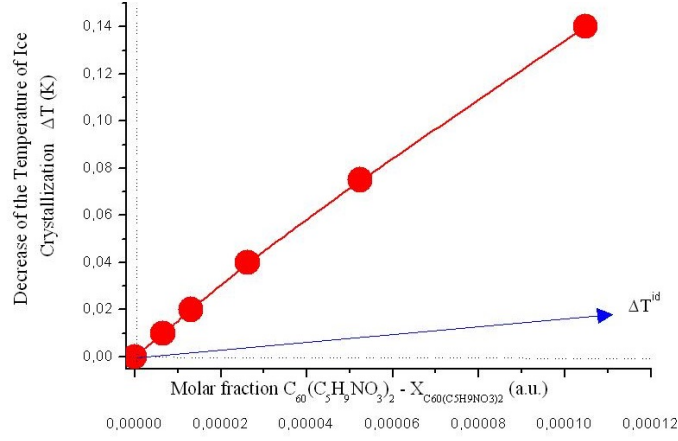
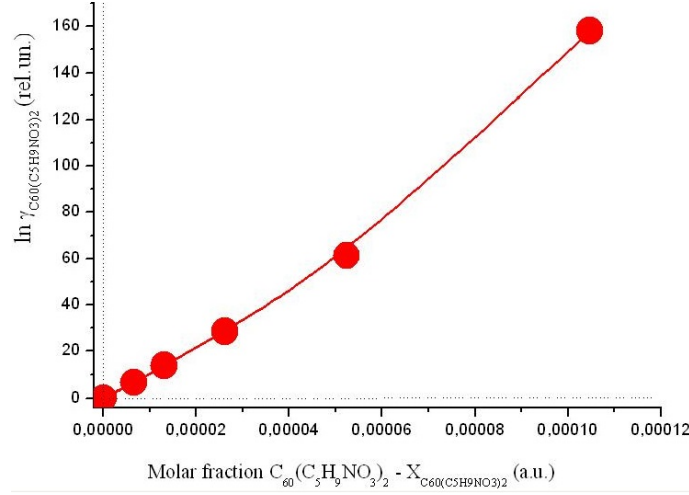
$$\frac{-\Delta H_W^f \Delta T - \Delta C_P \Delta T^2}{R(T_0^f - \Delta T)T_0^f} = \ln a_{H_2O}, \quad (1)$$

where: $\Delta H_W^f = 5990$ J/mole, $\Delta C_P = -38.893$ J/mole·K, $T_0^f = 273.15$ K are heat, temperature of ice fusion and change of heat capacity in the process of ice fusion, correspondingly. Eq. (1) was obtained in the symmetrical normalization scale for thermodynamic functions for both components:

$$a_{H_2O}(X_{H_2O} = 1) = \gamma_{H_2O}(X_{H_2O} = 1) = 1, \quad (2.1)$$

$$a_{nabis-adduct}(X_{bis-adduct} = 1) = \gamma_{bis-adduct}(X_{bis-adduct} = 1) = 1, \quad (2.2)$$

where: X_i and a_i , γ_i – molar fraction, activity and activity coefficient of i -th component. Authors [10, 11] calculated concentration dependencies in γ_{H_2O} , derivatives $d \ln \gamma_{H_2O} / dX_{bis-adduct}$ (numerically). Then authors [10, 11] calculated the dependencies $d \ln \gamma_{bis-adduct} / dX_{bis-adduct}$, (according to classical differential Gibbs–Duhem differential equation) and at the end by numerical integration the dependencies $\ln \gamma_{nabis-adduct}(X_{bis-adduct})$ were calculated. As a result, as was expected earlier, gigantic positive deviations of the solution from ideality for the functions $\ln \gamma_{bis-adduct}$ were obtained $\ln \gamma_{bis-adduct} \approx n(10^2)$ (in Fig. 2 typical example for the system with

FIG. 1. Liquidus temperature decrease in the system $C_{60}(C_5H_9NO_3)_2-H_2O$ (example)FIG. 2. Logarithm activity coefficient of bis-adduct in the system $C_{60}(C_5H_9NO_3)_2-H_2O$: dots – experiment, line – calculation according VSAD model

oxyproline bis-adduct – $C_{60}(C_5H_9NO_3)_2-H_2O$ is represented). Naturally, no existing thermodynamic model can describe such nontrivial behavior of nanocluster thermodynamic functions.

For the thermodynamic description of our systems, we have elaborated original semi-empirical model VD–AS (Virial Decomposition Asymmetric Model), based on the virial decomposition of molar Gibbs energy on the component molar fractions in the solution. This reception was often used previously for the description of binary and multicomponent solutions with different natures: electrolyte solutions [12–15], non-electrolyte melts [16–18], equivalent replacement solid solutions. The main equations of VD–AS model for the binary system are the following:

$$\ln \gamma_{H_2O}^{ass} \approx \sum_{i=2} i \Lambda_i X_{bis-adduct}^{i-1}, \quad (3.1)$$

$$\ln \gamma_{bis-adduct}^{ass} \approx \sum_{i=2} (1-i) \Lambda_i X_{bis-adduct}^i, \quad (3.2)$$

where: $\ln \gamma_i^{ass}$ – logarithm of activity coefficient of i -th solution component in asymmetrical normalization scale ($\ln \gamma_{H_2O}^0 = 0$, $\gamma_{H_2O}(X_{bis-adduct} \rightarrow 0) = \gamma_{H_2O}^0 = 1$, $\ln \gamma_{bis-adduct}^0 = 0$, $\gamma_{bis-adduct}(X_{bis-adduct} \rightarrow 0) = 1$), Λ_i – consolidated i -th virial coefficient of the decomposition.

Preliminary calculations show that three-coefficients VD–AS model (i.e. $i = 2, 3, 4$) is enough to describe our systems with high accuracy (see, for example, Fig. 2 for $\ln \gamma_{bis-adduct}^{ass}$):

$$\ln \gamma_{H_2O}^{ass} \approx 2\Lambda_2 X_{bis-adduct} + 3\Lambda_3 X_{bis-adduct}^2 + 4\Lambda_4 X_{bis-adduct}^3, \quad (4.1)$$

$$\ln \gamma_{bis-adduct}^{ass} \approx -2\Lambda_2 X_{bis-adduct}^2 - 2\Lambda_3 X_{bis-adduct}^3 - 3\Lambda_4 X_{bis-adduct}^4. \quad (4.2)$$

The VD–AS model also excellently describes pre-delamination or micro-heterogeneous-structure formation in solution (see Fig. 3). This calculation is confirmed by Dynamic Light Scattering data (ZetaSizer).

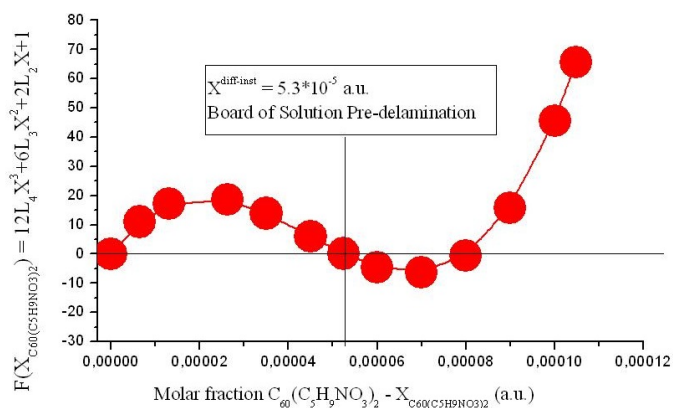


FIG. 3. Delamination board in the system $C_{60}(C_5H_9NO_3)_2-H_2O$ (example)

Acknowledgements

Investigations were supported by Russian Foundation for Basic Research RFBR (Projects No. 16-08-01206, 18-08-00143).

References

- [1] Semenov K.N., Charykov N.A., et al. Phase equilibria in fullerene-containing systems as a basis for development of manufacture and application processes for nanocarbon materials. *Rus. Chem. Rev.*, 2016, **85** (1), P. 38–59.
- [2] Semenov K.N., Charykov N.A., Murin I.V., Pukhareno Yu.V. Physico-Chemical Properties of C60-tris-malonic-derivative Water Solutions. *J. Mol. Liq.*, 2015, **202**, P. 50–58.
- [3] Semenov K.N., Charykov N.A., Murin I.V., Pukhareno Yu.V. Physico-chemical properties of the fullerenol-70 water solutions. *J. Mol. Liq.*, 2015, **202**, P. 1–8.
- [4] Manyakina O.S., Semenov K.N., et al. Physico-chemical properties of the water-soluble C70-tris-malonic solutions. *J. Mol. Liq.*, 2015, **211**, P. 487–493.
- [5] Semenov K.N., Charykov N.A., Arapov O.V., Alekseyev N.I. Solubility of light fullerenes in styrene. *J. Chem. Eng. Data*, 2009, **54** (3), P. 756–761.
- [6] Semenov K.N., Charykov N.A., Keskinov V.A. Fullerenol synthesis and identification. Properties of the fullerenol water solutions. *J. Chem. Eng. Data*, 2011, **56**, P. 230–239.
- [7] Lushin A.I., Charykov N.A., et al. Impact resistance of cement and gypsum plaster nanomodified by water-soluble fullerenols. *Ind. Eng. Chem. Res.*, 2013, **52**, P. 14583–14591.
- [8] Semenov K.N., Keskinov V.A., et al. Fullerenol-d solubility in fullerene-d-inorganic salt-water ternary systems at 25 °C. *Ind. Eng. Chem. Res.*, 2013, **52**, P. 16095–16100.
- [9] Shestopalova A.A., Semenov K.N., et al. Physico-chemical properties of the C60-arginine water solutions. *J. Mol. Liq.*, 2015, **211**, P. 301307.
- [10] Matuzenko M.Yu., Tyurin D.P., et al. Cryometry and excess functions of fullerenols and tris-malonic derivatives of light fullerenes – C60(OH)24±2 and C70[=C(COOH)2]3 aqueous solutions. *Nanosystems: Phys., Chem., Math.*, 2015, **6** (4), P. 704–714.
- [11] Matuzenko M.Yu., Shestopalova A.A., et al. Cryometry and excess functions of the adduct of light fullerene C60 and arginine – C60(C6H12N4O2)8H8 aqueous solutions. *Nanosystems: Phys., Chem., Math.*, 2015, **6** (5), P. 715–725.
- [12] Pitzer K.S. Thermodynamics of electrolytes. I. Theoretical basis and general equations. *J. Phys. Chem.*, 1973, **77** (2), P. 268–277.
- [13] Pitzer K.S., Kim J.J. Activity and osmotic coefficients for mixed electrolytes. *J. Amer. Chem. Soc.*, 1974, **96** (18), P. 5701–5707.
- [14] Filippov V.K., Charykov N.A., Romyantsev A.V. Calculation of phase equilibria of a solution-solid in three-component water-salt systems. *Rep. Rus. Acad. Sci.*, 1983, **273** (2), P. 393–396 (In Russian).
- [15] Charykova M.V., Charykov N.A. *Thermodynamic modelling of the process of evaporate sedimentation*. St. Petersburg, Nauka, 2003.
- [16] Charykov N.A., Litvak A.M., et al. Solid solution In_xGa_{1-x}As_ySb₂P_{1-y-z}: a new material for infrared optoelectronics. I. Thermodynamic analysis of the conditions for obtaining solid solutions, isoperiodic to InAs and GaSb substrates, by liquid-phase epitaxy. *Semiconductors*, 1997, **31** (4), P. 344–349.
- [17] Litvak A.M., Charykov N.A. New thermodynamic method of calculation of melt-solid phase equilibria (for the example of A₃B₅ systems). *Rus. J. Phys. Chem.*, 1990, **64** (9), P. 2331–2335.
- [18] Baranov A.N., Guseinov A.A., et al. Obtaining the GaInAsSb solid solutions lattice-matched to GaSb in the vicinity of immiscibility gap. *Tech. Phys. Lett.*, 1990, **16** (5), P. 33–36.

Interactions of nanodiamonds and surfactants in aqueous suspensions

A. M. Vervald¹, S. A. Burikov¹, I. I. Vlasov², O. A. Shenderova³, T. A. Dolenko¹

¹Physical Department, M. V. Lomonosov Moscow State University, Moscow, Russia

²A. M. Prokhorov General Physics Institute, Russian Academy of Sciences, Moscow, Russia

³Adamas Nanotechnologies, Inc., Raleigh, NC, USA

alexey.vervald@physics.msu.ru

PACS 61.46.-w, 82.30.Rs, 82.70.Uv

DOI 10.17586/2220-8054-2018-9-1-49-51

In this study, with the use of laser Raman spectroscopy the significant difference in intermolecular interactions of detonation nanodiamonds with hydrophilic and hydrophobic surface groups in aqueous solution of surfactants was observed. It was found that at low concentrations of sodium octanoate (before the micelle formation) the weakening of hydrogen bonds by nanodiamonds has a different dynamics for hydrophobic and hydrophilic nanodiamonds. However, with the addition of surfactants, this effect gradually decreases for both types of nanodiamonds and ends after the formation of micelles. Such effects are explained by the “shielding” effect of surfactant molecules surrounding nanodiamond particles.

Keywords: nanodiamonds, surfactants, suspensions, hydrogen bonds, dispersibility.

Received: 20 June 2017

Revised: 11 September 2017

1. Introduction

One of the features for nanodiamonds (NDs) is their complex chemically active surface, due to which NDs can be widely used in biomedicine as drugs carriers, adsorbents, or as the basis for various bioconjugates [1, 2]. Alternatively, the chemical activity of the surface groups leads to the formation of ND’s aggregates [3]. To improve the NDs’ dispersibility, surfactants are often added in suspensions [4]. However, physical picture of the interactions between these nanoparticles and molecules of surfactants is not fully understood.

It is known that in suspensions, surfactants [5], as well as NDs [3, 6, 7], substantially change the structure of solvent and, primarily, the strength of hydrogen bonds. The authors [6, 7] showed that in aqueous suspensions the detonation nanodiamonds (DNDs) weaken the hydrogen bonds in bulk water and such changes depend on the type of ND’s surface groups.

In this study, we investigated the interactions of hydrophilic (DND–COOH) and hydrophobic (DND–H) surface groups of DNDs with the surfactant sodium octanoate in water using dynamic light scattering and Raman spectroscopy techniques.

2. Experimental part

The functionalization and preparation of the initial aqueous suspensions of DND–COOH (10 g/L) and of DND–H (5.3 g/L) was carried out by Adamas Nanotechnologies, Inc. (USA) and in Diamond Sensors Laboratory, CEA (France) [7], accordingly. As a surfactant, sodium octanoate ($C_8H_{15}NaO_2$, hereinafter NaC8) of the pure ph. Eur class (AppliChem) was used. The critical micelle concentration (CMC) of NaC8 at which spherical micelles are formed is around 330 – 370 mM [8]. From the initial suspensions, two aqueous suspensions with concentration 0.5 g/L for DND–COOH and 0.25 g/L for DND–H were prepared. During the experiment, NaC8 was added in the water and DNDs suspensions so that the concentration of NaC8 in these three samples was changed in the range of 0 – 1700 mM with the step 20 – 100 mM.

The sizes of DNDs in the suspensions were measured by dynamic light scattering (DLS) using device ALV-CGS 5000/6010 (Germany). The size of DND–COOH in aqueous suspension was 12 nm, the size of DND–H was 180 nm. With the addition of 200 mM of NaC8 the second fraction of DND–COOH with size 70 nm (20 % of the total number of particles) was formed. With the addition of 200 mM of NaC8 the DND–H aggregates broke up into two fractions: 60 % of the total number with the size 24 nm, 40 % – with the size 71 nm.

Raman spectra of the prepared solutions and suspensions were obtained with argon laser excitation (488 nm, 400 mW) from 400 – 4500 cm^{-1} [6] (Fig. 1a). From 3000 – 3900 cm^{-1} , the band of OH stretching vibrations is located, while the bands for CHx stretching vibrations of different symmetries were found from 2820 – 3000 cm^{-1} . The fluorescent pedestal was approximated by the 2nd degree polynomial.

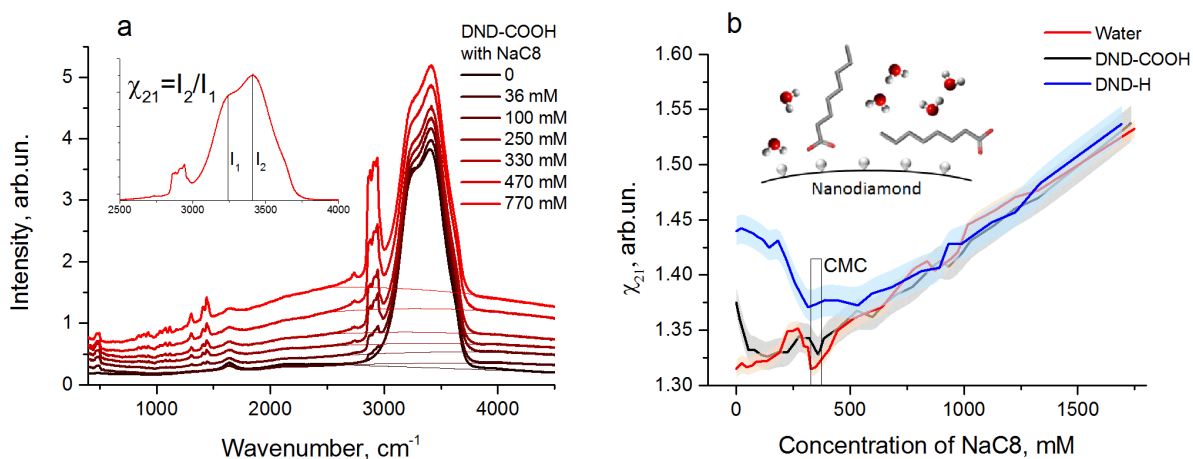


FIG. 1. (a) Raman spectra of aqueous suspension of DND-COOH (0.5 g/L) with NaC8 at various concentrations; (b) Dependencies of the parameter χ_{21} on the NaC8 concentration in three examined suspensions; in the inset, there is illustration of probable interactions of surfactant molecules with the surface of DND-H in water

3. Results and discussion

The stretching band of OH groups (Fig. 1a) is very sensitive to the changes in the hydrogen bond strength. Low-frequency range of the stretching band (I_1 region) is caused by the vibrations of OH groups with strong hydrogen bonds, high-frequency range (I_2 region) is caused by the vibrations of OH groups with weak hydrogen bonds. Thus, the parameter χ_{21} equals the ratio of intensity I_1 to intensity I_2 (Fig. 1a, inset), which characterizes the strength of hydrogen bonds. When the parameter χ_{21} increases, the hydrogen bonds are weakened, when the parameter χ_{21} decreases they are strengthened. In Fig. 1b, the dependencies of the parameter χ_{21} on concentration C of sodium octanoate in water and DNDs suspensions are shown. In these dependencies, two parts can be clearly distinguished: the complex behavior of the $\chi_{21}(C)$ at low concentrations of NaC8 and the monotonic growth of the $\chi_{21}(C)$ at $C > \text{CMC}$.

In an aqueous solution of NaC8 with the increase of NaC8 concentration up to the CMC, the hydrogen bonds are significantly weakened. At the beginning of micelle formation (in CMC region), the hydrogen bonds are sharply strengthened (the parameter χ_{21} sharply decreases) due to water extrusion and compression by the forming micelles [5]. After micelle formation ($C > \text{CMC}$), with the addition of NaC8 in the suspension, the monotonic weakening of the hydrogen bonds is observed.

The presence of hydrophilic and hydrophobic DNDs in water weakens the hydrogen bonds [6, 7]. With the addition of NaC8, the aggregation of DND-COOH (see results of DLS), or the decrease of the DND-COOH total surface, takes place. As a result, the influence of DND-COOH on the hydrogen bonds decreases: χ_{21} for the DND-COOH suspension tends to that for the aqueous solution of NaC8 at $C = 250$ mM (Fig. 1b). With further addition of NaC8 in the DND-COOH suspension, the dynamic of hydrogen bonds repeats the dynamic of those in the NaC8 aqueous suspension.

The dynamic of hydrogen bonds in the DND-H suspension in the presence of NaC8 differs from that in the DND-COOH suspension significantly. Since DND-H disaggregates with the addition of NaC8 (see results of DLS), it would be expected that the hydrogen bonds would be further weakened. However, at $C < \text{CMC}$ the χ_{21} for the DND-H gradually decreases up to CMC without any wavering, and then it behaves like the parameter $\chi_{21}(C)$ for other samples. We explain this by the gradual “shielding” of the surface of DND-H from water by the molecules of NaC8 (the inset in Fig. 1b). Due to the hydrophobic positively charged surface of the DND-H, the molecules of NaC8 can be attracted to it by their head (Coulomb interaction) or tail (proximity of the hydrophobic areas). At $C > \text{CMC}$ the second method become favorable and that results in the further similarity of the dependencies $\chi_{21}(C)$.

Thus, using Raman spectroscopy the significant difference in the intermolecular interactions of hydrophobic and hydrophilic DNDs in the aqueous solutions of surfactants was found. For suspensions of DND-H, the partial “shielding” of DND-H by the surfactant molecules from the interactions with the solvent and the subsequent complete “shielding” under micelle formation were observed. Such complex interactions between nanodiamonds and surrounding molecules should be considered when using nanodiamonds in biomedicine.

Acknowledgements

This study has been performed with support from the grant of Russian Science Foundation (project No. 17-12-01481). The authors express their deep appreciation to Petit T., Girard H. A. and Arnault J.-Ch. for DND–H suspensions samples.

References

- [1] Turcheniuk K., Mochalin V.N. Biomedical Applications of Nanodiamond (Review). *Nanotechnology*, 2017, **28**, P. 252001–252027.
- [2] Rosenholm J.M., Vlasov I.I., et al. Nanodiamond-Based Composite Structures for Biomedical Imaging and Drug Delivery (Review). *J. Nanosci. Nanotechnol.*, 2015, **15**, P. 959–971.
- [3] Batsanov S.S., Lesnikov E.V., DanKin D.A., Balakhanov D.M. Water shells of diamond nanoparticles in colloidal solutions. *Appl. Phys. Lett.*, 2014, **104**, 133105.
- [4] Neugart F., Zappe A., et al. Dynamics of diamond nanoparticles in solution and cells. *Nano Lett.*, 2007, **7** (12), P. 3588–3591.
- [5] Dolenko T.A., Burikov S.A., et al. Raman Spectroscopy of Micellization-Induced Liquid-Liquid Fluctuations in Sodium Dodecyl Sulfate Aqueous Solutions. *J. Mol. Liq.*, 2015, **204**, P. 44–49.
- [6] Vervald A.M., Burikov S.A., et al. Relationship Between Fluorescent and Vibronic Properties of Detonation Nanodiamonds and Strength of Hydrogen Bonds in Suspensions. *J. Phys. Chem. C*, 2016, **120** (34), P. 19375–19383.
- [7] Petit T., Puskar L., et al. Unusual Water Hydrogen Bond Network around Hydrogenated Nanodiamonds. *J. Phys. Chem. C*, 2017, **121**, P. 5185–5194.
- [8] Rosenholm J.B. The structure and properties of medium-chain surfactant solutions: a case study of sodium octanoate. *Adv. Colloid Interface Sci.*, 1992, **41** (1), P. 197–239.

Isotopic effects in impurity-vacancy complexes in diamond

E. A. Ekimov¹, V. S. Krivobok², S. G. Lyapin¹, P. S. Sherin^{3,4}, V. A. Gavva⁵, M. V. Kondrin¹

¹Institute for High Pressure Physics RAS, 142190 Troitsk, Moscow, Russia

²Lebedev Physical Institute RAS, 117942, Leninsky pr. 54, Moscow, Russia

³International Tomography Center SB RAS, 630090, Institutskaya str. 3A, Novosibirsk, Russia

⁴Novosibirsk State University, 630090, Pirogova str. 2a, Novosibirsk, Russia

⁵Institute of Chemistry of High-Purity Substances RAS, 603950, Tropinina St. 49, Nizhny Novgorod, Russia
mkondrin@hppi.troitsk.ru

PACS 33.15.Pw, 33.50.Dq, 42.50.Ex, 63.20.kp, 63.20.P

DOI 10.17586/2220-8054-2018-9-1-52-54

We consider isotopic effects on the photoluminescence of recently discovered germanium-vacancy (GeV^-) color center in diamond produced by the high-pressure high-temperature (HPHT) treatment. It was demonstrated that the influence of isotopic composition on the position of zero-phonon line (ZPL) and its first vibronic peak (local vibrational mode, LVM) provides valuable information on the electronic and structural properties of this center.

Keywords: diamond, defects, color centers, split-vacancy, high pressures.

Received: 19 June 2017. Revised: 15 December 2017

Investigation of isotopic effects on the photoluminescence of split-vacancy centers in diamond allows one to obtain deeper insight into their electronic, structural and optical properties. Due to the bright and almost monochromatic luminescence, the two already-known representatives of these class of defects SiV and recently discovered GeV [1–4] are considered as possible candidates for single-phonon emitters in quantum communications or photoluminescence markers in biomedical applications. Although the attractiveness of these centers is mostly caused by the large Debye–Waller factor (the intensity of the ZPL relative to the overall intensity of the center emission), the study of the luminescence sideband is still very informative.

In this paper, we discuss only negatively charged GeV center which was produced in nano- and microdiamonds by HPHT synthesis from organic substances [4, 5]. This split-vacancy complex consists of impurity atoms located almost midway between two vacant sites. Ideally the symmetry of the center is $\bar{3}m$. However, due to the incompletely filled doubly degenerate impurity electron level in the diamond band gap, this structure is Jahn–Teller unstable and the degeneracy should be lifted. Thus, the actual symmetry of the center should be lower. It is believed that the physical mechanism, which lifts this degeneracy in split-vacancy centers is caused by the spin-orbit coupling [4, 6, 7]. Thus, the fluorescence line caused by the promotion of an electron from the lower e_u level to this incompletely filled e_g one (with separation energy of about 2.059 eV), is split into quadruplet Z_{1-4} with two characteristic splitting energies 0.2 and 1.1 THz (corresponding to the energy difference in e_g and e_u levels respectively). This splitting is clearly seen in Fig. 1a–b) and Fig. 2a). Still, according to electronic paramagnetic resonance measurements, the trigonal symmetry of the center is retained [8, 9]. Oscillation of the heavy impurity Ge atom gives rise to LVM in the diamond phonon spectrum which is observed ≈ 45 meV apart from the strongest component of ZPL line in the fluorescence sideband of this center (see Fig. 1a–b). Both the absolute energy of the strongest component of ZPL (Z_1) and relative energy of LVM (L_1) almost linearly depends on the isotope number of Ge atom m (see Fig. 1c). In the harmonic approximation, the LVM energy scales as a square root of the mass of oscillating atom but due to the small relative range $\delta m = m - m'$ of isotope numbers of Ge atoms (70 – 76) it can be approximated by the linear dependence with the coefficient $\frac{\delta L_1}{\delta m} \approx \frac{L_1}{2m}$ well reproduced in experiment (see Fig. 1c).

On the other hand, a rather strong linear dependence of absolute ZPL energy on Ge isotope number is an indication of different binding energies of the excited and ground electronic states of the GeV center (see inset in Fig 2). According to the Keil model [10] the frequency defect Δ (the difference in binding energies between the excited and the ground electronic states) leads to the following dependence of the isotopic shift of ZPL energy (δZ) on the mass of vibrating atom: $\delta Z = (1 - (m/m')^{1/2})\Delta/2$. If the isotope number difference δm is small, then this relation can be reduced to the simple linear dependence: $\frac{\delta Z}{\delta m} \approx \frac{\Delta}{4m}$. So the observed isotopic shift of the ZPL in GeV center indicates that the binding energy of Ge atom in the two-vacancy void of diamond lattice in

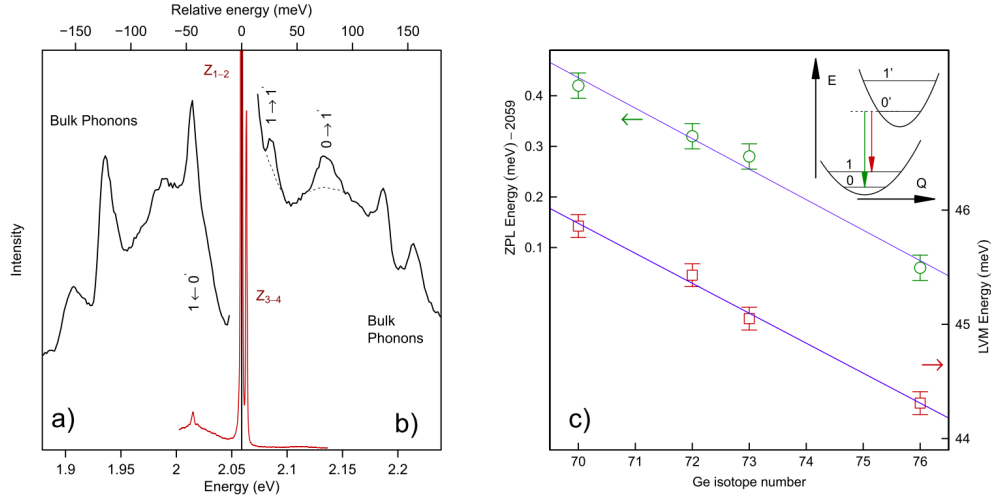


FIG. 1. Panels a) and b) represent PL and PLE sidebands respectively of GeV^- center taken at $T = 77$ K. The thin line in the middle of the plot represents photoluminescence of GeV^- center around ZPL (Z_{1-4}). c) the isotope shift of Z_1 ZPL component and LVM energy. Inset in panel c) represents the Huang–Rhys model where the arrows correspond to the energies of ZPL and LVM transitions in photoluminescence

the excited electronic state is almost 50 % higher than in the ground one (about 67 and 45 meV respectively). A similar isotopic shift was previously observed in SiV^- center too and was also attributed to the difference in the potential surface curves in the excited and the ground electronic states [11].

The frequency defect Δ can be also observed in the difference between luminescence and absorption sidebands of GeV^- center as shown in Fig. 1a–b. Actually, the high-energy sideband was registered using the photoluminescence excitation technique, but it can be considered as a more sensitive substitute for light absorption. The two sharp features in PLE sideband correspond to transitions $1 \rightarrow 1'$ and $0 \rightarrow 1'$, while in the luminescence sideband, only one line corresponding to transition $0' \rightarrow 1$ is observed (here tick marks designate excited electronic state). This yields a slightly different curvature for the potential surface in the excited state (73 meV) than the value obtained from isotopic shifts but it can be caused by anharmonicity effects not considered in this simple model.

The presence of an anharmonicity effects manifests itself in the isotopic shifts of ZPL caused by substitution of carbon atoms (^{12}C to ^{13}C). In this case, the isotopic shift reaches an impressive value of 3.2 meV. This can only be partially accounted for by isotopic contraction of diamond lattice (≈ 0.8 meV of this value). Because carbon atoms do not directly participate in the local oscillations (it can be demonstrated by independence of LVM energy on carbon atoms mass, Fig. 2a), so the remaining part of this energy shift should be attributed to anharmonicity effects [12] or to some “silent” vibronic modes (involving oscillation of carbon atoms), which for some reason, does not contribute to the sideband of this center.

Note that the isotopic substitution of either impurity or carbon atoms both indicates that LVM is due to the vibrations of impurity atom alone. These findings might be a hint of the possible resulting symmetry (broken due to the Jahn–Teller effect) of this center.

In the previous consideration, we follow the Franck–Condon principle (also known as the Huang–Rhys model) which assumes that the electronic dipole moment of transition does not depend on the coordinates of the impurity atom. This is a natural assumption when one is dealing with allowed electronic transitions, which is the case for the GeV^- center. However, in previous studies [13,14], there is a tendency to consider the next term in the decomposition of the electronic dipole moment on the coordinates of impurity atom (the Herzberg–Teller effect) as an additional free parameter of the model that also might explain asymmetry in the luminescence and the absorption sidebands. Remarkably, the isotopic shifts also provide a means for experimental evaluation of the relative amplitude of the Franck–Condon and Herzberg–Teller effects (see Fig. 2b). In the Herzberg–Teller treatment, the change of the impurity atom mass should influence its dynamics that, in turn, should bring about relative changes of vibrational modes amplitudes on either sideband of ZPL. This is not actually observed in the substitution of Ge isotopes in GeV^- center. On the other hand, the energy shift of LVM line (caused by the Franck–Condon effect) is clearly observed in the same experiment, so this discrepancy demonstrates negligibility of the Herzberg–Teller effect in GeV^- center.

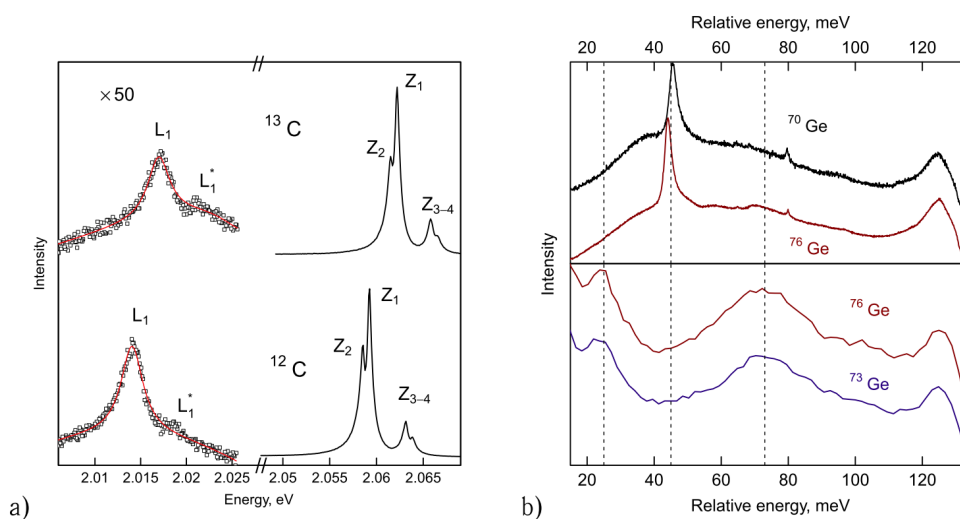


FIG. 2. a) Isotopic shift of ZPL (Z_{1-4}) and LVM (L_1) on the isotope substitution of carbon atoms observed at $T = 4.2$ K. b) Luminescence (upper part) and absorption (lower panel) sidebands relative to Z_1 line of GeV^- center in samples with different Ge isotopes ($T = 77$ K)

We conclude that HPHT synthesis is a powerful tool for the production of optical color centers in diamond which are in demand for potential application and (as a side effect) it is also capable of controlled introduction of the pure isotope components into resulting products. As a result, the study of isotopic effects on the properties of color centers in diamond enables one to obtain useful information regarding the electronic and structural properties of these centers.

Acknowledgements

This work was supported by the RFBR grant 17-52-50075. Photoluminescence excitation measurements were supported by FASO Russia (project 0333-2016-0001).

References

- [1] Iwasaki T., Ishibashi F., Miyamoto Y., Doi Y., Kobayashi S., Miyazaki T., Tahara K., Jahnke K. D., Rogers L. J., Naydenov B., Jelezko F., Yamasaki S., Nagamachi S., Inubushi T., Mizuochi N., Hatano M. Germanium-Vacancy Single Color Centers in Diamond. *Scientific Reports*, 2015, **5**, P. 12882.
- [2] Palyanov Y. N., Kupriyanov I. N., Borzdov Y. M., Surovtsev N. V. Germanium: a new catalyst for diamond synthesis and a new optically active impurity in diamond. *Scientific Reports*, 2015, **5**, P. 14789.
- [3] Ralchenko V. G., Sedov V. S., Khomich A. A., Krivobok V. S., Nikolaev S. N., Savin S. S., Vlasov I. I., Konov V. I. Observation of the Ge-vacancy color center in microcrystalline diamond films. *Bulletin of the Lebedev Physics Institute*, 2015, **42**, P. 165.
- [4] Ekimov E. A., Lyapin S. G., Boldyrev K. N., Kondrin M. V., Khmelniitskiy R., Gavva V. A., Kotereva T. V., Popova M. N. Germanium-vacancy color center in isotopically enriched diamonds synthesized at high pressures. *JETP Letters*, 2015, **102** (11), P. 701–706.
- [5] Ekimov E. A., Kondrin M. V. Vacancy-impurity centers in diamond: perspectives of synthesis and applications. *Physics Uspekhi*, 2017, **60** (6), P. 539.
- [6] Rogers L. J., Jahnke K. D., Doherty M. W., Dietrich A., McGuinness L. P., Müller C., Teraji T., Sumiya H., Isoya J., Manson N. B., Jelezko F. Electronic structure of the negatively charged silicon-vacancy center in diamond. *Phys. Rev. B*, 2014, **89** (23), P. 235101.
- [7] Gali A., Maze J. R. *Ab initio* study of the split silicon-vacancy defect in diamond: Electronic structure and related properties. *Phys. Rev. B*, 2013, **88** (23), P. 235205.
- [8] Nadolnny V., Komarovskikh A., Palyanov Y., Kupriyanov I., Borzdov Y., Rakhmanova M., Yuryeva O., Veber S. EPR study of Si- and Ge-related defects in HPHT diamonds synthesized from Mg-based solvent-catalysts. *physica status solidi (a)*, 2016, **213** (10), P. 2623–2628.
- [9] Komarovskikh A., Dmitriev A., Nadolnny V., Palyanov Y. A DFT calculation of EPR parameters of a germanium-vacancy defect in diamond. *Diamond and Related Materials*, 2017, **76**, P. 86 – 89.
- [10] Keil T. H. Shapes of Impurity Absorption Bands in Solids. *Phys. Rev.*, 1965, **140** (2A), P. A601–A617.
- [11] Dietrich A., Jahnke K. D., Binder J. M., Teraji T., Isoya J., Rogers L. J., Jelezko F. Isotopically varying spectral features of silicon-vacancy in diamond. *New Journal of Physics*, 2014, **16** (11), P. 113019.
- [12] Ekimov E. A., Krivobok V. S., Lyapin S. G., Sherin P. S., Gavva V. A., Kondrin M. V. Anharmonicity effects in impurity-vacancy centers in diamond revealed by isotopic shifts and optical measurements. *Phys. Rev. B*, 2017, **95** (9), P. 094113.
- [13] Osad'ko I. S. Determination of electron-phonon coupling from structured optical spectra of impurity centers. *Soviet Physics Uspekhi*, 1979, **22** (5), P. 311.
- [14] Naumova N., Vasil'eva I., Naumov A., Osad'ko I. Evaluation of parameters of intramolecular interaction from absorption and fluorescence spectra of substituted arylpolyene with poor resolved vibrational structure. *Journal of Luminescence*, 2005, **111** (1-2), P. 37 – 45.

Study of optical properties of the NV and SiV centres in diamond at high pressures

S. G. Lyapin¹, I. D. Ilichev¹, A. P. Novikov¹, V. A. Davydov¹, V. N. Agafonov²

¹L. F. Vereshchagin Institute for High Pressure Physics, Russian Academy of Sciences, Troitsk, Moscow, Russia

²L. E. M. A., UMR CNRS-CEA 6157, University F. Rabelais, Tours, France

vdavydov@hppi.troitsk.ru

PACS 33.50.Dq, 62.50-p

DOI 10.17586/2220-8054-2018-9-1-55-57

We report photoluminescence studies of micro- and nano-sized diamonds with NV⁰, NV⁻ and SiV⁻ centers under hydrostatic pressure up to 50 GPa. Diamonds have been obtained by high-pressure high-temperature (HPHT) treatment of metal-free growth systems based on mixtures of hydrocarbon, fluorocarbon, and silicone-containing organic compounds.

Keywords: diamond, colour centres, high pressures, DAC.

Received: 20 June 2017

Revised: 11 October 2017

1. Introduction

Color centers in diamond are considered now as an important basic element for different quantum-physical and biomedical applications. Although the properties of color centers in diamond have been studied very intensively for a long time, the pressure effect on photoluminescence is not well known. Knowledge of changes in the energy of the zero-phonon line (ZPL) with hydrostatic stress is crucial in analyzing temperature dependences [1,2], isotope shift [3] of ZPL. To our knowledge, the pressure coefficient was measured only for NV⁻ centers [4,5].

Here, we report pressure effect on zero-phonon line in SiV⁻, NV⁰ and NV⁻ centers under hydrostatic pressure up to 50 GPa.

2. Experimental

Homogeneous mixtures of naphthalene (C₁₀H₈), fluorographite (CF_{1.1}) and tetrakis(trimethylsilyl)silane (C₁₂H₃₆Si₅) were used as starting materials for synthesis of diamond with optically active SiV⁻, NV⁰ and NV⁻ point defects. The synthesis was performed in a high-pressure apparatus of “Toroid” type [6]. Cylindrical samples of the initial mixtures (4 mm diameter and 5 mm height) obtained by cold pressing were put into graphite containers which were placed in the high-pressure apparatus. The experimental procedure consisted in loading the apparatus up to 8 GPa, heating up to the desired temperature (~ 1200 °C) and short isothermal exposure under constant load for 5 – 10 s. The SEM images of the obtained products, which are mixtures of nano- and submicrometer-size fraction of diamond, show that the formation of diamond occurs with virtually 100 % yield.

Photoluminescence (PL) spectra were recorded using the 488 nm Ar⁺ laser line for excitation and a triple-grating spectrometer (Princeton Instruments TriVista 555) with a liquid-nitrogen-cooled CCD detector. Diamond samples, representing distinct agglomerates of micro- and nanoscale diamonds, were placed in a diamond-anvil cell (DAC) along with ruby crystal, serving as a pressure sensor. Helium was used as pressure-transmitting medium. For measurements at room temperature, a 50× objective (NA = 0.50) of a confocal microscope (Olympus BX51) was used to focus the laser beam and to collect the PL signal. To perform measurements at 80 K, the DAC was put into a He cryostat (Oxford Instruments OptistatSXM) and an achromatic lens was used for focusing the laser beam and collecting the signal. The laser spot on the sample inside the cryostat was ~ 5 μm.

3. Results and discussion

Figure 1 shows typical photoluminescence spectra collected on diamonds doped with silicon of natural isotope composition. Because of unintentional doping of diamond with nitrogen occurred during synthesis, some of our samples contain nitrogen-vacancy defects (neutral NV⁰ and negatively charged NV⁻) detectable already at room temperature 296 K [6]. Two types of diamonds were used in pressure experiments i) with high concentration SiV⁻ centers in order to track ZPL from SiV⁻ centers; ii) with low concentration SiV⁻ centers to allow detection of ZPL from NV centers. We were able to follow ZPL from SiV⁻ and NV⁰ centers up to ~ 52 GPa (the maximum pressure achieved in our experiment). However, ZPL from NV⁰ centers became undetectable above ~ 40 GPa.

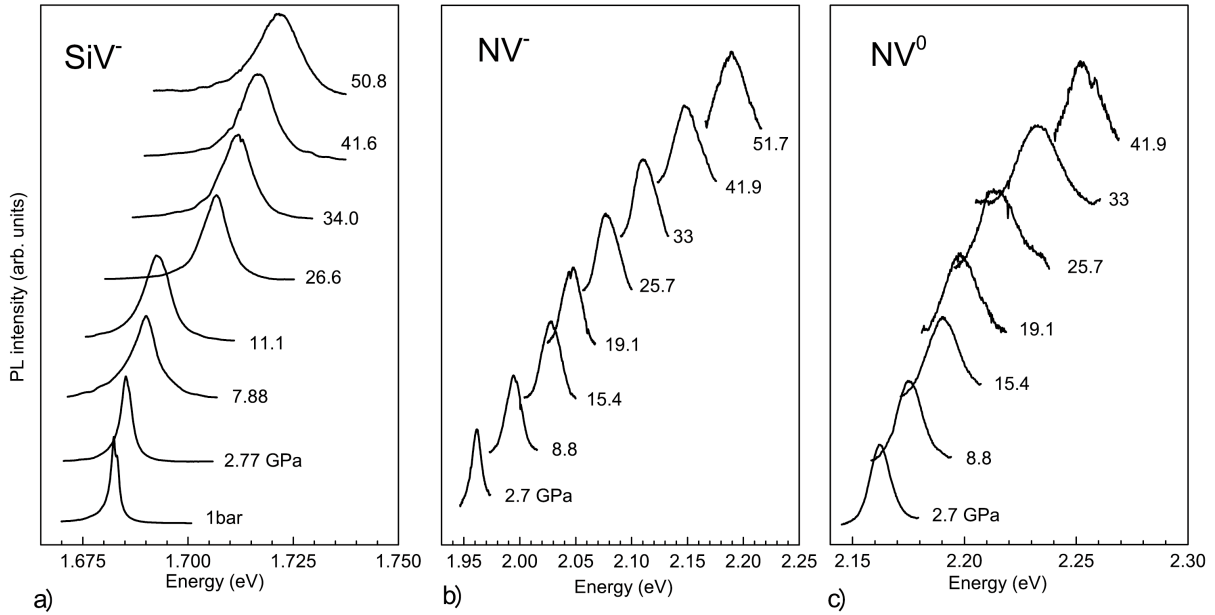


FIG. 1. Normalized PL spectra of diamond with SiV^- (a), NV^- (b), NV^0 (c) centres at various pressures at 80 K. The background for spectra in panel (b) and (c) was subtracted for clarity

Pressure dependences of ZPL of negatively charged NV^- and SiV^- centers at 80 and 296 K were approximated by the second order polynomial equation: $E(P) = E_0 + \alpha P + \beta P^2$, while that of the neutral NV^0 center was found to be linear with rather good precision (Fig. 2, Table 1). If we use equation of state for diamond [7] to replot ZPL position versus natural logarithm of lattice constant of diamond ($\ln[a(P)/a_0]$), the nonlinear dependence of peak position for negatively charged NV and SiV centers remains.

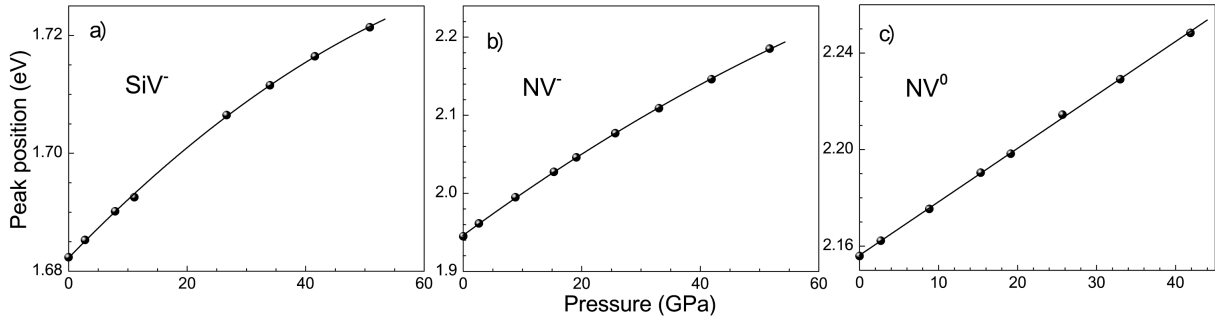


FIG. 2. Pressure dependence of ZPL in SiV^- (a), NV^- (b), NV^0 (c) centres at 80 K

The pressure coefficients α for NV^- centers are in good agreement with those obtained at 77 K [4] and at room temperature [5] and they are reasonably close to the pressure coefficients of the direct and indirect gaps in diamond [8,9]. The obtained data show that the effect of pressure on the position of zero-phonon lines most sharply manifested in the case NV^- centers, for which the α coefficient value at 296 K is equal to 5.81 meV/GPa. In the case of the SiV^- center, the α coefficient is equal to 1.09 meV/GPa, which is 5-fold less than the previous value. The α coefficient value for neutral NV centers is 2.14 meV/GPa, meaning it has an intermediate value between the corresponding values of negatively charged NV^- and SiV^- centers. Significant difference in the α coefficient values of negatively charged NV^- and SiV^- centers is associated, obviously, with the different structures for these two types of diamond lattice defects.

TABLE 1. Pressure coefficients for ZPL in SiV⁻, NV⁻ and NV⁰ centres at 296 and 80 K

$E(P) = E_0 + \alpha \cdot P + \beta \cdot P^2$						
	296 K			80 K		
Center	E_0 (eV)	α (meV/GPa)	$\beta \cdot 10^{-3}$ (meV/GPa ²)	E_0 (eV)	α (meV/GPa)	$\beta \cdot 10^{-3}$ (meV/GPa ²)
SiV ⁻	1.680	1.09	-5.7	1.682	1.04	-5.3
NV ⁻	1.943	5.81	-25	1.946	5.57	-19
NV ⁰	2.156	2.14	0	2.156	2.21	0

Acknowledgements

The work was supported by the Russian Foundation for Basic Research (Grant No. 18-03-00936).

References

- [1] Neu E., Hepp C., et al. Low-temperature investigations of single silicon vacancy colour centres in diamond. *New J. Physics*, 2013, **15** (4), 043005.
- [2] Jahnke K.D., Sipahigil A., et al. Electronphonon processes of the siliconvacancy centre in diamond. *New J. Physics*, 2015, **17**, 043011.
- [3] Collins A.T., Davies G., Kanda H., Woods G.S. Spectroscopic Studies of C-13 Synthetic Diamond. *J. Physics C: Solid State Physics*, 1988, **21** (8), P. 1363–1376.
- [4] Kobayashi M., Nisida Y. High-Pressure Effects on Photoluminescence Spectra of Color-Centers in Diamond. *Jpn. J. Appl. Phys.*, 1993, **32**, P. 279–281.
- [5] Doherty M.W., Struzhkin V.V., et al. Electronic properties and metrology applications of the diamond NV⁻ center under pressure. *Phys. Rev. Lett.*, 2014, **112** (4), 047601.
- [6] Davydov V.A., Rakhmanina A.V., et al. Production of nano- and microdiamonds with Si–V and N–V luminescent centers at high pressures in systems based on mixtures of hydrocarbon and fluorocarbon compounds. *JETP Lett.*, 2014, **99** (10), P. 585–589.
- [7] Occelli F., Loubeyre P., Letoullec R. Properties of diamond under hydrostatic pressures up to 140 GPa. *Nature Mater.*, 2003, **2** (3), P. 151–154.
- [8] Wei S.H., Zunger A. Predicted band-gap pressure coefficients of all diamond and zinc-blende semiconductors: Chemical trends. *Phys. Rev. B*, 1999, **60** (8), P. 5404–5411.
- [9] Onodera A., Hasegawa M., et al. Pressure-Dependence of the Optical-Absorption Edge of Diamond. *Phys. Rev. B*, 1991, **44** (22), P. 12176–12179.

Effect of heat treatment and tension on the surface morphology of thin Pt foils

V. E. Korsukov¹, P. N. Butenko¹, A. G. Kadomtsev¹, M. M. Korsukova¹, V. S. Levitskii²,
I. A. Nyapshaev^{1,2}, B. A. Obidov¹

¹Ioffe Institute, 194021 St. Petersburg, Russia

²R&D Center TFTE, 104064 St. Petersburg, Russia

vjacheslav.korsukov@mail.ioffe.ru

PACS 68.35.bd; 68.35.Ct; 68.37.Ps; 81.05.uf; 81.05.ug; 81.40-z DOI 10.17586/2220-8054-2018-9-1-58-60

We investigated the formation of nanostructures on the surface of rolled thin platinum foils at the heating and “tension–compression” cycles in ultrahigh vacuum. The surface was characterized by LEED, AES, AFM, optical microscopy and micro Raman spectroscopy (MRS). Quantitative characterization of the surface relief was made by fractal analysis. About 95 % of the Pt foil surface was made by close packed Pt (111) face with unidirectional rippled multi-scale relief. Under the applied tension, changes in the LEED and AFM patterns were observed and it was found that, preceding the formation of the main crack, the surface becomes diffractively disordered with relief fractality turning to an isotropic one. Moreover, at the foil surface, near the clips of the sample holder (about 5 % of the surface area), the surface groups of micro crystals with sizes about 10 μm were observed which were identified by MRS as microdiamonds and diamond-like carbon.

Keywords: surface relief of Pt foil, fractals, dynamic re-crystallization, microdiamonds.

Received: 15 June 2017

Revised: 24 October 2017

1. Introduction

It has been found that by varying the regimes of cold rolling, re-crystallization and loading of thin Pt foils, one can obtain flat, practically single-crystalline substrates Pt (111) promising for preparation of nanosensors – gas analyzers [1, 2] On the contrary, applications in catalysis require thin Pt foils with more developed surface with multiscale nanorelief [3]. Furthermore, thin Pt foils with fractal unidirectional rippled surface relief may serve as a base for manufacturing of reflective diffraction gratings resistant to high temperatures that can operate in a broad range from the infrared to vacuum ultraviolet [4]. Combination of such methods as LEED and AFM permits one to obtain a better judgment on the morphology of surface layers. The aim of the present work is to investigate the effects of dynamic re-crystallization and mechanical tension on the atomic structure and surface relief of Pt, as well as the formation of diamond microcrystals and diamond-like carbon on the surface.

2. Experimental

The samples were $30 \times 3 \times 0.02$ mm strips cut from 99.99 % pure cold-rolled Pt foil. The samples were polished with GOI paste #2* [5]. Before re-crystallization, the surface was cleaned with isopropanol and acetone. After that, the samples were subjected to cycles of dynamic re-crystallization annealing in UHV and in oxygen atmosphere under O_2 pressure of 10^{-4} Pa at temperatures of 1000 – 1800 K. Sample heating was carried out by a current transmission trough the sample. The temperature in the vicinity of the sample holders was 500 – 1300 K. The surface was characterized by LEED, AES, AFM, optical microscopy (OM) and micro Raman spectroscopy (MRS).

3. Results and discussion

3.1. Effect of dynamic re-crystallization and tension

Figure 1 shows a scheme of the sample stretching (a), optical pattern of the region covered by the primary electron beam at diffraction (b) and typical AFM image of the surface after dynamic re-crystallization (c). Such AFM images were obtained from about 95 % of the surface. Fig. 2 displays LEED patterns after dynamic re-crystallization in UHV (a) and under the tension (b,c). Analysis of the optical (Fig. 1b) and LEED pattern (Fig. 2a) showed that after the dynamic re-crystallization the surface of the Pt foil is represented by the close-packed Pt (111)

*Composition of the GOI paste: Cr_2O_3 – 65 to 74 parts, stearine – 10 parts, split fat – 10 parts, kerosene – 2 parts, oleinic acid – 2 parts, silicagel – 1 part, sodium bicarbonate – 0.2 parts

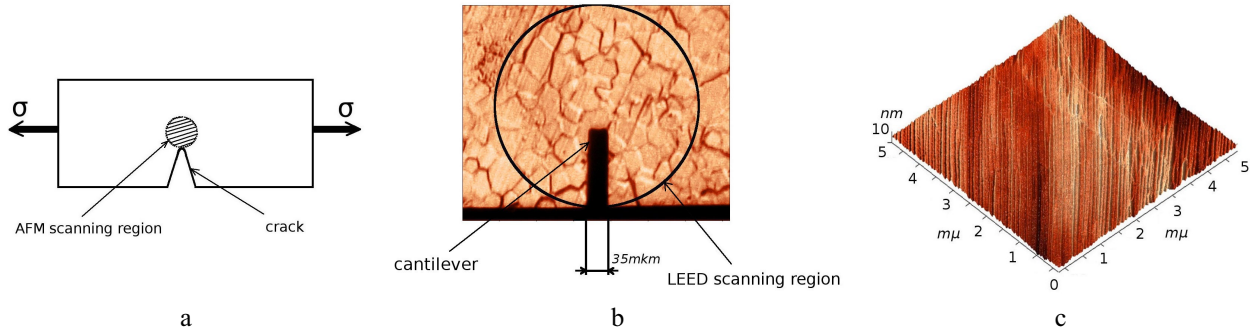


FIG. 1. Scheme of the sample stretching (a), optical picture of the surface (b), AFM topography of Pt surface after dynamic re-crystallization (c)

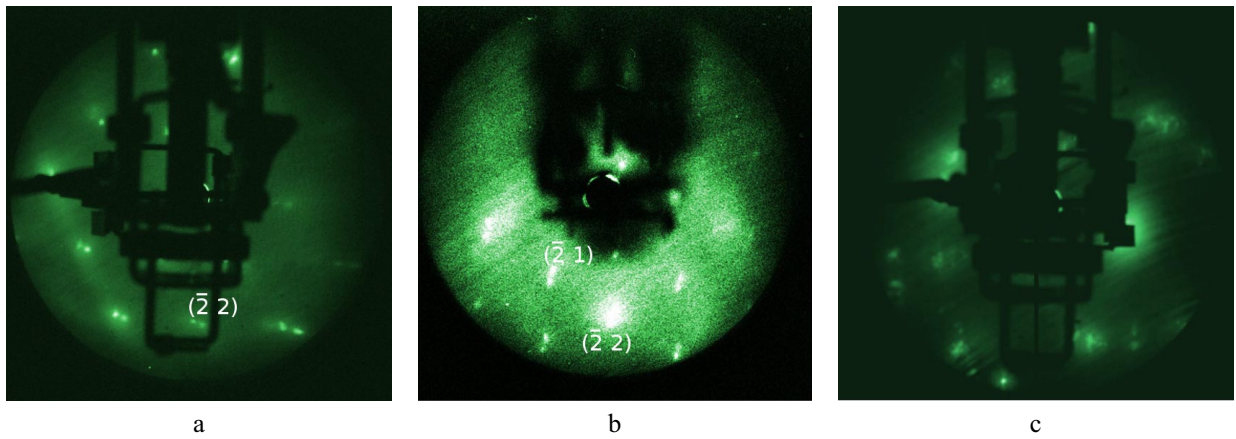


FIG. 2. LEED patterns of Pt sample: after dynamic re-crystallization (a), under tension of 50 MPa (b), under tension of 70 MPa (c)

face with misorientation of crystallites less than 1° . Broadening of reflections (see Fig. 2a,b) we attribute to the segregated graphite originated from the migration of the dissolved carbon from the bulk to the surface.

Estimation of the fractal dimension of the surface by box counting, Gwiddion, Fraclab methods gave:

$$D_{Gw} \sim D_{\parallel} + D_{\perp} = 2.4,$$

where D_{Gw} is the total fractal dimension, calculated by Gwiddion, D_{\parallel} is the fractal dimension along the ripples, D_{\perp} is the fractal dimension across the ripples, calculated by Fraclab.

LEED patterns from the surface of Pt sample at the tension of 50 and 70 MPa are presented on Fig. 2(b,c). One can see that reflections become blurred and the surface relief becomes isotropic (see AFM image in Fig. 3a). Estimation of the fractal dimension for the sites 1×1 , 3×3 and $30 \times 30 \mu\text{m}$ gave a value of $D_{Gw} = 2.2 - 2.4$. At the state preceding the sample's fracture (i.e. formation of main crack, see Fig. 1a), the LEED pattern disappears, but the surface relief remains isotropic. Blurring of reflections and disappearance of the diffraction pattern give evidence for a turn of blocks and possible amorphization of Pt lattice. These phenomena may be considered as signs of the forthcoming rupture of the sample.

3.2. Formation of micro diamonds

It should be noted that in the present experiment, polishing of the samples with GOI paste, unlike polishing with diamond paste, excluded contamination of the Pt surface by micro-diamonds from the paste.

However, we suppose that most carbon is left on the surface after the polishing with GOI paste. Even cleaning of the sample's surface with acetone and isopropanol followed by alternating cycles (8 to 10) of annealing in UHV and O_2 does not completely remove carbon: some traces of carbon still remain according to AES and LEED [1]. Since the solubility of C in Pt increases with increasing temperature [6], there should be diffusion of C from colder to the hotter zone where C combines with O_2 and is eliminated from the system. However, in the colder zone, carbon can precipitate from the solid solution in Pt with formation of graphite, "graphitic carbon" [7] and

the synthesis of microdiamonds occurs in the presence of hydrogen (traces of hydrogen were detected by mass spectrometry). The optimal substrate temperature in the CVD processes is about 973 K [8], which correlates with the temperature in the vicinity of the sample holder where the crystals were observed (500 – 1300 K).

Scratching with the polishing agent promotes the probability of micro diamond formation [9]. We noted that after cold rolling of Pt foils without polishing some crystals (less than 1 μm in size) were observed, but not identified.

The microcrystals obtained in the present work were identified by MRS technique. MRS spectra confirmed the formation of diamond and diamond-like microcrystals [10, 11] (see Fig. 3c).

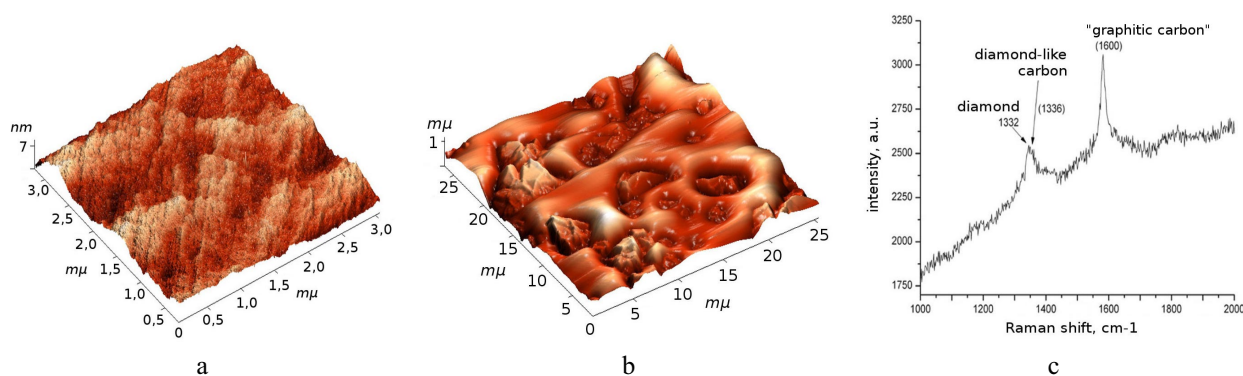


FIG. 3. AFM topography of the samples surface preceding the fracture (a), diamond and diamond-like micro crystals (b), MRS spectrum of diamond, diamond-like micro crystals and “graphitic carbon” (c)

4. Conclusions

The forthcoming fracture of the samples is characterized by a turn of blocks on the close packed Pt (111) face and by a transition of surface fractality from an anisotropic to an isotropic form. Scratching of the sample surface by the polishing agent and dynamic re-crystallization in UHV apparently promote the formation of diamond and diamond-like carbon micro-crystals.

Acknowledgements

This work was partially supported by the Russian Scientific Foundation, grant No. 15-12-30010.

References

- [1] Knyazev S.A., Korsukov V.E., et al. Transformation of Graphite Islets on the Surface of Recrystallized Platinum Foil under the Action of Mechanical Loading. *Technical Physics*, 2007, **52** (8), P. 1098–1100.
- [2] Berner U., Schiernau K.-D. Cerium oxides and cerium-platinum surface alloys on Pt(111) single-crystal surfaces studied by scanning tunneling microscopy. *Phys. Rev. B*, 2002, **65** (23), 235404(10).
- [3] Korsukov V.E., Knyazev S.A., et al. Manifestation of flat and rippled surface reliefs on platinum foils in LEED patterns. *Techn. Phys. Lett.*, 2013, **39** (4), P. 384–387.
- [4] Korsukov V.E., Malygin G.A., et al. Fabrication of rippled surfaces for diffraction gratings by plastic deformation of platinum foil and metallic glasses. *Phys. Solid State*, 2015, **57** (12), P. 2537–2542.
- [5] Sokolov S.P. *Fine Grinding and Operational Development*. Mashgiz, Leningrad, 1961, 87 p. (in Russian).
- [6] Lyakishev N.P. *Phase Diagrams of Binary Metallic Systems*. Mashinostroenie, Moscow, 1996, V. 1, 996 p. (in Russian).
- [7] Sun Jie, Nam Youngwoo, et al. Growth mechanism of grapheme on platinum: surface catalysis and carbon segregation. *Appl. Phys. Lett.*, 2014, **104**, 152107(4).
- [8] Mankevich Yu.A., May P.W. New insights into the mechanism of CVD diamond growth. *Diam. Relat. Mater.*, 2008, **17**, P. 1021–1028.
- [9] Belton D.N., Schmieg S.J. States of surface carbon during diamond growth on Pt. *Surf. Sci.*, 1990, **233** (1–2), P. 131–140.
- [10] Ferrari A.C. Determination of bonding in diamond-like carbon by Raman spectroscopy. *Diam. Relat. Mater.*, 2002, **11** (3–6), P. 1053–1061.
- [11] Li L., Zhang H., et al. Structural analysis of arc deposited diamond-like carbon films by Raman and X-ray photoelectron spectroscopy. *Mater. Sci. Engin. B*, 2002, **94** (1), P. 95–101.

Hemisorption of hydrogen on the diamond surface containing a “boron + vacancy” defect

O. Yu. Ananina¹, O. V. Ponomarev², A. I. Ryazanova^{2,3}, N. A. Lvova^{2,3}

¹Physical Faculty, Zaporizhzhya National University, Zaporizhzhya, Ukraine

²Technological Institute for Superhard and Novel Carbon Materials, Troitsk, Moscow, Russia

³Moscow Institute of Physics and Technology, Dolgoprudny, Moscow Region, Russia

ananyina@znu.edu.ua, oleg.ponomarev@phystech.edu, ryazanova@phystech.edu, nlvova@tisnum.ru

PACS 68.43.-h, 81.05.ug, 03.67.Lx

DOI 10.17586/2220-8054-2018-9-1-61-63

In this paper, we present the results of quantum-chemical modeling for atomic hydrogen adsorption on the C(100)-(2 × 1) diamond surface containing a “boron + monovacancy” complex defect. We also provide a comparison of the energy characteristics of adsorption (activation energy and adsorption heat) for an ordered diamond surface, graphene surface, and a surface containing a “boron + monovacancy” complex defect.

Keywords: C(100)-(2 × 1) diamond surface, quantum-chemical modeling, complex defect, BV-complex, adsorption.

Received: 19 June 2017

Revised: 18 October 2017

1. Introduction

Boron-doped diamond is a *p*-type semiconductor and due to its unique natural properties, it is a promising material for microelectronics [1]. Goss and coworkers studied boron aggregates in diamond [2]. According to *ab initio* calculations, the B₄V- and BV-complexes correspond to the lowest energy of formation attributed to a single B atom. In [3], the authors study the electronic structure of a BV-center in diamond for its various charge states – BV⁰, BV⁺¹, BV⁻¹ and BV⁻² – using first-principles calculations. The charge state of the BV⁻¹ complex defect is stable and is suitable for qubit realization. However, for the reconstructed C(100)-(2 × 1) surface, the BV-complexes remain insufficiently studied. Such a complex defect located on the surface or in the near-surface layers can lead to local surface restructuring, to the charge distribution between the atoms around the defect, and can influence the energy of particle adsorption. Atomic hydrogen takes part in the growth mechanisms of CVD diamonds [4], in diamond etching for use in microelectronics [5].

In this paper, we investigate the energy characteristics of hydrogen adsorption on a C(100)-(2 × 1) diamond surface with BV-complexes by quantum-chemistry methods.

2. Calculation technique

A clean reconstructed C(100)-(2 × 1) diamond surface was reproduced with use of C₁₉₅H₁₁₂ and C₁₉₈H₁₀₀ cluster models containing 5 and 8 atomic layers, respectively. Calculations involved semi-empirical quantum-chemical methods implemented in the MOPAC software package [6]. The distance between the hydrogen atom and the surface carbon atom was chosen as the reaction coordinate for calculation of H adsorption. The calculation procedure is described in detail in [7].

3. Adsorption of atomic hydrogen on the diamond surface with a BV-complex

Calculations carried out for the cluster surface models have shown [8] that the lowest energy belongs to the state of a complex defect in which boron is in the fourth layer, and the vacancy is in the third layer (Fig. 1, defect 1). The position of boron in the first layer, with the same position of the vacancy in the third layer, is less energetically favorable (Fig. 1, defect 2). The feature of defect 1 is the formation of C1–C6 hexagonal structure on the surface [8]. The order of bonds between the “hexagon” atoms differs significantly from the order of these atomic bonds on the ordered surface and is close to the bond order of carbon atoms in graphene (Table 1). Two types of adsorption centers can be distinguished among atoms of the “hexagon” on the surface: they are C1–C2 and C3–C4 atoms (initially, atoms of the surface dimers) and C5 and C6 atoms (initially, the second-layer atoms). In the structure of defect 2, replacing the C5 carbon atom by the B boron atom resulted in distortion of the “graphene-like” structure: all sides of the “hexagon” have different lengths. The most bound pairs of atoms are C1–C6 and C4–C3.

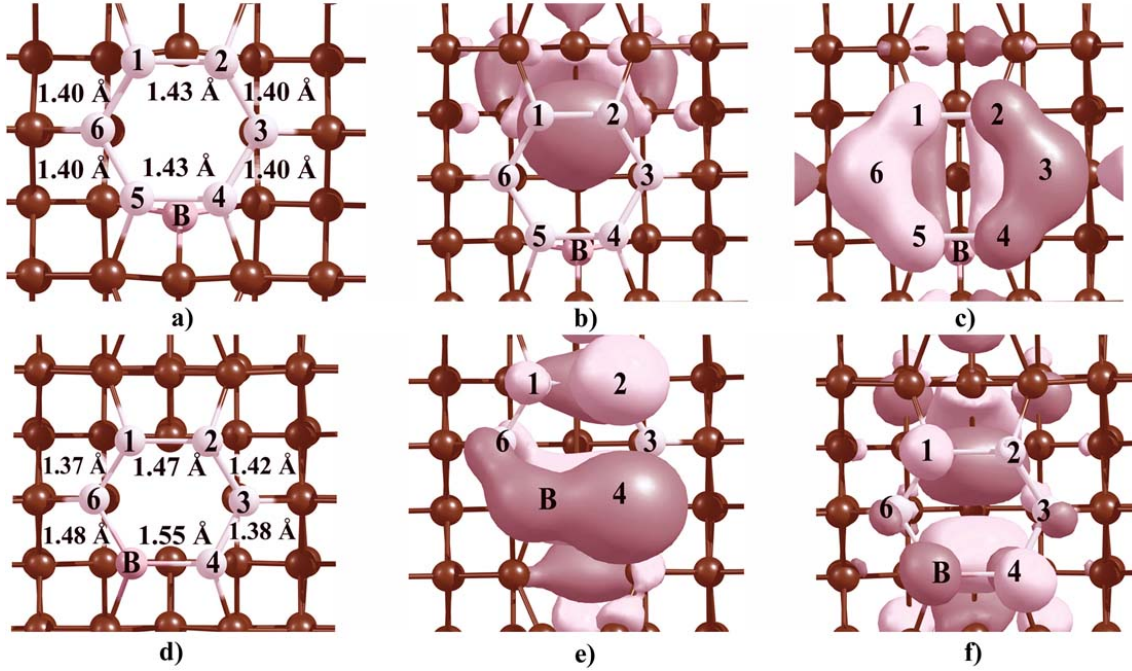


FIG. 1. a), d) defect 1 and defect 2; b), e) HOMO electron density isosurfaces; c) isosurface of the electron density of MO localized on the atoms of the “hexagon”; f) LUMO electron density isosurfaces. Atoms of the “hexagon” are shown in light gray color

TABLE 1. Bond orders (b.o) and interatomic distances (d) of carbon atoms on the C(100)-(2 × 1) diamond surface containing a “boron+vacancy” complex, and in graphene

Atoms	Ordered surface		Defect 1		Defect 2		Graphene [9, 10]	
	b.o	d , Å	b.o	d , Å	b.o	d , Å	b.o	d , Å
C1–C2	1.85	1.400	1.35	1.430	1.15	1.472	1.32	1.420
C2–C3	0.96	1.508	1.39	1.402	1.29	1.421	1.32	
C3–C4	0.96	1.508	1.39	1.401	1.53	1.383	1.32	
C5(B)–C4	1.85	1.400	1.35	1.431	1.04	1.550	1.32	
C5(B)–C6	0.96	1.508	1.38	1.401	1.13	1.482	1.32	
C1–C6	0.96	1.508	1.39	1.403	1.60	1.371	1.32	

The energy of the dimeric π -bond on the C(100)-(2 × 1) surface was estimated by *ab initio* methods in [11], and for different cluster models it was 0.67 – 1.17 eV. The authors of [12] estimated the activation energy of atomic hydrogen chemisorption on the surface dimer atoms as $E_{act} = 0.65$ eV using semiempirical quantum chemistry methods. Comparison of the $E_{act} = 0.85$ – 1.11 eV values obtained in this work for a hexagonal graphene-like structure on the surface with a BV-complex (defect 1) with the data of [11, 12] suggests that the chemisorption of hydrogen will primarily occur on the ordered areas of the surface where surface dimer atoms are the adsorption centers ($E_{act} = 0.65$ eV), and only then on hexagon atoms – predominantly on the C1, C2, C4 and C5 atoms, for which the activation energy of the first hydrogen atom adsorption is $E_{act} = 0.85$ eV (Table 2).

All hexagon atoms in defect 2 can be called adsorption centers of different types; they are characterized by different interatomic distances with neighboring atoms, different values for the charge localized on the atom and of the energy characteristics of chemisorption (Table 2). Comparison of $E_{act} = 0.40$ – 0.78 eV for a hexagonal graphene-like structure on the surface with a BV-complex (defect 2) with the literature data [11, 12] suggests that the chemisorption of hydrogen will primarily occur on the C1, C2 and C4 atoms of the “hexagon”, for which the

TABLE 2. The geometry and energy characteristics of a hydrogen atom adsorption on the diamond surface containing a “boron + vacancy” complex

Surface atom	E_{act} (eV)		Heat of adsorption q (eV)		C (B) – H distance d , Å	
	Defect 1	Defect 2	Defect 1	Defect 2	Defect 1	Defect 2
C1	0.85	0.43	3.18	2.74	1.102	1.115
C2	0.85	0.41	3.24	3.54	1.103	1.110
C3	1.10	0.64	2.64	2.43	1.116	1.134
C4	0.86	0.40	3.23	3.60	1.103	1.109
C5 (B)	0.86	0.52	3.20	2.98	1.118	1.160
C6	1.11	0.78	2.72	3.22	1.124	1.125

activation energy of the first hydrogen atom adsorption is $E_{act} = 0.40 - 0.43$ eV, and only next on the dimer atoms in the ordered surface areas ($E_{act} = 0.65$ eV).

Thus, BV-complexes in the near-surface layers of C(100)–(2 × 1) diamond lead to a significant change in the geometry and electronic state of the surface: there appear some active centers of chemisorption that affect the mechanism and energy of the whole process.

Acknowledgements

The work was supported by the Ministry of Education and Science of the Russian Federation, scientific project #14.580.21.0003 (RFMEFI58015X0003).

References

- [1] Kraft A. Doped diamond: a compact review on a new, versatile electrode material. *Int. J. Electrochem. Sci.*, 2007, **2**, P. 355–385.
- [2] Goss J.P., Briddon P.R. Theory of boron aggregates in diamond: First-principles calculations. *Phys. Rev. B*, 2006, **73**, 085204.
- [3] Kunisaki A., Muruganathan M., Mizuta H., Kodera T. First-principles calculation of a negatively charged boron-vacancy center in diamond. *Jpn. J. Appl. Phys.*, 2017, **56**, 04CK02.
- [4] Stallcup II R.E., Villarreal L.M., et al. Atomic structure of the diamond (100) surface studied using scanning tunneling microscopy. *J. Vac. Sci. Technol. B*, 1996, **14**, P. 929–932.
- [5] Ristein J. Surface science of diamond: Familiar and amazing. *Surf. Sci.*, 2006, **600**, P. 3677–3589.
- [6] Stewart J.J.P. MOPAC2016, Version 16.158W, Stewart Computational Chemistry, URL: <http://OpenMOPAC.net/>.
- [7] Lvova N.A., Ananina O.Yu. Quantum chemical simulations of water adsorption on a diamond (100) surface with vacancy defects. *Rus. J. Phys. Chem. A*, 2013, **87** (9), P. 1515–1519.
- [8] Lvova N.A., Ponomarev O.V., Ananina O.Yu., Ryazanova A.I. Boron atoms in the diamond subsurface layers: quantum-chemical modeling. *Rus. J. Phys. Chem. A*, 2017, **91** (8), P. 1320–1325.
- [9] Butrimov P.A., Ananina O.Yu., Yanovskii A.S. Quantum-chemical study of interaction of hydrogen atoms with graphene. *J. Surf. Investigation, X-ray, Synchrotron Neutron Techniques*, 2010, **4** (3), P. 476–479.
- [10] Lvova N., Ananina .Yu. Theoretical study of graphene functionalization by F- and FHF- ions from associates with water molecules. *Comp. Mater. Sci.*, 2015, **101**, P. 287–292.
- [11] Hukka T.I., Pakkanen T.A., D’Evelin M.P. Chemisorption of hydrogen on the diamond (100)2 × 1 surface: an ab initio study. *J. Phys. Chem.*, 1994, **98**, P. 12420–12430.
- [12] Filicheva Yu.A., Lvova N.A., Ananina .Yu. Quantum-chemical simulation of interaction of hydrogen with diamond nanoclusters. *Fuller. Nanotub. Car. N.*, 2012, **20**, P. 616–621.

DNA-nanodiamond interactions influence on fluorescence of nanodiamonds

E. N. Vervalde¹, K. A. Laptinskiy¹, I. I. Vlasov^{2,3}, O. A. Shenderova⁴, T. A. Dolenko^{1,3}

¹Lomonosov Moscow State University, Moscow, Russia

²A. M. Prokhorov General Physics Institute, Russian Academy of Science, Moscow, Russia

³National Research Nuclear University MEPhI, Moscow, Russia

⁴Adamas Nanotechnologies, Inc, Raleigh, NC, USA

en.khusainova@physics.msu.ru

PACS 87.64.-t, 87.64.kv, 87.64.kp, 87.64.K-

DOI 10.17586/2220-8054-2018-9-1-64-66

In this study, the interaction between DNA and the surface of detonation nanodiamonds and nanodiamonds with NV centers is investigated, and the quantitative parameters of this interaction are calculated. The influence of interaction of DNA with nanodiamonds on the fluorescent properties of nanodiamonds is established. A correlation was found between the efficiency of DNA interaction with the surface of the detonation nanodiamonds and the changes of their fluorescence: the more DNA bonds with the nanodiamond surface groups – the stronger the fluorescence of detonation nanodiamonds increases in water.

Keywords: nanodiamonds, DNA, interactions, fluorescence.

Received: 20 June 2017

Revised: 20 September 2017

1. Introduction

Unique properties of nanodiamonds (NDs) such as nontoxicity, biocompatibility, photostability, ability to be covered with different surface groups allow using them as theranostic agents. There are many publications where it was shown that NDs can successfully be used as fluorescent biomarkers [1], platform for drug delivery [2], adsorbents of heavy metals, viruses and proteins [3, 4]. However, to understand all the possibilities for NDs applications in biomedicine it is important to study their interactions with biomacromolecules.

In this study, the interactions of detonation nanodiamonds (DNDs) and nanodiamonds with NV centers (ND–NV) and calf thymus DNA molecules in water were investigated.

2. Materials and methods

The DNDs functionalized with carboxyl groups with sizes of 5 nm and 10 nm, and ND–NV with size of 100 nm with polyfunctional surfaces were used in this study. The synthesis of the samples is described in [5, 6]. We note here that 10 nm DNDs and 5 nm DNDs were treated differently, as the results of which DNDs 5 nm were obtained with much more intense fluorescence (FL) due to production of tiny carbon dots on the DNDs surface [7]. Deoxyribonucleic acid sodium salt from calf thymus (Sigma-Aldrich) was used as a DNA sample.

The studies of the interactions of DNA and NDs in aqueous suspensions were carried out using laser Raman spectroscopy (RS) and fluorescence spectroscopy. The Raman spectra and FL spectra of the samples were obtained using a laser spectrometer, as described in [5, 6].

3. Results and discussion

3.1. Interaction of DNA chains and the nanodiamond surface

To study the DNA interaction with the NDs the initial aqueous suspensions of DNDs and ND–NV with concentrations of 2 and 0.2 g/L, respectively, and the aqueous solutions of DNA with concentration of 13 g/L were prepared. They were mixed with each other in the ratio 1:1. After 2 h of interactions and 40 min of centrifugation (13000 rpm) the supernatant was separated from the precipitate.

The change in the concentrations of DNA in the initial mixture and in the supernatant allowed to determine the amount of DNA bonded with the NDs. The DNA concentration was measured using intensity of the RS marker lines of the complementary pair of guanine (G) and cytosine (C) (Fig. 2 in [8]). It is known that studied DNA consists of 42 % of pairs of G–C. Using these facts and the measured changes in the G–C concentration, the total change in the DNA concentration in the solution after bonding was obtained. The estimations showed that 38 % of the initial number of DNA molecules bonded with the 5 nm DNDs, 34 % – with the 10 nm DNDs, 20 % – with the ND–NV. The interaction parameter (P) of each NDs with DNA was calculated. P is the ratio of the amount

of bonded substance by weight to the ND's surface area. The hydrodynamic radii, obtained by dynamic light scattering method, were used to calculate the surface area of NDs in suspensions. According to [9], the fraction of micropores is less than 1 %, which is why we treat our particles as spheres. The obtained results of surface areas are the following: for DND 10 nm – $17.1 \cdot 10^{-2} \text{ m}^2$, for DND 5 nm – $34.3 \cdot 10^{-2} \text{ m}^2$, for ND–NV – $2 \cdot 10^{-2} \text{ m}^2$.

The following values were obtained: for DND 5 nm $P = 3.6 \text{ mg/m}^2$, for DND 10 nm $P = 6.5 \text{ mg/m}^2$, for ND–NV $P = 370 \text{ mg/m}^2$. Thus, the ND–NV has the highest P . In all likelihood, the polyfunctional surface of ND–NV interacts with DNA strands more strongly than with COOH groups. For the DND 5 nm, P is the smallest. Apparently, this is due to the presence of carbon dots on the DND 5 nm surface (see p. 2), which weakly interact with the DNA molecules.

3.2. The influence of DNA–NDs interaction on ND fluorescence

The initial aqueous suspensions of DNDs and ND–NV were prepared with concentrations of 1 and 0.06 g/L, respectively, so as the initial aqueous solutions of DNA with concentrations of 6.3 and 3.75 g/L. The initial suspensions of NDs and DNA were mixed with each other in the ratio 1:1. The FL and Raman spectra of the aqueous ND suspensions, the solutions of DNA and the mixtures of (NDs + DNA) were obtained. As one can see from Fig. 1, the spectra contain water Raman valence band and broad band of FL in the range from 420 nm to 750 nm (a) and from 540 nm to 850 nm (b).

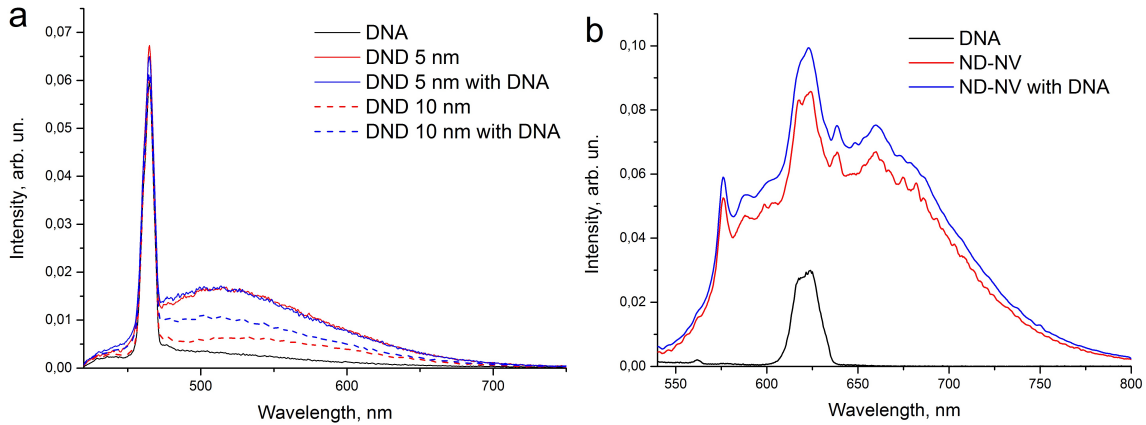


FIG. 1. Raman and fluorescence spectra of DNA, NDs and NDs with DNA mixtures: (a) DND 5 nm and DND 10 nm, concentration of DNA is 3.15 g/L, $\lambda_{ex} = 405 \text{ nm}$; (b) NDNV, concentration of DNA is 1.875 g/L, $\lambda_{ex} = 514.5 \text{ nm}$

It was found that in all samples (NDs + DNA) the FL intensity is not reduced compared with that of NDs in water (Fig. 1). The parameter F_0 , which equals to the ratio of integral FL intensity to integral intensity of water valence band [5], was calculated for each spectrum for quantitative estimations of change in FL of NDs. The calculations showed that as a result of interaction between DNA and NDs, the parameter F_0 for DND 5 nm almost did not change ($\Delta F_0 = (1 \pm 4) \%$), F_0 for DND 10 nm increased by $(49 \pm 4) \%$, F_0 for ND–NV increased by $(15 \pm 4) \%$. The presented results are averaged over 5 experiments.

Thus, there is the correlation between the efficiency of DNA and DNDs interactions and the change in their FL. The higher P – the more change in FL: P for 10 nm DND is almost 2 times more than that of 5 nm DND. We explain this by the fact that DNA “shields” surface defects of ND (which cause ND FL [10]) from water molecules which usually quench FL.

Despite the highest P of the ND–NV, the change in its FL is insignificant. From these data, it is clear that the surface defects are responsible for FL of DNDs [10], but the main sources of ND–NV FL are color centers, which are inside the volume, not on the surface. According to [11] the NV centers react to significant interactions of the surface groups with environment up to depth of 20 nm from the surface. Apparently, the interactions of ND–NV 100 nm with DNA are not strong enough to change FL of NV centers significantly and therefore to change the FL of ND–NV.

4. Conclusion

The significant interactions of DNA molecules with DNDs of 5 nm and 10 nm and with ND–NV of 100 nm have been demonstrated, the parameter of these interactions P for each ND was calculated.

The influence of interactions of NDs with DNA on the NDs FL properties was observed. The correlation between the efficiency of DNDs–DNA interactions – the parameter P – and the change in FL of DNDs were found: the more DNDs P – the more increase of FL intensity. Despite the highest P of ND–NV, the change of its FL is minor, since the surface defects play small role in the FL of ND–NV.

Acknowledgements

This study has been performed with support of the grant of Russian Science Foundation project No. 17-12-01481 (E.N.V., K.A.L., T.A.D. – planning and conducting of the experiment, discussion of physical results) and was partially supported by the MEFPh Academic Excellence Project contract Nos. 02.a03.21.0005, 27.08.2013 (I.I.V. – discussion of results).

References

- [1] Mochalin V., Shenderova O., Ho D., Gogotsi Y. The properties and applications of nanodiamonds. *Nat. Nanotechnol.*, 2011, **7** (1), P. 11–23.
- [2] Chen M., Pierstorff E.D., et al. Nanodiamond-mediated delivery of water-insoluble therapeutics. *ASC Nano*, 2009, **7** (3), P. 2012–2022.
- [3] Giammarco J., Mochalin V.N., Haeckel J., Gogotsi Y. The adsorption of tetracycline and vancomycin onto nanodiamond with controlled release. *J. Colloid Interface Sci.*, 2016, **468**, P. 253–261.
- [4] Girard H., Pager V., Simic V., Arnault J.-C. Peptide nucleic acid-nanodiamonds: Covalent and stable conjugates for DNA targeting. *RSC Adv.*, 2014, **4**, P. 3566–3572.
- [5] Vervalde A., Burikov S., et al. Relationship between fluorescent and vibronic properties of detonation nanodiamonds and strength of hydrogen bonds in suspensions. *J. Phys. Chem. C*, 2016, **120**, P. 19375–19383.
- [6] Laptinskiy K., Burikov S., et al. Monitoring of nanodiamonds in human urine using artificial neural networks. *Phys. Status Solidi A*, 2016, **213** (10), P. 2614–2622.
- [7] Shenderova O., Hens S., et al. Carbon dot-decorated nanodiamonds. *Part. Part. Syst. Char.*, 2014, **31** (5), P. 580–590.
- [8] Laptinskiy K., Burikov S., Dolenko T. Improvement of reliability of molecular DNA computing: solution of inverse problem of Raman spectroscopy using artificial neural networks. *Laser Physics*, 2017, **27** (2), P. 025203(8).
- [9] Kachevskii S., Golubina E., Lokteva E., Lunin V. Palladium on ultradisperse diamond and activated carbon: the relation between structure and activity in hydrodechlorination. *Russian J. Phys. Chem. A*, 2007, **81** (6), P. 866–873.
- [10] Xiao J., Jun P., Li L., Yang G. Fluorescence origin of nanodiamonds. *J. Phys. Chem. C*, 2015, **11**, P. 2239–2248.
- [11] Petrakova V., Benson V., et al. Imaging of transfection and intracellular release of intact, non-labeled DNA using fluorescent nanodiamonds. *Nanoscale*, 2016, **8** (23), P. 12002–12012.

High pressure photoluminescence studies of diamond with GeV centers

S. G. Lyapin¹, A. A. Razgulov^{1,2}, A. P. Novikov¹, E. A. Ekimov¹, M. V. Kondrin¹

¹L. F. Vereshchagin Institute for High Pressure Physics, RAS, Troitsk, Moscow, Russia

²Moscow Institute of Physics and Technology (State University), Dolgoprudny, Moscow, Russia

lyapins@hppi.troitsk.ru

PACS 33.50.Dq, 62.50-p

DOI 10.17586/2220-8054-2018-9-1-67-69

We report low temperature (80 K) photoluminescence studies of microcrystalline diamond with germanium-vacancy (GeV) centers under hydrostatic pressure up to 6 GPa. Powders of Ge-doped diamond crystals were synthesized from hydrocarbons at high-pressures and high-temperatures. Due to the high quality of the samples, we were able to resolve the distinct quadruplet structure of the zero-phonon line (ZPL) of the GeV center already at 80 K and to trace it up to ~ 6 GPa. The pressure dependence of ZPL was found to be linear with the pressure coefficient $dE/dP = 3.1$ meV/GPa, which is nearly 3 times higher than that for the isomorphous SiV⁻ center. The experimentally observed pressure coefficients of GeV⁻, NV⁻ and NV⁰ centers are compared with results of *ab-initio* DFT calculations, using Quantum ESPRESSO software package.

Keywords: diamond, colour centers, high pressure, DAC.

Received: 19 June 2017

Revised: 19 September 2017

1. Introduction

The GeV colour center is a new recently discovered point defect in diamond [1–4] and a promising candidate for possible application as a single-photon emitter in quantum information processing, as luminescent marker in biology. Here we report pressure effect on the zero-phonon line (ZPL) in GeV⁻ centers under hydrostatic pressure up to 6 GPa. Knowledge of changes in the energy E of the zero-phonon line with hydrostatic stress is crucial in analysing temperature dependences and isotope shift of ZPL.

2. Experiment

Ge-doped diamond crystal powders were synthesized at high-pressures and high-temperatures from organic compound, naphthalene, mixed with Ge of natural isotopic composition [4]. Because of unintentional doping of diamond with nitrogen during synthesis, some of our samples contain nitrogen–vacancy defects (NV⁻ and NV⁰) [4]. The presence of NV⁰ and NV⁻-related peaks in the luminescence spectra of diamonds was revealed only upon cooling to 80 K, which indicates low concentration of such defects.

Photoluminescence (PL) spectra were recorded using the 488 nm Ar⁺ laser line for excitation and a triple-grating spectrometer (Princeton Instruments TriVista 555) with a liquid-nitrogen-cooled CCD detector. Diamond samples of 10 – 15 μm were placed in a diamond-anvil cell (DAC) along with ruby crystal, serving as a pressure sensor. Helium was used as pressure-transmitting medium. For low temperature measurements, the DAC was put into a He cryostat (Oxford Instruments OptistatSXM) and an achromatic lens was used for focusing the laser beam and collecting the signal. The laser spot on the sample inside the cryostat was about 5 μm . Loading the pressure cell with the single diamond crystal containing both GeV and NV centers allowed us to study pressure effect on these three types of color centers in the same crystal and under the same conditions.

3. Results and discussion

Due to the high quality of the samples, we were able to resolve the distinct quadruplet structure of the zero-phonon line (ZPL) of the GeV center at all temperatures up to 80 K and to trace it up to 6.09 GPa – the highest pressure achieved in the experiment (Fig. 1). The pressure dependence of ZPL was found to be linear with the pressure coefficient $dE/dP = 3.11$ meV/GPa for the largest peak of the quadruplet (Fig. 2a, Table 1), which is nearly 3 times higher than that for the isomorphous SiV⁻ center [5]. The four-peak fine structure of ZPL is related to four optically allowed transitions between the split ground and excited states (Fig. 1b). Within the experimental error ± 0.01 meV/GPa, the splitting of the ground state ΔE_1 was insensitive to hydrostatic pressure, while the pressure coefficient of the splitting of the excited state ΔE_2 was found to be 0.02 meV/GPa (Fig. 2b).

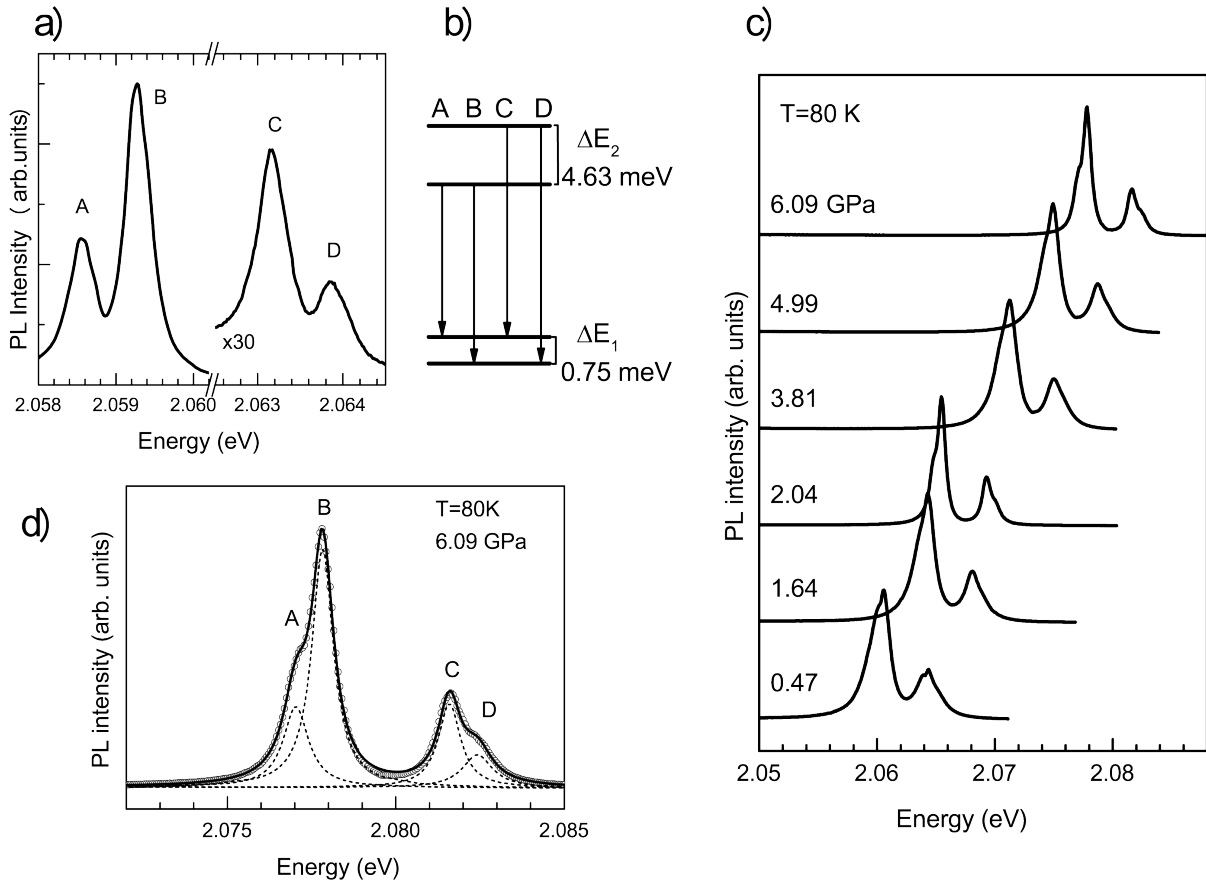


FIG. 1. a) High resolution PL spectrum revealing a quadruplet structure of ZPL of the GeV center at $T = 10$ K, $P = 1$ bar. b) Energy-level diagram with the split ground and excited states corresponding to four optical transitions presented at panel (a). c) Normalized PL spectra of diamond with GeV centers at various pressures at 80 K. d) Example of ZPL deconvolution into 4 Lorentz components, shown by dashed lines, reveals the quadruplet structure, corresponding to the energy-level diagram at panel (b) ($P = 6.09$ GPa, $T = 80$ K)

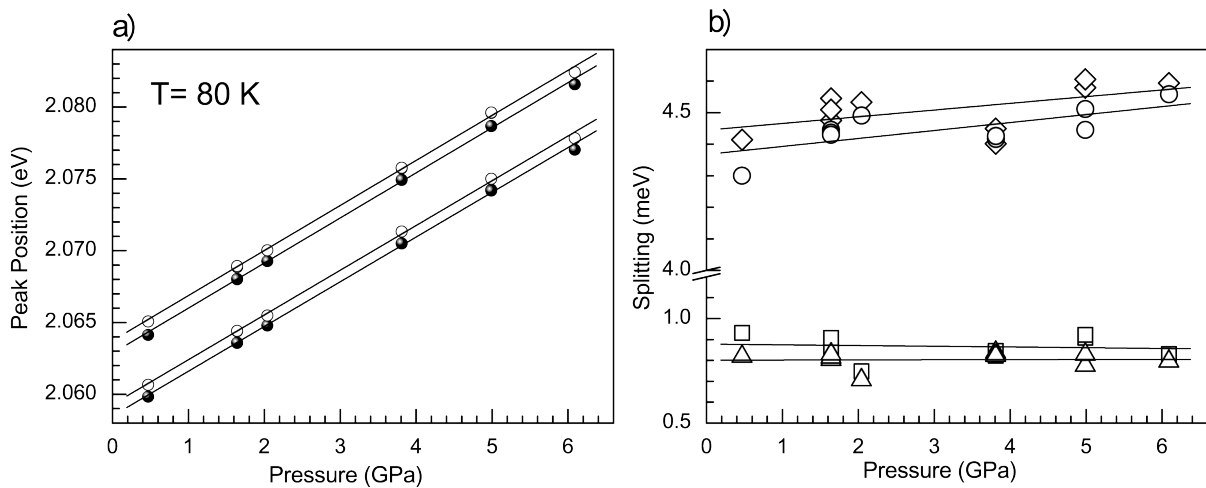


FIG. 2. a) Pressure dependence of peak positions of ZPL (E_A , E_B , E_C and E_D , shown in Fig. 1). b) Pressure effect on the splitting of the excited ($E_C - E_A$, $E_D - E_B$) and the ground ($E_B - E_A$, $E_D - E_C$) levels of the GeV center

TABLE 1. Experimental $\alpha = dE/dP$ and calculated α' pressure coefficients for ZPL in GeV⁻, NV⁻, NV⁰ centers (present work) and SiV⁻ centers (taken from Ref. [5]) (in meV/GPa)

	GeV ⁻	SiV ⁻	NV ⁻	NV ⁰
α (experiment)	3.11 ± 0.03	1.04 ± 0.03	5.75 ± 0.07	2.18 ± 0.03
α' (DFT)	3.08	1.5	6.5	5.3

The pressure dependence of ZPL for NV⁻ and NV⁰ centers was found to be linear with the coefficients 5.75 meV/GPa and 2.18 meV/GPa, correspondingly. Pressure coefficient for NV⁻ peak is in good agreement with those obtained for diamond with only NV⁻ centers [6, 7] as well as with data obtained for diamond with SiV and residual NV centers [5]. Because of the rather small investigated pressure range, we did not observe the nonlinearity of the pressure dependence of ZPL for NV⁻ centers reported in Ref. [5].

The pressure coefficients for ZPL in GeV⁻, NV⁻, NV⁰ centers (present work) and SiV⁻ centers (taken from Ref. [5]) are compared in Table 1 with results of *ab-initio* DFT calculations with HSE06 nonlocal corrections, using Quantum ESPRESSO software package. In these calculations only redistribution of electron density with pressure increase was taken into account. Nevertheless, there is a reasonable agreement between calculated and experimentally observed pressure coefficients of GeV⁻, SiV⁻ and NV⁻ centers. The only obvious deviation is the pressure coefficient of the neutral NV⁰ center and in our opinion it might indicate more complicated structure of this center or stronger spin correlation effects, which were not considered in our calculations.

Acknowledgements

This work was supported by the Russian Foundation for Basic Research, Projects 17-52-50075.

References

- [1] Iwasaki T., Ishibashi F., et al. Germanium-Vacancy Single Color Centers in Diamond. *Sci. Rep.*, 2015, **5**, 12882.
- [2] Palyanov Y.N., Kupriyanov I.N., Borzdov Y.M., Surovtsev N.V. Germanium: a new catalyst for diamond synthesis and a new optically active impurity in diamond. *Sci. Rep.*, 2015, **5**, 14789.
- [3] Ralchenko V.G., Sedov V.S., et al. Observation of the Ge-vacancy color center in microcrystalline diamond films. *Bull. Lebedev Phys. Institute*, 2015, **42** (6), P. 165–168.
- [4] Ekimov E.A., Lyapin S.G., et al. Germanium-vacancy color center in isotopically enriched diamonds synthesized at high pressures. *JETP Lett.*, 2015, **102** (11), P. 701–706.
- [5] Lyapin S.G., Ilichev I.D., et al. Study of optical properties of the NV and SiV centers in diamond at high pressures. *Book of Abstracts, 13th Intern. Conf. "Advanced Carbon Nanostructures"*, 2017, St. Petersburg, Russia.
- [6] Kobayashi M., Nisida Y. High-Pressure Effects on Photoluminescence Spectra of Color-Centers in Diamond. *Jpn. J. Appl. Phys.*, 1993, **32**, Suppl. 32-1, P. 279–281.
- [7] Doherty M.W., Struzhkin V.V., et al. Electronic properties and metrology applications of the diamond NV⁻ center under pressure. *Phys. Rev. Lett.*, 2014, **112** (4), 047601.

Influence of admixture atom chemisorption on properties of p-electron conjugated system of open carbon nanotubes

O. B. Tomilin, E. V. Rodionova, E. A. Rodin, E. E. Muryumin

N. P. Ogarev National Research Mordovian State University, Saransk, Russia

tomilino@mail.ru, rodionova.j87@mail.ru, evg.rodin54@gmail.com, mur_ee@mail.ru

PACS 61.46.+w, 61.48.De, 68.43.-h, 79.70.+q

DOI 10.17586/2220-8054-2018-9-1-70-72

Basing on the hypothesis of the emission molecular orbitals (EMO) existence in single-walled carbon nanotubes generated by in-plane-electron conjugation of p -electrons, we studied influences of adsorbate (H_2 and F_2) nature on characteristics of electrons field emission from open single-walled ultrashort carbon nanotubes of chirality $(n, 0)$. It has been shown that the adsorption of admixture atoms on the graphene surface increases the work function of the electron, moreover more considerable value of work function corresponds to more considerable electronegativity of the chemisorption atom.

Keywords: carbon nanotube, p-electron conjugated system, chemisorption atoms, hydrogen, fluorine.

Received: 22 June 2017

Revised: 8 October 2017

1. Introduction

At present, carbon nanotubes (CNTs) confidently expand the field of their practical application. Unique mechanical, electro-physical properties, high chemical and thermal stability of CNTs make it possible to use them as part of modern vacuum electronic devices. The most widely used cold field emitters are based on CNTs. Similar cathode materials are used in flat panel displays with increased luminescence brightness, cathode tubes, X-ray sources and other devices [1].

Fowler–Nordheim (FN) theory is used to describe emission of electrons from CNTs under the action of a uniform constant electric field. Initially, this theory was developed for metallic flat emitters [2]. Specific features of the CNTs structure lead to the introduction of different correction factors in various modifications of this theory [3]. However, the fundamental position of the FN theory – the tunneling effect is in no way connected with the characteristics of the real structure of CNTs, which is a deterrent theoretical factor with a purposeful improvement of the operational properties of real cathode materials.

The electron concentration at the ends of CNTs under field emission was experimentally recorded by electron spectroscopy methods, as the field emission process is accompanied in many cases by luminescence [4]. Thus, a non-controversial theory of electron emission from a CNT should proceed from the existence of a molecular state in which the electron density will be mainly localized at the ends of nanotubes.

Papers [5, 6] show that in cylindrical carbon molecules due to in-plane electron conjugation of p -electrons [7] are formed of emission molecular orbitals (EMO) with extreme localization electrons on the ends of open single-walled CNT (SWCNT) with chirality $(n, 0)$ and (n, n) , are formed, as shown in Fig. 1. The resulting EMO are vacant. Despite the fact that the electric field is not taken into account, the study of EMO characteristic and the influence on them factors of real structure CNT are important for qualitative estimating the parameters of field emission of electrons from the SWCNT.

CNT exhibit the ability to adsorb various low molecular weight gaseous substances (H_2 , CO_2 , etc.) [8]. Adsorption of molecules on the graphene surface of CNTs leads to a change in the nanotubes' electronic and, consequently, emission characteristics of nanotubes.

2. Model and method

In this paper, we investigated the effect of chemisorption of H_2 and F_2 molecules on the surface of open ultrashort SWCNT (usSWCNT) of chirality $(n, 0)$ at $n = 5 - 9$ on the properties of the conjugate system of p -electrons. The model molecules studied were formed by the consecutive combination of cyclic trans-carbon chains, located on a cylindrical surface usSWCNT symmetrically cylindrical axis of the nanotube. The number of chains, i , was varied from 2 – 10.

Calculations of the electronic structure of model molecules were carried out by the non-empirical Hartree–Fock (HF) method in the 3-21G basis from the FireFly application package with complete geometry optimization [9].

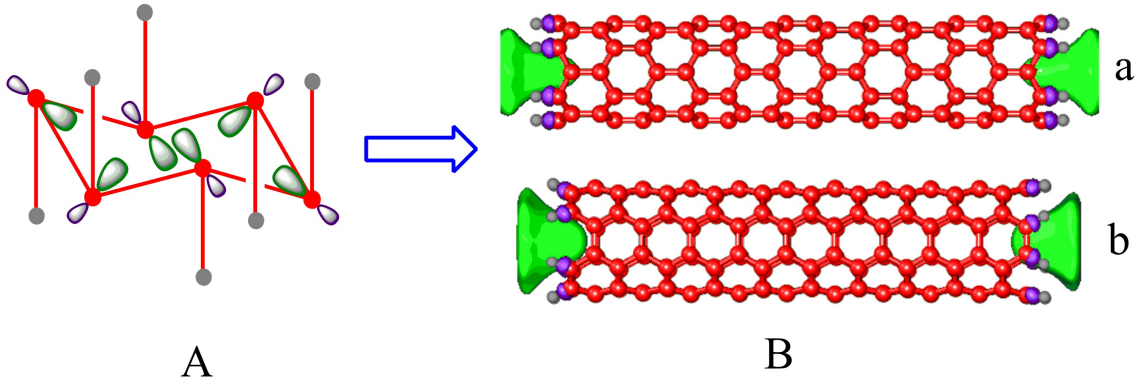


FIG. 1. A) Orientation of *p*-orbitals of carbon atoms in monocyclic hydrocarbons CNHN in in-plane conjugation; B) Realization of emission molecular orbitals with in-plane-electron conjugation in carbon nanotubes: a – SWCNT (6,0), b – SWCNT (4,4) [4]

The arrangement of H_2 and F_2 molecules on the graphene surface of model molecules was carried out randomly with the help of a random number generator, while maintaining the approximate value of the ratio of the number of chemisorption atoms to the total number of carbon atoms in molecule, which was 1/15.

The possibility of H_2 and F_2 chemisorption for the model molecules was estimated from the value of the adsorption energy of H/F atoms calculated by the formula (1):

$$E_{ad} = (E^{usSWNT+A} - E^{usSWNT} - NE^A) / N, \quad (1)$$

where $E^{usSWNT+A}$ is the total energy of an optimized model molecule with adsorbed atoms; E^{usSWNT} is the total energy of an optimized model molecule without admix atoms, E^A is the total energy of free adatoms; N is the number of adatoms in the model molecule. The negative values of E_{ad} indicate on the realization of chemisorption in all usSWCNTs irrespective of their length and diameter.

Analysis of the structure of molecular orbitals in model molecules with adsorbed H/F atoms showed the presence of two emission MOs (Fig. 2). As well as for “pure” opened usSWCNTs the emission orbitals have a vacant character.

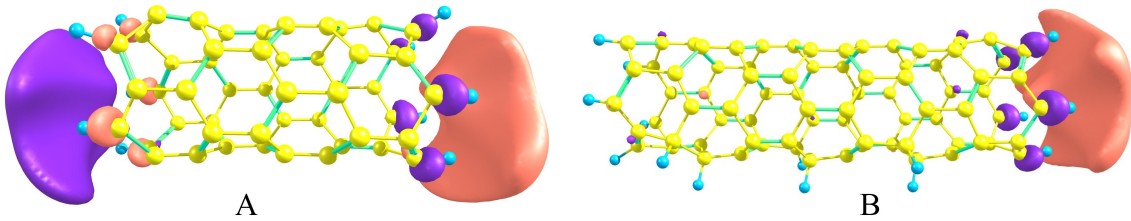


FIG. 2. Structure of EMO: A) “pure” opened usSWCNTs; B) opened usSWCNTs with chemisorbed atoms

For all model molecules, the EMO energies tend to one asymptotic limit with an increasing number of cyclic trans-carbon chains, turning into a doubly degenerate state. Previously, a similar result was shown for EMO in “clean” opened usSWCNTs [5].

The energy of the EMO (E^{EMO}) at $i = 10$ decreases monotonically with increasing chirality index n . The values of E^{EMO} in the model molecules depend on the electronegativity of the chemisorbed atoms: $E^{EMO}(H) < E^{EMO}(\text{“pure”}) < E^{EMO}(F)$.

The work function of the CNT’s electron can be qualitatively compared with the value of ΔE , equal to $\Delta E = E^{EMO} - E^{HOMO}$, where HOMO is the highest occupied molecular orbital.

ΔE is an estimate of the transition process energy of the *p*-electrons conjugated system from the delocalization state along the carbon core to the state with localization of the electron density at the ends of the carbon nanotube. This supposition is in correspondence with the stepwise emission process of the FN theory, as well as the available experimental data [4].

Figure 3 shows the graphical dependencies of ΔE on the chirality index n in model molecules at $i = 10$ for “pure” usSWCNT and usSWCNT with chemisorbed atoms on the graphene surface. Fig. 3 shows that the value of ΔE for usSWCNTs $(n, 0)$ with chemisorbed atoms is greater than the value of ΔE for “pure” usSWCNTs. Moreover, for the chemisorption of fluorine atoms, the value of ΔE is greater than in the case of chemisorption of hydrogen atoms.

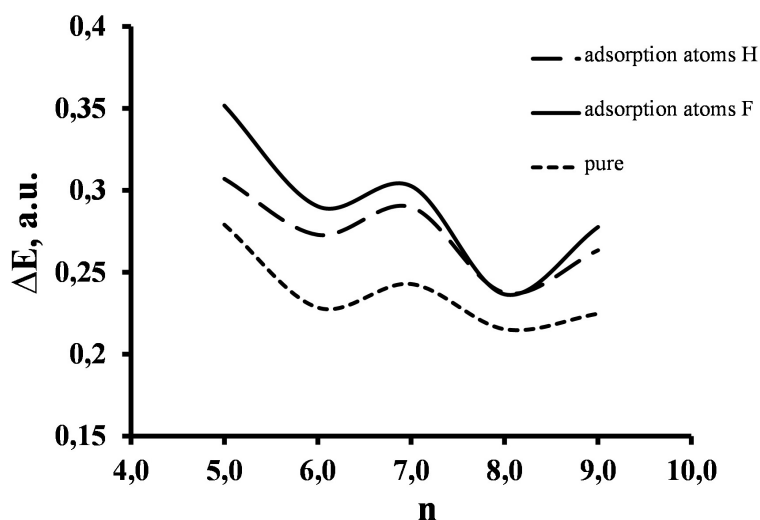


FIG. 3. Dependence of ΔE on the chirality index n in usSWCNTs $(n, 0)$ with the number of cyclic trans-carbon chains $i = 10$

The results of the research proved that the population of the emission state in SWCNT $(n, 0)$ with chemisorbed atoms is less than in “pure” carbon nanotubes, so adsorption of gases on the graphene surface of a CNT should lead to a decrease in the emission current density. This result corresponds to the experimental data of [10], where it is shown that annealing of carbon nanotubes (removal of impurity atoms from a graphene surface) leads to an increase in the density of the emission current.

References

- [1] Rakov E.G. Carbon nanotubes in new materials. *Russian Chem. Rev.*, 2013, **82** (1), P. 27–47.
- [2] Fowler R.H., Nordheim L. Electron emission in intense electric fields. *Proc. Roy. Soc. London. A*, 1928, **119** (781), P. 173–181.
- [3] Eletskiĭ A.V. Carbon nanotube-based electron field emitters. *Physics – Uspekhi*, 2010, **53**, P. 863–892.
- [4] Bonard J.-M., Stockli T., et al. Field-emission-induced luminescence from carbon nanotubes. *Phys. Rev. Lett.*, 1998, **81** (7), P. 1441–1444.
- [5] Tomilin O.B., Rodionova E.V., Muryumin E.E., Rodin E.A. Mechanism of field emission of electrons in carbon nanotubes. *Proc. 5th Intern. Conf. on Nanostructured Materials 2016*, Minsk, Belarus, November 22–25, 2016, Belarusian Science, 400 p.
- [6] Tomilin O.B., Stankevich I.V., Muryumin E.E., Rodionova E.V. Electronic conjugation of carbon atoms in spherical and cylindrical molecules. *Carbon*, 2012, **50**, P. 5217–5225.
- [7] Schleyer P.v.R., Jiao H., et al. Double Aromaticity in the 3,5-Dehydrophenyl Cation and in Cyclo[6]carbon. *J. Amer. Chem. Soc.*, 1994, **116**, P. 10129–10134.
- [8] Bauschlicher C.W., Jr. Hydrogen and fluorine binding to the sidewalls of a (10,0) carbon nanotube. *Chem. Phys. Lett.*, 2000, **322**, P. 237–241.
- [9] Schmidt M.W., Baldrige K.K., et al. General Atomic and Molecular Electronic Structure System. *J. Comput. Chem.*, 1993, **14**, P. 1347–1363.
- [10] Zhao G., Zhang J., et al. Fabrication and characterization of single carbon nanotube emitters as point electron sources. *Appl. Phys. Lett.*, 2006, **89**, 193113(3).

Optical properties of defective carbon nanotube (7,7)

S. A. Sozykin, V. P. Beskachko

South Ural State University, Chelabinsk, Russia

sozykinsa@susu.ru, beskachkovp@susu.ru

PACS 42.50.Ct

DOI 10.17586/2220-8054-2018-9-1-73-75

The current article presents the results of a study of the effect of single-walled carbon nanotubes carcass defects on their electronic structures and optical properties. The study was carried out using an ab-initio quantum mechanical approach: the pseudo-potential method in the density functional theory (DFT) framework in the local density approximation. It is shown that the defects of a single or double vacancy, and Stone-Wales change the absorption spectrum of nanotubes. This can be expressed in the appearance of absorption in the low-energy region and in the smearing of the absorption peaks corresponding to electron transitions between Van Hove singularities near the Fermi energy.

Keywords: carbon nanotube, density of states, band structure, adsorption.

Received: 20 June 2017

Revised: 22 October 2017

1. Introduction

The electronic structure of carbon nanotubes (CNTs) has been studied theoretically in several papers using various methods and approximations. It has been shown that in the energy spectrum of a CNT there are a number of Van Hove singularities unique for each pair of chirality indices (n, m). Transitions between singularities symmetrically disposed about E_F , correspond to pronounced peaks in the absorption spectrum (transitions of the type M_{ii} for CNTs with metallic conductivity, where i belongs to the set of natural numbers). This allows us to use optical spectra to determine the chiral indices of CNTs. The paper [1] reports on the observation of characteristic absorption energies in 46 different CNTs. We can assume that the electronic structure and absorption spectra of perfect nanotubes have been studied quite well. At the same time, nanotubes can contain various defects in the structure of natural or artificial origin, which can influence the discussed properties of CNTs. In the literature, at present, data on this is insufficient to judge the observability of the corresponding effects and their use to identify defective structures. In this paper, we estimate the influence of defects on the electronic structure and the absorption spectrum of nanotubes with a metallic type of conductivity, using the methods of first-principle modelling.

2. Model and method of modelling

As the object of study, a single-walled CNT (7,7) with the metallic type of conductivity and with the relatively small unit cell of 14 atoms was chosen. The model was a fragment of a perfect tube of 224 carbon atoms (16 elementary cells) with periodic boundary conditions. As shown in [2], the use of such “long” models is necessary for the correct modelling of CNTs containing defects. Given the size of the simulated cell, we chose the SIESTA package, which is not too demanding for computational resources, using the pseudo-potential formalism. The standard norm conserving Troullier-Martins pseudo-potentials are utilized. For exchange-correlation, potential local-density approximation given by D. M. Ceperley and B. J. Alder has been used. The absorption spectrum was calculated in the polarized mode, which is implied by the application of an electric field in “z” direction (nanotube axis). A MeshCutoff of 200 Ry is used for the grid to represent the charge density and the mesh of k-points for Brillouin zone integrations is $1 \times 1 \times 32$. We used finer mesh of $3 \times 3 \times 50$ k-points for optical calculations. The structures are optimized by minimizing the forces on individual atoms (below 0.4 eV/nm).

3. Results

In Fig. 1a we show the calculated band structure of the perfect CNT (7,7). It qualitatively coincides with the band structure given in the paper [3]. In the vicinity of the Fermi level at ~ 2 eV DOS is nonzero and almost constant. This region corresponds to a linear dispersion in the band structure. It would seem that in the presence of unoccupied states directly above the Fermi energy, absorption must be observed in the low-energy region. This, however, does not occur (see Fig. 2a): there is no absorption up to previously mentioned 2 eV. A similar arrangement of the peaks M_{11} and M_{22} have also been experimentally [4]. As noted in the paper [5], the optical transition between the highest occupied molecular orbital and lowest unoccupied molecular orbital sub-bands in

armchair CNTs is symmetry forbidden. It is shown in Fig. 2a that the parameters M_{11} , M_{22} and M_{33} were equal to 2.11 eV, 3.34 eV and 3.77 eV, respectively. The following values [6] of these parameters were obtained in the full-potential method in the WIEN2k package: 2.2 eV, 3.5 eV and 4.0 eV. The result for M_{11} obtained in [6] slightly agrees with experiment (2.43 eV [1]) than the result of this work, but this agreement remains at a level of 10 %.

In Fig. 1(b-f), it is shown how the band structure and DOS of a nanotube change when defects of the Stone-Wales type and vacancies appear on it. The presence of a single vacancy leads to an increase in the density of states immediately above the Fermi level and a change in the behavior of DOS near the Van Hove singularities (Fig. 1b). Due to a change in DOS near the Fermi level, absorption appears in the low-energy region. The corresponding peak in Fig. 2b is comparable in magnitude with the more diffuse, and one and a half times less intense compared to defect-free nanotubes peaks M_{11} , M_{22} and M_{33} .

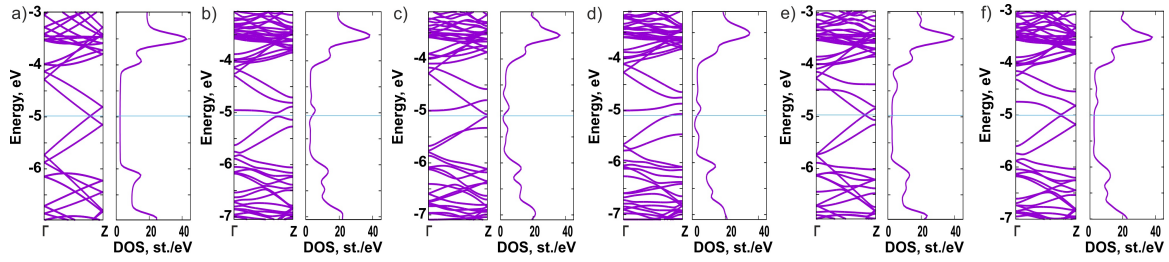


FIG. 1. Band structure and electronic structure (density of states) of defect-free (perfect) CNTs (7,7) (a) and CNTs (7,7) with defects: single vacancy (b); Double vacancies in orientations of n (c) and t (d); Stone-Wales defects in n (e) and t (f) orientations. The horizontal line shows the position of the Fermi level

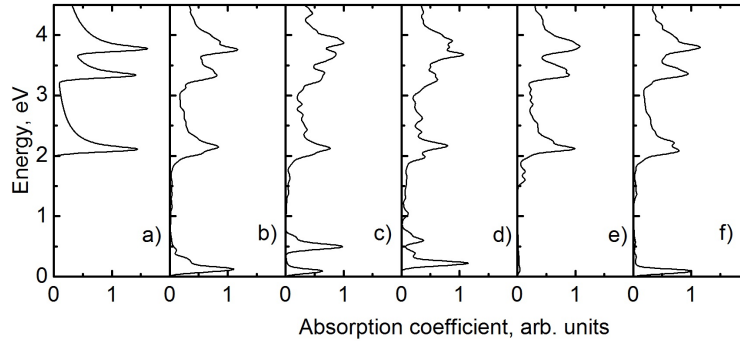


FIG. 2. The absorption spectra of defect-free (a) and nanotubes with defects of single (b), double vacancies in orientations of n (c) and t (d), Stone-Wales defects in n (e) and t (f) orientations

In the energy spectrum of CNTs with defects of a double vacancy of type $2V_n$ and $2V_t$, there is a significant number of valence states above and below the Fermi level (Fig. 1c,d), between which the transition is not prohibited. This leads to the appearance of two peaks in the absorption spectra in the energy range up to 1 eV (Fig. 2c,d).

In the case of a Stone-Wales defect of the first type (in the n -orientation), DOS in the vicinity of the Fermi level is noticeably higher than that of a defect-free nanotube (Fig. 1e). This leads to the appearance of an absorption peak in the energy region of less than 0.25 eV (Fig. 2e). The introduction of a first type (n -orientation) Stone-Wales defect into the CNT structure increases DOS only above the Fermi level (Fig. 1e). This does not lead to a change in the absorption spectrum in the low-energy region (Fig. 2e).

It is seen that for all considered types there are five dispersion curves near the Z point in the band structure. The appearance of the additional curve cannot be associated with localized charges on the defect. When using the chosen basis set that could occur when the length of model less than 1 nm, but in our work, this length was 2 nm.

A common feature of the absorption spectra of defective nanotubes, according to the results obtained by us, is the smearing of the characteristic peaks M_{11} , M_{22} and M_{33} in the absence of noticeable displacements of these peaks.

4. Conclusion

Thus, the article presents information on the effect of the most common defects on the electronic structure and the absorption spectrum of a carbon nanotube with an initially metallic type of conductivity. It was found that the defects considered do not lead to the appearance of a forbidden band in the energy spectrum of CNTs (7,7). Differences in the nature of the spectra (the presence–absence of one or two absorption peaks in the low-energy part of the spectrum, as well as the degree of blurring of peaks M_{11} , M_{22} and M_{33}) indicate the possibility of identifying the type of defect by empirical means.

Acknowledgements

The work was supported by Act 211 Government of the Russian Federation, contract No. 02.A03.21.0011.

References

- [1] Fantini C., Jorio A., Souza M., Strano M., Dresselhaus M., Pimenta M. Optical Transition Energies for Carbon Nanotubes from Resonant Raman Spectroscopy: Environment and Temperature Effects. *Phys. Rev. Lett.*, 2004, **93**(14), P. 147406.
- [2] Sozykin S.A., Beskachko V.P., Vyatkin G.P. Calculation of Adsorption Parameters for Lithium on Carbon Nanotube (7,7) with a Double Vacancy. *Mater. Sci. Forum*, 2016, **843**, P. 132–138.
- [3] Su W.-S. Electronic and structural properties of carbon nanotubes modulated by external strain. *J. Appl. Phys.*, 2013, **113**, P. 244308.
- [4] Matea A., Baibarac M., Baltog I. Optical properties of single-walled carbon nanotubes highly separated in semiconducting and metallic tubes functionalized with poly(vinylidene fluoride). *J. Mol. Structure*, 2017, **1130**, P. 38–45.
- [5] Malić E., Hirtschulz M., Milde F., Knorr A., Reich S. Analytical approach to optical absorption in carbon nanotubes. *Phys. Rev. B*, 2006, **74**(19), P. 195431.
- [6] Gharbavi K., Bادهian H. Optical properties of armchair (7,7) single walled carbon nanotubes. *AIP Advances*, 2015, **5**(7), P. 77155.

The memristive behavior of non-uniform strained carbon nanotubes

M. V. Il'ina, O. I. Il'in, N. N. Rudyk, A. A. Konshin, O. A. Ageev

Southern Federal University, Research and Education Center “Nanotechnologies”, Taganrog, Russia
 mailina@sfnu.ru, ageev@sfnu.ru

PACS 73.63.Fg, 77.65.Ly

DOI 10.17586/2220-8054-2018-9-1-76-78

It is shown that the non-uniform elastic strain is the memristive switching origin in carbon nanotubes (CNT). The dependence of the resistance ratio in high- and low-resistance states of the non-uniformly strained CNT on the value strain is obtained. The process of the strain redistribution and its effect on the conductivity of CNT under action of the external electric field strength is studied. The obtained results can be used to develop memristor structures with reproducible parameters based on non-uniformly strained of carbon nanotubes.

Keywords: carbon nanotube, strain, memristive switching, piezoelectric effect, scanning tunnel microscopy.

Received: 16 June 2017

1. Introduction

The evolution of electronic devices creates a constant demand for the development of new technologies and of operation principles for non-volatile memory. One of the promising development directions in this area is the creation and investigation of memristor structures based on aligned carbon nanotubes (CNT). Previously, we have experimentally shown that vertically aligned CNTs exhibit a memristive switching associated with their strain and polarization [1–3]. Analysis of the literature [4–6] has shown that non-uniform strain in carbon nanostructures can lead to the appearance of a piezoelectric effect and the corresponding internal electric field in them. We put forward a proposal that the non-uniform strain of the CNT acts as an additional source of resistance which depends on the value of the current flowing. The application of an external electric field to the non-uniformly strained nanotube can lead to the redistribution of the strain and a reproducible switch of nanotube resistance.

The aim of the research is to study a memristive behavior of carbon nanotubes at different non-uniform strain values.

2. Experimental studies

The experimental sample of the aligned carbon nanotube array was created by plasma-enhanced chemical vapor deposition (PECVD). CNT array images were obtained by scanning electron microscopy (SEM) Nova NanoLab 600 (FEI, Netherlands) and scanning tunneling microscopy (STM) using probe nanolaboratory Ntegra (NT-MDT, Russia) are shown in Fig. 1. The study of the sample by the Raman spectrometer Renishaw InVia Reflex (Renishaw plc, UK) showed the presence of D-, G-, and G' -modes, which is typical for multi-walled aligned carbon nanotubes [7].

The memristive behavior of the individual strained CNT with diameter (D) of 92 nm and length (L) of 2.2 μm was investigated by the STM in the current spectroscopy mode at applying a sawtooth voltage pulse with amplitude U from ± 1 to ± 10 V. The localization of the STM probe over the individual nanotube top was carried out after the scanning of the CNT array in the constant current mode of STM (Fig. 1b). The upper electrode was a tungsten probe with a radius of 146 nm. The lower electrode was a conducting layer on the substrate surface. The non-uniform elastic strain $\Delta L(x)$ in the nanotube was created under the action of an external electric field before the measuring the current–voltage characteristics (CVCs). The strain value $\Delta L(L)$ from 0.2 to 3.0 nm was controlled by the STM feedback system. The surface potential of strained nanotubes was obtained by the Kelvin Probe method (nanolaboratory Ntegra probe).

3. Results and discussion

The dependence of resistance ratio in high- and low-resistance states (R_{HR}/R_{LR}) of the individual strained CNT ($D = 92$ nm, $L = 2.2$ μm) on the strain value is shown in Fig. 2. This dependence was obtained based on the CVCs of the CNT at $U = 8$ V and the reading voltage at 1 V. It was found that the maximum value of the R_{HR}/R_{LR} corresponded to the $\Delta L(L) = 1.2$ nm, a decrease or increase in this value $\Delta L(L)$ led to decrease in the ratio R_{HR}/R_{LR} (Fig. 2). This was due to the fact that strain $\Delta L(L) = 1.2$ nm corresponds to the condition of the compensation of the initial internal electric field of the non-uniform strained CNT by the piezoelectric field

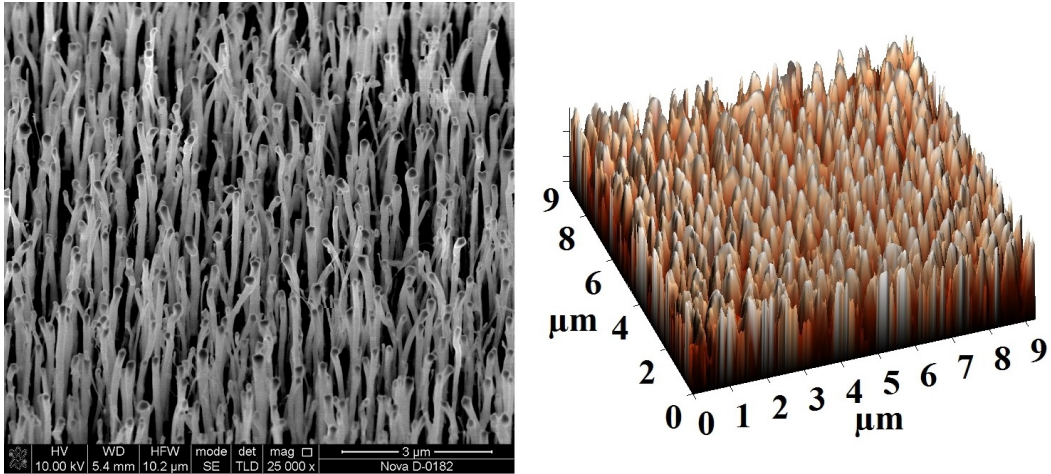


FIG. 1. The experimental sample of the CNT array: SEM image (a) and STM image (b)

that occurred at applying an external electric field. The resistance of the CNT having small strain (> 0.5 nm) changes insignificant (~ 48 M Ω , $R_{HR}/R_{LR} \approx 1$) at applying an external electric field due to low value of the internal electric field of the nanotube. Increasing the strain $\Delta L(L)$ to 3 nm leads to the fact that the value of the arising piezoelectric field becomes insufficient to compensate substantially increased internal electric field in the strained CNT. As a result, the resistance of the strained CNT increases to 252 M Ω and the ratio $R_{HR}/R_{LR} \approx 1$ (Fig. 2).

The results for investigation of the strain redistribution process and its effect on the conductivity of CNT at $\Delta L(L) = 1.0$ nm are shown in Fig. 3.

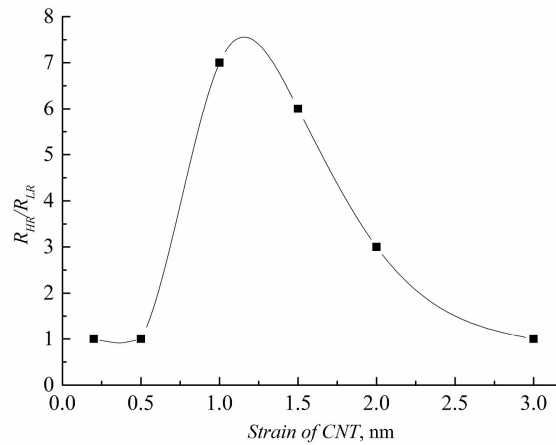


FIG. 2. The dependence of CNT R_{HR}/R_{LR} on the strain value at $U = 8$ V

Analysis of the obtained CVCs of the strained CNT (Fig. 3) showed that at low voltage pulse amplitude values ($U \leq 4$ V), the ratio R_{HR}/R_{LR} was also close to 1. This is due to the insufficient external electric field strength value for the strain redistribution in the nanotube under the action of a piezoelectric effect. A further increase in the voltage pulse amplitude led to an increase in the external electric field strength and the gradual redistribution of the CNT strain and a change in its internal electric field. As a result, the ratio R_{HR}/R_{LR} began to increase with increasing the amplitude value.

The study of the strained carbon nanotubes by the Kelvin probe method confirmed on their tops the presence of a positive surface potential from 3 to 78 mV depending on the magnitude of the tension. The cause of surface potentials at the nanotube tops may be the non-uniform elastic strain and piezoelectric effect [6].

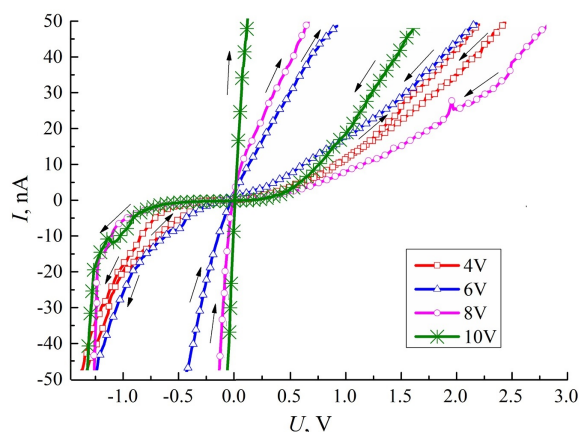


FIG. 3. The CVCs of the nanotube with $\Delta L = 1.0$ nm at different value of the U

4. Conclusion

Thus, the strain in the nanotube acts as a source of additional resistance and the redistribution of this strain caused by an external electric field leads to a change of nanotube resistance and the emergence of current–voltage curve hysteresis. The resistance ratios in high- and low-resistance states of the non-uniformly strained CNT are determined by strain values and the external electric field strength.

The conducted researches are directed to development of the interdisciplinary scientific direction – straintronics, which studies the change in the physical properties of nanostructures due to elastic strain arising under the action of controlled external influences. The results obtained can be used to develop promising elements of nanosystems and nanoelectronics based on non-uniformly strained carbon nanotubes, in particular, memristor structures with reproducible parameters.

Acknowledgements

The results were obtained using the equipment of Research and Education Center and the Center for Collective Use “Nanotechnologies” of Southern Federal University.

This work was supported by the Russian Foundation for Basic Research (project No. 16-29-14023 ofi_m) and by Southern Federal University (grant No. VnGr-07/2017-26).

References

- [1] Ageev O.A., Blinov Yu.F., Il'in O.I., Kolomiitsev A.S., Konoplev B.G., Rubashkina M.V., Smirnov V.A., Fedotov A.A. Memristor Effect on Bundles of Vertically Aligned Carbon Nanotubes Tested by Scanning Tunnel Microscopy. *Tech. Phys.*, 2013, **58**(12), P. 1831–1836.
- [2] Ageev O.A., Blinov Yu.F., Il'in O.I., Konoplev B.G., Rubashkina M.V., Smirnov V.A., Fedotov A.A. Study of the Resistive Switching of Vertically Aligned Carbon Nanotubes by Scanning Tunneling Microscopy. *Phys. Solid State*, 2015, **57**(4), P. 825–831.
- [3] Ageev O.A., Blinov Yu.F., Ilina M.V., Il'in O.I., Smirnov V.A. Modeling and experimental study of resistive switching in vertically aligned carbon nanotubes. *J. Phys. Conf. Ser.*, 2016, **741**(1), P. 012168.
- [4] Zelisko M.A., Hanlummyuang Y.B., Yang S.C., Liu Y.D., Lei C.D., Li J.D., Ajayan P.M., Sharma P. Anomalous piezoelectricity in two-dimensional graphene nitride nanosheets. *Nat. Commun.*, 2014, **5**, P. 4284.
- [5] Chandratre S., Sharma P. Coaxing graphene to be piezoelectric. *Appl. Phys. Lett.*, 2012, **100**, P. 023114.
- [6] Wang X., Tian H., Xie W., Shu Y., Mi W.-T., Mohammad M.A., Xie Q.-Y., Yang Y., Xu J.-B., Ren T.-L. Observation of a giant two-dimensional band-piezoelectric effect on biaxial-strained grapheme. *NPG Asia Materials*, 2015, **7**, P. e154.
- [7] Antunes E.F., Lobo A.O., Corat E.J., Trava-Airoldi V.J. Influence of diameter in the Raman spectra of aligned multi-walled carbon nanotubes. *Carbon*, 2007, **45**, P. 913–921.

Sensitivity of carboxyl-modified carbon nanotubes to alkaline metals

N. P. Boroznina, I. V. Zaporotskova, S. V. Boroznin

Volgograd State University, Universitetskii prospect, 100, 400062 Volgograd, Russia

polikarpova.natalya@volsu.ru, irinazaporotskova@gmail.com

PACS 85.35.Kt

DOI 10.17586/2220-8054-2018-9-1-79-84

This paper considers the fabrication of a superminiaturized sensor based on carboxyl-modified carbon nanotubes. The possibility of using nanotubes modified by carboxyl group for detection of alkaline metals is analyzed. Simulation results have been reported for the binding process of carboxyl group to the nanotube surface and interaction of the nanosystem fabricated with atoms of potassium, sodium and lithium. The simulation has been carried out using the molecular cluster model and the MNDO and DFT calculation methods. Sensor properties of surface and boundary carboxyl-modified nanotubes for alkaline metals have been compared. It has been proved that surface carboxyl-modified nanotubes are characterized by higher sensitivity for the selected atoms.

Keywords: carbon nanotubes, sensor properties, sensors on the basis of carbon nanotubes, boundary modified nanotubes, surface-modified nanotubes, carboxyl group.

Received: 20 June 2017

Revised: 25 October 2017

1. Introduction

The discovery of carbon nanotubes (1D nanostructures) is one of the most important achievements of modern science. Considered as a new material with unique physicochemical properties, nanotubes show good promise for a wide range of applications [1–6]. Nanotubes can be used in flat displays, lithium battery anodes, gas discharge tubes in telecommunication networks, nanoprobe and sensors, supercapacitors, gas storage, etc. [7, 8]. Nanotube-based systems display a combination of multiple properties that cannot be achieved in conventional single crystal and polycrystalline structures, so the current stage of research into the nanotubular forms of materials is characterized by a great interest in development and improvement of their synthesis methods, study of the properties of these nanomaterials and attempts for their commercial applications.

As a nanotube is a surface structure, its whole weight is concentrated in its surface layers. This feature is the origin of the uniquely large unit surface of tubulenes which in turn predetermines their electrochemical and adsorption properties [9, 10]. The high sensitivity of the electronic properties of nanotubes to molecules adsorbed on their surface and the unparalleled unit surface providing for this high sensitivity make CNT a promising starting material for the development of superminiaturized chemical and biological sensors [11–20]. The operation principle of these sensors is based on changes in the V–I curves of nanotubes as a result of adsorption of specific molecules on their surface. The use of CNT in sensor devices is one of their most promising applications in electronics. These sensors should have high sensitivity and selectivity, as well as rapid response and recovery.

The paper studies the possibility for fabricating superminiaturized high-sensitivity sensor based on carboxyl-modified carbon nanotube and analyzes the process of the sensor interaction with alkaline metal atoms (sodium, potassium and lithium). Two variants of nanotube modification with the carboxyl group are considered, namely the boundary and surface binding of the –COOH group, and a comparative analysis of the sensor properties that takes into account location of the carboxyl group binding to the CNT is carried out. Simulation results for a carboxyl group binding process to a carbon nanotube and the system's interaction with the selected potassium, sodium and lithium ions are obtained within the framework of the molecular cluster model using the DFT calculation method [21].

2. The study of the mechanism of nanotube modification with carboxyl group –COOH binding to the nanotube surface

The mechanism for the boundary functionalization of a nanotube by a carboxyl group is reported in [22]. The present paper studies the mechanism for nanotube surface modification with carboxyl group –COOH. A model of a nanotube of type (6, 0) molecular cluster is considered. The cluster contained five layers of carbon hexagons located along the axis of the nanotube. The cluster boundaries were closed by pseudoatoms of hydrogen. The carboxyl group bound a carbon atom located on a surface site approximately in the middle of the cluster to exclude

the effect of pseudoatoms. The mechanism of the functional group -COOH binding to the selected atom was modeled with increment of 0.1 \AA along a perpendicular that was drawn to the axis of the nanotube and passed through the selected carbon atom of the surface. The calculations were carried out using the DFT method. Fig. 1 shows a model of surface-modified carbon nanotube (6, 0) with carboxyl group. The performed calculations enabled us to plot an energy interaction curve (Fig. 2), the analysis of which shows that a value of interaction energy between the CNT and the carboxyl group is 183 eV . This value indicates the formation of chemical bond between the nanotube and -COOH at the distance of 166 \AA that proves the possibility of surface functionalization of single-walled carbon nanotubes with a carboxyl group to fabricate chemically active sensory probes.

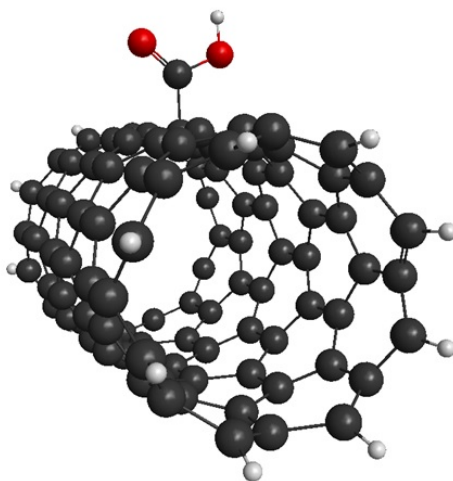


FIG. 1. Model of carbon nanotube with surface modified by carboxyl group

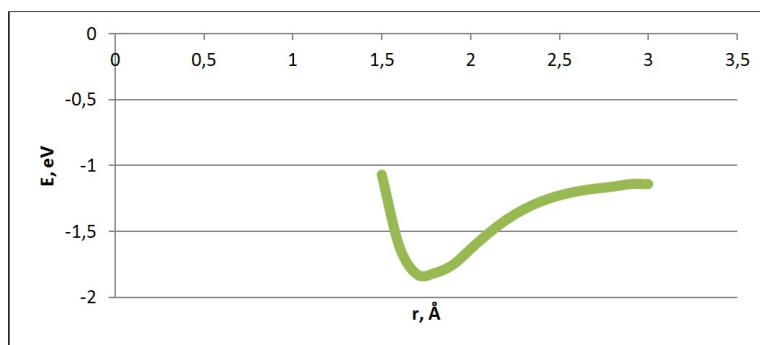


FIG. 2. Interaction energy curve of CNT with carboxyl group

3. Study of interaction between the “CNT-carboxyl group” system and atoms of alkali metals

Further, interaction of lithium, sodium, and potassium atoms with the edge atoms of hydrogen and oxygen in the carboxyl group modifying the carbon nanotube surface was studied. The process is modeled incrementally by moving alkaline metals (Na, K, Li) towards O or H atoms of the functional group. As a result, profiles of potential energy surface of the system “nanotube + COOH-metal atom” are plotted (Fig. 3). Simulation results reveal barrier-free nature of the selected metal atoms binding process to the atoms of the functional group. As the interaction distances are sufficiently large, it can be concluded that the functional group atoms and the selected metal atoms are held together by weak van der Waals forces. This result confirms the possibility of reusing the fabricated sensor probe, as chemical bond formation with the selected alkaline metal atoms would have caused destruction of the fabricated sensor. In addition, the Schottky barrier between the “nanotube + COOH” system and the electrodes of the sensor can vary during the interaction process with metal atoms, which will be recorded during the sensor operation.

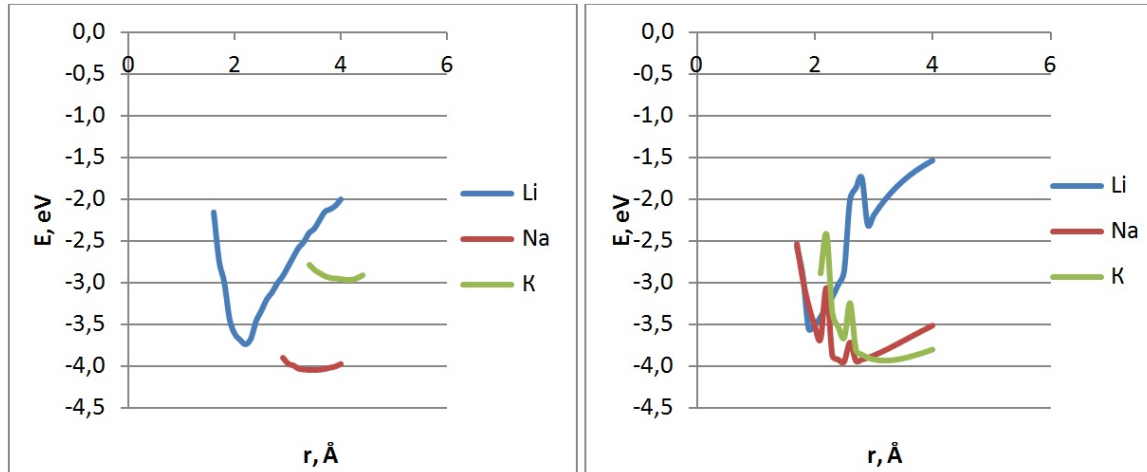


FIG. 3. Energy curves plotted for surface modified by carboxyl group nanotube interaction with Li, Na, K atoms depending on a distance: a – between atoms of selected metals and an H atom of the system; b – between atoms of selected metals and an O atom of the system

Analysis of the charge state of the system revealed that electron density is transferred from the metal atoms to a surface-modified by carboxyl group nanotubular system, which increases the number of carriers in the system and ensures a change in its electrical properties.

Simulation results for interaction between the boundary modified by carboxyl group carbon nanotube (6, 0) and Na, K, Li atoms of alkaline metals are presented in [23]. Table 1 summarizes the interaction results of the selected atoms with surface- and boundary-modified by carboxyl group CNTs.

TABLE 1. Main characteristics of the binding process of Na, K, Li atoms to the edge O and H atoms of carboxyl group boundary and surface modifying the carbon nanotube: r_{int} – interaction distance between a metal atom and an O (or H) atom of the functional, E_{int} – interaction energy

Atom bonds	r_{int} , Å	E_{int} , eV	Charge on the metal atoms
Boundary-modified nanosystem			
Na–O	2.2	–3.21	+0.7
Na–H	1.8	–1.77	+0.7
K–O	2.5	–4.30	+0.4
K–H	1.8	–1.04	+0.4
Li–O	2.0	–4.39	+0.9
Li–H	1.9	–4.62	+0.9
Surface-modified nanosystem			
Na–O	3.0	–2.57	+0.7
Na–H	3.4	–2.70	+0.7
K–O	4.2	–2.12	+0.4
K–H	4.1	–1.57	+0.4
Li–O	1.9	–3.92	+0.9
Li–H	2.2	–2.43	+0.9

4. Modeling scanning of surface with atoms of alkaline metals

Scanning of a random site on the nanotube surface that contains Li, Na or K atoms is performed and sensitivity of the nanotube modified by carboxyl group to the atoms selected is defined. The process was modeled incrementally by moving a metal atom to the functional group along the line parallel to the nanotube surface (Fig. 4). Analysis of interaction energy curves (Fig. 5) shows that the modified nanotube is sensitive to the selected metals as the curve has a minimum that indicates a stable interaction of metal atoms with the “CNT + COOH” system.

Simulation results of sensor activity for a boundary modified by a carboxyl group nanotube are presented in [23]. Table 2 summarizes the results of the interaction for sensor based on surface- and boundary-modified by carboxyl group nanotubes with atoms of the selected metals. A comparison of the interaction energies E_{int} shows that the surface-modified by the COOH group nanotubular system display higher sensitivity for the selected potassium, lithium and sodium atoms.

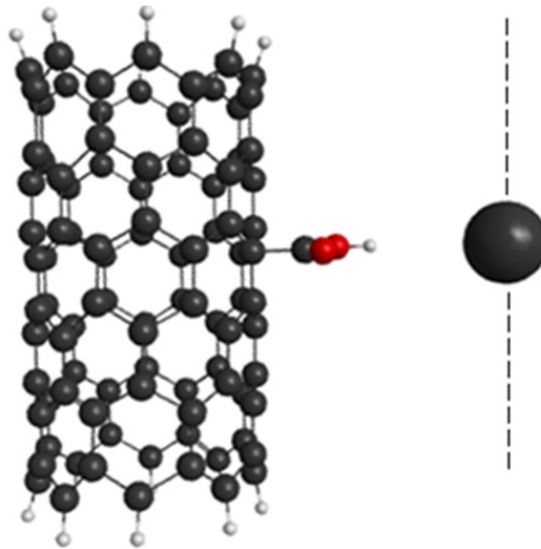


FIG. 4. Scanning of a random site on the nanotube surface that contains Li atom (a grey ball of a bigger size); the dotted line indicates the trajectory of the Li atom in relation to the nanotube modified by carboxyl group

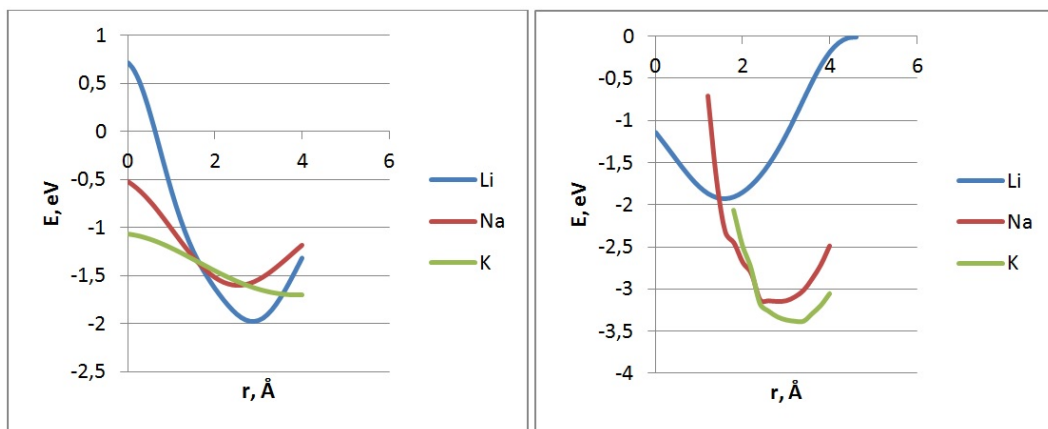


FIG. 5. Interaction energy profiles plotted for atoms of metals and a surface modified nanotubular structure; 0 point corresponds to the point located under atom H of carboxyl group, as well as one of atoms H of amino group and atom O of nitrogroup: a) with H atom b) with O atom

TABLE 2. Interaction characteristics between the boundary-modified by carboxyl group nanotube system and Na, K, Li atoms: r_{int} – sensor interaction distance, E_{int} – sensor interaction energy

Atom (group –COOH)	r_{nt} , Å	E_{int} , eV
Boundary-modified nanostem		
Na–O	3.0	–0.64
Na–H	2.6	–1.73
K–O	2.5	–1.77
K–H	2.8	–1.76
Li–O	3.0	–0.93
Li–H	3.0	–1.63
Surface-modified nanosystem		
Na–O	3.0	–3.38
Na–H	3.4	–4.05
K–O	4.2	–3.75
K–H	4.1	–3.00
Li–O	1.9	–4.00
Li–H	2.2	–3.74

5. Conclusion

As theoretical and experimental studies have shown, carbon nanotubes present a unique material for further research and application in various fields. Advancement in nanotechnology leads to fabrication of new physical objects with properties that are of great scientific and research interest. The proven possibility of carbon nanotube modification by a carboxyl group can be used to create probes with high selectivity. Simulation results prove the possibility of repeated use of modified carbon nanotubes as sensor probes for certain elements and radicals. The presence of these elements and radicals can be experimentally documented by changing the potential in a sensor system based on a nanotube modified by a functional group. When the fabricated sensor interacts with metal atoms, electron density is transferred to the atoms of the carboxyl nanotubular system. Thus, the number of carriers in the surface modified nanotube system increases and a change in the electrical properties of the nanosystem can be fixed. The fabricated sensor element will have a distinctive selectivity that is determined by the energies of the modified tubular nanosystem's interaction with various elements, which will provide a different response for the system to the presence of alkaline metal atoms. Sensors fabricated in this manner will respond to the presence of extremely small amounts of substances, namely atoms or ions of metals, which form part of salts and alkalis, which opens up their potential use in chemistry, biology, medicine, etc.

References

- [1] Dresselhaus M.S., Dresselhaus G., Eklund P.C. *Science of Fullerenes and Carbon Nanotubes*. Academic Press, Inc., 1996, 965 p.
- [2] Saito R., Dresselhaus M.S., Dresselhaus G. *Physical properties of carbon nanotubes*. Imperial College Press, 1999, 251 p.
- [3] Ivanovskii A.L. *Kvantovaya khimiya v materialovedenii. Nanotubulyarnye formy veshchestva [Quantum chemistry in materials science. Nanotubular forms of matter]*. UrORAN, Ekaterinburg, 1999, 176 p.
- [4] Kharris P. *Uglerodnye nanotruby i rodstvennyye struktury. Novye materialy XXI veka [Carbon nanotubes and related structures. New materials of the 21-st century]*. Tekhnosfera, Moscow, 2003, 336 p.
- [5] Zaporotskova I.V. *Uglerodnye i neuglerodnye nanomaterialy i kompozitnye struktury na ikh osnove: stroenie i elektronnye svoistva [Carbon and non-carbon nanotubes and composite structures on their basis: structure and electronic properties]*. Izd-vo VolGU, Volgograd, 2009, 490 p.
- [6] Eliseev A.A., Lukashin A.V. *Funktsional'nye nanomaterialy [Functional nanomaterials]*. Fizmatlit, Moscow, 2010, 456 p.
- [7] Michael F.L. De Volder, Sameh H. Tawfick, Ray H. Baughman, A. John Hart. Carbon Nanotubes: Present and Future Commercial Applications. *Science*, 2013, **339**(6119), P. 535–539.

- [8] Dresselhaus M.S., Dresselhaus G., Avouris. *Carbon nanotubes: synthesis, structure, properties, and application*. Springer-Verlag, 2000, 464 p.
- [9] D'yachkov P.N. Elektronnyye svoystva i primeneniye nanotrubok [Electronic properties and applications of nanotubes]. BINOM. Laboratoriya znaniy, Moscow, 2010, 488 p.
- [10] Elets'kii A.V. Sorption properties of carbon nanostructures. *Phys. Usp.*, 2004, **47**(11), P. 1119–1154.
- [11] Akhmadishina K.F., Bobrinetskii I.I., Komarov I.A., Malovichko A.M., Nevolin V.K., Petukhov V.A., Golovin A.V., Zalevskii A.O. Flexible biological sensors based on carbon nanotube films. *Nanotechnologies in Russia*, 2013, **8**(11-12), P. 721–726.
- [12] Zhang Wei-De, Zhang Wen-Hui. Carbon Nanotubes as Active Components for Gas Sensors. *J. Sensors*, 2009, Article ID 160698, 16 p.
- [13] Zaporotskova I.V., Boroznina N.P., Parkhomenko Y.N., Kozhitov L.V. Carbon nanotubes: Sensor properties. A review. *Modern Electronic Materials*, 2016, **2**(4), P. 95–105.
- [14] Barsan M.M., Ghica M.E., Brett C.M.A. Electrochemical sensors and biosensors based on redox polymer/carbon nanotube modified electrodes. *Analytica Chimica Acta*, 2015, **881**, P. 1–23.
- [15] Boyd A., Dube I., Fedorov G., Paranjape M., Barbara P. Gas sensing mechanism of carbon nanotubes: from single tubes to high-density networks. *Carbon*, 2014, **69**, P. 417–423.
- [16] Liu S.F., Lin S., Swager T.M. An organocobalt-carbon nanotube chemiresistive carbon monoxide detector. *ACS Sens.*, 2016, **1**(4), P. 354–357.
- [17] Im J., Sterner E.S., Swager T.M. Integrated gas sensing system of swcnt and cellulose polymer concentrator for benzene, toluene, and xylenes. *Sensors*, 2016, **16**(2), P. 183.
- [18] Kwona Y.J., Naa H.G., Kanga S.Y., Choib S.-W., Kimb S.S., Kima H.W. Selective detection of low concentration toluene gas using Pt-decorated carbon nanotubes sensors. *Sens. Actuators B: Chem.*, 2016, **227**, P. 157–168.
- [19] Kim J., Choi S.-W., Lee J.-H., Chung Y., Byun Y.T. Gas sensing properties of defect-induced single-walled carbon nanotubes. *Sens. Actuators B: Chem.*, 2016, **228**, P. 688–692.
- [20] Polikarpova N.P., Zaporotskova I.V., Boroznin S.V., Zaporotskov P.A. About using carbon nanotubes with amino group modification as sensors. *J. Nano-Electron. Phys.*, 2015, **7**(4), P. 04089.
- [21] Koch W.A., Holthausen M. *Chemist's Guide to Density Functional Theory*. Wiley-VCH. Weinheim, 2002, P. 19–28.
- [22] Polikarpova N.P., Vil'keeva D.E. Sensor activity of carbon nanotubes with a boundary functional group. *Nanosci. Nanotechnol. Lett.*, 2013, **5**(11), P. 1169–173.
- [23] Polikarpova N.P., Zaporotskova I.V., Vilkeeva D.E., Polikarpov D.I. Sensor properties of carboxyl-modified carbon nanotubes. *Nanosystems: Phys., Chem., Math.*, 2014, **5**(1), P. 101–106.

Filling carbon nanotubes with argon

G. S. Bocharov¹, M. S. Egin¹, A. V. Eletskii¹, V. L. Kuznetsov²

¹National Research University MPEI, Moscow, Russia

²G. K. Boreskov Institute of Catalysis, Siberian Branch of RAS, Novosibirsk, Russia
eletskii@mail.ru

PACS 68.43.Mn, 68.43.Nr

DOI 10.17586/2220-8054-2018-9-1-85-88

The specific surface area of multi-walled carbon nanotubes (MWCNT) of different geometry and structures is measured by the method BET. The nanotubes were synthesized by the use of highly effective Fe–Co catalysts through the method of polymerized complex precursors. In some cases, the measured specific surface area considerably exceeds that calculated under the assumption that the Ar adsorption occurs on the outer surface of CNTs. This permits one to conclude that in some cases a part of argon adsorbed fills the internal hollow of nanotubes.

Keywords: carbon nanotubes, specific surface area, sorption properties.

Received: 1 June 2017

Revised: 24 August 2017

1. Introduction

One of the prominent features of carbon nanotubes (CNT) relates to the existence of an internal cavity where various gaseous and condensed substances can be accumulated (see reviews [1–3] and the works cited there). This feature permits one to consider CNTs as a potential reservoir for storage of gases and harmful substances and to use them as a natural chamber for performing chemical reactions. Determination of the content of substances filling the internal hollow of CNTs requires complex apparatus, the usage of which is accompanied by an intense action onto the material and can result in the depletion of CNT cavity. Thus, the authors of the work [4] studied filling single walled CNT with nitrogen and oxygen using X-ray diffraction measurements and isotherm absorption analysis. It has been observed that molecular gases fill the inner cavity of CNTs only in the case of thermally treated samples resulting in opening the nanotube's ends. The adsorption capacity of single-wall carbon nanotubes (SWCNTs) bundles with regard to the pure CH₄, N₂, CO and CO₂ gases at 298 K and pressures ranging from 0.01 to 2.0 MPa has been investigated experimentally and computationally in [5]. In the present work, special attention is paid to the possibility of relatively simple determination of gaseous argon content inside CNTs based on the analysis of the specific surface area measurements for the material.

2. Experiment

Multi-walled CNTs (MWCNT) of different geometry have been synthesized in G. K. Boreskov Institute of Catalysis, Siberian Branch RAS, Novosibirsk, by the use of high effective Fe–Co catalysts through the method of polymerized complex precursors [6]. Ca, Al and Mg ions were used as the catalyst precursors. In the classic version of this method, the salts of the selected metals are mixed with citric acid and ethylene glycol or ethylenediamine, the condensation of which at high temperature, results in the formation of a 3D polymer matrix. Practically homogeneous distribution of metal ions in the organic matrix is reached due to coordination of these ions with carboxyl groups of citric acid. Subsequent burning off the organic substance results in formation of a system of mixed spinel oxides. If this step is performed at relatively moderate temperatures, oxide particles obtained can be found in a dispersed, practically amorphous state [7–9]. Variation of the oxide component of catalyst (Ca, Al, Mg), that is not reduced during the CNT synthesis and, in essence, a carrier, permits one to vary the dispersion of metal particles due to the reduction by the substrate (ethylene) [10]. This results in production of MWCNT having different distribution over diameter (MWCNT 1, MWCNT 2, MWCNT 3). One should note that processing these base samples (oxidation, grinding) did not result in change of their diameter distribution. Therefore these distributions are true also for functionalized samples.

The mean diameter of MWCNT was controlled through changing the concentration of the active component in the catalyst. Diameter distribution of MWCNT and structural changes of graphene shaving covering the nanotube's surface were determined by means of HR-TEM (JEM-2010). The diameter distribution was determined for each sample on the basis of analysis of 300–600 TEM images of MWCNTs (Fig. 1), obtained at magnification of 50,000× and 400,000×. Fig. 2(a,b,c) present the typical diameter distributions for MWCNTs. These distributions

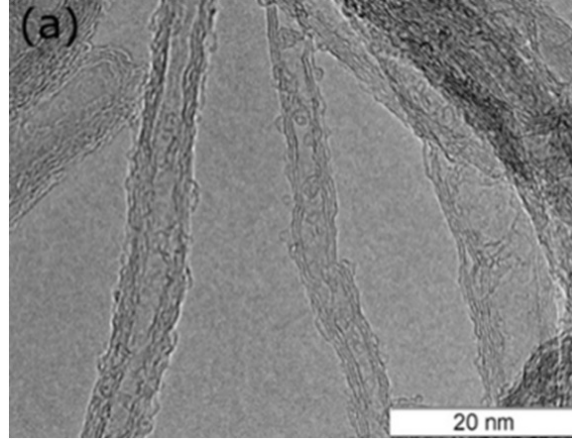


FIG. 1. CNT image of MWCNT-1

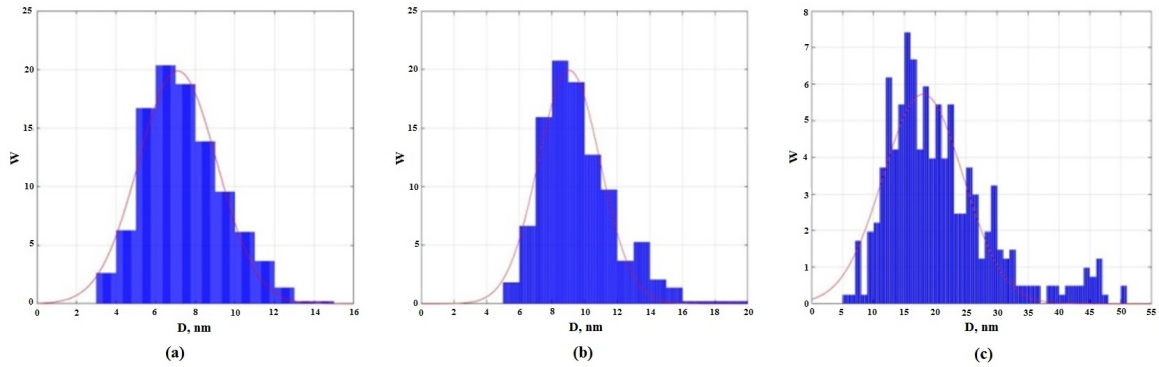


FIG. 2. Typical diameter distributions of MWCNT determined through the treatment of microimages: MWCNT-1 (a); MWCNT-2 (b); MWCNT-3 (c). The distributions have been normalized by unity. The diameter distributions smoothed by the Gauss function are shown by the lines

are readily reproducible for different sample sets produced with the use of specific catalyst types. The accuracy of determination of the maximum of the distribution accounts ± 0.5 nm for thin (7–10 nm) and ± 1.5 nm for thicker CNTs (~ 20 nm). Characteristics of the multi-walled CNTs under investigation are given in Table 1.

3. Specific surface area of MWCNTs

The specific surface area of MWCNTs was measured by the standard BET method using the SORBI-M setup. MWCNT samples of 20–40 mg in mass were placed into a camera where the argon sorption-desorption cycles at a liquid nitrogen temperature were performed. The measured data were treated by means of a computer program and averaged by three cycles. The results of such a treatment are given in the 4th column of Table 1.

The calculation of the specific area of MWCNT samples was performed using the typical diameter distributions (Fig. 2(a,b,c)). Considering MWCNT as a solid cylinder of the density ρ and D in diameter, the external specific surface area S of such a cylinder is expressed by the following relation:

$$S = \frac{4}{(D \cdot \rho)}. \quad (1)$$

This relation is valid if the nanotube length considerably exceeds its diameter, and the number of layers $n \gg 1$. If the nanotube is considered not as a solid medium but as a set of concentric cylinders inserted into each another and having the distance between the neighboring walls of $d = 0.34$ nm, then the external specific surface area will depend on the radius of the smallest cylinder r_0 :

$$S = \frac{D\sigma}{r_0 n \left[1 + \frac{(n-1)d}{r_0} \right]}, \quad (2)$$

TABLE 1. Characteristics of the samples under investigation

Sample	Mean diameter(nm)	Mean length (the width of distribution) (nm)	Specific surface area (m ² /g)		
			Measurement	Calculation	
				(1)	(3)
MWCNT-1-LRP ¹	7.2	Up to 50000	342.2±1.9	247	271
MWCNT-1-LRP APF ²	7.2	220 (20–500)	285±12	247	271
MWCNT-1-LRP APF O _x Na ³	7.2	220 (20–500)	323±15	247	271
MWCNT-2-LRP ¹	9.4	Up to 50000	320.0±1.9	189	195
MWCNT-2-LRP APF ²	9.4	220 (20–600)	290±3	189	195
MWCNT-2-LRP APF O _x Na ³	9.4	220 (20–600)	328±5	189	195
MWCNT-3-LRP ¹	18	Up to 30000	100.2	99	111
MWCNT-3-LRP APF ²	18	520 (20–500)	113.2	99	111
MWCNT-3-LRP APF O _x Na ³	18	520 (20–500)	110.7	99	111

¹The catalyst is washed out. ²The catalyst is washed out, grinded. ³The catalyst is washed out, grinded, oxidized.

The carboxyl groups content 0.75–0.9 nm⁻¹.

where $n \approx D/2d$ is the number of layers in the nanotube, $\sigma \approx 1300$ m²/g is the specific surface area of the hexagonal plane constituting the basis of the nanotube structure. Using the obvious relation $\rho = (\sigma d)^{-1}$ the equation (2) is reduced to the more simple relation (1) under the condition $n \gg 1$. The Eq. (2) is more correct than (1), however it contains an indefinite parameter r_0 therefore the specific surface area was calculated using Eq. (1). The calculations imply that the error caused decreases as the outer nanotube's diameter D increases and the smallest nanotube's radius r_0 decreases. The typical value of r_0 lies in the range of between 0.7 and 0.9 nm, therefore for nanotubes with outer diameter of 7 nm this error accounts 8–10 % while for more wide nanotubes ($D = 9.4$ and 18 nm) this error accounts 5–10 and 2–4 %, correspondingly. Such an error is within the accuracy of determination of nanotube's diameter.

The external specific surface area is expressed as follows:

$$S = \int_0^{\infty} \frac{4W(D)}{(D\rho)} dD. \quad (3)$$

Here, $W(D)$ is the diameter distribution of CNT (Fig. 2), which is approximated by the Gauss function. The results of calculation of the specific surface area of CNTs of different types are given in the 5-th and 6-th columns of Table 1. The data presented in the 5-th column have been obtained on the basis of Eq. (1) supposing that all the nanotubes have a fixed (mean) diameter. The data of the 6-th column have been obtained on the basis of Eq. (3) with taking into account the real CNT diameter distribution. As is seen, taking into consideration the real CNT diameter distribution changes the calculated values of the specific surface area within the range of 10 %.

The analysis of the specific surface area values presented in Table 1 indicates that for samples MWCNT1 and MWCNT2 the measured values of the specific surface area exceed by 20–30 % those obtained through the calculation of the external specific surface area. This permits one to conclude that the nanotubes of the above-mentioned types not only adsorb argon by their external surface but also store it in its inner cage.

4. Conclusion

The specific surface area of MWCNT produced by using highly productive Fe–Co based catalysts utilizing the method of polymerized complex precursors has been measured by the BET method. Argon at a liquid nitrogen temperature has been used as an adsorbed gas. For some MWCNT samples, the measured value of the specific surface area notably exceeded the relevant calculation data obtained under the assumption that argon is desorbed

by the external surface of the nanotubes. Therefore, argon is adsorbed by both the external surfaces and by the internal cavities of the nanotubes under consideration.

Acknowledgements

The work is supported by the State Tasks No 3.1414.2017 and No 3.7131.2017.

References

- [1] Eletsii A.V. Sorption properties of carbon nanostructures. *Physics-Uspechi*, 2004, **47**(11), P. 1119–1154.
- [2] Zhao J. Gas Adsorption of Carbon Nanotubes: Tube-Molecule Interaction and Technological Applications. *Current Nanoscience*, 2005, **1**(2), P. 169–176.
- [3] Pietraß T. Gas Adsorption on Carbon Nanotubes. In: *Modern Magnetic Resonance*, ed. by G. A. Webb. Springer, 2008, P. 1479–1485.
- [4] Fujiwara A., Ishii K., Suematsu H., Kataura H., Maniwa Y., Suzuki S., Achiba Y. Gas adsorption in the inside and outside of single-walled carbon nanotubes. *Chem. Phys. Lett.*, 2001, **336**, P. 205–211.
- [5] Lithoxoos G.P., Labropoulos A., Peristeras L.D., Kanellopoulos N., Samios J., Economou I.G. Adsorption of N₂, CH₄, CO and CO₂ Gases in Single Walled Carbon Nanotubes: A Combined Experimental and Monte Carlo Molecular Simulation Study. *J. Supercrit. Fluids*, 2010, **55**(2), P. 510–523.
- [6] Kakihana M., Yoshimura M. Synthesis and Characteristics of Complex Multicomponent Oxides Prepared by Polymer Complex Method. *Bull. Chem. Soc. Japan*, 1999, **72**(7), P. 1427–1443.
- [7] Usoltseva A., Kuznetsov V., Rudina N., Moroz E., Haluska M., Roth S. Influence of catalysts' activation on their activity and selectivity in carbon nanotubes synthesis. *Phys. Status Solidi*, 2007, **244**(11), P. 3920–3924.
- [8] Kuznetsov V.L., Usoltseva A.N. Method of production fine-grained supported catalysts and synthesis of carbon nanotubes. *Patent.2373995* Russia: 27.11.2009 Bull. 33.
- [9] Elumeeva K.V. *Production of multi-walled carbon nanotubes with predetermined properties*. Thesis. Novosibirsk. Institute of Catalysis, Siberian Branch of RAS, 2012, 161 p.
- [10] Kuznetsov V.L., Krasnikov D.V., Schmakov A.N., Elumeeva K.V. *In situ and ex situ* time resolved study of multi-component Fe-Co oxide catalyst activation during MWNT synthesis. *Phys. Status Solidi B*, 2012, **249**(12), P. 2390–2394.

Formation of the nanoscale contacts structure based on cross-junction of carbon nanotubes for the study of organic materials

Yu. A. Polikarpov, A. V. Romashkin, V. A. Petukhov, V. K. Nevolin

National Research University of Electronic Technology, Moscow, Russia

jurij.polikarpov@yandex.ru

PACS 73.40.Cg, 73.63.Rt, 81.07.Lk, 81.15.-z

DOI 10.17586/2220-8054-2018-9-1-89-91

Using the dielectrophoresis method with unipolar rectangular pulses for the deposition of carbon nanotubes (CNTs), functionalized by COOH groups, single nanosized contacts based on a single-walled CNT and a functionalized single-walled CNT have been formed, the specific contact resistance of which, according to the estimate, was about $0.25 \mu\Omega\cdot\text{cm}^2$ or about $6 \text{ M}\Omega$ per one cross-junction of CNTs. The possible usage of the proposed technique for the nanoscale contacts formation based on the cross-junction of CNTs in various layers for the study of organic materials and charge transport in a nanoscale channel is considered.

Keywords: organic electronics, carbon nanotube, nanoscale contact, dielectrophoresis.

Received: 26 October 2017

Revised: 6 November 2017

1. Introduction

The study of charge transport in organic materials in conjunction with deposition methods, intermolecular interaction and contacts influence, is an actual task of organic electronics. Improving devices' characteristics and functionality is required to reveal the mechanisms that occur at the level of individual molecules and their functional groups. To this end, it is possible to use carbon nanotubes (CNTs) which form a transition from micro- to nanoscale, that makes it possible to develop principles of reducing the contact resistance [1], to study high-structured in the nanoscale organic materials [2], and to form nanoscale contacts [3]. However, existing technological approaches do not allow to form a large quantity of nanoscale contact structures for study different organic molecules and the contribution of the contact resistance to the characteristics of transistor structures based on them.

2. Materials and methods

We used an oxidized silicon substrate with a pre-deposited non-percolated array of single-walled CNTs (SWCNT), synthesized by the gas-phase method [4] over 20 s. Using group photolithography methods, the Au/Cr micro-contacts having opposite protrusions were formed. Then, SWCNTs were etched in an oxygen plasma using photoresist protective mask, and as a result, many structures were formed in which the SWCNTs had contact only with one of the micro-contacts (Fig. 1a,b). To deposit CNTs of the top layer and to form structures with individual contacts of CNT-CNT (Fig. 1c), deposition from a solution using COOH-functionalized SWCNTs (fSWCNTs) (Carbon Solutions, USA) was performed.

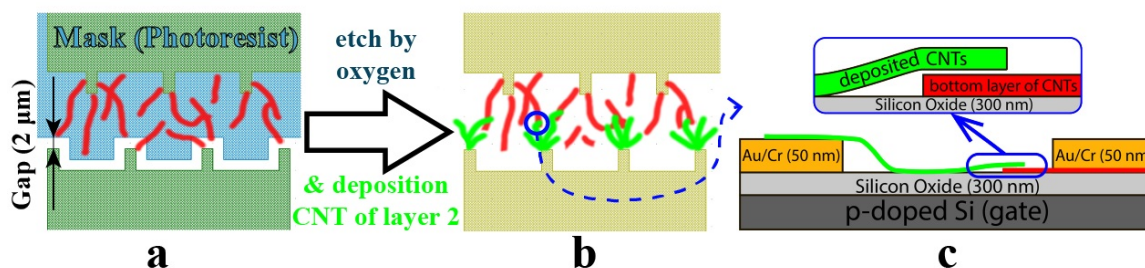


FIG. 1. Structures with micro-contacts before (a) and after (b) oxygen plasma etching and deposition of fSWCNTs as the top layer; SWCNTs form the bottom layer; cross section diagram of the nanocontact (c)

Before deposition, fSWCNTs dispersion was ultrasonically treated for 2 min and then centrifuged at $\sim 10,000$ g. Deposition was carried out by dielectrophoresis technique from the solution (volume $\sim 0.5 \mu\text{L}$ per iteration) with a substrate heated to 60°C , and nanoscale contacts were formed as the cross-junction of CNT between two layers (Fig. 1c). As a solvent, isopropanol (IP), N-methylpyrrolidone (NMP), cyclopentanone (CP) were chosen [5]. It was found that NMP has a very low evaporation rate and resistance, which led to the destruction of microcontacts due to the high current density and the absence of CNTs in the gap. IP had a low colloid stability time, which did not allow centrifugation. CP had a high evaporation rate ($0.01 \mu\text{L/s}$), a long colloid stability time (~ 3 h) and low conductivity, and was selected as the optimal solvent. Based on the topography obtained by the atomic force microscopy (AFM), we found optimal parameters of fSWCNTs solution, which provide the formation of single contacts of SWCNT-fSWCNT: concentration was $1 \mu\text{g/mL}$ or optical transparency 98 % in comparison with pure CP. So, the grid of fSWCNTs (length of separate fSWCNT $\sim 2 \mu\text{m}$) was formed.

3. Results and discussion

Several depositions of fSWCNTs from CP by dielectrophoresis using unipolar rectangular pulses (pulse time 5, 10 and 250 ms with period of 4 times longer than pulse time, amplitude 10 V) were carried out. The positive potential was applied to the contact without CNTs. This technique allows us to deposit fSWCNTs predominantly near one of the micro-contacts (see lower contact in Fig. 2a), preserving the edge of the second micro-contact practically clean (with a significantly lower density of fSWCNTs). At the ends of the nanotubes of the bottom layer, fields with a strength of more than $5 \cdot 10^6$ V/m were formed, however, according to the results of the AFM study, the deposition of the fSWCNTs was determined by the mean field at the microscale, i.e. $0.7 \cdot 10^6$ V/m, and it was not revealed the influence of localization of the field on the CNT of the first (bottom) layer on the deposition process of CNTs of the second (top) layer. At a pulse time of 5 ms, deposition occurred slowly (channels with CNT-CNT contact was not formed even after several iterations) with the formation of a grid of SWCNTs only directly near the protrusions of the micro-contacts. But, at pulse time of 250 ms, the channels of the top layer fSWCNTs were formed too quickly, that formed shunting channel in $14 \mu\text{m}$ gap between metallization without participation of CNTs of the bottom layer as second nanocontacts (one iteration was sufficient). Thus, such deposition was unmanageable.

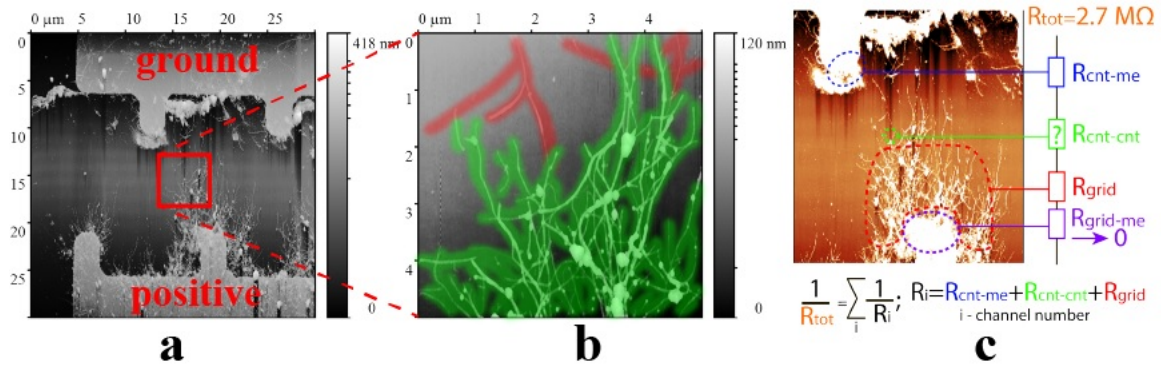


FIG. 2. AFM images of micro-contacts after dielectrophoretic deposition with pulse time of 10 ms (a) and amplitude of 10 V and increased contact site of SWCNT-fSWCNT (b). The red ones represent the SWCNTs of the previously deposited bottom layer, the green ones are fSWCNTs of the deposited top layer. An explanation of total resistance of the structure is given by the formula (c)

At a pulse time of 10 ms, single contacts of CNT-CNT as the cross-junction of CNTs between different layers were formed (Fig. 2a,b). The grid of deposited fSWCNTs was quite dense, but it grew gradually, forming single nanotubes at the edges, which formed contact. Based on the measured output current-voltage characteristic (CVC), the total resistance (R_{tot}) at $2.7 \text{ M}\Omega$ was estimated. The total resistance is determined the sum of the parallel channels (R_i), each of which includes: the resistance of SWCNT-metal (R_{cnt-me}), SWCNT-fSWCNT ($R_{cnt-cnt}$), and also the grid of deposited fSWCNT (R_{grid}). Therefore, to determine $R_{cnt-cnt}$, it was necessary to estimate each of them separately (Fig. 2c). The resistance of the SWCNT and the contact of fSWCNT grid with metal can be relied on to be negligibly small in comparison with other components. The estimation of the contact resistance of SWCNT-metal was carried out based of SEM images by counting the number of CNTs having contact to both

micro-contacts (before plasma etching operation) and output CVC of the structure and was for SWCNT-Cr/Au 600 k Ω for one contact or specific contact resistance 1.2 k $\Omega \cdot \mu\text{m}$ (recalculation on the SWCNT diameter ~ 2 nm), which is comparable with the literature data (~ 1 k $\Omega \cdot \mu\text{m}$ [6]). The estimation of the fSWCNT grid resistance of the top layer was carried out based on the results of analysis of fSWCNT films of similar density (using the four probe method) and was no more than 3 M Ω per square.

Thus, with considering the resistance of SWCNT-metal and also the resistance of the grid of the fSWCNT of the top layer, the resistance of SWCNT-fSWCNT nano-contact was 6.1 M Ω per one pair of CNTs or specific contact resistance 0.25 $\mu\Omega \cdot \text{cm}^2$ (with a SWCNT diameter of 2 nm), which agrees with the literary data, in particular, the contact resistance between a semiconductor and a metal CNTs (similar to the contact obtained in this work due to the use of fSWCNT having functional groups and SWCNT) was ~ 8 M Ω per one pair [7]). The proposed method of nano-contact formation allows using a cluster of organic molecules or their layer that can be formed before deposition of top layer CNTs for the formation of nanoscale OFET and studying its characteristics and using different molecules.

4. Conclusion

Thus, a technique for the formation of nanoscale contacts based on CNTs with the possibility of forming and studying molecular layers was proposed, and the contact resistance of fSWCNT-SWCNT was estimated with consideration of structural features, which should be useful for the study of charge transport in CNT-molecule-CNT structures.

Acknowledgements

This work was supported by the Ministry of Education and Science of the Russian Federation, agreement No. 14.575.21.0125 (unique ID RFMEFI57517X0125).

References

- [1] Hou J.-L., Kasemann D., Widmer J., Günther A.A., Lüssem B., Leo K. Reduced contact resistance in top-contact organic field-effect transistors by interface contact doping. *Appl. Phys. Lett.*, 2016, **108**(10), P. 103303.
- [2] Bobrinetskii I.I., Nevolin V.K., Romashkin A.V. Quasi-one-dimensional molecular transistors based on polyaniline and carbon nanotubes as electrodes. *Semiconductors*, 2012, **46**(13), P. 1593–1597.
- [3] Thiele C., Vieker H., Beyer A., Flavel B.S., Hennrich F., Torres D.M., Eaton T.R., Mayor M., Kappes M.M., Götzhäuser A., Löhneysen H.V., Krupke R. Fabrication of carbon nanotube nanogap electrodes by helium ion sputtering for molecular contacts. *Appl. Phys. Lett.*, 2014, **104**, P. 103102.
- [4] Moiala A., Nasibulin A.G., Brown D.P., Jiang H., Khriachtchev L., Kauppinen E.I. Single-walled carbon nanotube synthesis using ferrocene and iron pentacarbonyl in a laminar flow reactor. *Chem. Eng. Sci.*, 2006, **61**(13), P. 4393–4402.
- [5] Ausman K.D., Piner R., Lourie O., Ruoff R.S. Organic Solvent Dispersions of Single-Walled Carbon Nanotubes: Toward Solutions of Pristine Nanotubes. *J. Phys. Chem. B*, 2000, **104**(38), P. 8911–8915.
- [6] Song Y., Kang S.J. Improvement of contact resistance between carbon nanotubes and metal electrodes for high performance electronics. *J. Vac. Sci. Technol. B*, 2011, **29**(1), P. 011011.
- [7] Fuhrer M.S., Nygård J., Shih L., Forero M., Yoon Y.-G., Mazzone M.S.C., Choi H.J., Ihm J., Louie S.G., Zettl A., McEuen P.L. Crossed Nanotube Junctions. *Science*, 2000, **288**, P. 494–497.

The growth temperature effect on vertically aligned carbon nanotubes parameters

O. I. Il'in¹, M. V. Il'ina¹, N. N. Rudyk², A. A. Fedotov², O. A. Ageev¹

¹Southern Federal University, Research and educational center of “Nanotechnology”, Russia

²Southern Federal University, Laboratory of nanobiotechnologies and new materials, Russia
oiilin@sfnedu.ru, ageev@sfnedu.ru

PACS 61.46.Fg, 61.46.Np

DOI 10.17586/2220-8054-2018-9-1-92-94

We studied the influence of the synthesis temperature on geometric parameters and structural perfection for vertically aligned carbon nanotubes (VACNT). We established that a synthetic temperature of 750 °C allows one to obtain the lowest concentration of defects in VACNT, with a diameter of 44±3 nm and a height of 80±9 nm. When temperature is increased up to 800 °C, an increase of the VACNT geometric dimensions was observed, which may be due to an increase in the catalytic centers (CCs) migration rate and their integration into larger centers. Also, at 800 °C, the concentration of defects in the nanotubes was increased due to the violation of carbon bonds during the acceleration of the acetylene desorption process from the surface of the sample.

Keywords: carbon nanotube, chemical vapor deposition, raman spectroscopy, catalytic centers, synthesis.

Received: 17 June 2017

1. Introduction

Due to unique properties of vertically aligned carbon nanotubes, they are widely applied as elements of micro- and nanoelectronic devices [1], fillers of various composite materials and high-strength adhesives (“dry” glue) [2]. Of particular interest are arrays of VACNT with certain geometric dimensions and conductivity. In this regard, there is a need for the synthesis of VACNT with controlled geometrical parameters, properties and structure.

The method of plasma enhanced chemical vapor deposition (PECVD), which allows to grow aligned CNTs on substrates with specially prepared catalytic centers (CC), is the most promising [3]. A large number of interrelated parameters of the PECVD method (temperature, pressure, process gas flows, etc.) have significant influence on the growth processes and properties of the VACNT [3–5]. One of the most important parameters that determines the geometric dimensions and structure of the VACNT is the synthesis temperature.

The aim of the work is to study the influence of the growth temperature of the VACNT by the PECVD method on their geometric parameters and structural perfection.

2. Experiments and methods

The synthesis of the VACNT was carried out by the “top-mechanism” in the PECVD module of nanotechnology complex NANOFAB NTK-9 (NT-MDT, Russia). A Si (100) wafer was used as a substrate, on which films of a buffer sublayer of Cr (20 nm) and a catalytic layer of Ni (10 nm) were formed by magnetron sputtering. Ni/Cr films were used as a combination of metals in the catalyst/sublayer, because they provide high homogeneity of the parameters of carbon nanotubes [6]. The growth of VACNT was carried out in a mixture of gases NH₃ (210 sccm) and C₂H₂ (70 sccm), at a chamber pressure of 4.5 Torr for 20 min. The synthesis temperature varied from 650 to 800 °C.

We studied the VACNT samples using a scanning electron microscope (SEM) Nova NanoLab 600 (FEI, Netherlands). The diameter and height of the VACNT array were evaluated by means of statistical processing of SEM images. The structural analysis of the VACNT arrays was conducted by a Raman spectrometer Renishaw InVia Reflex (Renishaw plc, UK).

3. Results and discussion

The analysis of the obtained SEM images of the experimental samples showed that the VACNTs were grown by the “top-mechanism”. For samples obtained at 650 °C (Fig. 1a), the height and diameter of the CNTs in the array were 65±5 nm and 25±3 nm, respectively. Also presented are disoriented CNTs (Fig. 1a). Increasing the temperature to 700 °C (Fig. 1b) made possible the removal of the disoriented CNTs. In this case, the geometrical dimensions of CNTs are practically unchanged (diameter of 25±4 nm, height of 66±5 nm). This effect can be associated with a better desorption of hydrogen during the decomposition of acetylene on CC, which leads to the formation of a less “defective” layer of carbon on the CC surface, which does not branch and violate the vertical

orientation of the CNT. As the temperature was increased to 750 °C (Fig. 1c), an increase in the diameter and height of the VACNT (44 ± 3 nm and 80 ± 9 nm, respectively) occurred, as well as the growth of individual CNTs with a diameter of 70 ± 3 nm and a height of 350 ± 10 nm. This may be due to the activation of diffusion exchange of atoms between the film and the substrate and, the association of small CCs into larger ones. At 800 °C (Fig. 1d), the diameter and height of CNT arrays were 51 ± 6 nm and 100 ± 12 nm, respectively. The growth of individual CNTs with a height of up to 600 ± 14 nm and a diameter of 52 ± 2 nm is also observed. The increase in the diameter of the CNT and the almost complete absence of nanotubes of diameter less than 25 nm indicated an ongoing process of diameter increasing, possibly resulting from CC or small center sublimation at this temperature.

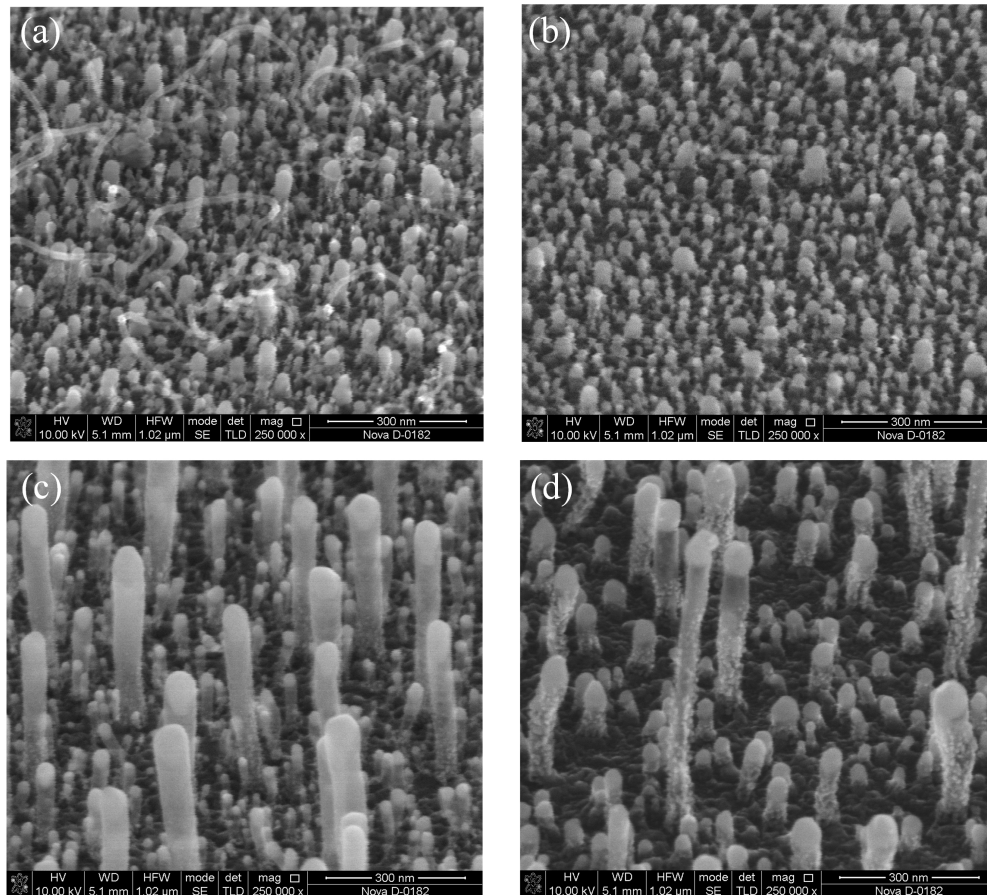


FIG. 1. SEM images of arrays of vertically aligned CNTs: 650 °C (a); 700 °C (b); 750 °C (c); 800 °C (d)

Structural analysis of the experimental samples grown at temperatures of 650, 700, 750 and 800 °C (Fig. 2) showed the presence of D- and G-mode typical for carbon nanotubes [7]. The absence of the RBM mode in the $0\text{--}200\text{ cm}^{-1}$ range in all samples indicated a multiwall type of the grown nanotubes [8].

In addition, the amplitude ratio of the I_D/I_G peaks of the experimental samples allowed us to estimate the influence of the growth temperature on the defectiveness of the VACNTs and was 0.92, 0.88 and 0.90 for 700, 750 and 800 °C, respectively. The maximum defect concentration ($I_D/I_G = 0.92$) was observed for VACNT grown at 700 °C, which is probably due to the influence of the material of the catalytic center occupying most of the volume of the entire nanotube, leading to a violation of the symmetry of the graphite layer with sp^2 -hybridization. Increasing the synthesis temperature to 750 °C resulted in an increase in the aspect ratio and volume of the nanotubes, reducing its defectiveness to $I_D/I_G = 0.88$. With a subsequent increase in the synthesis time, the I_D/I_G value increased again, which is due to the violation of carbon bonds due to the acceleration of the acetylene desorption process from the sample surface. As a consequence, the carbon-containing gas did not have time to react with the CC and was pumped out by the vacuum system. As a result, graphenated multi-wall carbon nanotubes were formed (Fig. 1d).

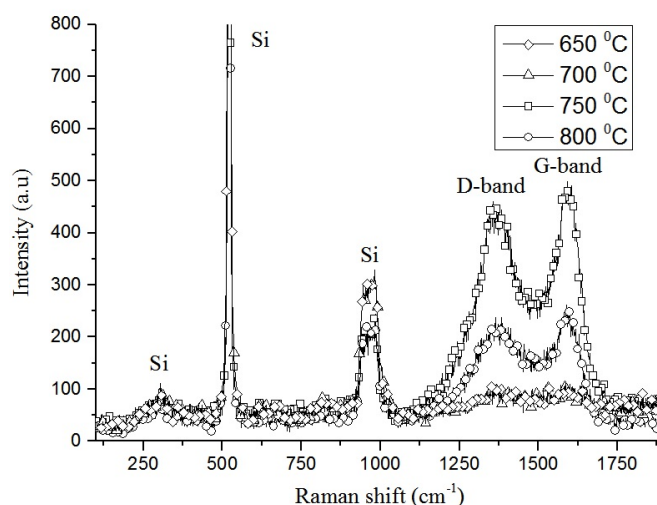


FIG. 2. Raman spectra of images with CNTs are grown at different temperatures

4. Conclusion

Experimental studies of the influence of the synthesis temperature of the VACNT by PECVD on their geometric parameters and structural perfection were performed. It was found that the growth temperature 750 °C allows one to obtain a CNT with the diameter of 44 ± 3 nm, the height of 80 ± 9 nm and a minimal concentration of defects.

When temperature is increased to 800 °C, increases in the diameter and height of the VACNT were observed up to 51 ± 6 nm and 100 ± 12 nm, respectively, which may be associated with an increase in the migration rate of catalytic centers and their integration into larger centers. Structural studies have also shown smallest defects for VACNT were for those synthesized at 750 °C. At 800 °C, the defectiveness of nanotubes was increased due to the violation of carbon bonds during the acceleration of the acetylene desorption process from the surface of the sample. Thus, it is shown that control of the growth temperature allows optimization of the technological process of growing CNTs, to obtain nanotubes of the lowest numbers of defects and high concentration.

The obtained results can be used for the development of technological processes for the formation of vertically aligned carbon nanotubes for functional elements for emission nanoelectronics devices, memory cells and adhesion coatings.

Acknowledgements

This work was funded by the Russian Foundation for Basic Research according to the research project No. 16-29-14023 of f.m and internal grant Internal grant of the Southern Federal University No. VnGr-07/2017-26.

References

- [1] Ageev O.A., Blinov Yu.F., Il'in O.I., Konoplev B.G., Rubashkina M.V., Smirnov V.A., Fedotov A.A. Study of the resistive switching of vertically aligned carbon nanotubes by scanning tunneling microscopy. *Phys. Solid State*, 2015, **57**, P. 825–831.
- [2] Jeong H.E., Suh K.Y. Nanohairs and nanotubes: Efficient structural elements for gecko-inspired artificial dry adhesives. *Nano Today*, 2009, **4**, P. 335–346.
- [3] Saeidi M. Influence of partial pressure on base-growth of single carbon nanotube. *J. Cryst. Growth*, 2014, **404**, P. 34–38.
- [4] Shah K.A., Tali B.A. Synthesis of carbon nanotubes by catalytic chemical vapour deposition: A review on carbon sources, catalysts and substrates. *Mater. Sci. Semicond. Process*, 2016, **41**, P. 67–82.
- [5] Ageev O.A., Il'in O.I., Rubashkina M.V., Smirnov V. A., Fedotov A.A., Tsukanova O.G. Determination of the electrical resistivity of vertically aligned carbon nanotubes by scanning probe microscopy. *Techn. Phys.*, 2015, **60**(7), P. 1044–1050.
- [6] Ando Y., Zhao X., Sugai T., Kumar M. Growing carbon nanotubes. *Mater. Today*, 2004, **7**, P. 22–29.
- [7] Maultzsch J., Reich S., Thomsen C. Raman scattering in carbon nanotubes revisited. *Phys. Rev. B*, 2002, **65**, P. 233402.
- [8] Saito R., Hofmann M., Dresselhaus G., Jorio A., Dresselhaus M.S. Raman spectroscopy of graphene and carbon nanotubes. *Adv. Phys.*, 2011, **60**(3), P. 413–550.

Graphene on silicon carbide as a basis for gas- and biosensor applications

S. P. Lebedev^{1,a}, V. Yu. Davydov^{1,b}, D. Yu. Usachov^{2,c}, A. N. Smirnov^{1,3,d}, V. S. Levitskii^{4,e}, I. A. Eliseyev^{1,f}, E. V. Guschina^{1,g}, M. S. Dunaevskiy^{1,h}, O. Yu. Vilkov^{2,i}, A. G. Rybkin^{2,j}, A. A. Lebedev^{1,k}, S. N. Novikov^{5,l}, Yu. N. Makarov^{6,m}

¹Ioffe Institute, 26 Politekhnikeskaya, 194021 St.Petersburg, Russia

²Saint Petersburg State University, 199034 St.Petersburg, Russia

³ITMO University, 49 Kronverkskiy prospekt, 197101 St.Petersburg, Russia

⁴R&D Center TFTE, 28 Politekhnikeskaya, 194064 St. Petersburg, Russia

⁵Aalto University, Micronova, Tietotie 3, FI-02150, Espoo, Finland

⁶Nitride Crystals Inc., 11729 Deer Park, NY, United States

^alebedev.sergey@mail.ioffe.ru, ^bvalery.davydov@mail.ioffe.ru, ^cdmitry.usachov@spbu.ru,

^dalex.smirnov@mail.ioffe.ru, ^elev-vladimir@yandex.ru, ^fzoid95@yandex.ru, ^gkatgushch@yandex.ru,

^hMike.Dunaeffsky@mail.ioffe.ru, ⁱol.vilkov@gmail.com, ^jartem.rybkin@spbu.ru, ^kShura.Lebe@mail.ioffe.ru,

^lsergeyv59@gmail.com, ^myuri.makarov@nitride-crystals.com

PACS 78.67.Wj, 68.37.Ps, 74.25.nd

DOI 10.17586/2220-8054-2018-9-1-95-97

The structural, chemical, and electronic characteristics of graphene grown by thermal decomposition of a singlecrystal SiC substrate in Ar atmosphere are presented. It is shown that this technology allows the creation of high-quality monolayer graphene films with a small fraction of bilayer graphene inclusions. The performance of graphene on SiC as a gas sensor or a biosensor was tested. The sensitivity of gas sensors to NO₂ on the order of 1 ppb and that of biosensors to fluorescein with concentration on the order of 1 ng/mL and to bovine serum albumin–fluorescein conjugate with concentration on the order of 1 ng/mL were determined.

Keywords: graphene, silicon carbide, thermal decomposition, Raman spectroscopy, AFM, XPS, ARPES.

Received: 20 June 2017

1. Introduction

Graphene is a promising material with unique properties, such as high surface-to-volume ratio, low electrical noise, and exceptional transport properties associated with its two-dimensional structure [1]. One of the most promising techniques for graphene synthesis, which can be integrated into industrial production, is the thermal decomposition of the surface of semi-insulating silicon carbide (SiC) substrates [2]. The main advantages of this method are the high structural perfection of the resulting graphene films and the possibility of growing a graphene film on a semi-insulating substrate. In this paper, we present the results obtained in the study of the characteristics of graphene films grown by thermal decomposition on the SiC surface and in the performance test of graphene as a gas sensor and a biosensor.

2. Experimental

Graphene films were grown by thermal decomposition of single-crystal semi-insulating 6H-SiC and 4H-SiC substrates under Ar at 1800–1850 °C over 10 min. The growth was carried out on the Si-face [SiC (0001)] of a substrate. Before synthesis, organic and inorganic solvents were used to clean the substrate surface. The structural, chemical, and electronic characteristics of graphene were monitored by Raman spectroscopy, atomic force microscopy (AFM), X-ray photoelectron and angle-resolved photoemission spectroscopy (XPS and ARPES).

3. Results

Raman spectroscopy and AFM were used to determine the thickness uniformity of a graphene film. Fig. 1a presents an array of Raman spectra measured in the range of 1300–2800 cm⁻¹ at a sample area of 12.5 × 12.5 μm². An analysis of the G line intensity map obtained by processing this array revealed a quite uniform distribution of the line intensity. This suggests that the graphene film has good thickness uniformity in the area being analyzed. It was found that the 2D-line is symmetric in most of spectra and is well fitted by a single Lorentzian, which is a fingerprint of the single-layer graphene [3]. Fig. 1b shows the map of the surface potential distribution, furnished by Kelvin probe microscopy. It was found that the potential difference between the light and dark areas

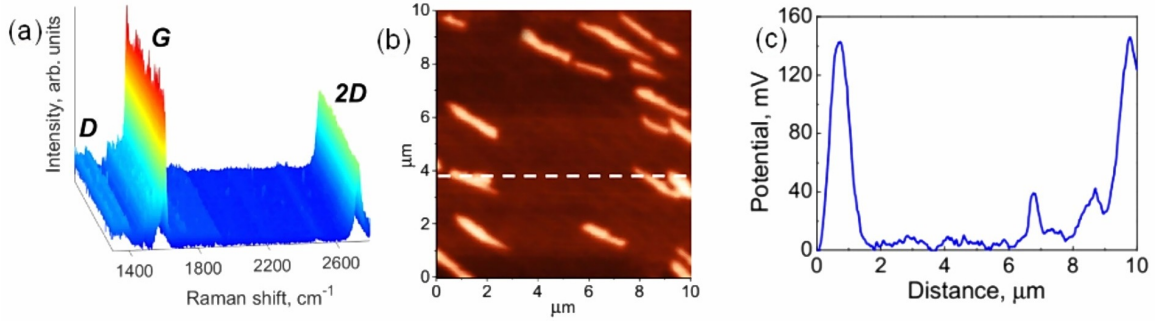


FIG. 1. Array of Raman spectra for a sample grown on the Si face of 6H-SiC (a). Surface potential distribution (b) and the corresponding profile (c)

is ~ 140 mV (Fig. 1c). This value corresponds to the surface potential difference between one- and two-layer graphene [4].

In order to reliably determine the thickness of graphene, XPS spectra were measured at four photon energies, which provided different depths of analysis in the range 5–23 Å. The layer thickness was determined by choosing the thicknesses of graphene and the buffer layer that ensured the best match between the calculated and measured intensities of individual components of the C 1s spectra. The results are shown in Fig. 2c, which presents relative intensities for the optimal thicknesses, i.e., 3.3 Å for the buffer layer and 5.5 Å for graphene. This corresponds to 1.0 and 1.6 carbon sp^2 layers for the buffer layer and graphene, respectively. The ARPES data representing the electronic structure of the valence band of the graphene/SiC(0001) system are shown in Fig. 2b. An unsplit Dirac cone indicating that a single-layer graphene coating dominates on the surface is seen at the K point.

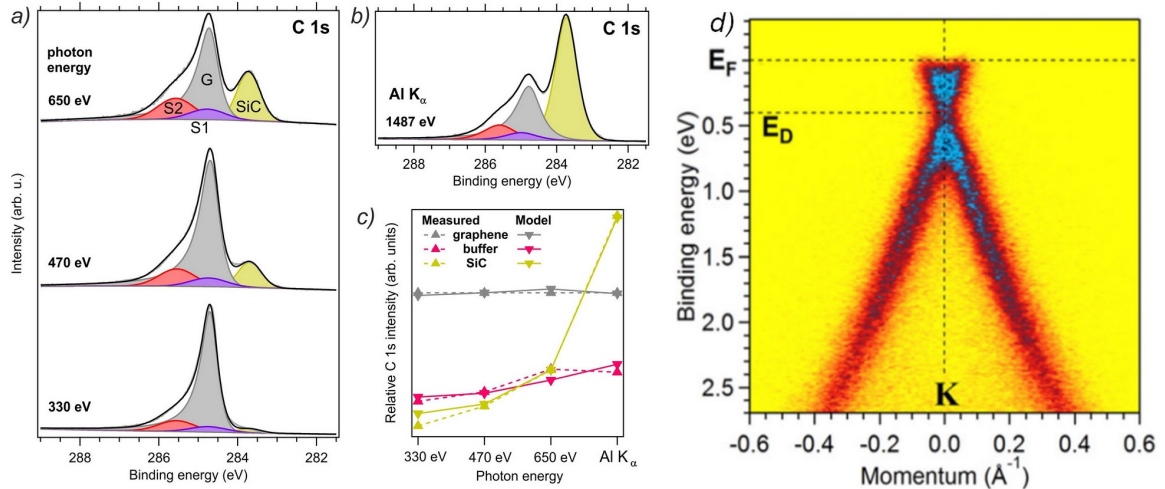


FIG. 2. XPS spectra measured in the C 1s region at various photon energies (a, b). Intensities of individual spectral components, compared with the results of simulation (c). ARPES map of the valence band at the K point of the Brillouin zone ($h\nu = 40.8$ eV) (d)

In order to perform surface sensitivity measurements of graphene films on SiC, a sensor structure with Ohm contacts was fabricated. The sensor topology was provided by photolithography over AZ5214 resist. The reactive ion etching in argon and oxygen plasma was used to remove the graphene layer from uncoated areas. A Ti/Au metallization was used to fabricate Ohm contacts.

To measure the sensitivity of a sensor for gas detected in dry air, gas-mixing and gas-supplying system was used. The operation of the gas sensor was tested with NO_2 present in low concentrations in dry air. The sensor sensitivity r was determined as the relative change of sample resistance in presence of a gas recorded in the gas mixture:

$$r = \frac{R - R_0}{R_0}. \quad (1)$$

Here, R is the resistance of the sensor exposed to the gas mixture, and R_0 is the initial resistance in the absence of the gas to be detected in the incoming air flow.

Figure 3a shows the response of a graphene sensor exposed to a gas mixture containing NO_2 gas at 20 °C. It can be seen that the NO_2 concentration as low as 0.5 ppb is easily detectable.

The working capacity of the biosensor was tested against an immunochemical system constituted by fluorescein and monoclonal antibodies (mAbs) binding this dye. The antibodies were attached to the graphene surface via amino groups formed by a number of electrochemical reactions. The biosensor was placed in a buffer borate solution to which fluorescein molecules were added. The attachment of fluorescein molecules to the antibodies situated on the graphene surface changed the total resistance of the graphene film. It was found that the sensor detects a fluorescein concentration on the order of 1–10 ng/mL (Fig. 3b) and a concentration of conjugate of bovine serum albumin with fluorescein on the order of 1–5 ng/mL (Fig. 3c).

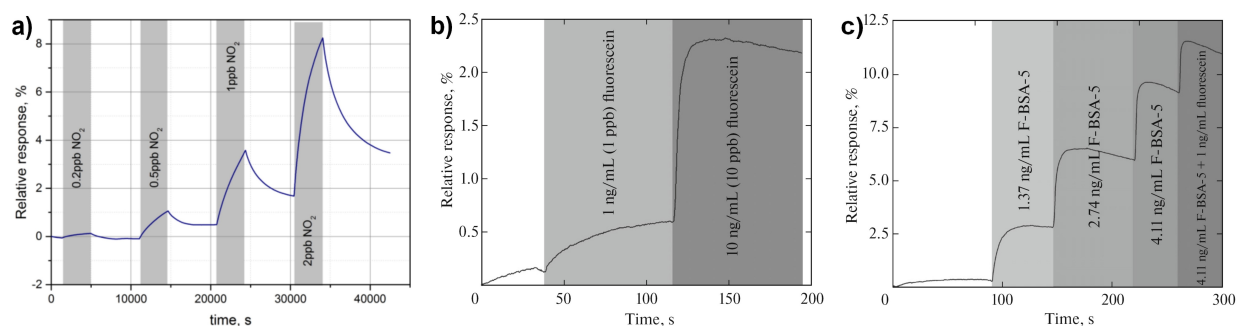


FIG. 3. Response of a graphene sensor exposed to (a) the gas mixture containing NO_2 gas, (b) solutions containing free fluorescein (at indicated concentrations), (c) solutions containing BSA–fluorescein conjugate (F-BSA-5) or a mixture of this conjugate with free fluorescein (at indicated concentration)

4. Conclusion

Graphene films grown by thermal decomposition of SiC under argon and the application of these films as a gas or a biosensor were studied. It was found that this technology allows the synthesis of high-quality monolayer graphene films with a small fraction of bilayer graphene inclusions. Tests of gas sensors and biosensors based on SiC-supported graphene films showed an extremely high sensitivity to detectable substances. These results demonstrate that the graphene growth technology on SiC is promising for development of next-generation sensors.

Acknowledgements

Lebedev S. P. expresses gratitude for the support of the scholarship of the President of the Russian Federation for young scientists and PhD students (Order No. 1684 of December 30, 2016). The authors acknowledge Helmholtz Zentrum Berlin für Materialien und Energie for support under the bilateral Russian-German Laboratory program. D.Yu.U. acknowledges Russian Foundation for Basic Research (Grant No. 17-02-00427) and Saint-Petersburg State University for a research grant No. 11.65.42.2017.

References

- [1] Novoselov K.S., Fa-lko V.I., Colombo L., Gellert P.R., Schwab M.G., Kim K. A roadmap for graphene. *Nature*, 2012, **490**(7419), P. 192–200.
- [2] Yazdi R., Yakimov T., Yakimova R. Epitaxial Graphene on SiC: A Review of Growth and Characterization. *Crystals*, 2016, **6**(5), P. 53–97.
- [3] Ferrari A.C., Basko D.M. Raman spectroscopy as a versatile tool for studying the properties of graphene. *Nature Nanotech.*, 2013, **8**(4), P. 235–246.
- [4] Panchal V., Pearce R., Yakimova R., Tzalenchuk A., Kazakova O. Standardization of surface potential measurements of graphene domains. *Sci. Rep.*, 2013, **3**, P. 2597–2604.

Electrical properties of thermally reduced graphene oxide

G. S. Bocharov¹, A. V. Eletskaa¹, V. P. Mel'nikov²

¹National Research University MPEI, Moscow, Russia

²N. N. Semenov Institute of Chemical Physics, Russian Academy of Sciences, Moscow, Russia
Eletskaa@mail.ru

PACS 68.43.Mn, 68.43.Nr

DOI 10.17586/2220-8054-2018-9-1-98-101

Graphene oxide produced by the standard Hammers method was annealed at various temperatures. The measurements indicate a monotone enhancement of the electric conductivity of the annealed graphene oxide samples with the increase of the annealing temperature. The most prominent jump in the conductivity (about five orders of magnitude) occurs between 150 and 180 °C. At the annealing temperature of 800 °C, the conductivity of reduced graphene oxide reaches the values typical for highly oriented pyrolytic graphite. The measurements demonstrate a non-linear character of conduction of reduced graphene oxide (RGO) samples, which manifests itself in a sensitivity of the sample conductivity to the magnitude of the applied voltage. This phenomenon is explained in terms of the percolation conduction mechanism of the RGO samples, in accordance with which the charge transport is provided by a limited number of percolation paths formed by contacting RGO fragments. A model simulation performed on the basis of the percolation mechanism of RGO conduction agrees qualitatively with the experimental data obtained.

Keywords: graphene oxide, thermal reduction, non-linear conduction.

Received: 1 June 2017

Revised: 2 October 2017

1. Introduction

Realization of a great potential of graphene in practical applications requires the development of effective methods for production of this material in macroscopic quantities. One of the most promising ways to solve this problem is based on the procedure of graphene oxide (GO) reduction. Among various approaches to the realization of such a procedure, the thermal reduction of GO seems to be of the most interest in terms of the practical use [1–4]. This approach is characterized by a relative simplicity in realization and does not require the use of harmful or dangerous chemical compounds. For the development and optimization of this method, it is necessary to understand the nature of physical and chemical processes occurring during the thermal treatment of GO. This problem was stated by many authors, who used various experimental methods. For example, Hall measurements were used in Ref. [5] for determination of the character of conduction in samples of GO reduced at various temperatures. X-ray diffraction analysis has also been used for studying the dynamics of the thermal reduction of GO [3, 4]. Combining approaches such as differential scanning calorimetry, thermal gravimetric analysis and X-ray photoelectron spectroscopy, has permitted the determination of thermodynamic characteristics for the thermal reduction of GO and the main composition of the released gases [2]. The composition of gases evolved during the annealing of GO was also studied by the authors of [6], who used mass-spectrometry and IR spectrometry measurements for this purpose. In distinction of the above-cited papers, in the present work, the electrical properties of partially reduced GO are used as the main indicator of the degree of reduction.

2. Experiment

Graphene oxide, produced by the standard Hummers method [7], was used as the starting material. The paper-like sheets of graphene oxide 40–60 μm thick were about 1.2 g/cm^3 in density, which is about two-fold lower than that of crystalline graphite (2.25 g/cm^3). The sheets were cut into rectangular fragments of 10–15 mm in width and 15–25 mm in length and were studied with the results being presented below.

The thermal treatment of graphene oxide samples was performed in a high temperature furnace planar GROW-2S (PlanarTech). The thermal treatment of samples was performed at a slow flow of Ar (50 cm^3/min sccm) at a pressure of 1 Torr. Heating the samples at a rate higher than 1 °C/s promotes an explosion-like destruction of the material. For this reason the furnace was heated from room temperature up to 200 °C at a rate of 1 °C/min while the rate of the subsequent heating up to the treatment temperature was about 20 °C/min. The duration of the thermal treatment was 10 min for all temperatures.

The density of samples was measured by the use of the balance Sartorius QUINTIX124. Therewith the sizes of samples were measured by means of a micrometer. The measurements show a spread of 20 % of the sample thicknesses. Since this parameter is used for the determination of the conductivity of samples, this non-homogeneity is the main source of measurement error.

The electric characteristics of partially reduced GO (RGO) samples were measured by means of a standard apparatus. A sample was clamped between contacts of the measurement device by means of copper foil crampons providing a homogeneous flow of the electrical current through all the film. X-ray photoelectron (XPS) and Auger spectra of initial samples and those experienced to the thermal treatment were measured by the use of the spectrometer PHI 5500 ESCA (Physical Electronics). The photo emission was initiated by MgK_{α} radiation with the energy of quantum of 1253.6 eV and 350 W in the power. The analysis area was 1.1 mm in diameter. The spectra $C1s$ and $O1s$ were measured at the analyzer transmission energy of 11.75 eV and the density of data collection of 0.1 eV/step, for the spectra $C\ KLL$ these quantities were equal to 93.9 eV and 0.8 eV/step, correspondingly.

3. Experimental results

Figure 1 presents the measured dependence of the conductivity on the treatment temperature. As is evident from the figure, the most prominent change in the conductivity of the samples occurs within the temperature interval between 150 and 200 °C, where the conductivity changes by about five orders of magnitude – from 10^{-3} up to 100 S/m. The maximum value of conductivity (~ 3500 S/m) reached at the temperature of 800 °C is about one order of magnitude lower than the reference value of the conductivity of graphite. However taking into account that the density of RGO treated at a temperature of 800 °C is about 0.5 g/cm^3 (see Fig. 2) which is about 4.5 times as low as the density of crystalline graphite, one obtains that the conductivity of the material accounted for one graphene layer is only two times lower than that for graphite. Fig. 2 presents the dependence of the sample density on the thermal treatment temperature. As it is seen heating the samples to 800 °C results in a decrease of their density by about 2.4 times – from 1.2 to 0.5 g/cm^3 .

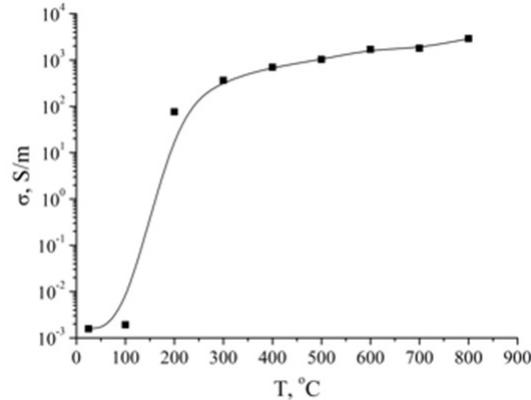


FIG. 1. The conductivity of samples RGO vs thermal treatment temperature

The quantitative data on the content of oxygen and other elements in the samples RGO subjected to the thermal treatment at various temperatures have been obtained as a result of the analysis of XPS spectra. Such an analysis was performed using the standard approach described in particular in [8, 9]. This allowed one to determine the dynamics of changing of the chemical composition of the material depending on the treatment temperature. These data are given in Table 1.

Figure 3 presents typical current–voltage characteristics of RGO samples annealed at various temperatures. The conductivity of RGO increases at higher annealing temperatures. Fig. 4 presents the dependences of the conductivity of RGO samples annealed at various temperatures on the applied voltage. The degree of non-linearity of RGO conductivity can be characterized by the parameter k defined through the relation $\sigma = \sigma_0[1+k(U-U_0)/U_0]$ where σ is the conductivity of a sample at applied voltage U_0 . Fig. 5 (points) presents parameter k as a function of the annealing temperature. This dependence simulated on the basis of the percolation model of the conductivity is also shown in Fig. 5 by the solid line. The reason of dependence of the degree of sensitivity of the conductivity to the applied voltage is in the dependence of the contact resistance on the applied voltage.

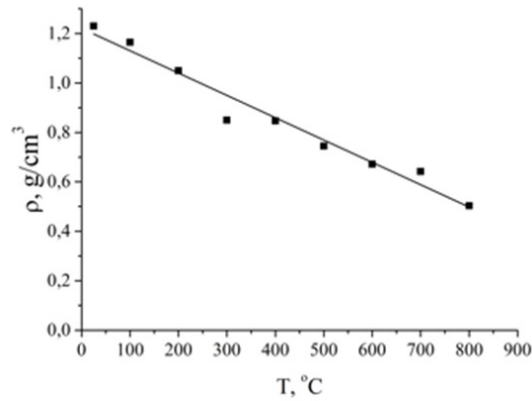


FIG. 2. Dependence of the density of samples RGO on the thermal treatment temperature

TABLE 1. Chemical composition of the initial sample and the samples experienced to the thermal processing at various temperatures as determined on the basis of XPS spectra

Temperature annealing, °C	C, at%	O, at%	N, at%	S, at%	Si, at%
25	74.7	23.0	1.3	0.5	0.4
150	73.6	25.1	0.7	0.5	–
200	82.0	15.2	1.6	0.5	0.7
600	90.6	8.1	0.5	–	0.7

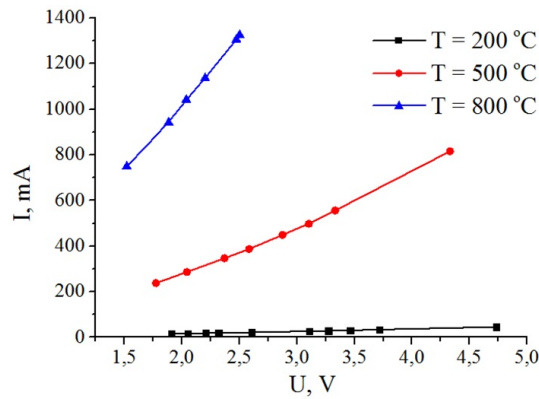


FIG. 3. Current-voltage characteristics of GO samples annealed at various temperatures

4. Conclusion

Thermal treatment results in a reduction of GO, which is indicated by a rise of the conductivity. The most abrupt rise is observed at the annealing temperature of between 150 and 180 °C when the conductivity increases by about 5 orders of magnitude. At the annealing temperature of 800 °C the conductivity reaches about 3500 S/m, which corresponds to that of crystalline graphite (with taking into account the loss in the density of samples). Experiments imply a non-linear conduction of RGO samples, so that the conductivity increases with the applied voltage. This feature is explained qualitatively within the framework of the percolation model of conduction. The non-linear electrical behavior of the samples is caused by a dependence of the contact resistance on the applied voltage.

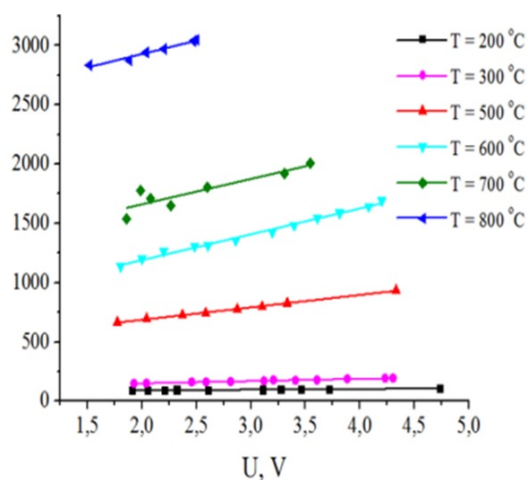


FIG. 4. Dependences of the conductivity of RGO samples annealed at various temperatures on the applied voltage

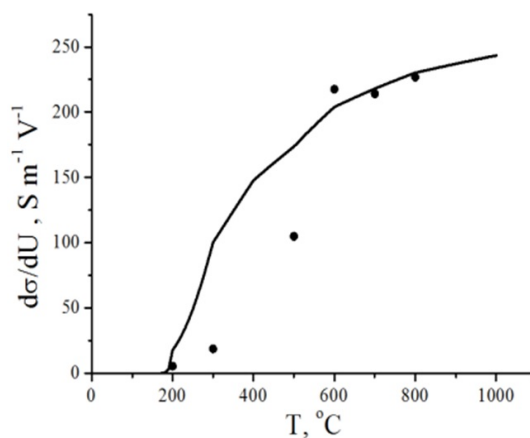


FIG. 5. Dependence of the degree of non-linearity of the RGO conductivity on the annealing temperature: points – experiment; line – model simulation

Acknowledgements

The work has been supported by the Russian Science Foundation within the frame of the Grant No. 16-19-10027.

References

- [1] Titelman G.I., Gelman V., Bron S., Khalfin R.L., Cohen Y., Bianco-Peled H. Characteristics and microstructure of aqueous colloidal dispersions of graphite oxide. *Carbon*, 2005, **43**, P. 641–649.
- [2] Yin K., Li H., Xia Y., Bi H., Sun J., Liu Z., Sun L. Thermodynamic and Kinetic Analysis of Low temperature Thermal Reduction of Graphene Oxide. *Nano-Micro Lett.*, 2011, **3**(1), P. 51–55.
- [3] Jeong H.K., Lee, Y.P., Jin M.H., Kim E.S., Bae J.J., Lee Y.H. Thermal stability of graphite oxide. *Chem. Phys. Lett.*, 2009, **470**, P. 255–258.
- [4] Huh S.H. Thermal Reduction of Graphene Oxide. In: *Physics and Applications of Graphene- Experiments*, 2011. URL: <https://www.intechopen.com/books/physics-and-applications-of-graphene-experiments/thermal-reduction-of-graphene-oxide>.
- [5] Tu N.D.K., Choi J., Park C.R., Kim H. Remarkable Conversion Between n- and p-Type Reduced Graphene Oxide on Varying the Thermal Annealing Temperature. *Chem. Mater.*, 2015, **27**(21), P. 7362–7369.
- [6] Shulga Y.M., Martynenko V.M., Muradyan V.E., Baskakov S.A., Smirnov V.A., Gutsev G.L. Gaseous products of thermo- and photo-reduction of graphite oxide. *Chem. Phys. Lett.*, 2010, **498**, P. 287–291.
- [7] Hummers W.S., Offeman R.E. Preparation of Graphitic Oxide. *J. Am. Chem. Soc.*, 1958, **80**, P. 1339.
- [8] Gelius U., Heden P.F., Hedman J., Lindberg B.J., Marine R., Nordberg R., Nordling C., Siegbahn K. Molecular Spectroscopy by Means of ESCA. III. Carbon compounds. *Physica Scripta*, 1970, **2**, P. 70–80.
- [9] Kundu S., Wang Y., Xia W., Muhler M. Thermal Stability and Reducibility of Oxygen-Containing Functional Groups on Multiwalled Carbon Nanotube Surfaces: A Quantitative High-Resolution XPS and TPD/TPR Study. *J. Phys. Chem. C*, 2008, **112**, P. 16869–16878.

Composite materials using fluorinated graphene nanoplatelets

A. N. Blokhin^{1,*}, T. P. Dyachkova¹, A. K. Sukhorukov¹, D. E. Kobzev¹,
E. V. Galunin¹, A. V. Maksimkin¹, A. S. Mostovoy¹, A. P. Kharitonov²

¹Tambov State Technical University, Tambov, Russia

²Branch of the Talrose Institute for Energy Problems of Chemical Physics,
Russian Academy of Sciences, Chernogolovka, Moscow Region, Russia

*cha-cha@rambler.ru

PACS 82.35.NP

DOI 10.17586/2220-8054-2018-9-1-102-105

The changes occurring on the surface of graphene nanoplatelets (GNPs) during treatment with gaseous fluorine are shown. According to Raman and IR spectroscopy, C–F covalent bonds are formed. As the fluorination temperature increases, the destructive changes in the GNPs become more noticeable, as evidenced by the results of X-ray diffraction analysis and the specific surface area of the samples. The presence of fluorine-containing functional groups contributes to better dispersion of the GNPs in the epoxy matrix and to an increase in their strengthening effect. The epoxy composite containing 0.1 wt% of the GNPs treated with fluorine at 450 °C presents the maximum strength characteristics: in comparison with the unmodified material, the tensile stress increases by more than 2 times, the tensile modulus – by 20 %, the breaking stress at bending – by 80 %, and the modulus of elasticity at bending – by 60 %.

Keywords: grapheme nanoplatelets, fluorination, epoxycomposites, strength properties, reinforcement.

Received: 19 June 2017

1. Introduction

Graphene nanoplatelets (GNP) are layered structures based on graphene planes and, due to their properties, they can act as ideal filler for polymer composites.

In particular, in [1], it was shown that when injected into epoxy resins at a concentration of 5 wt%, GNPs promote an increase in the electrical conductivity by an order of magnitude and exhibition of pronounced hydrophobic properties; however, due to poor interaction with the matrix, they practically do not affect the mechanical parameters.

To improve the GNP interaction, various functionalization methods can be used [2]. By analogy with carbon nanotubes [3], it should be expected that the fluorination of GNPs must lead to an increase in their reinforcing effect when employed as a component of epoxy composites.

The purpose of the present research was to study 1) the effect of the conditions of direct fluorination of GNPs on the chemical composition of their surface, 2) the integrity of graphene layers, 3) and the effectiveness of their application for strengthening epoxy binders.

2. Experimental

The GNPs (produced at NanoTechCenter Ltd., Tambov, Russia) with an average thickness of individual structural units of about 5 nm was used herein. They were fluorinated in a steel reactor at a pressure of gaseous fluorine of 1 atm at temperatures of 350–450 °C. For the production of composites, a BFE-170 Bisphenol-F epoxy resin (Chang Chun Plastics Co., LTD, China) and an L-19 polyaminoamide hardener (CHIMEX Limited, Russia) were used.

Infrared (IR) spectra of the samples of the initial and fluorinated GNPs were recorded on a Nicolet 380 spectrometer. Roentgen photoelectron spectra were recorded on a ULVAC-PHI Versa Probe I device. Monochromatic Alk α -radiation (1486.6 eV) with a power of 50 W was used to excite photoemission. The powders were pressed into the In plate with a thin continuous layer. The diameter of the analysis area was 200 μ m. X-ray diffraction patterns of the initial and fluorinated GNP were recorded on a Difrey-401 instrument with Bragg-Brentano focusing method. The specific surface area was measured by nitrogen adsorption at 77 K using the multipoint BET method on a Nova 1200e Quantachrome instrument. TEM images are obtained with a JOEL JEM 2000 FX microscope.

Effective sizes of GNP agglomerates in epoxy dispersions were determined by the dynamic light scattering method using a Nicomp 380 ZLS instrument.

The mechanical properties of the epoxy-based nanocomposites were tested on a Testometric M350-5AT universal test machine. Surface images of the composites were obtained on a JEOL JSM-6610LV scanning electron microscope.

3. Results and discussion

As seen from the IR spectra of the fluorinated GNPs, the intensity of the absorption bands due to the presence of hydroxyl groups and/or adsorbed moisture (about 3400 cm^{-1}) and carboxyl groups (about 1630 cm^{-1}) decreases, indicating the removal of oxide formations present on the surface of the initial GNPs. The presence of a band at 1200 cm^{-1} indicates the formation of covalent bonds between the fluorine and carbon atoms.

The typical panoramic and C1s XPS spectra of the fluorinated GNP are shown in Fig. 1. The expanded spectra of photoelectronic lines have a shape characteristic of graphene-like structures: an asymmetric narrow peak at 284.4 eV, and a π satellite at 291.0 eV. Low-intensity peaks from the oxygen bonds at 286.6 eV (3.0 %) and 288.5 eV (1.5 %) (single and double, respectively) and sulfur bond at 229.2 and 162.3 eV can also be observed. This is due to the presence of oxygen- and sulfur-containing functional groups formed during the production of the initial GNPs.

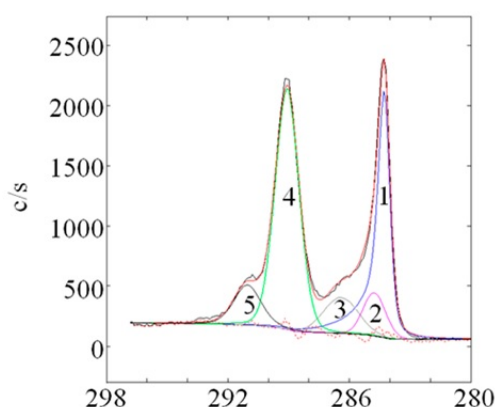


FIG. 1. Expanded XPS spectra for carbon photoelectronic lines of the GNPs subjected to direct fluorination at 350 °C

In the course of the fluorination, the total amount of oxygen and sulfur in the materials decreases down to the complete removal of the sulfur-containing surface formations at 400 and 450 °C. The peaks at 284.8–285.2, 286.4–287.7, 289.1–289.2 and 291.1–291.3 eV are associated with the formation of C–F chemical bonds [4]. The preferred coordination of the carbon atoms is as follows: one bond with fluorine, and the remaining bonds with the carbon atoms also associated with fluorine. There is also a small fraction of the carbon atoms having two bonds with fluorine. About 30 % of the carbon atoms in the fluorinated samples at 350 and 450 °C and 45 % in the fluorinated sample at 400 °C were found not to change their initial chemical state.

No significant destructive changes in the structure of GNPs can be detected on the TEM image (Fig. 2) due to fluorination. The particles of amorphous carbon are probably visualized as black dots on the surface. According to the X-ray diffraction analysis data, the fluorination promotes disordering of the regular hexagonal structure of graphite planes and the appearance of amorphous halo due to the higher temperature of the nanographene treatment with fluorine. The specific surface area of the GNPs during the fluorination increases by 2.47-fold, which may also be due to the availability of the amorphous phase on the GNP surface.

The average effective size of the agglomerates of the initial GNPs in the epoxy binder is about 1.2 μm . The GNP fluorination promotes their more uniform distribution in the matrix; the effective particle size of the dispersed phase does not exceed 900 nm.

The changes occurring with the surface of the GNPs during the fluorination contribute to an increase in their effectiveness as a strengthening additive to the epoxy composites (Table 1).

In comparison with the initial matrix, the greatest effect is achieved when using the GNPs fluorinated (f-GNPs) at 450 °C (0.1 wt%): the tensile stress ($G_{tensile}$) increases by more than 2 times, the tensile modulus ($E_{tensile}$) – by 20 %, the breaking stress at bending ($G_{bending}$) – by 80 %, and the modulus of elasticity at bending ($E_{bending}$) – by 60 %. The obtained increase in the strength is superior to that reported in the published data in the case of using the initial and functionalized graphene structures [5–7].

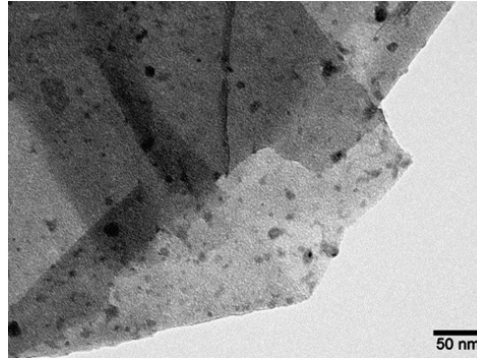


FIG. 2. TEM image of the fluorinated GNPs

TABLE 1. Results of strength tests of the BFE-170 Bisphenol-F resin-based composites

Filler and mass fraction thereof	$G_{tensile}$, MPa	$E_{tensile}$, MPa	ε , %	$G_{bending}$, MPa	$E_{bending}$, MPa
–	38 ± 1.8	2204 ± 88	2 ± 0.10	107 ± 5.5	1683 ± 68
Initial GNPs, 0.01 %	56 ± 2.8	2260 ± 91	2.5 ± 0.10	124 ± 6.0	1850 ± 74
Initial GNPs, 0.1 %	62 ± 3.1	2480 ± 99	3.5 ± 0.15	131 ± 6.2	2189 ± 88
Initial GNPs, 0.5 %	46 ± 2.3	2678 ± 105	2.5 ± 0.10	120 ± 6.0	2581 ± 100
f-GNPs 350 °C, 0.01 %	65 ± 3.2	2281 ± 91	4.2 ± 0.17	136 ± 6.5	2010 ± 80
f-GNPs 350 °C, 0.1 %	71 ± 3.5	2305 ± 92	5 ± 0.20	170 ± 8.0	2639 ± 105
f-GNPs 350 °C, 0.5 %	58 ± 2.8	2937 ± 115	2.7 ± 0.11	124 ± 6.0	2660 ± 105
f-GNPs 340 °C, 0.01 %	69 ± 3.4	2384 ± 95	3.5 ± 0.15	142 ± 6.9	2210 ± 88
f-GNPs 450 °C, 0.1 %	84 ± 3.8	2592 ± 104	5 ± 0.20	192 ± 7.5	2699 ± 107
f-GNPs 450 °C, 0.5 %	63 ± 3.1	2791 ± 110	3.5 ± 0.15	146 ± 7.1	2766 ± 110

The rupture surfaces of all the composites (Fig. 3) have a structure similar to each other, independent of the presence or absence of the initial and fluorinated GNPs. The GNPs were not detected on the rupture surface of the filled nanocomposites, which can be explained by their fairly good adhesion to the epoxy matrix.

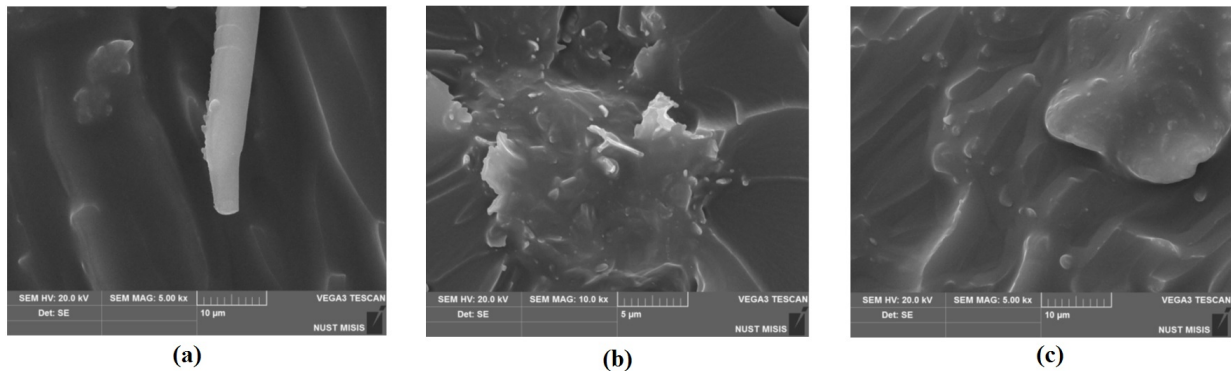


FIG. 3. SEM images of the epoxy matrix surfaces: (a) unmodified, and modified with (b) the initial and fluorinated (c) GNPs

4. Conclusion

GNPs are an effective filler of epoxy matrices that contribute to the improvement of their physical and mechanical properties. GNP treatment with gaseous fluorine results in the formation of fluorine-containing surface functional groups that enhance interaction with the epoxy matrix and contribute to more uniform dispersion therein.

However, when choosing a fluorination mode, it is necessary to take into account destructive changes taking place in the GNPs. Due to the fluorination, a higher strengthening effect, surpassing the literature data, has been achieved.

Acknowledgements

The research has been supported by the Russian Science Foundation grant 15-13-10038.

References

- [1] Prilongo S.G., Moriche R., Jiménez-Suárez A., Sánchez M., Ureña A. Advantages and dis-advantages of the addition of graphene nanoplatelets to epoxy resins. *Eur. Polymer J.*, 2014, **61**, P. 206–214.
- [2] Punetha V.D., Rana S., Yoo H.J., Chaurasia A., McLeskey J.T., Ramasamy M.S., Sahoo N.G., Cho J.W. Functionalization of carbon nanomaterials for advanced polymer nanocompo-sites: A comparison study between CNT and graphene. *Progr. Polymer Sci.*, 2017, **67**, P. 1–47.
- [3] Kharitonov A.P., Simbirtseva G.V., Tkachev A.G., Blohin A.N., Dyachkova T.P., Maksim-kin A.A., Chukov D.I. Reinforcement of epoxy resin composites with fluorinated carbon nano-tubes. *Comp. Sci. Technol.*, 2015, **107**, P. 162–168.
- [4] Beamson G., Briggs D. High Resolution XPS of Organic Polymers. *J. Chem. Educ.*, 1993, **70**(1), P. A25.
- [5] Hadden C.M., Klimek-McDonald D.R., Pineda E.J., King J.A., Reichenadter A.M., Miskioglu I., Gowtham S., Odegard G.M. Mechanical Properties of Graphene Nanoplatelet, Carbon Fiber, Epoxy Hybrid Composites: Multiscale Modeling and Experiments. *Carbon*, 2015, **95**, P. 100–112.
- [6] Ming-Yuan Shen, Tung-Yu Chang, Tsung-Han Hsieh, Yi-Luen Li, Chin-Lung Ciang, Hsiharng Yang, Ming-Chuen Yip. Mechanical Properties and Tensile Fatigue of Graphene Nanoplatelets Reinforced Polymer Nanocomposites. *J. Nanomater.*, 2013. URL: <http://downloads.hindawi.com/journals/jnm/2013/565401.pdf>.
- [7] Minoo Naebe, Jing Wang, Abbas Amini, Hamid Khayyam, Nishar Hameed, Lu Hua Li, Ying Chen, Bronwyn Fox. Mechanical Property and Structure of Covalent Functionalised Graphene, Epoxy Nanocomposites. *Sci. Reports*, 2014. URL: <http://www.nature.com/articles/srep04375.pdf>.

Catalytic pyrene and pyrene butyric acid condensation as a means of producing graphene

O. A. Shinkarenko^{1,2}, M. V. Pozharov³, A. S. Kolesnikova², A. S. Chumakov^{1,2},
A. J. K. Al-Alwani⁴, O. Yu. Tsevtkova², E. G. Glukhovskoy^{1,2}

¹Department of Nano- and Biomedical Technologies, Saratov State University, Saratov, Russia

²Education and Research Institute of Nanostructures and Biosystems,
Saratov State University, Saratov, Russia

³Institute of Chemistry, Saratov State University, Saratov, Russia

⁴Babylon University, Babylon, Iraq

oksana.sh63@mail.ru, dm89@yandex.ru, kolesnikova.88@mail.ru, lehahares@rambler.ru,
ammarhamlet2013@yahoo.com, olgatsvetkova77@gmail.com, glukhovskoy@gmail.com

PACS 68.65.Pq, 68.47.Pe

DOI 10.17586/2220-8054-2018-9-1-106-109

In the present study, we have conducted molecular modeling of a potential method of graphene sheet formation. As the nano-sized blocks from which graphene can be synthesized, pyrene and pyrene butyric acid are chosen. The potential of several compounds (namely, Pt, Pd, Ni, AlCl₃ and PdCl₄) as catalysts for hydrocarbon condensation has been estimated by semiempirical calculations. The heat of formation in the series Pt, Pd, Ni, PdCl₄, AlCl₃ for pyrene is reduced to a minimum and reaches a value of 99 kJ/mol, and for pyrene butyric acid in the series Pt, Ni, Pd, PdCl₄, AlCl₃ decreases to 295 kJ/mol. According to the results of calculations, Pt and Ni can be the most effective catalysts for this reaction. As a substrate (or 2D nanoscale), we propose to use a surface of water or a monolayer of surfactants on water (this method is realized by the Langmuir–Blodgett method) having a 2D crystal structure whose state can be controlled by external conditions.

Keywords: graphene, catalytic condensation, Langmuir–Blodgett method, polycyclic aromatic hydrocarbons, semiempirical computations, 2D nanotemplate.

Received: 20 June 2017

Revised: 31 October 2017

1. Introduction

Graphene is a promising material, as it possesses unique properties, very interesting from the point of view of practical implementations in the form of unique instruments and of nanoelectronics devices. Currently there are a number of areas where graphene could be used [1–3]. But, in spite of a vast array of potential applications, a universal methodology that would allow obtaining high-quality graphene samples of a large area on a production scale has not yet been found. All published methods for obtaining samples have drawbacks and graphene samples can only be used for a specific purpose. Consequently, the development of new methods for the synthesis of graphene is an area of intense interest and relevant topics in its study.

Contemporary methods of monolayer graphene synthesis can be divided into two main groups – “top-down” methods and “bottom-up” methods. The “top-down” methods [4, 5] involve transforming a graphene slab into thinner layers by breaking the bonds between layers of initial sheet and stabilizing the resulting compound structure. This can be achieved by chemical cleavage or mechanical exfoliation of its precursors (graphite, carbon nanotubes, etc.) using Scotch tape, centrifugation, exposure to ultrasound, strong acids, etc.

“Bottom-up” methods involve cross-linking of various molecular fragments to produce large-scale graphene sheets [6, 7]. One of the most common is the method of deposition from the gas phase, which makes it possible to obtain large sheets of graphene, but its main disadvantages are the use of high temperatures and the possibility of contamination of the product obtained. Another example of this approach is the production of graphene from so-called nanografens. As such substances, polycyclic aromatic hydrocarbon molecules are used. These methods are a promising direction in the field of graphene synthesis.

In this study, we propose the next stage in the development of the method that we described in [8, 9]. By analogy with the Shole reaction, we have described a method for producing graphene sheets by crosslinking molecules of polycyclic aromatic hydrocarbons (such as naphthalene, pyrene, pyrene butyric acid). However, in the synthesis methods (like the Shole method), the mutual approach to the required distance and the favorable orientation of the reacting molecules is a critical condition. For these purposes, most often any solid surfaces are used on which synthesis reactions are carried out. Such surfaces (for example, plates of copper, nickel, etc.)

simultaneously serve as an orienting surface and catalyst. As a rule, such reactions require vacuum conditions, the use of plasma as a stimulating action, the supply of particularly pure reagents, etc.

In this article, we develop a previously-proposed approach, according to which the water-air interface or the surface of an ordered monomolecular surfactant layer formed at the water-air interface is used as a 2D nanoscale. Experimentally, this approach can be implemented without high vacuum or high temperatures. All the processes are realized in Langmuir baths with the help of the Langmuir-Blodgett method, which is based on the principles of self-organization of surfactant molecules at interfaces.

In this paper, we assume that the molecules lie on some 2D template and, for simplicity, are located one below the other and lie in the same plane.

2. Materials and methods

In this paper, we studied the effect of various catalysts (Pt, Pd, Ni, PdCl₄ and AlCl₃), chosen as a result of the analysis of scientific information, on the condensation reaction of pyrene and pyrene butyric acid, to select the most promising catalyst for subsequent synthesis using semiempirical calculations. Semiempirical calculations of potential intermediate complexes between catalysts and compound have been performed using PM7 method implemented in MOPAC2012 software.

3. Results and discussions. Quantum chemical computations

Pyrene and pyrene butyric acid, which belong to the class of aromatic hydrocarbons, were chosen as starting materials for the further graphene formation (Fig. 1a,b). They were chosen because of their structural similarity to graphene and interesting physicochemical characteristics – they have low water solubility, are solid under normal conditions. Also, the selected substances are soluble in chloroform, which is an important aspect for further synthesis. Since using the Langmuir–Blodgett technique it is necessary to dissolve the substance in a volatile solvent (e.g., chloroform).

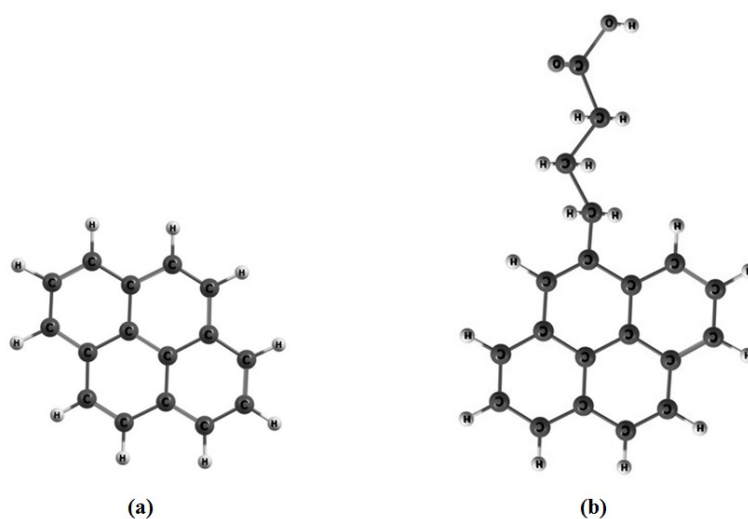


FIG. 1. Molecules: a) pyrene; b) pyrene butyric acid

To form the required structure of graphene from molecules of aromatic hydrocarbons, it is necessary to carry out the dehydrogenation reaction, as a result of which hydrogen atoms located at the edges of the molecules are removed from the molecule. To carry out the dehydrogenation reaction, different catalysts were used in our approach. As a result of the analysis of literature data, the following catalysts were selected for calculations: Pd, Pt, AlCl₃, Ni and PdCl₄. The influence of the nature of catalysts on the state of hydrogen atoms in hydrocarbon molecules was investigated. In the presence of catalysts, the crosslinking in graphene was simulated for a given distance between the molecules. The reaction mechanisms for pyrene and pyrene butyric acid are shown in Figs. 2 and 3.

Simulating the reaction of the interaction of aromatic hydrocarbons and catalysts, the heat of formation of the catalysts, the starting molecule and the intermediate complex formed during the reaction was found. On the basis

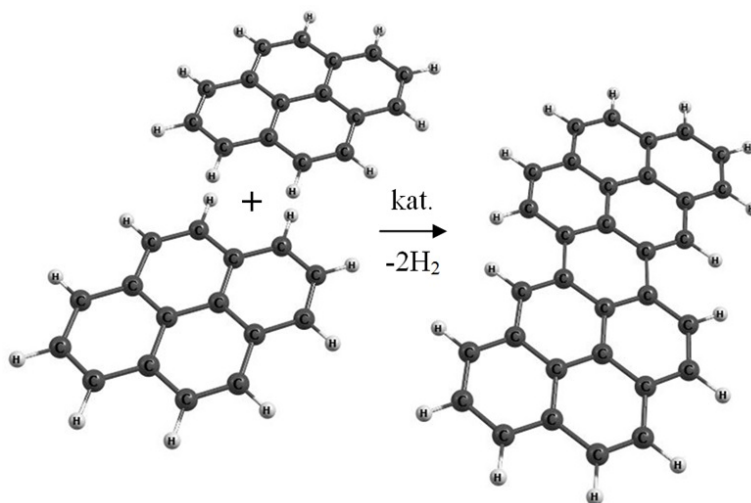
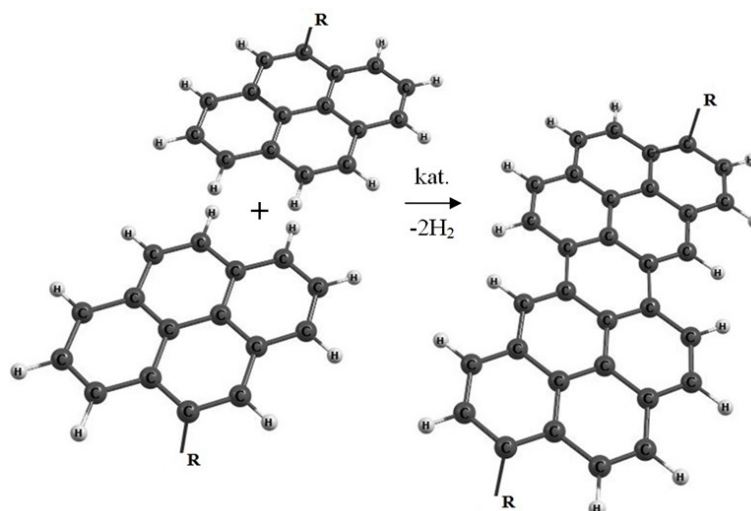


FIG. 2. The mechanism of the condensation reaction for pyrene

FIG. 3. The mechanism of the condensation reaction for pyrene butyric acid, where R is $\text{CH}_2\text{-CH}_2\text{-COOH}$

of these data, the enthalpy of the reaction was calculated by the following formula:

$$\Delta H_r = \Delta H_{f_{comp}} - (\Delta H_{f_{kat}} - \Delta H_{f_{pyrene}}), \quad (1)$$

where ΔH_r – enthalpy of reaction $\Delta H_{f_{comp}}$ – heat of formation of intermediate complex, $\Delta H_{f_{kat}}$ – heat of catalyst formation $\Delta H_{f_{pyrene}}$ – heat of formation of initial compound.

The results of calculations are presented in Table 1.

Thus, according to the results of calculations, the use of platinum and nickel, as the most effective catalysts, can be recommended for the condensation reaction of pyrene or pyrenbutanoic acid. This can be suggested, as the catalyst component system has a higher heat of formation than the other studied catalysts, 1768 kJ/mol and –361 kJ/mol, respectively.

4. Conclusion

The potential of several compounds, including Pt, Pd, Ni, AlCl_3 and PdCl_4 as catalysts for pyrene and pyrene butyric acid condensation has been estimated by semiempirical calculations. According to calculation results, the most efficient catalyst for proposed selected substances condensation is Pt, followed by Ni.

TABLE 1. Calculated enthalpies of studied compounds

	Pyrene		Pyrene butyric acid	
	ΔH_f , kJ/mol	ΔH_r , kJ/mol	ΔH_f , kJ/mol	ΔH_r , kJ/mol
Compound	262	–	233	–
Pt	1660	–	1660	–
Compound-Pt system	416	–1768	115	–2000
Pd	377	–	377	–
Compound-Pd system	333	–568	144	–953
Ni	631	–	631	–
Compound-Ni system	794	–361	–31	–1120
AlCl ₃	–593	–	–593	–
Compound-AlCl ₃ system	–240	–99	–422	–295
PdCl ₄	–83	–	–83	–
Compound-PdCl ₄ system	342	–347	–88	–571

Acknowledgements

This work was supported by grants from the Russian Foundation for Basic Research 16-07-00093 and 16-07-00185.

References

- [1] Mattevi C., Eda G. Evolution of electrical, chemical, and structural properties of transparent and conducting chemically derived graphene thin films. *Adv. Funct. Mater.*, 2009, **19**, P. 1–7.
- [2] Narita A. New advances in nanographene chemistry. *Chem. Soc. Rev.*, 2015, **44**(18), P. 6616–6643.
- [3] Al-Alwani A.J.K., Chumakov A.S., Shinkarenko O.A., Gorbachev I.A., Pozharov M.V., Venig S., Glukhovskoy E.G. Formation and optoelectronic properties of graphene sheets with CdSe/CdS/ZnS quantum dots monolayer formed by Langmuir-Schaefer hybrid method. *Applied Surface Science*, 2017, **424**, P. 222–227.
- [4] Novoselov K.S., Jiang D., Schedin F., Booth T.J., Khotkevich V.V., Morozov S.V., Geim A.K. Two-dimensional atomic crystals. *PNAS*, 2005, **102**(30), P. 10451–10453.
- [5] Hamilton C.E., Lomeda J.R. High-yield organic dispersions of unfunctionalized graphene. *Nano Lett.*, 2009, **9**(10), P. 3460–3462.
- [6] Zhang L. Catalyst-Free Growth of Nanographene Films on Various Substrates. *Nano Res.*, 2011, **4**(3), P. 315–321.
- [7] Rempala P., Kroulík J. Investigation of the Mechanism of the Intramolecular Scholl Reaction of Contiguous Phenylbenzenes. *J. Am. Chem. Soc.*, 2004, **126**, P. 15002–15003.
- [8] Kolesnikova A.S., Safonov R.A., Shinkarenko O.A., Chumakov A.S., Soldatenko E.M., Glukhovskoy E.G. Graphene Synthesis from Naphthalene Molecules on Top of Langmuir Monolayer. *J. Surf. Invest.-X-ray+*, 2017, **11**(3), P. 510–516.
- [9] Shinkarenko O.A., Safonov R.A., Kolesnikova A.S., Al-Alwani Ammar J.K., Pozharov M.V., Glukhovskoy E.G. Naphthalene condensation as a means of producing nanostructured graphene. *Appl. Surf. Sci.*, 2017, **424**, P. 177–173.

Electron overheating during field emission from carbon island films due to phonon bottleneck effect

A. V. Arkhipov, A. M. Zhurkin, O. E. Kvashenkina, V. S. Osipov, P. G. Gabdullin

Peter the Great St. Petersburg Polytechnic University, St. Petersburg, Russia

arkhipov@rphf.spbstu.ru

PACS 79.70.+q; 79.60.Jv; 81.05.uj; 81.07.b

DOI 10.17586/2220-8054-2018-9-1-110-113

The paper discusses a possible model of low-field electron emission that could be applicable to carbon island films on silicon. Such films were recently showed to have emission thresholds as low as 0.4–1.5 V/ μm . Discontinuity of the film – and not the presence of field-enhancing morphological features or low-workfunction spots – seems to be the necessary condition for good emission capability. We suggest a hot-electron emission model with emission center representing a single isolated nanosized island of sp^2 carbon having the properties of a quantum dot. Quantization of its electron energy spectrum determines electron/phonon decoupling (“phonon bottleneck” effect) and long electron relaxation times, which makes emission the dominating option for hot electrons of sufficient energy injected in the island. The consequences of this suggestion are quantitatively considered for typical experimental situation.

Keywords: low-field electron emission, carbon films, quantum dots, electron–phonon interaction, “phonon bottleneck” effect.

Received: 15 June 2017

Revised: 31 October 2017

1. Introduction and problem formulation

In our previous works [1–3], we observed field electron emission with threshold fields as low as 0.4–1.5 V/ μm from island films of graphitic carbon deposited on Si wafers. Comprehensive investigations performed with ~ 50 samples did not reveal the presence of either high-aspect morphological features or low-work-function spots, which excludes employment of many known emission facilitation mechanisms for explanation of the experimental results. Typically, the films with the best emission properties were composed of sp^2 -C islands with lateral size $d \approx 10$ nm and height $h \approx 3$ nm. The films were deposited on oxidized Si wafers, so that some of the islands had ohmic contact with the substrate while others were separated by Schottky barriers. Work function for the islands was measured by different methods which gave similar values $e\phi \approx 4.7$ eV. The difference in work function between the islands and the surrounding open substrate areas did not exceed 1 eV. We have to suggest a model of low-field electron emission relevant to this object.

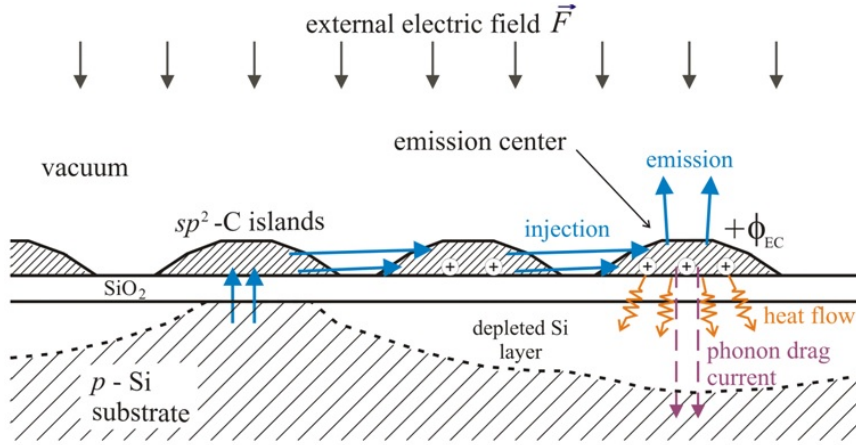
2. Emission model

2.1. General scheme

We propose for consideration the following version of hot-electron emission model (Fig. 1). The emission center (EC) represents one of the carbon islands insulated from the substrate. The island is positively charged, so that its electric potential relative to the substrate ($+\phi_{EC}$) approximately matches the work function value $e\phi$. Hot electrons are injected in the EC from Fermi level of another island that has ohmic contact with the substrate. Electron transfer via a chain of intermediary islands is also possible. Energy of electrons injected in the EC is close to the local vacuum level, which secures high probability of their emission. External field applied to the cathode suffices to remove emitted electrons. This scheme has two obvious weak points.

1) Steady-state maintenance of the EC positive potential and charge needs to be explained. Some, even if a minor, part of injected hot electrons would fail to be emitted and accumulate. They should be removed from the EC’s Fermi level against the action of the EC’s own electric field. One possible solution of this problem we associate with thermoelectric effect, which may have huge magnitude at nanoscale, due to the peculiar character of phonon drag induced by ballistic phonon flow [4]. This issue is left beyond the limits of this paper and has been discussed elsewhere [5].

2) Energy relaxation times for hot electrons injected in the EC must be sufficient to allow their ballistic transport to vacuum boundary and emission. Further discussion addresses this problem.


 FIG. 1. To the mechanism of low-field emission from sp^2 carbon island films

2.2. Hot-electron relaxation slowing

Obstructed energy dissipation processes are a typical feature for many low-dimensional and nanosized objects with discrete energy spectra. Slowing of hot-electron cooling can be determined by the so-called “phonon bottleneck” effect [6, 7]. If spacing between allowed energy levels exceeds the maximum phonon energy (~ 35 meV; given by Debye temperature Θ_D), direct emission of phonons is prohibited, and hot electron relaxation goes via slower processes. Relaxation times as large as $\tau = 0.1\text{--}1$ ns have been observed for semiconductor QDs [8, 9]. This phenomenon attracts substantial interest because of its possible applications in solar batteries, infrared sensors, etc. Experimental information on electron relaxation rates in graphene and graphitic QDs is not so abundant (see, for instance in the review [10]). Though, the corresponding effects are expected to be “especially efficient owing to the unique properties of graphene: fast carrier–carrier scattering dominates over electron–phonon scattering” [10]. Among sp^2 -carbon nanomaterials capable of low-field electron emission [11], evidence of suppressed electron–phonon interaction were reported for NPC [12, 13].

The regarded experimental situation satisfies both main requirements set by the basic theory for realization of the “phonon bottleneck”. Maximum quantization gaps in energy spectra of QD of the given size ($10 \times 10 \times 3$ nm) were estimated as ≈ 200 meV $\gg k_B \Theta_D$ (k_B is Boltzmann constant). The second condition requires hot electron density $\sim 10^{18}$ /cm³ or higher [7]. In an island of the considered dimensions, this requirement would be fulfilled for current (in Amps) of injected hot electrons $I \geq 5 \cdot 10^{-20} / \tau$ – for instance, starting from $I = 1$ nA for relaxation time as low as $\tau = 50$ ps.

The presented argumentation allows us to assume that hot electron relaxation time in the studied island films is much greater than that in bulk materials or continuous films. Consequences of this assumption for the emission process are discussed below. For quantitative estimates, relaxation time value $\tau = 1$ ns (determined in [8] for semiconductor QDs) will be used – because of the absence of experimental information more relevant for the considered object.

2.3. Electron thermalization and emission

Suppression of electron–phonon interaction could make either emission or scattering at other charge carriers the most probable option for hot electrons injected in the EC. In the latter case, hot-electron energy will be distributed among the EC free carriers to increase their temperature T_e above the temperature of the lattice. We can roughly estimate it as:

$$T_e \approx \frac{I \phi_{EC} \tau}{\frac{3}{2} k_B N}, \quad (1)$$

where I is the current of injected hot electrons with excessive energy $e \phi_{EC}$; denominator is the heat capacity of EC electron subsystem expressed via the number of “intrinsic” charge carriers N in the EC. Correct calculation of this number for a given EC requires knowledge of the density-of-states (DOS) function which is discrete and depends on the EC shape, dimensions, surface states’ termination, etc [14]. These data are unavailable. For approximate estimates made for an “average” EC, we will use macroscopic formulae giving a smooth envelope for DOS functions relating to many different ECs [14]. For similar reason, we will use the simplest DOS formula for single-layer graphene, understanding that it is fully correct only near the Dirac point.

In these assumptions, the number of mobile charge carriers may be calculated from the density of conduction electrons in graphene n_e (per area unit):

$$N = \frac{2V \cdot n_e}{b}, \quad (2)$$

where $V \approx hd^2$ is the island's volume, $b \approx 0.335$ nm is interplanar distance in graphite; factor 2 accounts for both holes and electrons.

Density n_e can be obtained by integration of Fermi distribution:

$$n_e = \int_0^{\infty} \frac{\nu(E)dE}{1 + \exp(E/k_B T_e)}, \quad (3)$$

where $\nu(E)$ is energy density of allowed states; $E = 0$ corresponding to Fermi level. Ignoring the fine details of the distribution, we can use the known formula for graphene:

$$\nu(E) = \frac{g_S g_V}{2\pi \hbar^2 v_F^2} |E|. \quad (4)$$

Here, $v_F \approx 10^6$ m/s is Fermi velocity, g_S and g_V are spin and valley degeneracy factors. The modulus signifies equivalent distributions for electrons and holes. Finally, we come to:

$$T_e = \left(\frac{8I\phi_{EC}\tau b \hbar^2 v_F^2}{\pi g_V g_S V k_B^3} \right)^{1/3}. \quad (5)$$

For the previously assumed numeric values and typical emission (injection) current from on EC $I = 1 \mu\text{A}$, the formula gives physically implausible electron temperature $T_e \approx 1.7 \cdot 10^4$ K. At such temperatures, the current of thermionic emission would be $\gg I$. This disagreement could be formally resolved by introduction in (1) of a Nottingham heat term determined by the excess of emitted electrons' mean energy over the local Fermi level. Thus, the model (1) – (5) for injection current $I = 1 \mu\text{A}$ describes emission process as thermionic emission driven by greatly increased electron temperature in the EC. Notably, broad energy distributions of electrons field-emitted by carbon films have been described in literature (for instance, in [15]), they corresponded to effective emitter temperatures as high as $\sim 10^3$ K.

Formula (5) describes very slow dependence of $T_e(I)$ which would be additionally slowed by the account of Nottingham cooling. This can witness of possible relevance of the depicted emission mechanism over a wide range of current values. For yet lower values of injection current electron energy distributions can be expected to deviate from quasi-equilibrium Fermi law. Density of states near Fermi level in graphitic carbon is low; hence electron temperature reduction will result in a rapid decrease of the carrier density. This will slow down thermalization of hot electrons via electron–electron scattering, the effect further enhanced by large difference in effective masses between hot and thermalized carriers. Thus, injected hot electrons emission can have greater probability than thermalization, and electron population would split in two separate groups. In this regime, emitted electrons could have relatively narrow energy distribution near the highest “phonon bottleneck” position.

Acknowledgements

The work was supported by State Assignment for Higher Education Institutions (basic part), project 3.5469.2017.

References

- [1] Arkhipov A.V., Gabdullin P.G., Krel S.I., Mishin M.V., Shakhmin A.L., Gordeev S.K., Korchagina S.B. Field-induced electron emission from graphitic nano-island films at silicon substrates. *Fuller. Nanotub. Car. N.*, 2012, **20**(4-7), P. 468–472.
- [2] Arkhipov A.V., Gabdullin P.G., Gordeev S.K., Zhurkin A.M., Kvashenkina O.E. Photostimulation of conductivity and electronic properties of field-emission nanocarbon coatings on silicon. *Tech. Phys.*, 2017, **62**(1), P. 127–136.
- [3] Andronov A.N., Shkitun P.A., Budylyna E.V., Gabdullin P.G., Gnuchev N.M., Kvashenkina O.E., Arkhipov A.V. Characterization of thin-film carbon field emitters. *Tech. Digest 30-th Int. Vac. Nanoelectr. Conf. (IVNC'2017)*, Regensburg, Germany, 2017, P. 276–277.
- [4] Eydelman E.D., Vul' A.Ya. The strong thermoelectric effect in nanocarbon generated by ballistic phonon drag of electrons. *J. Phys. Condens. Matter*, 2007, **19**(7), P. 266210–266223.
- [5] Arkhipov A.V., Gabdullin P.G., Kvashenkina O.E., Osipov V.S. Nanoscale phonon drag as a part of low-field electron emission mechanism for nanocarbons. *Tech. Digest 30-th Int. Vac. Nanoelectr. Conf. (IVNC'2017)*, Regensburg, Germany, 2017, P. 28–29.
- [6] Inoshita T., Sakaki H. Electron-phonon interaction and the so-called phonon bottleneck effect in semiconductor quantum dots. *Physica B*, 1996, **227**(1-4), P. 373–377.
- [7] Nozik A.J. Spectroscopy and hot electron relaxation dynamics in semiconductor quantum wells and quantum dots. *Annu. Rev. Phys. Chem.*, 2001, **52**, P. 193–231.
- [8] Pandey A., Guyot-Sionnest P. Slow electron cooling in colloidal quantum dots. *Science*, 2008, **322**, P. 929–932.

- [9] Tisdale W.A., Williams K.J., Timp B.A., Norris D.J., Aydil E.S., Zhu X.-Y. Hot-electron transfer from semiconductor nanocrystals. *Science*, 2010, **328**, P. 1543–1547.
- [10] Zhu S., Song Y., Zhao X., Shao J., Zhang J., Yang B. The photoluminescence mechanism in carbon dots (graphene quantum dots, carbon nanodots, and polymer dots): Current state and future perspective. *Nano Res.*, 2015, **8**(2), P. 355–381.
- [11] Arkhipov A., Davydov S., Gabdullin P., Gnuchev N., Kravchik A., Krel S. Field-induced electron emission from nanoporous carbons. *J. Nanomater.*, 2014, P. 190232.
- [12] Popov V.V., Gordeev S.K., Grechinskaya A.V., Danishevskii A.M. Electrical and thermoelectric properties of nanoporous carbon. *Phys. Solid State*, 2002, **44**(4), P. 789–792.
- [13] Veinger A.I., Shanina B.D., Danishevskii A.M., Popov V.V., Gordeev S.K., Grechinskaya A.V. Electrophysical studies of nanoporous carbon materials prepared of silicon carbide powders. *Phys. Solid State*, 2003, **45**(6), P. 1197–1206.
- [14] Abdelsalam H., Espinosa-Ortega T., Luk'yanchuk I. Electronic and magnetic properties of graphite quantum dots. *Low Temp. Phys.*, 2015, **41**(5), P. 508–513.
- [15] Reich K.V., Eidelman E.D., Vul' A.Ya. Determination of temperature difference in carbon nanostructures in field emission. *Tech. Phys.*, 2007, **52**(7), P. 943–946.

An equilibrium study of the liquid-phase sorption of Lead (II) ions on nanoporous carbon materials

A. E. Kucherova, I. V. Burakova, A. E. Burakov,
E. V. Galunin, A. V. Babkin, E. A. Neskromnaya

Tambov State Technical University Tambov, Russia

Anastasia.90k@mail.ru, iris.tamb68@mail.ru, m-alex1983@yandex.ru,
evgeny.galunin@gmail.com, flex.trol@mail.ru, lenok.n1992@mail.ru

PACS 81.05.U, 81.07.De, 89.60.Ec

DOI 10.17586/2220-8054-2018-9-1-114-116

The present paper describes the adsorption of lead (II) ions on conventional and nanoporous materials. Equilibrium studies were performed by implementing the empirical Freundlich and Langmuir isotherm models. It was found that all the isotherms constructed on the basis of experimental results fitted well to those models, thereby indicating the efficiency of the nanoporous materials as adsorbents of heavy metals. The experimental lead (II) maximum adsorption capacity of the materials under study – CNTs “Taunit-M”, highly porous carbon, CNTs “Taunit”, BAU-An activated carbon, and bentonite clay – was found to be 23, 14, 13, 10, and 7 mg·g⁻¹, respectively. Due to the high sorption characteristics and unique physical and chemical properties of these materials, the adsorption technologies developed herein may act as good sustainable options for heavy metal removal from industrial effluents.

Keywords: adsorption, heavy metal ions, lead, isotherm, carbon nanotubes.

Received: 19 June 2017

1. Introduction

Water pollution by heavy metal ions has become a serious environmental issue especially due to their toxicity and tendency for bioaccumulation [1]. Industrial wastewater is considered the main source of lead impurities. Excessive exposure to lead may result in anemia, mental retardation, coma, seizures, and bizarre behavior. Thus, it is necessary to remove this species from wastewater prior to its discharge into the environment. There exist various chemical and physical–chemical methods for the treatment of lead-containing wastewater: chemical precipitation, electrochemical reduction, ion exchange, biosorption, adsorption, among others [2]. Even though there are so many adsorbents available, there is still a need for developing novel materials to more effectively remove metal ions [3]. In this regard, a new type of adsorbent materials has been proposed – nanoporous carbon. It retains a great potential for the removal of a wide range of pollutants such as lead, chromium, nickel, copper, and other ions [4]. Researchers have found that nanoporous carbon materials such as carbon nanotubes (CNTs) have a relatively large surface area, extraordinary surface morphology and good chemical and mechanical properties that provide a good opportunity for the removal of heavy metals [5].

2. Experimental

2.1. Research methods

Experimental studies on the lead (II) adsorption from aqueous solutions were performed with conventional and nanoporous materials (see Sec. 2.2 below). Each series consisted of six 50-mL tubes containing the corresponding adsorbent. 15 mL of 200, 500, 700, 1000 and 2400 mg·L⁻¹ Pb(NO₃)₂ solutions were separately added into those tubes using Pasteur pipettes. Then, the tubes were end-over-end shaken on Bio RS-24 programmable rotators at 100 rpm during the equilibrium time previously found for the adsorbent. After the adsorption process was finished, the solutions were centrifuged using a 5810 R centrifuge at 10,000 rpm for 10 min to separate the phases. Next, the liquid phase was placed into 30-mL tubes with the Pasteur pipettes, preventing ingress of the solid phase and the suspension thereof. Finally, the metal concentrations in the solutions were measured according to the method of quantitative elemental analysis on an MGA-915MD atomic absorption spectrometer.

2.2. Adsorbents

In the present research, the following nanoporous adsorption materials were employed: “Taunit”-series CNTs (Taunit, Taunit-M) produced by JSC “NanoTechCenter” (Tambov, Russia), and highly porous carbon (HPC) also synthesized at JSC “NanoTechCenter” via alkaline activation of a carbon product obtained by heat treatment of a mixture of phenol-formaldehyde resin, carboxymethyl cellulose and graphene nanoplatelets (this procedure may considerably increase the quality of purification of aqueous systems containing heavy metals, in particular, lead).

Besides, the efficiency of the above-mentioned nanomaterials was estimated in comparison with the following conventional adsorbents used as references: BAU-A activated carbon produced by JSC “Sor bent” (Perm, Russia), and bentonite clay (BC) acquired from “Bentonit Company” (Moscow, Russia).

3. Adsorption studies

The adsorption capacity is an important factor since it determines how much of an adsorbent is required for quantitative enrichment of adsorbates from a given solution. In the present research to study lead (II) adsorption on conventional and nanoporous materials, the adsorption equilibrium data were fitted using the Langmuir and Freundlich models, which correspond to homogenous and heterogeneous adsorbent surfaces, respectively.

The Langmuir model assumes that adsorption takes place at uniform energy sites on the adsorbent surface, whereas the Freundlich model is an empirical equation that considers multilayer adsorption due to the diversity of adsorption sites. The linear Langmuir and Freundlich isotherm models can be expressed as given in Eqs. (1) and (2):

$$\frac{C_e}{q_e} = \frac{1}{bq_m} + \frac{C_e}{q_m}, \quad (1)$$

$$\lg q_e = \lg K + \frac{1}{n} \lg C_e, \quad (2)$$

where, C_e ($\text{mg}\cdot\text{L}^{-1}$) is the equilibrium concentration of lead (II) in the solution, q_e ($\text{mg}\cdot\text{g}^{-1}$) is the equilibrium adsorption capacity of the material, q_m ($\text{mg}\cdot\text{g}^{-1}$) is the maximum amount of lead (II) adsorbed per unit mass of the adsorbent required for monolayer coverage of the surface, b ($\text{L}\cdot\text{mg}^{-1}$) is a constant related to the adsorption free energy, K and n are Freundlich constants (K ($\text{L}\cdot\text{g}^{-1}$) represents multilayer adsorption capacity at unit concentration of adsorbate and is a relative measure of adsorption capacity of adsorbents, and n represents adsorption intensity which varies with heterogeneity of the adsorbent surface – when n approaches to zero, the surface site heterogeneity increases; for a favorable adsorption process, n should lie in the range 1–10 [6]).

The adsorption parameters found using the above-mentioned models are presented in Table 1.

TABLE 1. Isotherm constants obtained for the Lead (II) adsorption on the conventional and nanoporous materials

Material	Langmuir constants			Freundlich constants		
	q_m	b	R^2	K	n	R^2
BAU-A	83.33	$5.19\cdot 10^{-5}$	1.000	0.0005	1.048	0.999
BC	10.20	$4.94\cdot 10^{-4}$	0.989	0.017	1.323	0.985
HPC	23.26	$9.06\cdot 10^{-4}$	0.993	0.182	1.736	0.900
Taunit	27.74	$6.66\cdot 10^{-4}$	0.982	0.148	1.678	0.902
Taunit-M	62.50	$3.93\cdot 10^{-4}$	0.988	0.175	1.546	0.905

It was found that for a range of small lead (II) concentrations (200–700 $\text{mg}\cdot\text{L}^{-1}$), it is preferable to implement the Langmuir model. Based on the obtained values of the sorption equilibrium constants of this equation, it can be assumed that the lead ions in lower concentrations interact with active sorption sites located at the surface of the materials under study and are responsible for physical adsorption. The range of high concentrations does not satisfy the boundary conditions for the applicability of the Langmuir model with the monomolecular sorption mechanism, and active sorption within this range can serve as the foundation for an indirect confirmation of the applicability of the Freundlich model. Based on the values of the empirical constants of the Freundlich equation, favorable conditions for chemical adsorption can be assumed. This sorption type is associated with energy heterogeneity of the adsorption sites.

Furthermore, the obtained experimental results demonstrate that the lead (II) sorption capacity increases in the following sequence: BC ($7 \text{ mg}\cdot\text{g}^{-1}$) < BAU-A ($10 \text{ mg}\cdot\text{g}^{-1}$) < Taunit ($13 \text{ mg}\cdot\text{g}^{-1}$) < HPC ($14 \text{ mg}\cdot\text{g}^{-1}$) < Taunit-M ($23 \text{ mg}\cdot\text{g}^{-1}$).

Thus, it can be concluded that the nanoporous carbon materials can make a significant contribution to the adsorption process and can be successfully used to remove heavy metals (in particular, lead) from water and wastewater in contrast to the materials (activated carbons and clays) commonly used in the industry.

Acknowledgements

The research was funded by the Ministry of Education and Science of the Russian Federation (Project No. 16.1384.2017/PCh).

References

- [1] Heidari A., Younesi H., Mehraban Z. Removal of Ni(II), Cd(II), and Pb(II) from a ternary aqueous solution by amino functionalized mesoporous and nano mesoporous silica. *Chem. Engin. J.*, 2009, **153**(1-3), P. 70–79.
- [2] Saeed A., Iqbal M., Akhtar M.W. Removal and recovery of lead(II) from single and multimetal (Cd, Cu, Ni, Zn) solutions by crop milling waste (black gram husk). *J. Hazard. Mater.*, 2005, **117**, P. 65–73.
- [3] Hsieh S.H. Growth of carbon nanotube on micro-sized Al_2O_3 particle and its application to adsorption of metal ions. *J. Mater. Res.*, 2006, **21**, P. 1269–1273.
- [4] Tehrani M.S., Azar P.A., Namin P.E., Dehaghi S.M. Removal of lead ions from aqueous solution using multi-walled carbon nanotubes: The effect of functionalization. *J. Appl. Environ. Biol. Sci.*, 2014, **4**, P. 316–326.
- [5] Yang S., Hu J., Chen C., Shao D., Wang X. Mutual effects of Pb(II) and humic acid adsorption on multiwalled carbon nanotubes/polyacrylamide composites from aqueous solutions. *Environ. Sci. Technol.*, 2011, **45**, P. 3621–3627.
- [6] Ghaedi M., Khafri H.Z., Asfaram A., Goudarzi A. Response surface methodology approach for optimization of adsorption of Janus Green B from aqueous solution onto $\text{ZnO}/\text{Zn}(\text{OH})_2$ -NP-AC: kinetic and isotherm study. *Spectrochim. Acta Mol. Biomol. Spectrosc.*, 2016, **152**, P. 233–240.

Kinetics of the Cu(II) sorption from aqueous solutions by carbon nanomaterialsA. V. Babkin, I. V. Burakova, A. E. Burakov, E. A. Neskoromnaya,
A. E. Kucherova, D. A. Kurnosov

Tambov State Technical University, Tambov, Russia

flex_trol@mail.ru, iris_tamb68@mail.ru, m-alex1983@yandex.ru, lenok.n1992@mail.ru,
anastasia.90k@mail.ru, ozikimoziki@mail.ru**PACS 81.05.U, 81.07.De, 89.60.Ec****DOI 10.17586/2220-8054-2018-9-1-117-119**

The present paper contains comprehensive studies on the adsorption properties of graphene oxide (GO), coconut activated carbon (AC) and “Taunit-M” carbon nanotubes (CNTs). Cu(II) ions served as extracted component. Measurements of the Cu(II) content in water were performed using electrothermal atomization atomic absorption spectroscopy. The obtained experimental data indicate high adsorption capacity of the GO along with CNTs and AC. Kinetic parameters of the adsorption process on the graphene oxide were calculated using standard models (pseudo-first- and pseudo-second-order, external and intraparticle diffusion, and Elovich models). The presented results demonstrate the prospects of using the GO in selective extraction of heavy and rare-earth metal ions from aqueous media.

Keywords: sorption, graphene oxide, kinetic study, copper.*Received: 19 June 2017**Revised: 20 October 2017***1. Introduction**

Along with carbon nanotubes (CNTs) and materials on a similar basis, graphene oxide and its modifications have become widespread. Like any carbon nanomaterial, graphene possesses a number of unique physical and chemical properties, to which its two-dimensional structure and the corresponding thermal, electroconductivity (zero width of the forbidden band) and optical characteristics, as well as high specific surface, can be related. The latter opens great prospects for using graphene oxide (GO) in selective extraction of harmful impurities of different chemical nature from gaseous and aquatic media. CNTs and GO are currently one of the promising materials in the field of extraction of heavy metal ions from aqueous solutions [1].

In the present work, the adsorption of Cu(II) ions from aquatic media using carbon nanostructures such as CNTs and GO, along with conventional materials such coconut activated carbon (AC) was studied.

Table 1 gives comparative results reported elsewhere for the Cu(II) adsorption on both the nanostructured and commercially available adsorbents. From this table, it can be seen that the CNTs exhibit the adsorption characteristics similar to those of the commercial materials, but the adsorption time in their case is reduced by 2- to 3-fold.

TABLE 1. The Cu(II) adsorption on different materials

Adsorbent	Adsorption capacity (mg/g)	C_{init} (mg/L)	Adsorption time (min)
Activated carbon (chemical activation) [2]	7	40	210
Activated carbon [2]	11.5	40	200
Activated carbon from hazelnut husks [3]	6.65	200	60
CNT sheets [4]	6	100	70
CNT sheets (oxidized) [4]	14	100	70
As-produced CNTs [5]	8.92	50	1440

2. Materials

Nanocarbon materials – “Taunit-M” CNTs and GO as nanoplatelet aggregates obtained via thermal oxidation of pyrolytic graphite (both – NanoTechCenter Ltd., Tambov, Russia) – were used as adsorbent samples for testing. The diameter of the CNTs is 15–20 nm, the orientation of graphene layers is cylindrical. The main characteristics of AC (AQUACARB 207C, Chemviron Carbon, UK) used as reference materials are as follows: surface area 1150–1350 m²/g, adsorption capacity regarding methylene blue 230–270 mg/g, and bulk density 0.47–0.51 g/cm³.

3. Research methods

To determine the adsorption kinetic parameters, experiments were carried out with 0.02 g of the CNTs, 0.1 g of the GO, and 1.0 g of the AC. The volume of aqueous solutions was 30 mL at the initial concentration of Cu(NO₃)₂·3H₂O (Laverna Ltd., Moscow, Russia) equal to 100 mg/L. Each solution and each adsorbent were equilibrated by agitating on an end-over-end rotator (Multi Bio RS-24, Biosan, Riga, Latvia) at 120 rpm for 1 h, and then centrifuged on a centrifuge (5810 R, Eppendorf, Hamburg, Germany). The Cu(II) equilibrium concentration was determined by electrothermal atomization atomic absorption spectrometry on an MGA-915MD instrument (Atompribor Ltd., Saint Petersburg, Russia).

4. Result and discussion

To identify characteristic features of the Cu(II) adsorption process, kinetic studies aimed at determining the time required to achieve equilibrium in the systems under study were performed.

As seen in Fig. 1, for the GO, at the initial stage, the adsorption rate is sufficiently high, and about 90 % of the adsorbate is extracted during the first 5–10 min. It can be clearly observed that the Cu(II) maximum adsorption capacity of the GO is superior to that of the other materials studied. To describe kinetic mechanisms of the adsorption, the well-known mathematical models (pseudo-first- and pseudo-second-order, external and intraparticle diffusion, and Elovich models) – were implemented herein (Figs. 2, 3).

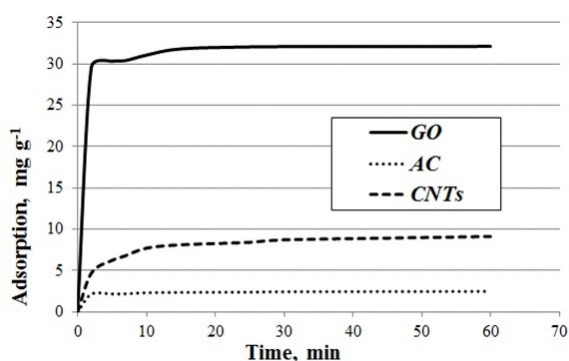


FIG. 1. Kinetic curves constructed for the Cu(II) adsorption on the GO

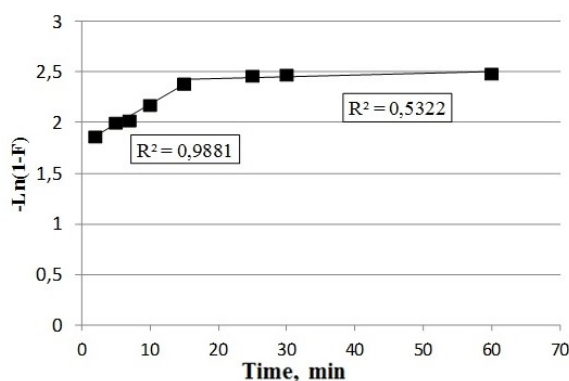


FIG. 2. External diffusion curve constructed for the Cu(II) adsorption on the GO

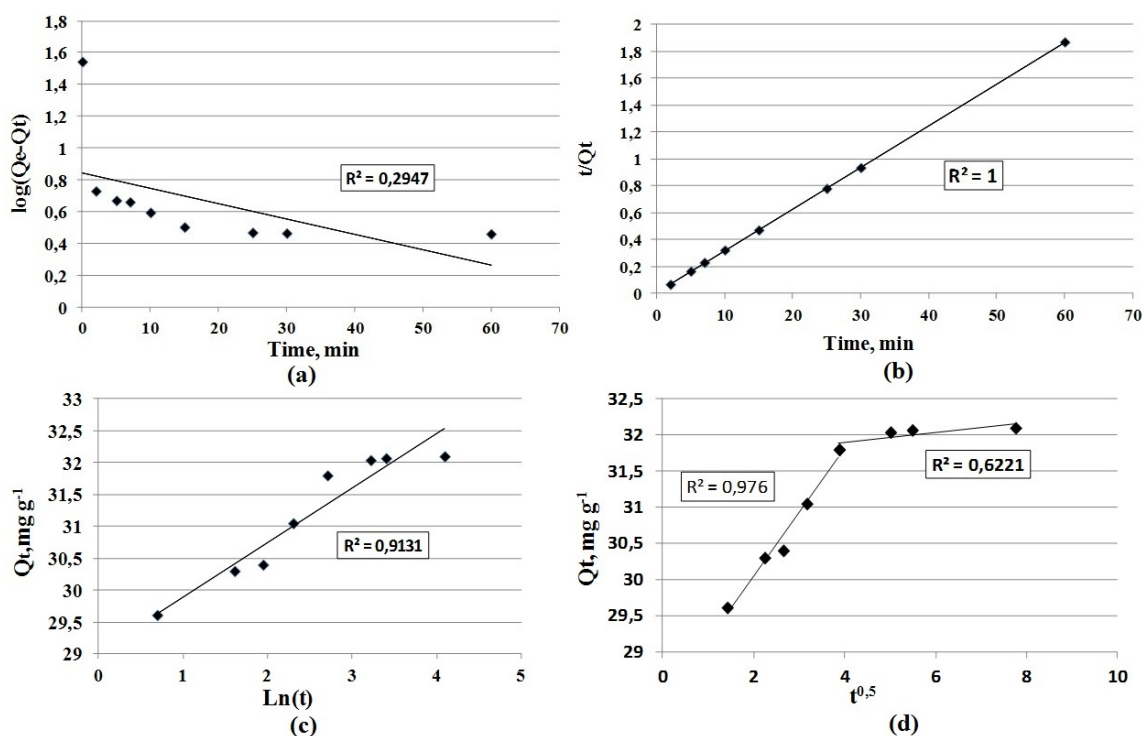


FIG. 3. Kinetic models of the Cu(II) adsorption on the GO – a) pseudo-first order; b) pseudo-second order; c) Elovich model; d) intraparticle diffusion

Figure 2 demonstrate chemical interactions during the adsorption process (F is the fraction attainment at equilibrium, $F = \frac{Q_t}{Q_e}$; Q_e – Cu(II) amount adsorbed onto the adsorbent surface at equilibrium; Q_t – Cu(II) amount adsorbed onto the adsorbent surface at time t) (Fig. 3b). It can be seen that the results of the experimental data are mostly fitted to the pseudo-second-order model, thereby indicating that the rate of chemical bond formation is limited by the interaction of the adsorbate ions with each other. The adsorption process is of the complex nature, and it is affected by both the structure of the adsorption material and the features of its chemical interaction with the extracted component.

5. Conclusion

Within the framework of the present paper, the kinetic mechanisms of Cu(II) adsorption from aqueous solutions using the nanostructured and conventional materials were studied. The results of the comparative kinetic tests demonstrate a 10-fold superiority of the GO over the commercially available coconut AC regarding the maximum Cu(II) adsorption capacity.

Acknowledgements

The research was funded by the Ministry of Education and Science of the Russian Federation under Project No. 16.1384.2017/PCh.

References

- [1] Zhao G., Li J., Ren X., Chen C., Wang X. Few-layered graphene oxide nanosheets as superior sorbents for heavy metal ion pollution management. *Environ. Sci. Technol.*, 2011, **45**(24), P. 10454–10462.
- [2] Kadirvelu K., Faur-Brasquet C., Le Cloirec P. Removal of Cu(II), Pb(II), and Ni(II) by adsorption onto activated carbon cloths. *Langmuir*, 2012, **16**(22), P. 8404–8409.
- [3] Imamoglu M., Tekir O. Removal of copper (II) and lead (II) ions from aqueous solutions by adsorption on activated carbon from a new precursor hazelnut husks. *Desalination*, 2008, **228**(1-3), P. 108–113.
- [4] Tofiqhy M.A., Mohammadi T. Adsorption of divalent heavy metal ions from water using carbon nanotube sheets. *J. Hazard. Mater.*, 2011, **185**(1), P. 140–147.
- [5] Wu C.-H. Studies of the equilibrium and thermodynamics of the adsorption of Cu^{2+} onto as-produced and modified carbon nanotubes. *J. Colloid Interface Sci.*, 2007, **311**(2), P. 338–346.

New superparamagnetic fluorescent Fe@C-C₅ON₂H₁₀-Alexa Fluor 647 nanoparticles for biological applications

A. S. Garanina^{1,2}, I. I. Kireev³, I. B. Alieva³, A. G. Majouga^{2,4}, V. A. Davydov⁵, S. Murugesan⁶,
V. N. Khabashesku⁶, V. N. Agafonov¹, R. E. Uzbekov^{7,8*}

¹GREMAN, UMR CNRS 7347, Francois Rabelais University, Tours, France

²National University of Science and Technology “MISiS”, Moscow, Russia

³Belozersky Institute of Physico-Chemical Biology, Moscow State University, Moscow, Russia

⁴Faculty of Chemistry, Lomonosov Moscow State University, Moscow, Russia

⁵L. F. Vereshchagin Institute for High Pressure Physics of the RAS, Moscow, Russia

⁶Center for Technology Innovation, Baker Hughes a GE Company, Houston, TX, USA

⁷Faculty of Medicine, Francois Rabelais University, Tours, France

⁸Faculty of Bioengineering and Bioinformatics, Moscow State University, Moscow, Russia

*rustem.uzbekov@univ-tours.fr

PACS 68.37.Lp, 75.75.Cd

DOI 10.17586/2220-8054-2018-9-1-120-122

The structure and physical properties of superparamagnetic Fe@C nanoparticles (Fe@C NPs) as well as their uptake by living cells and behavior inside the cell were investigated. Magnetic capacity of Fe@C NPs was compared with Fe₇C₃@C NPs investigated in our previous work, and showed higher value of magnetic saturation, 75 emu.g⁻¹ (75 Am².kg⁻¹), against 54 emu.g⁻¹ (54 Am².kg⁻¹) for Fe₇C₃@C. The surface of Fe@C NPs was alkylcarboxylated and further aminated for covalent linking to the molecules of fluorochrome Alexa Fluor 647. Fluorescent Fe@C-C₅ON₂H₁₀-Alexa Fluor 647 NPs (Fe@C-Alexa NPs) were incubated with HT1080 human fibrosarcoma cells and investigated using fluorescent, confocal laser scanning and transmission electron microscopy. No toxic effect on the cell physiology was observed. In a magnetic field, the NPs became aligned along the magnetic lines inside the cells.

Keywords: superparamagnetic fluorescent Fe@C nanoparticles, electron microscopy, magnetic field.

Received: 9 May 2017

Revised: 12 September 2017

1. Introduction

The search for applications of magnetic nanoparticles (NPs) in biology and medicine has become an area of extensive research. The influence of shape, size, composition, modifications and magnetic properties of NPs in living cells is being actively explored. Superparamagnetic NPs with chemical formula Fe₇C₃@C were previously obtained by us at high pressure and temperature and investigated by physico-chemical and biological methods [1–4].

In this work, new superparamagnetic carbon coated iron NPs (Fe@C) with higher magnetic saturation compared with Fe₇C₃@C were treated by acids to eliminate uncoated iron NPs, selected by magnet, chemically modified, labeled with fluorescent marker Alexa Fluor 647 and studied for further biological application.

2. Experimental section

The pristine NPs of Fe@C formula (carbon coated magnetic iron nanopowder of 25 nm APS purchased from Sigma Aldrich, USA) were suspended in water and treated by high power ultrasound to break up large aggregates. Fe@C NPs were then treated by a mixture of H₂SO₄ and HCl acids to eliminate the uncoated iron NPs, and then selected by magnet to dispose of non-magnetic NPs. The carbon onion-like surface of NPs was alkylcarboxylated and further aminated similar to work [5] for covalent linking to the molecules of fluorochrome Alexa Fluor 647. The magnetization curve was obtained out in GREMAN laboratory on a Quantum Design physical property measurement system magnetometer (PPMS).

These fluorescent superparamagnetic NPs were added to HT1080 human fibrosarcoma cells seeded on glass-bottomed Petri dishes (LabTek, USA) at density of 10⁵ cells/ml. NPs concentration in the culture medium was 20 μg/ml. After 24 h of co-cultivation, a permanent commercial NdFeB magnet (cube with 5 mm edge length, magnetic field of 0.15 T), protected by gold shell, was placed in Petri dish [4]. Cells were observed at such conditions for 16–24 h using time-lapse confocal microscopy. An environmental chamber was kept at 37 °C and

under 5 % of CO₂. The chamber was mounted on an Olympus IX70 inverted microscope equipped with CCD-camera Orca-RT+ (Hamamatsu, Japan) and controlled by Micromanager 1.4 software. Illumination conditions (ND filters, lamp voltage, exposure time) were set to minimize photo toxicity. Subsequently, cells were washed several times with fresh pre-warmed medium to remove free particles, fixed in 2.5 % glutaraldehyde in 100 mM phosphate buffer (pH 7.4) for 2 hours with subsequent post-fixation in 1 % OsO₄, and finally embedded in Epon (Sigma, USA). Serial ultrathin sections (70 nm) were prepared with Leica ultramicrotome and observed using JEM 1011 transmission electron microscope (JEOL, Japan) at 100 kV.

3. Results and discussion

The obtained suspension contained NPs of spherical shape with average size of 25 nm, as specified by the provider and was shown by our HRTEM study. Their surface was coated with multiple layers of onion-like carbon. A magnetization curve (M vs. H) of Fe@C, obtained at room temperature with SQUID instrument, showed the typical superparamagnetic behavior with a high value of magnetic saturation, 75 emu.g⁻¹ (75 Am² kg⁻¹), which was higher than that for Fe₇C₃@C 54 emu.g⁻¹ (54 Am² kg⁻¹). It was shown that cells began to absorb the aggregates of NPs during first 30 minutes of co-cultivation. Prolonged biological experiments demonstrated that Fe@C NPs displayed high efficiency of cellular uptake and didn't affect cytophysiological parameters (cell proliferation, spreading, and cell death) of cultured HT1080 human fibrosarcoma cells. In a magnetic field, aggregates of Fe@C NPs became aligned along the magnetic lines inside the cells (Fig. 1a). Fluorescence signal of Alexa Fluor 647 was precisely co-localized with the NPs aggregates visible in phase contrast microscopy (Fig. 1b).

Transmission electron microscopy analysis showed that aggregates of Fe@C NPs were localized directly in the cell cytoplasm without membrane surrounding. We did not detect an ultrastructure defects of cells containing NPs. Inside the cells, NPs retained carbon onion-like layers on their surface, known to be stable in cellular environment [1,2] which protected cells from pure iron influence (Fig. 1c-e).

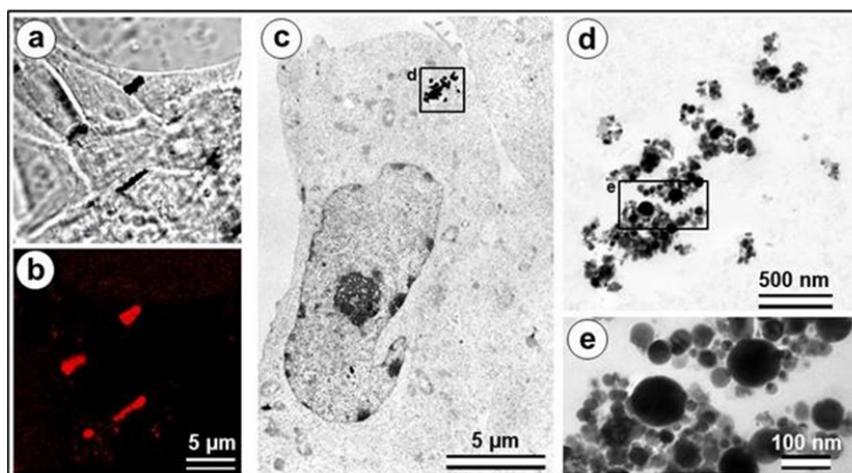


FIG. 1. Representative micrographs of the cells with Fe@C-Alexa NPs inside under magnetic field. Cells were incubated with 20 $\mu\text{g/ml}$ of NPs for 24 h, then placed in magnetic field for 16 h. NPs aggregates are oriented along the magnetic field lines. a) Phase contract microscopy; b) confocal laser scanning microscopy of the same cells; c) transmission electron microscopy photograph of whole cell with Fe@C-Alexa NPs aggregates inside at low magnification; d) magnified view of Fe@C-Alexa NPs aggregates from the boxed area on panel c; e) high magnification of Fe@C-Alexa NPs in selected region on panel d

4. Conclusion

Fe@C-Alexa NPs are internalized by cells and show no significant effect on their cytophysiology.

The Magnetic properties of Fe@C-Alexa NPs are significantly higher than those for Fe₇C₃@C NPs and are therefore sufficient for successful manipulation at the intracellular level. The combination of confocal and phase-contrast microscopy shows that the fluorescent signal detected inside the cells corresponds to Fe@C-Alexa NPs.

Electron microscopy reveals that inside the cells, NPs retain carbon onion-like layers on their surface.

Fluorescent labeling of NPs with fluorochrome Alexa Fluor 647 provides an opportunity to reliably identify Fe@C-Alexa NPs inside the cells and in perspective inside the body of experimental animals.

Since the new Fe@C-Alexa NPs exhibit better superparamagnetic properties than previously-used NPs, they penetrate efficiently into the cell, do not cause a physiological harm and do not lose the protecting carbon layers and the fluorescent label, thus providing good opportunity for biological applications.

Acknowledgements

This study was supported by the Russian Foundation for Basic Research (grants 18-03-00936, 15-04-08550), Program of MSU development (PNR 5.13), Russian Science Foundation (17-15-01290) and IBiSA Electron Microscopy Facility of Francois Rabelais University.

References

- [1] Uzbekov R.E., Kireev I.I., Alieva I.B., Davydov V.A., Rakhmanina A.V., Agafonov V. Interaction of Iron Carbide Nanoparticles protected by Carbon Shell Onion-like Structure with living Cells. Joint Intern. Conf. "Advanced Carbon Nanostructures" (ACNS' 2013), St.Petersburg, Russia, P. 60.
- [2] Davydov V., Rakhmanina A., Kireev I., Alieva I., Zhironkina O., Strelkova O., Dianova V., Samani T. D., Mireles K., Yahia L.H., Uzbekov R., Agafonov V., Khabashesku V. Solid State Synthesis of Carbon-Encapsulated Iron Carbide Nanoparticles and Their Interaction with Living Cells. *J. Mater. Chem. B*, 2014, **2**, P. 4250–4261.
- [3] Alieva I., Kireev I., Rakhmanina A., Garanina A., Strelkova O., Zhironkina O., Cherepaninets V., Davydov V., Khabashesku V., Agafonov V., Uzbekov R. Magnet-induced behavior of Iron Carbide (Fe_7C_3 @C) Nanoparticles in the Cytoplasm of Living Cells. *Nanosystems: Phys., Chem., Math.*, 2016, **7**(1), P. 158–160.
- [4] Alieva I., Kireev I., Garanina A., Alyabyeva N., Ruyter A., Strelkova O., Zhironkina O., Cherepaninets V., Majouga A.G., Davydov V., Khabashesku V., Agafonov V., Uzbekov R. Magnetocontrollability of Fe_7C_3 @C superparamagnetic nanoparticles in living cells. *J. Nanobiotechnology*, 2016, **14**(1), P. 67–78.
- [5] Peng H., Alemany L., Margrave J., Khabashesku V. Sidewall Carboxylic Acid Functionalization of Single-Walled Carbon Nanotubes. *J. Am. Chem. Soc.*, 2003, **125**, P. 15174–15182.

Electrodes of supercapacitors from nanoporous carbon with nanocarbon additives

E. A. Kiseleva, M. A. Zhurilova, E. I. Shkolnikov

Joint Institute for High Temperatures, Russian Academy of Sciences,
Izhorskaya st. 13 Bd.2, Moscow, 125412, Russia
kanna787@mail.ru

PACS 61.46.+w

DOI 10.17586/2220-8054-2018-9-1-123-124

Electrochemical double-layer capacitors (EDLC) are emerging energy storage technology, highly demanded for rapid transition processes in transport and stationary applications, concerned with rapid power fluctuations. Rough structure of activated carbon, widely used as electrode material because of its high specific area, leads to poor electrode conductivity. Therefore there is the need for conductive additive to decrease internal resistance and to achieve high specific power and high specific energy. Usually, carbon black is widely used as conductive additives. In this paper, electrodes with different conductive additives – two types of carbon black and single-walled carbon nanotubes – were prepared and characterized in organic electrolyte-based EDLC cells. Electrodes are based on original wood-derived activated carbon produced by potassium hydroxide high-temperature activation at Joint Institute for High Temperatures RAS. Electrodes were prepared from slurry by cold-rolling. For electrode characterization cyclic voltammetry, equivalent series resistance measurements and galvanostatic charge – discharge were used.

Keywords: carbon nanotube, activated carbon, electrochemical double-layer capacitors, electronic properties.

Received: 19 June 2017

1. Introduction

Carbon nanotubes are a very attractive material for power source applications due to their high conductivity, chemical stability and excellent ability to form percolation clusters in an electrode structure [1]. Activated carbon is a more traditional and efficient electrode material, which allows specific capacitance of about 100 F/g for organic electrolyte EDLC and 150–200 F/g for aqueous EDLC [2]. So high surface area can be considered as the main advantage of activated carbon as an electrode material, but high surface area usually means rough surface, and, because of large structure defects amounts, low conductivity. This leads to loss of energy, stored in EDLC and low specific power, which is the most important EDLC parameter. To increase specific power, carbon nanotubes or other conductive, but chemically-stable, electrolyte solution-soluble additive must be used in the electrode structure.

2. Experimental

The strategy of our approach was to use high-quality carbon nanotubes, received from OCSiAl company [3] to improve the conductivity of electrode and decrease weight percentage of carbon additive (due to high aspect ratio of these nanotubes) which doesn't participate in electric double layer formation. Some traditional additives (carbon black Vulcan XC72R and P267E (RAS Institute for Hydrocarbon Processing Problems)) were used as reference materials to derive the effect of carbon nanotubes and compare them with traditional additives. To characterize electrochemical behavior of different conductive additives, composite electrodes were prepared and tested in a supercapacitor single cell. Slurry from activated carbon, conductive additive and PTFE emulsion was prepared, containing about 8 wt% (dry) PTFE, 10 wt% (dry) carbon additive (in the case of carbon black) and 82 wt% (dry) of activated carbon. In the case of carbon nanotubes (Tuball™ deionized water dispersion of single-walled carbon nanotubes (0.1 wt% of CNT), received from OCSiAl company), dry weight of conductive additive was 0.005–0.012 wt% (because of addition 5–10 wt% of dispersion to slurry), and activated carbon share increased up to about 95–96 wt%. The slurry was mechanically mixed using Ultra Turrax T10 during 10 min, after that, solvent was partly evaporated to receive active mass which was fed to rolling press MSK-HRP-MR100DC (MTI Corp., USA) and rolled several times to obtain a composite PTFE-bound carbon sheet with 100–140 μm thickness. A more thorough procedure for electrode preparation is given in [4]. These sheets were annealed at 250 °C in Binder™ vacuum chamber for 4 h to finally remove residual water and solvent from electrode. After annealing, electrode specimens of 30×30 mm area were prepared from sheets in Ar-filled glove box for testing in supercapacitor cells. Aluminum carbon-covered foils from MTI-Corp (USA) were used as current collectors. Cells were assembled in dry atmosphere (dry glove box filled with Ar gas) and filled with 1 M tetraethylammonium tetrafluoroborate (TEA-BF₄) in electrochemical grade (water content <50 ppm) dissolved in acetonitrile (AN) purchased from BASF, USA, using cellulose-based separator. Cells were laminated to prevent moisture and impurities penetration

from the environment was also conducted in a dry box under Ar atmosphere. To analyze carbon nanotubes content influence, three additional groups of electrodes were prepared – with 0.005, 0.008 and 0.012 wt% of carbon nanotubes additive.

In all experiments, activated carbon produced in Joint Institute for High Temperatures from pyrolyzed birch by alkaline activation technique based on described in [5] was used as active material of electrode.

Cyclic voltammetry (CVA) was carried out using the electrochemical analyzer VoltaLab PGZ 301, galvanostatic cycling (GC) with the current density of 10 mA/cm² and electrical impedance spectroscopy (EIS). All measurements were carried out in range from 1.25 up to 2.5 V of cell voltage.

3. Results and discussion

Results for primary GC and resistance (R) measurements by voltage drop for different electrodes are given in Table 1 (after 1000 cycles).

TABLE 1. Results of primary GC for different electrode composition

Electrode composition (conductive additive)	C_{spv} , F/cm ³	C_{spm} , F/g	R , Ohm	Energy efficiency, %
Tuball CNT, 0.005 wt%	20.42	123	0.18	95.9
Tuball CNT, 0.008 wt%	20.74	126	0.15	96.7
Tuball CNT, 0.012 wt%	23.8	152	0.13	97
P267E carbon black, 10 wt%	18.8	122	0.18	96.1
Vulcan XC72R carbon black, 10 wt%	19.1	114	0.23	95.4

Table 1 data shows, that 0.005 wt% of single-walled carbon nanotubes is enough to reach capacity, efficiency and R , close to those for 10 wt% of carbon black. Slight increase in capacity for Tuball CNT-containing electrode comparing to carbon blacks can be explained by increase of activated carbon weight share in electrode. This additional carbon, substituting carbon black, can introduce additional capacity. Further capacity growth (with CNT mass increase) may be caused by introduction of CNT between activated carbon particles thus preventing their agglomeration. Additional pore volume is available for electric double layer formation and electrode capacity increases. Two types of carbon black, involved in experiments, demonstrate close to each other parameters with slightly higher ESR for Vulcan XC72R and slightly lower capacity for P267E, which can be explained by more rough surface structure in case of Vulcan XC72R.

4. Conclusion

EDLC electrodes with single-walled carbon nanotubes and two types of carbon black as conductive additives were prepared and tested in model EDLC cells with 1 M tetraethylammonium tetrafluoroborate solution in acetonitrile as electrolyte. 0.005 wt% of CNT allowed us to obtain cell equivalent series resistance and energy efficiency close to those for 10 wt% of carbon black. Substitution of carbon black with activated carbon allowed an increase in the specific capacity of electrodes. Increase of CNT content up to 0.012 wt% led to a 25 % increase in the electrode specific volumetric capacitance and further equivalent series resistance, possibly due to percolation cluster formation from CNT and decrease of activated carbon agglomeration degree. Thus, high-quality single-walled carbon nanotubes can be used as conductive additive to EDLC electrode instead of carbon black, increasing capacitance and decreasing resistance.

Acknowledgements

This research has been supported by Leading Scientific School NSh.8406.2016.8.

References

- [1] Krause B., Potschke P., Ilin E., Predtechenskiy M. Melt mixed SWCNT-polypropylene composites with very low electrical percolation. *Polymer*, 2016, **98**, P. 45–50.
- [2] Pandolfo A.G., Hollenkamp A.F. Carbon properties and their role in supercapacitors. *J. Power Sources*, 2006, **157**, P. 11–27.
- [3] New production technology for single wall carbon nanotubes. *Reinforced Plastics*, 2014, **58**(4), P. 19. URL: <http://www.sciencedirect.com/science/article/pii/S0034361714701730>.
- [4] Kiseleva E.A., Lelin F.V., Zhurilova M.A., Shkolnikov E.I. Methods of forming electrodes of supercapacitors with aqueous and organs. *Russ. J. Appl. Chem.*, 2017, **90**(5), P. 712–715.
- [5] Volperts A., Dobele G., et al. Supercapacitor electrodes from activated wood charcoal. *Bulgar. Chem. Commun.*, 2016, **48**, P. 337–341.

Facile synthesis of 2D carbon structures as a filler for polymer composites

A. P. Voznyakovskii, A. Yu. Neverovskaya, Ja. A. Otvalko, E. V. Gorelova, A. N. Zabelina

S. V. Lebedev Research Institute of Synthetic Rubber, St. Petersburg, Russia

voznap@mail.ru, anna-neverovskaya@yandex.ru

PACS 61.48Gh

DOI 10.17586/2220-8054-2018-9-1-125-128

The method of self-propagating high-temperature synthesis has been employed to prepare 2D graphene structures (SHS-graphSHS procedure for carbonizing cyclic organic structures is a simple accessible method for making 2D graphene structures in practically needed amounts. The material obtained is designated as SHS-graphene. The study on starch carbonization product by combined complementary methods has shown the structure of SHS-graphene particles is similar to 2–3-layered graphene particles. The addition of graphene to NBR matrix results in the significant (to twice) enhancement of strength and thermal characteristics of composition material obtained, as compared to unfilled rubber. A set of complementary methods (scanning electron microscopy, Raman microscopy, X-ray diffraction analysis) evidenced 2–3-layer graphene structure of the substance obtained. SHS-graphene has been utilized to modify NBR and thereby markedly strengthen the polymer matrix.

Keywords: graphene, nitrile-butadiene rubber, self-propagating high-temperature synthesis.

Received: 20 June 2017

Revised: 3 October 2017

1. Introduction

Graphene (Gr) has emerged as a subject of enormous scientific interest due to its exceptional electron transport, mechanical properties, and high surface area. When incorporated appropriately, these atomically thin carbon sheets can significantly improve physical properties of host polymers at extremely small loadings. In the past, several synthetic approaches for graphene monolayers have been reported, including epitaxial growth on single-crystal SiC, direct growth on single-crystal metal film or polycrystalline film through chemical vapor deposition, and chemical reduction of exfoliated graphene oxide layers. Two obstacles prevent of Gr application in real industry of polymer composites: poor efficiency of modern methods of their preparing and, accordingly, their high price.

The present paper was aimed at the development of a single-step highly effective procedure for obtaining 2D carbon structures of reasonable cost and, therefore, useful in real polymeric material science.

The selection of initial organic as a base for synthesizing 2D structures was based on the fact that the said structures were polymers of hexatomic carbon cycles – hexagons. Thus, natural candidates for the initial substance were polysaccharides and starch in particular. The latter is a branched high-molecular plant polysaccharide of amylose and amilopectine [1]. Starch monomer unit is six-carbon sugar (hexose) – glucose. Currently, starch is widely being carbonized to make porous carbon sorbents which are turbostrat structure where, unlike graphite, alternate ordered and disordered regions of carbon rings – hexagons [2]. It could be consistently supposed that starch carbonization at temperatures much higher than those of pyrolysis (~800 °C) and with much faster carbonization rate would avoid hexagon turbostrat assembly, i.e., obtain 2D graphene structures.

The so-named process of hard-flame combustion, i.e. self-propagating high-temperature synthesis (SHS) is known to be characterized by extreme values of both rate and reaction temperature [3]. As compared to pyrolysis and hydrothermal carbonization, SHS processes are advantageous by the simple implementation method, high rate of the synthesis, no need in continuous power feed from external power sources, synthesis in any atmosphere or vacuum and no principal scale limits [4, 5].

2. Experimental

Synthetic procedure. Starch/oxidizer mix in a 1:1 stoichiometric ratio was charged to glass reactor purged with dry argon for 5 min. To start the SHS process, the reactor was lowered into Wood alloy pre-heated up to 200 °C. Start/end of intensive gas evolution in the trap with water evidenced the reaction start/end. The product obtained – carbonized starch (SC) – was a black powder. The yield of final product was approximately 40 %.

Composition material polymer–SC. Low-molecular nitrile-butadiene rubber (NBR) with chlorine-containing end groups was used. SC was gradually added with stirring to pre-heated NBR. The composition thus obtained was ultrasonicated for 1 h, then vulcanized and subjected to testing.

Raman spectroscopy. Spectrometer InVia (Renishaw, GB).

Electron microscopy. Electron micrographs of powders were taken by Raster electron microscopy Supra55VP (Carl Zeiss, Zeiss AG).

X-ray diffractometry. Pictures were taken by diffractometer Shimadzu XRD 7000, within the angle range $2\theta = (10 - 100)^\circ$, pitch 0.02 degree, point exposure 1 s.

3. Results and discussion

Electron micrographs of SC powder see in Fig. 1(a,b). As can be concluded from the data in Fig. 1, SC particles are bulk-plane scales.

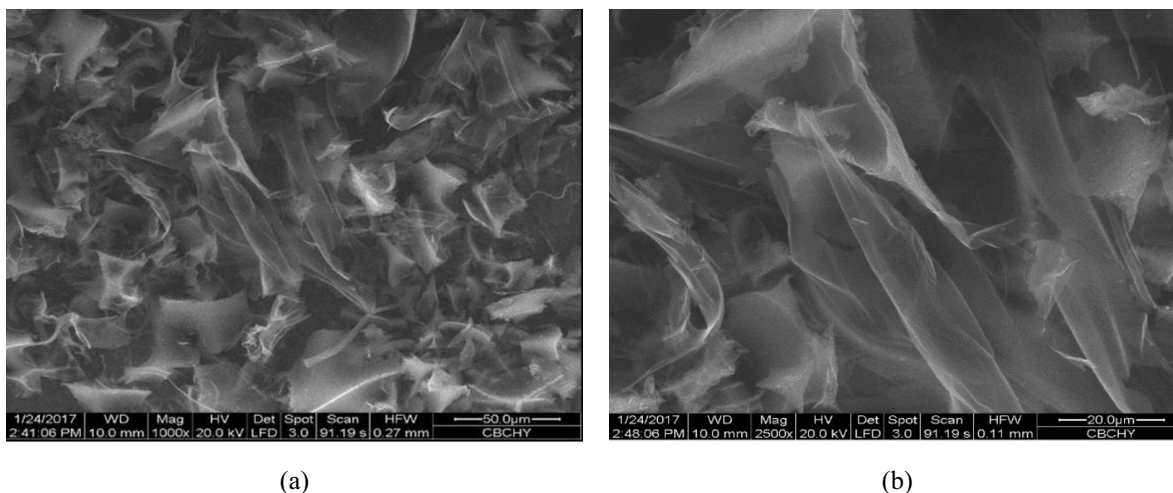


FIG. 1. Electron micrograph of SC powder: a) Mag=1000×; b) Mag=2500×

It should be noted that particles with SC-like geometry are typical for graphene particles [6].

To clarify the nature of the particles obtained, we used the method of X-ray diffractometry (Fig. 2). As can be seen from the data in Fig. 2, the structure of SC particles is radiomorphic and hence, graphite particles do not form in the carbonization by the method used.

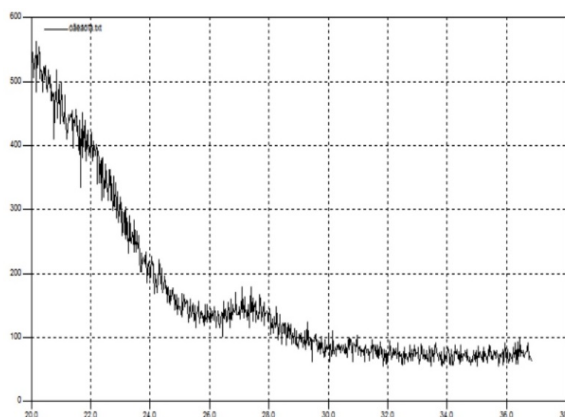


FIG. 2. X-ray diffractometry of SC powder

It is believed that the most reliable information about the architecture of carbon structures can be obtained from Raman spectroscopy data [7]. The corresponding data obtained for SC have been presented in Fig. 3. The general view of the curve by both the shape and peak maxima of respective bands (G peak – $1500-1630\text{ cm}^{-1}$; D peak – 1355 cm^{-1}), correspond to 2D-graphene structures. Indirect conclusions about the number of graphene layers in the SC powders made can be drawn from the comparison of the view of so called 2D band (2700 cm^{-1}) with the reported data (presented in the in cut of Fig. 3). Comparing this data, we can assume without significant error that the mean value of graphene layers in our experiments is 2–3.

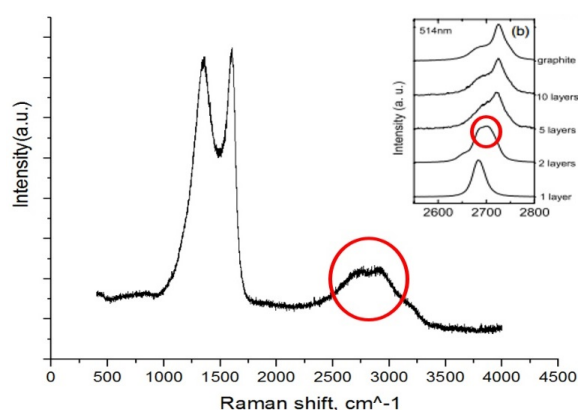


FIG. 3. Raman spectrum of carbonized starch powder

In general, SHS process is a redox chain reaction running under specific conditions. As classified, our version of SHS process falls under “solid–gas” systems, where polysaccharide (starch) is employed as reducing agent and gaseous products of ammonium nitrate thermal decomposition are oxidizers.

It should be emphasized that the proposed method for preparing 2D graphene structures principally differs from methods currently in use. Namely, it is based not on the exfoliation of ready graphene, but on complex processes of degradation/self-assembly of cyclic organics. In this regard, it is advisable to designate 2D carbon structures obtained as SHS-graphene.

One of indirect proof for the correlation of SHS-graphene and 2D carbon structures made through graphite exfoliation, can be significant strengthening attained by graphene adding to host polymer [8]. Nitrile-butadiene rubber with chlorine-containing end groups have been chosen as a base polymer.

Below are tabulated data on strength properties for initial and SHS-filled polymers (Table 1).

TABLE 1. SHS-graphene influence on nanocomposite strength characteristics

Indices	SHS-graphene content, % mass					
	0	1	2	4	6	6 ¹
Tensile strength at 20 °C, MPa	1.62	1.81	2.10	2.70	2.92	3.19
Elongation at break at 20 °C, %	182	173	163	176	124	134
Tensile strength at 125 °C, MPa	0.86	0.89	1.45	1.43	1.70	1.72
Elongation at break at 125 °C, %	59	50	41	54	47	36
Tear strength, kgf/cm	7.4	7.6	11.0	11.7	11.9	11.0

¹composition material was thermo-treated at 200 °C for 15 min.

As it is shown in Table 1, strength values of composition material increase (almost twice) with increasing SHS-graphene content. The increase in tensile strength at higher temperature (also twice as well) should be emphasized. The latter ensures a satisfactory stability of service properties.

Interesting results have been obtained after thermal treatment of filled polymer followed by the curing. Short-term heating of composition material over degradation temperature of initial NBR was found not to reduce, but improves strength characteristics of finished articles to some extent. One more characteristic of interest from practical viewpoint is tear strength (crack resistance) – it grows by 50 %. Tear strength characterizes the contribution of local tension centers in the bulk of polymer matrix to strength properties of composites. The higher the value, the lesser are defects in composite structure and, hence the longer service life of the finished product under, e.g. enhanced vibration. The growth of the value can be related to the fact that graphene particles fill in the elements of polymer void volume and thereby decrease the number of local tension centers and, respectively, lower the possible propagation of the main crack in the bulk of composition material. The said assumption is corroborated by polymer matrix T_g independence of graphene content (Table 2).

TABLE 2. Glass-transition temperature of NBR-based composition materials with SHS-graphene loading

Indices	Graphene content, % mass					
	0	1	2	4	6	6 ¹
T_g , °C	-59.3	-60.0	-59.9	-59.3	59.7	-

¹composition material was thermo-treated at 200 °C for 15 min.

Thus, the development of composite materials using graphene is a real prospect. It is easily introduced and distributed throughout the volume of the nitrile-butadiene polymer. Also graphene significantly improves the strength and thermal characteristics of the polymer matrix.

4. Conclusion

SHS procedure for carbonizing cyclic organic structures is a simple accessible method for making 2D graphene structures in practically needed amounts. The material obtained is designated as SHS-graphene.

The study on starch carbonization product by combined complementary methods has shown the structure of SHS-graphene particles is similar to 2–3-layered graphene particles.

The addition of graphene to NBR matrix results in the significant (to twice) enhancement of strength and thermal characteristics of composition material obtained, as compared to unfilled rubber.

References

- [1] *Starch in food: structure, function and applications*, ed. by Ann-Charlotte Eliasson. CRC Press, Cambridge: Woodhead Pub., 2004, 605 p.
- [2] Jin Dingfeng, Yang Xiao, Zhang Ming, Hong Bo, Jin Hongxiao, Peng Xiaoling, Li Jing, Ge Hongliang, Wang Xinqing, Wang Zhengbao, Lou Hui. A novel high surface area spherical carbon from cassava starch. *Mater. Lett.*, 2015, **139**, P. 262–264.
- [3] Sytschev A.E., Merzhanov A.G. Self-propagating high-temperature synthesis of nanomaterials. *Rus. Chem. Rev.*, 2004, **73**, P. 147–159.
- [4] Shuck C.E., Manukyan K.V., Rouvimov S., Rogachev A.S., Mukasyan A.S. Solid-flame: Experimental validation. *Combust. Flame*, 2016, **163**, P. 487–493.
- [5] Merzhanov A.G. History and Recent Developments in SHS. *Ceramics International*, 1995, **21**, P. 371–379.
- [6] Stankovich S., Dikin D.A., Piner R.D., Kohlhaas K.A., Kleinhammes A., Jia Y., Ruoff R.S. Synthesis of graphene-based nanosheets via chemical reduction of exfoliated graphite oxide. *Carbon*, 2007, **45**(7), P. 1558–1565.
- [7] Ferrari A.C., Basko D.M. Raman spectroscopy as a versatile tool for studying the properties of graphene. *Nat. Nanotechnol.*, 2013, **8**(4), P. 235–246.
- [8] Kim H., Abdala A.A., Macosko C.W. Graphene/Polymer Nanocomposites. *Macromolecules*, 2010, **43**(16), P. 6515–6530.

Ion sputtering of nanoclusters, fullerenes and carbon nanotubes

S. N. Kapustin¹, M. K. Eseev^{1,2}

¹Northern Arctic Federal University named after M. V. Lomonosov, Arkhangelsk, Russia

²Laverov Federal Center for Integrated Arctic Research RAS, Arkhangelsk, Russia

hare22@yandex.ru, m_eseev@mail.ru

PACS 79.20.Rf

DOI 10.17586/2220-8054-2018-9-1-129-131

The research of nanoparticle ion sputtering is interesting both from the fundamental point of view – for researching the interior structure of nanoobjects. Additions to the simple model of ion sputtering which allow one to consider special properties of the ion sputtering of nanoparticles, fullerenes and carbon nanotubes are introduced in this project.

Keywords: carbon nanotube, fullerene, ion sputtering, clusters, nanoparticles.

Received: 20 June 2017

Revised: 16 October 2017

1. Collisions of ions and nanoparticles

In the work [1] a model of metal ion sputtering based on simple physical principles was consequently developed. This model allows one to evaluate mass, charge and kinetic spectra of polyatomic clusters with an atom number of $4 < N < 70$ when the deposited ion's ranges in energy from 1–100 keV. The model also describes the sputtering of nonmetallic elements, particularly, carbon and silicon.

The passage of an ion through a nanoparticle is generally studied using methods of molecular dynamics [2, 3]. As an experimental work, this is very difficult because of the size of the target. The main characteristic of the ion sputtering process is the Y coefficient of sputtering, equal to the number of atoms knocked out by one deposited ion. If the length of free run of the bombing ion in the target (λ) is smaller than the cluster size (D), the Y value for the cluster is considered bigger than that for macro bodies. The reason for this is the closure of the collisions cascade in the small volume of the cluster and the big surface area, from which an emission of secondary clusters is possible. This has been confirmed by the work [2]. The cases when $D < \lambda$ and $D \sim \lambda$ are studied in the work [3]. The stochastic nature of collisions leads to the realization of extreme scenarios – in most cases the ion has time to transfer a small part of its energy, or a rare “successful” collision leads to the development of the collision cascade, large excitation and subsequent fragmentation of the cluster. Intermediate cases are unlikely. Consequently, the large-scale spectra of ion sputtering products will mostly be determined by “successful” collisions.

To apply the model to nanostructures, some nanoparticle characteristics need to be considered. In the case of a loose packaging of nanostructures or isolated nanostructures, the size of the excitation area can be considered nearly equal to the nanoparticle size. Using this supposition allows successful calculation of the relative yield of the clusters during fullerenes sputtering, without changing the rest of the model [1].

2. The double sputtering mechanism of fullerenes

In the case of closely packed nanoparticles [4] (a tablet of pressed C₆₀ fullerene powder), the experimental data allow one to suggest the existence of two sputtering mechanisms. In the ion track, where the substance is warmed up to high temperatures and destruction of C₆₀ molecules occurs, their structure does not influence the process of forming clusters. However outside the track, where the excitation is transferred from one molecule to another via collisions, the fullerene can be knocked out of the target as a unitary whole, and only then, it can vaporize several atoms. While calculating the impact of the additional mechanism of cluster yield, the fullerene was considered as a single particle. While dispersing the energy into targets, a depositing ion creates an excitation zone of N_0 atoms. Target atoms receive a q impulse which we find equal for every atom, directed accidentally or with equal probability. The C_n relative yield of clusters from the ion track was calculated by a standard technique [1].

However, collisions cascades spread outside the ion track. Suppose from the moment of the cascade exits outside the track of the bombarding ion until the moment of decreasing of the average energy involved in the ion cascade below E_d captures N_{0f} of fullerene molecules, transferring a q_f effective impulse to them. The value of fullerenes' impulse knocked out beyond the ion track is obviously limited both from above $q_f < 60q$ and below

$q_f > \sqrt{E_d 2m_f}$. In previous work [1], the expression (4) was obtained for W_N – the possibility of emission from the excited cluster zone consisting of N atoms with internal energy E_{int} :

$$\frac{dW_N}{dE_{int}} = \Omega \frac{\sqrt{2(Nq^2/(2m) - E_{int})}}{8\pi^{3/2}(\varepsilon/3)^{3/2}} \times \exp\left(-\frac{3(Nq^2/(2m) - E_{int})}{2\varepsilon}\right), \quad (1)$$

where Ω is the solid angle of the cluster emission, m – atom mass, q – average impulse, received by the atoms of the excited zone during the descent of the ion (in our case, in the ion track), ε – average atom energy, $\varepsilon = q^2/2m$. Suppose the energy of the U_f link of the fullerene is proportional to the cluster surface which contacts with neighboring clusters and equals hE_d , where h is a coefficient of the target looseness; $h = 1$ when fullerenes are as close to each other as possible. To calculate the probability of fragmentation for a C_{60} cluster at the expense of internal energy, we will integrate the spectrum of knocked out clusters with internal energy from $n\delta$ to $(n+1)\delta$:

$$W_N^n = \int_{n\delta}^{(n+1)\delta} \frac{dw_N}{dE_{int}}, dE_{int} \quad (2)$$

where δ is the sublimation energy of one carbon atom of fullerene, n – amount of vaporized from an overheated cluster of atoms. We will calculate the probability of the excited fullerene flying out which will turn into a cluster of $60 - n$ atoms after fragmentation. Fullerenes in the target are considered uncharged. The probability of the fullerene receiving charge during fragmentation was calculated according to the technique described in the work [1]. The results of the calculation are presented in the Fig. 1a.

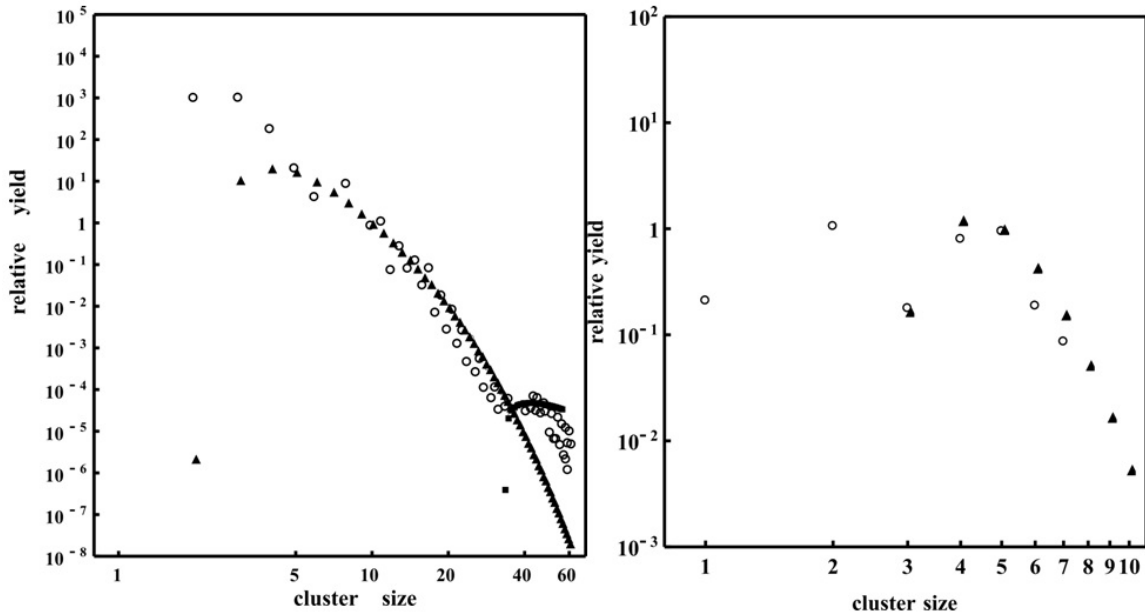


FIG. 1. Left – the relative yield of C_n^- – at C_{60} bombardment with Cs^+ 60 keV ions, triangle – classic model, square – improved model, circle – experiment [4]. Right – the relative yield of C_n^- at CNT bombardment with Cs^+ 5 keV ions, triangle – model, circle – experiment [8]

3. The sputtering mechanism of carbon nanotubes

Carbon nanotubes have a special property which can influence the process of sputtering. This special property is ballistic thermal conductivity [5]. In a perfect CNT, a phonon moves without experiencing any sputtering. In real CNTs there are always a certain number of defects, which is why the thermal conductivity of CNTs is often quasi-ballistic or diffusive, but still remains high.

We assume during the ion bombardment of CNTs in the elastic cascade mode an increase in size of the excitation zone concerning the plain graphite. This assumption is indirectly confirmed by previous work [6], where carbon fibers, possessing a greater thermal conductivity than graphite, are shown to have a greater sputtering coefficient.

CNTs often have inclusions in the form of metal particles. During the ion bombardment on the CNT surface metal nanoclusters can be formed. In the [7] project such CNTs are shown to have a greater sputtering coefficient than graphite. During a continuous bombardment Y increases. This effect is not present during the ion bombardment of graphite. This difference can be explained by the greater efficiency of transferring the impulse from the bombing ion to a metal cluster compared to that to a thin nanotube wall. Then the excitation is transferred from the cluster to the CNT. Graphite, on the other hand, is thick enough to stop the ion completely and absorb its whole impulse. The results of calculations and their comparison to the [8] experiment are shown in Fig. 1b. Calculations were conducted according to the standard model, the size of the excitation zone was considered doubled in comparison to the ordinary case.

4. Conclusion

It is shown that the mechanism of ion sputtering of a single nanoparticle differs very little from the mechanism for macrobodies sputtering. After the presented modernization, the model [1] has good agreement with the experimental data. It has been shown that the interaction between nanoparticles can contribute greatly in the forming of mass spectrum of clusters. Knowing the processes taking part in the ion bombardment of nanoparticles can be used for assessment of nanocoating sustainability, functional nanoaddition in composites, nanoelectronics components and also for obtaining nanoobjects functionalized with nanoclusters.

References

- [1] Kapustin S.N., Matveev V.I. Emission of Charged and Stable Clusters during the Ion Sputtering of Metal. *Bull. Russ. Acad. Sci., Physics*, 2016, **80**, P. 113–116.
- [2] Kissel R., Urbassek H.M. Sputtering from spherical Au clusters by energetic atom Bombardment. *Nucl. Instr. Meth. Phys. Res. B*, 2001, **180**, P. 293–298
- [3] Zhurkin E.E. Investigation of gold nanocluster spraying under bombarding by Au ions with energy 38 keV by the classical molecular dynamics method. *Surface. X-ray, Synchrotron and Neutron Studies*, 2008, **N3**, P. 27–33.
- [4] Verevkin I.V., et al. Emission and fragmentation of C_n and $C_{sm}C_n$ clusters during the fullerite bombardment with cesium ions. *Pis'ma v Zhurnal Tekhnicheskoi Fiziki (Tech. Phys. Lett.)*, 1995, **23**, P. 49–53.
- [5] Eletskii A.V. Transport properties of carbon nanotubes. *Phys. Usp.*, 2009, **52**, P. 209–224.
- [6] Syvorov A.L., Guseva M.I., Korshunov S.N., Zaluzhnyi A.G., Lazarev N.E. Sputtering of carbon materials with ions of hydrogen, deuterium and helium in the third-way region of energy. VANT (Problems of Atomic Science and Technology, Kharkov), 2000, **4**, P. 6–9.
- [7] Ahmad S., et al. Cs+ sputtered clusters from multi-walled carbon nanotubes and graphite. *Nucl. Instr. Meth. Phys. Res. B*, 2012, **271**, P. 55–60.
- [8] Javeed S., et al. Dynamics of fragmentation and multiple vacancy generation in irradiated single-walled carbon nanotubes. *Nucl. Instr. Meth. Phys. Res. B*, 2013, **295**, P. 22–29.

Influence of geometry of nanocrystals on the Raman spectra

A. V. Igo

Ulyanovsk State University, 432017, L. Tolstoy 42, Ulyanovsk, Russia

igoalexander@mail.ru

PACS 78.30-j; 61.46-w

DOI 10.17586/2220-8054-2018-9-1-132-135

It is shown that Raman spectra of nanocrystals with complex geometric shape can acquire additional broadening. In order to describe complex geometric shapes of nanocrystals in terms of its influence on the Raman spectrum, a parameter was introduced for the shape – roughness parameter. The roughness is defined as a relative parameter of the presence of additional volume on the faces of the cubic nanocrystal. The calculations for additional broadening of the Raman spectral line were made for 3–10 nm nanodiamonds.

Keywords: nanodiamonds, Raman spectra, nanocrystal.

Received: 26 April 2017

Revised: 11 October 2017

1. Introduction

Nanocrystals and technical systems based on them are increasingly being used in practice. Special physical and optical properties of nanoparticles are due to quantum size effects.

The size of a nanocrystal influences the Raman spectrum by spatial limitation of optical phonons (phonon confinement). This influence is studied in detail and described in literature [1]. In particular, it was found that the Raman spectrum of nanodiamond is shifted to the lower frequencies and the spectral line acquire additional broadening [2]. Together with the X-ray diffraction method, Raman spectra analysis has become almost a routine method for determining the size of the nanocrystals. This has become possible by obtaining empirical relations between the parameters of the spectral line and the size of the nanoparticles [1]. According to the relations, the frequency ω of the spectral peak and the width of the peak Γ depend on the size of a nanocrystal as:

$$\omega = \omega_0 + \frac{A}{d^{1.5}}; \quad \Gamma = \Gamma_0 + \frac{B}{d^{1.5}}. \quad (1)$$

Here, ω_0 and Γ_0 are the frequency and the width of the peak in the large crystal, and d is the size of the nanocrystal. The exponent at d depends on the type of a nanocrystal, for example, in diamond nanocrystals it equals one [3].

The theory of phonon confinement describes the observed phenomena in the spectra of nanoparticles, nevertheless, theoretical studies aimed at improving the model are in progress. The studies are concerning the relation between the size of nanocrystals and the peak shift [4–6] and the width of the peak [4, 5, 7].

It was shown by the method of numerical simulation [7], that the geometric form of nanocrystalline particles significantly influences the width of the Raman spectral line. This means that the empirical coefficient B in the equation (1) depends on a shape parameter of the nanocrystal. A mathematical model of the nanoparticles with the complex shape and the parameter of the geometric shape for the particle were introduced in [7].

This study summarizes the approach used in [7] and presents calculations of the spectral line broadening for some values of the shape parameter. An analytical equation correlating the spectral line width with the size and the shape parameter (roughness) of a nanocrystal is proposed.

2. Model

The intensity of Raman radiation in the model [7] is a sum of intensities from the core volume $V = d^3$ of a nanocrystal and from the additional volume ΔV (Fig. 1).

In accordance with the quantum mechanical approach, an optical phonon in the center of the Brillouin zone, when confined within the length d , acquires a wave vector with the minimum value of $q_d = 2\pi/d$. According to the dispersion law, this changes the frequency of the phonon to $\Omega(q_d)$, the value different from the phonon frequency $\Omega(0)$ in a large crystal.

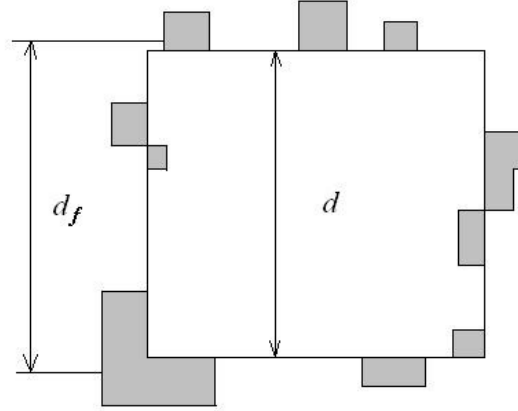


FIG. 1. Nanocrystal of size d_f . The nanocrystal has main volume $V = d^3$ and additional volume ΔV , corresponding to shaded area

The additional volume ΔV can be represented as a sum of volumes of cubes with edge length of d/n (n is an integer number). Given s_n is the probability to find the additional volume $(d/n)^3$ at any face of the main cube, the total additional volume is:

$$\Delta V = \sum_{n=2}^N 6s_n n^2 (d/n)^3 \cong 6sd^3 \sum_{n=2}^N (1/n). \quad (2)$$

The equation (2) assumes a uniform distribution of the probability to find the additional volume for different sizes on the face of the cube, and this probability is denoted by s . Each of the volumes will contribute to scattering of light on the combination frequency $\omega - \Omega(q_n)$, where $q_n = 2\pi n/d$. Here, ω is the frequency of the incident light. The parameter s in (2) may be referred as the roughness parameter of the nanoparticle, since it characterizes the additional volume which resides on the faces of the cube nanoparticle.

Thus, the Raman spectrum of a particle of size d has two contributions: the first one from the main particle volume, d^3 , and the second one from the additional volume generated by geometrical irregularities of the particle with the roughness s :

$$I(\omega) = \frac{(\Gamma/2)^2}{[\omega - \Omega(q_d)]^2 + (\Gamma/2)^2} + \sum_{n=2}^N \frac{6s(\Gamma/2)^2(1/n)}{[\omega - \Omega(q_n)]^2 + (\Gamma/2)^2}. \quad (3)$$

The spectrum (3) has a distinctive asymmetrical form, additionally broadened and shifted towards lower frequencies. The value of the asymmetry, and other parameters of the modified spectral line are determined by the dispersion function of the optical phonons. Here we used the dispersion function $\Omega(q_n)$ from the model of the cubic crystal lattice with additional constraints [8].

3. The spectral line width calculation

The total volume of the particle shown in Fig. 1, $V_f = d^3 + \Delta V$, roughly corresponds to the particle size $d_f = V_f^{1/3}$, and the corresponding Lorentzian intensity of the scattered light is:

$$I(\omega) = \frac{(\Gamma_f/2)^2}{[\omega - \Omega(q_f)]^2 + (\Gamma_f/2)^2}, \quad (4)$$

where $q_f = 2\pi/d_f$.

An actual spectrum is significantly asymmetric and this simple expression does not describe it in full. For the low-frequency wing of the Lorentzian alone ($\omega < \Omega(q_f)$) one can equate (3) and (4) for the same volume:

$$\frac{(\Gamma_f/2)^2}{[\omega - \Omega(q_f)]^2 + (\Gamma_f/2)^2} V_f = \frac{(\Gamma/2)^2}{[\omega - \Omega(q_d)]^2 + (\Gamma/2)^2} d^3 + \sum_{n=2}^N \frac{6sd^3(\Gamma/2)^2(1/n)}{[\omega - \Omega(q_n)]^2 + (\Gamma/2)^2}.$$

The equation must be true for any frequency $\omega < \Omega(q_f)$. Let consider the point $\omega = \Omega(q_d) - \Gamma/2$. In this case, the equation can be solved for the width of the spectral line Γ_f of the particle of a volume V_f with a

roughness parameter s . Given the notations:

$$\beta = \sum_{n=2}^N (1/n); \quad \gamma = \sum_{n=2}^N \frac{(1/n)}{(2^{\frac{\Omega(q_d) - \Omega(q_n)}{\Gamma}} - 1)^2 + 1}; \quad V_f = d^3(1 + 6s\beta), \quad (5)$$

we obtain:

$$(\Gamma_f/2)^2 = (\Omega(q_d) - \Omega(q_f) - \Gamma/2)^2 \frac{1/2 + 6s\gamma}{1/2 + 6s(\beta - \gamma)}. \quad (6)$$

The sizes d and d_f are nearly equal (Fig. 1). By expanding $\Omega(q_d)$ and $\Omega(q_f)$ in Taylor series in the vicinity of $q_f = 2\pi/d_f$ and leaving only the first non-zero term of the expansion, in view of $d_f = V_f^{1/3} = d(1 + 6s\beta)^{1/3}$, we get:

$$\Omega(q_d) - \Omega(q_f) = \left(\frac{\alpha}{d}\right)^2 \left(1 - \frac{d^2}{d_f^2}\right) = \left(\frac{\alpha}{d}\right)^2 \left(1 - \frac{1}{(1 + 6s\beta)^{2/3}}\right).$$

The factor α describing the dispersion of optical phonons in the vicinity of q_d depends on a type of nanocrystal. Finally, the width of the line is:

$$\Gamma_f = \left[\Gamma + 2 \left(\frac{\alpha}{d}\right)^2 \left(1 - \frac{1}{(1 + 6s\beta)^{2/3}}\right) \right] \left(\frac{1/2 + 6s\gamma}{1/2 + 6s(\beta - \gamma)}\right)^{1/2}. \quad (7)$$

Calculations of Γ_f were made for nanoparticles of diamond with the size d in the range of 10–20 lattice constants and the roughness parameter s in the range from 0.01 to 0.2 (Fig. 2). The additional width of the spectral line varies from 0 to 7 cm^{-1} .

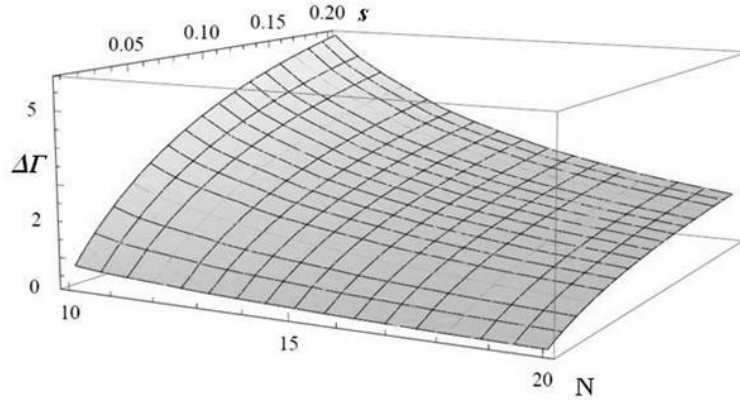


FIG. 2. Additional width of the Raman spectral line of a diamond nanoparticle with size from 10 to 20 lattice constants and a roughness s from 0.01 to 0.2

In many cases of practical importance, it is convenient to deal with spherical crystalline nanoparticles. One can assume that there is an additional volume $\Delta V \approx 0.4d^3$ on the faces of the cube inscribed in such a particle. The estimation of the roughness parameter with (5) and (2) gives $s = \Delta V/(6d^3\beta) \approx 0.07$.

The additional broadening of the spectral line can be taken into account when comparing the theory with an experiment. In [7] such a comparison was performed for spherical nanocrystals of silicon. The additional broadening was added to the theoretical curve obtained in [4]. In this case, the total width of the Raman spectral line more accurately describes the experimental data.

The equation (7) can be simplified for a case when s is small. Assuming $6s\beta \ll 1$ and $\beta > \gamma$, we obtain:

$$\Gamma_f \approx \Gamma + 8\alpha^2 s \frac{\beta}{d^2}. \quad (8)$$

Thus, the additional width is proportional to the value of dispersion of the optical phonons and the roughness of a nanocrystal. The size dependence is determined by the value of β/d^2 . As seen from (5), β is a function of particle size expressed in units of lattice period, $N = d/a$. Direct calculation shows that for a diamond nanocrystal 2–10 nm, β can be approximated by a power law $\beta(d) \sim d^k$, where k is in the range from 0.5 to 0.3. The obtained equation (8) is in a good agreement with the empirical equation (1).

4. Conclusion

The analytical equation for a width of a Raman spectral line in nanocrystals of a complex shape is obtained. The additional broadening of the line is calculated for the nanodiamonds of 3–10 nm in size. This broadening depends on the shape parameter and on the size of the nanocrystal. The proposed analytical equation for the low roughness approximation is in good agreement with the known empirical relation.

References

- [1] Arora A.K., Rajalakshmi M., Ravindran T.R., Sivasubramanian V. Raman spectroscopy of optical phonon confinement in nanostructured materials. *J. Raman Spectrosc.*, 2007, **38**, P. 604–617.
- [2] Mikov S.N., Igo A.V., Gorelik V.S. Raman scattering of light by diamond quantum dots in a potassium bromide matrix. *Phys. Solid State*, 1995, **37**, P. 1671–1673.
- [3] Yoshikawa M., Mori Y., Obata H., Maegawa M., Katagiri G., Ishida H., Ishitani A. Raman scattering from nanometer-sized diamond. *Appl. Phys. Lett.*, 1995, **67**, P. 694–696.
- [4] Faraci G., Gibelisco S., Russo P., Pennisi A.R., Faraci C. Quantum size effects in Raman spectra of Si nanocrystals. *J. Appl. Phys.*, 2011, **109**, P. 074311.
- [5] Volodin V.A., Sachkov V.A. Improved model of optical phonon confinement in silicon nanocrystals. *J. Exp. Theor. Phys.*, 2013, **116**, P. 87–94.
- [6] Meilakhs A.P., Koniakhin S.V. New explanation of Raman peak redshift in nanoparticles. *Superlatt. Microstruct.*, 2017, **110**, P. 319–323.
- [7] Igo A.V. Inhomogeneous size broadening of the Raman scattering spectral line in nanocrystals. *Optics and Spectroscopy*, 2016, **120**(4), P. 529–533.
- [8] Gorelik V.S. Idealized models of crystal lattices and the spectra of real crystals. *Tr: Fiz. Inst. AN*, 1987, **180**, P. 87–126.



NANOSYSTEMS:

PHYSICS, CHEMISTRY, MATHEMATICS

INFORMATION FOR AUTHORS

The journal publishes research articles and reviews, and also short scientific papers (letters) which are unpublished and have not been accepted for publication in other magazines. Articles should be submitted in English. All articles are reviewed, then if necessary come back to the author to completion.

The journal is indexed in Web of Science Core Collection (Emerging Sources Citation Index), Chemical Abstract Service of the American Chemical Society, Zentralblatt MATH and in Russian Scientific Citation Index.

Author should submit the following materials:

1. Article file in English, containing article title, the initials and the surname of the authors, Institute (University), postal address, the electronic address, the summary, keywords, MSC or PACS index, article text, the list of references.
2. Files with illustrations, files with tables.
3. The covering letter in English containing the article information (article name, MSC or PACS index, keywords, the summary, the literature) and about all authors (the surname, names, the full name of places of work, the mailing address with the postal code, contact phone number with a city code, the electronic address).
4. The expert judgement on possibility of publication of the article in open press (for authors from Russia).

Authors can submit a paper and the corresponding files to the following addresses: nanojournal.ifmo@gmail.com, popov1955@gmail.com.

Text requirements

Articles should be prepared with using of text editors MS Word or LaTeX (preferable). It is necessary to submit source file (LaTeX) and a pdf copy. In the name of files the English alphabet is used. The recommended size of short communications (letters) is 4-6 pages, research articles– 6-15 pages, reviews – 30 pages.

Recommendations for text in MS Word:

Formulas should be written using Math Type. Figures and tables with captions should be inserted in the text. Additionally, authors present separate files for all figures and Word files of tables.

Recommendations for text in LaTeX:

Please, use standard LaTeX without macros and additional style files. The list of references should be included in the main LaTeX file. Source LaTeX file of the paper with the corresponding pdf file and files of figures should be submitted.

References in the article text are given in square brackets. The list of references should be prepared in accordance with the following samples:

- [1] Surname N. *Book Title*. Nauka Publishing House, Saint Petersburg, 2000, 281 pp.
- [2] Surname N., Surname N. Paper title. *Journal Name*, 2010, **1** (5), P. 17-23.
- [3] Surname N., Surname N. Lecture title. In: Abstracts/Proceedings of the Conference, Place and Date, 2000, P. 17-23.
- [4] Surname N., Surname N. Paper title, 2000, URL: <http://books.ifmo.ru/ntv>.
- [5] Surname N., Surname N. Patent Name. Patent No. 11111, 2010, Bul. No. 33, 5 pp.
- [6] Surname N., Surname N. Thesis Title. Thesis for full doctor degree in math. and physics, Saint Petersburg, 2000, 105 pp.

Requirements to illustrations

Illustrations should be submitted as separate black-and-white files. Formats of files – jpeg, eps, tiff.



NANOSYSTEMS:

PHYSICS, CHEMISTRY, MATHEMATICS

Журнал зарегистрирован

Федеральной службой по надзору в сфере связи, информационных технологий и массовых коммуникаций

(свидетельство ПИ № ФС 77 - 49048 от 22.03.2012 г.)

ISSN 2220-8054

Учредитель: федеральное государственное автономное образовательное учреждение высшего образования

«Санкт-Петербургский национальный исследовательский университет информационных технологий, механики и оптики»

Издатель: федеральное государственное автономное образовательное учреждение высшего образования

«Санкт-Петербургский национальный исследовательский университет информационных технологий, механики и оптики»

Отпечатано в Учреждении «Университетские телекоммуникации»

Адрес: 197101, Санкт-Петербург, Кронверкский пр., 49

Подписка на журнал НФХМ

На второе полугодие 2018 года подписка осуществляется через

ОАО Агентство «Роспечать»

Подписной индекс 57385 в каталоге «Издания органов научно-технической информации»